Manufacturing Technologies and Applications
İmalat Teknolojileri ve Uygulamaları
(MATECA)

İÇİNDEKİLER (CONTENTS)

Derleme Makale (Review Article)

Manufacturing Technologies and Applications
MATECA

Investigation of Joinability Of 25% Recycled Al6016 Sheets by Friction Stir Butt Welding at Different Tool Rotation Speed

Halil Kırdemir[1,2*] 🆔, Cihan Yakupoğlu[1,2] 🆔, Faruk Varol[2] 🆔, Serkan Apay[3] 🆔

¹Akpres Metal Yedek Parça Mak. San. Ve Tic. A.Ş., Ar-Ge, Sakarya, Türkiye
²Sakarya University of Applied Sciences, Graduate Education Institute Sakarya, Türkiye
³Düzce Üniversitesi, Mühendislik Fakültesi, Düzce, Türkiye

ABSTRACT

In this study, 2 mm thick Al6016 aluminum sheets containing 25% recycled material, commonly used in automotive body and chassis components, were joined using the friction stir welding (FSW) method in a butt joint configuration. Welding was performed on a mold milling machine using a conical tool made of 2379 grade steel, hardened to 62–64 HRC. Constant process parameters included a welding speed of 400 mm/min, tool plunge depth of 1.8 mm, shoulder diameter of 15 mm, and tool tilt angle of 90°. Tool rotation speeds were varied as 600, 1200, 1800, 2400, 3000, and 3600 rpm. Heat input was calculated for each condition. Mechanical performance of the joints was evaluated through tensile, bending, and hardness tests. Macro and microstructural examinations were also conducted, including fracture surface analysis. The highest tensile strength (214 MPa) was obtained at 1800 rpm, while the lowest (83 MPa) occurred at 600 rpm. In bending tests, no fractures were observed at 2400 and 3000 rpm, indicating good ductility and joint integrity. The highest hardness in the weld zone was 97.4 Hv, measured at 600 rpm. Macrostructural observations showed full penetration at all rotation speeds. Microstructural analysis revealed progressive grain refinement from the base metal toward the stir zone, confirming effective plastic deformation and recrystallization. The results demonstrate that tool rotation speed significantly affects joint quality. Optimal mechanical properties were achieved at intermediate speeds, particularly 1800 rpm, highlighting its potential for automotive applications involving recycled Al6016 sheets.

Keywords: Friction stir welding, Recycled Al6016, C2379

%25 Geri Dönüştürülmüş Al6016 Sacların Sürtünme Karıştırma Alın Kaynağı İle Farklı Takım Devir Hızlarında Birleştirilebilirliğinin İncelenmesi

ÖZET

Bu çalışmada, otomotiv gövde ve şasi parçalarında yaygın olarak kullanılan, %25 geri dönüştürülmüş malzeme içeren 2 mm kalınlığındaki Al6016 alüminyum levhalar, alın birleştirme konfigürasyonunda sürtünme karıştırma kaynağı (FSW) yöntemiyle birleştirilmiştir. Kaynak işlemi, yüzey sertliği 62–64 HRC'ye kadar artırılmış konik geometrili 2379 kalite çelikten üretilmiş bir takım ile kalıp freze tezgahında gerçekleştirilmiştir. Süreç parametrelerinden kaynak ilerleme hızı (400 mm/dak), takım daldırma derinliği (1.8 mm), omuz çapı (15 mm) ve takım eğim açısı (90°) sabit tutulmuştur. Takımın dönme hızı ise 600, 1200, 1800, 2400, 3000 ve 3600 dev/dak olacak şekilde değiştirilmiştir. Her hız için ısı girdisi hesaplanmıştır. Birleştirme kalitesi, çekme, eğme ve sertlik testleriyle değerlendirilmiştir. Ayrıca makro ve mikro yapısal incelemeler ile kırılma yüzey analizleri gerçekleştirilmiştir. En yüksek çekme dayanımı (214 MPa) 1800 dev/dak'ta elde edilirken, en düşük değer (83 MPa) 600 dev/dak'ta gözlemlenmiştir. Eğme testlerinde 2400 ve 3000 dev/dak'ta kırılma oluşmamış, bu da iyi süneklik ve kaynak bütünlüğü göstermiştir. Kaynak bölgesinde en yüksek sertlik 97.4 Hv ile 600 dev/dak'ta ölçülmüştür. Makroyapısal gözlemler, tüm dönme hızlarında tam nüfuziyet olduğunu göstermiştir. Mikroyapı incelemeleri, temel metalden kaynak bölgesine doğru ilerledikçe tane boyutunun inceldiğini ve etkin plastik deformasyon ile dinamik yeniden kristalleşmenin gerçekleştiğini ortaya koymuştur. Sonuçlar, takım dönme hızının birleştirme kalitesi üzerinde önemli etkileri olduğunu göstermektedir. Özellikle 1800 dev/dak'ta elde edilen mekanik performans, geri dönüştürülmüş Al6016 levhaların otomotiv uygulamalarında kullanım potansiyelini desteklemektedir.

Anahtar Kelimeler: Sürtünme karıştırma kaynağı, Geri dönüştürülmüş Al6016, C2379

1. INTRODUCTION

The aluminum sheet used in automotive sector production is widely used in the industry due to its strength and lightness. The European Green Agreement aims to switch to a clean, circular economy and to

increase the efficient use of resources by reducing climate change, biodiversity loss, recycling and pollution. Waste aluminum is chopped into small particles and then these pieces are melted in large furnaces. Thus, recycled aluminum, called aluminum, is obtained for reducing carbon emissions [1]. Sectors where friction stir welding is used include automotive, space, aviation, railway transportation, tool tips and ship industries. It is used in welding axles, shafts, pipes and transmission parts in automotive. This method is also one of the methods used in welding parts such as flanges, fittings, pipes and shafts in the machine manufacturing industry [2, 3].

In 1991, the British TWI (The Welding Friction stir welding, which was discovered by the Institute, is a new solid phase welding method that is still being researched a lot. This method was first used to join aluminum materials [4]. Friction stir welding is known as a solid state welding method. Unlike other welding methods, the parts to be joined are joined with the help of heat energy generated by mechanical rotation and applied pressure. In the method in question, the material is welded without melting, by undergoing plastic deformation with friction heat. Since no molten state is formed, no change occurs in the structure of the material. In this way, the mechanical properties of the material will not change after the welding process [4].

The use of the FSW method in industry seems to be increasing rapidly. When compared to gas metal arc welding methods, the absence of consumable elements such as protective gas, electrode or powder makes the method cheaper. The heat input generated in the joining of aluminum alloys with the fusion welding method can cause pore and crack formation in the weld seam as a result of the wide solidification temperature ranges of these alloys and their high thermal expansion. This situation causes the dissolution of hardening precipitates in the heat welding region in age-hardened aluminum alloys, which reduces the strength and hardness in the region under the effect of heat. In addition, welding causes mechanical incompatibility and changes the structural integrity. Today, many metal alloys such as aluminum, unalloyed steels, copper, stainless steels, magnesium and titanium can be joined successfully. The application of the FSW welding method is carried out using a special tip on conventional vertical milling machines [5].

It has been found that FSSW process improves the mechanical properties of the material for hardness, strength, fracture toughness, ductility, fatigue life, and corrosion resistance criteria [6]. The effects of tool-related friction stir welding parameters on different materials have been investigated. The parameters are: rotation speed, dwell time, vertical pressure, inclination angle, and tool geometry [7-11].

Barlas, Z. [12], The effect of tool inclination angle on tensile-shear failure load and weld zone characteristics for 1050 aluminum sheets welded by friction stir overlap welding was investigated. For this purpose, the tool inclination angle was varied from 0° to 5° under fixed other parameters such as tool geometry, tool rotation speed of 1200 rpm and tool movement speed of 30 mm/min. According to the general results, the tool inclination angle has a reasonable effect on the joint strength and weld defect formation. If the tool axis was perpendicular to the plate surface or a larger tool inclination angle was used, such configurations had a detrimental effect on the weld zone.

Barlas, Z. et al. [13], friction stir welding (FSW) parameters of tool rotation speed, tool inclination angle and tool rotation direction were used to join AlMg3 aluminum alloy (Al 5754) sheets with butt joints. When the tool was rotated counterclockwise, a solid and flawless weld was obtained with a tool rotation speed of 1100 rpm and a tool inclination angle of 2 degrees. The maximum tensile strength in the joint made with FSW parameters was 217 MPa, which was 14% lower than that of Al 5754 base metal. In this weld, a value closer to a symmetrical microhardness distribution was measured and the hardness values of the weld nugget region increased slightly, reaching approximately 82 HV.

De Caro, D. et al. [14], analyzed the sheet-aluminum 6181 alloy produced with different scrap content and compared it with a 6181 alloy from primary production. They showed that the alloys from secondary production contained higher amounts of manganese, iron and copper. They observed that the tensile properties did not change significantly, but a small increase in strength, probably related to the increased Cu and Mg content. However, they found the presence of defects in the form of inclusions at the fracture initiations, although the ductility did not change significantly.

D.N. Wang'ombe et al. [15], investigated the effects of feed and rotation speed on the tensile properties, microstructure and microhardness (HV) of extruded recycled Al 6061 alloy by friction stir welding. The studies on friction stir welding of recycled product mainly focused on the alloy content of primary Al 6061, which is different from that of Al 6061. The microstructure of the alloy consists of four zones, namely heat affected zone, thermo-mechanically affected zone, base metal and stirred zone. The average grain size of the gap was 93 μm. For the joints at 530 rpm and 100 mm/min, the average grain sizes were 7 μm in the stirred zone, 183 μm in the heat affected zone and 93 μm in the base metal. It was found that the tensile damage occurred in the heat affected zone exposed to high temperature. It was observed that the hardness decreased to a minimum in the heat affected zone, then there was a short increase in the thermo-mechanically affected

zone and reached another maximum in the stirred zone. The hardness developed in the machined zone was found to be inversely proportional to the tool rotation speed. It was found that the increase in speed increased the increasing heat which deteriorated the properties.

This study was carried out to investigate the mechanical and chemical structure properties of 6016 series sheets by using variable parameters in friction stir welding method for butt welding of 2 mm thick aluminum sheets with 25% recycled content. Test samples were prepared in accordance with TS EN ISO 25239 standards in the joints. For macro and micro imaging, the samples were sanded, polished and etched using Keller reagent (190 ml Pure Water + 3 ml HCl + 2 ml HF + 5 ml HNO3) reagents for 30 seconds. A 500x capacity optical microscope was used for imaging. Tensile strength, hardness measurements and bending tests of the trial joints were also performed.

2. MATERIAL AND METHOD

2.1. Materials Used in Experiments

25% recycled AL6016 alloy series 2 mm thick sheets and 2379 steel material are given in Table 1, and the chemical composition properties are given in Table 2.

Table 1. Mechanical properties of test specimens and agitator tool tip.

Description	(σAk)	(σmax)	Elongation (%)	Hardness (HRC)
AL6016	103 MPa	182 MPa	24	-
2379	1200 MPa	1590 MPa	-	54-60

Tablo 2. Chemical composition (%) of test sample and stirrer tool tip.

Description	Fe	C	Si	Mn	Cr	Al
AL6016	0.24	0.001	0.57	0.14	0.03	98.3
2379	85	1.45-1.6	0.10-0.60	0.20-0.60	11.00-13.00	-

Figure 1. a In accordance with the dimensions given, 2379 quality steel was processed in a lathe and heat treated to 60-64 HRC hardness. 2379 quality tool steel with 60-64 HRC was used in the experiments. The pin to be connected to the milling cutter has a diameter of 20 mm, a shoulder of 15 mm and a length of 90 mm. The mixing tip was manufactured from 2379 tool steel, whose melting point is approximately two and a half times higher than the melting point of the aluminum material. The pin sinking tip of 2379 tool steel was given a conical shape and the tip was machined at an angle of 10 ^{o}.

In friction stir welding, a conical angle structure was created between the shoulder and the part of the mixer tip that will be connected to the vertical milling machine in order to reduce the heat generated by the mixer tip. The reason for this is to increase the contact area of the mixer tip with the air during welding and to discharge the heat generated by friction. The shoulder is the surface that sits on both plates during the friction stir welding stage. Since the shoulder part rubs against the contact surface of the two plates to be joined in friction stir welding, it provides the critical friction heat in friction stir welding. By covering the friction stir welding seam from the top, it minimizes the movement of the material moving upwards caused by the rotation of the tip during welding in Figure 1. b; in this direction, the material is pushed downwards by the shoulder. In Figure 1. c, the welding shoulder is ensured to sink approximately 1.8 mm into the surface of the material to be welded during the mixer tip welding process [16].
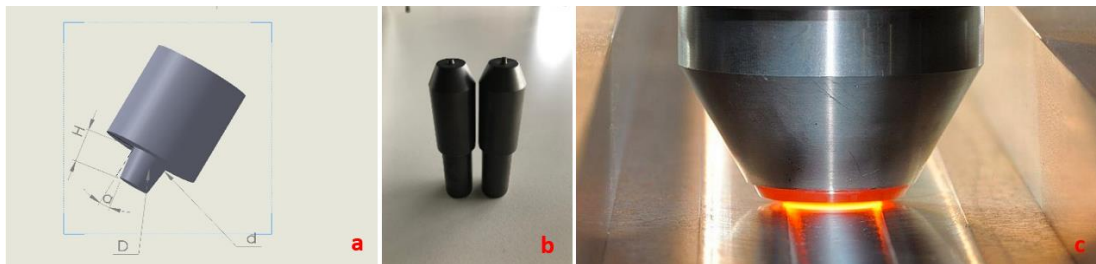
Figure 1. Tool pin desing (a), Tool pin (b), FSW butt weld (c).

2.2. Preparation of Test Samples

During friction stir welding, the aluminum alloy material was not subjected to any oxide removal before welding. The test samples were prepared from Al6016 sheets with dimensions of 2x1200x2400 mm by laser cutting. In friction stir welding, the sheets subject to the process were fixed and connected to the vertical milling machine table by means of connection shoes in a way that they would contact the edges to be welded. 2379 quality tool steel was specially turned and subjected to grinding process. The 25 mm body diameter mixer tip was connected to the vertical milling machine's vertical shaft and friction stir welding was applied to aluminum test sheets using the joining parameters shown in Table 3.

2.3. Applied Method

The joints were made by using the friction stir method in the butt-to-butt position on 25% recycled 2 mm 6016 Al series sheets with the condition of connecting to the milling machine by selecting the 2379 steel tool tip. 3 samples were prepared for each experiment for tensile and bending tests. Test samples were cut and prepared as 200x100 mm. Automatic operating mode was used in the milling machine system for applications. As seen in Figure 2, a special apparatus was manufactured to provide the butt-to-butt joining position and was positioned on the milling machine. Test samples of Al-Al plates joined at different rotation speeds (600 rpm, 1200 rpm, 1800 rpm, 2400 rpm, 3000 rpm, 3600 rpm) were prepared using laser cutting. Tensile test on ZwickRoell Z100 machine ISO 6892–1:2001 Bending tests were carried out according to the TSE EN ISO 5173:2010/A1 standard with a capacity of 50 kN Zwick 3-axis bending method was performed with Roell Z50 device. Hardness values of the samples were taken using Vickers method according to EN ISO 6507 standard with 100 gr load and pyramid indenter.

Figure 2. Milling machine (a), FSW application (b).

For micro and macro imaging, the samples were sanded, polished and etched using Keller reagent (190ml Pure Water + 3ml HCl + 2ml HF + 5ml HNO3) reagents for 30 seconds. A 500x capacity optical microscope was used for imaging. The applied source parameters are shown in Table 3.

2.4. Hardness Measurements

The hardness points of the joints are shown in Figure 3. Sample samples taken in all joining methods (Instron Wolpert) Hardness scanning was obtained at 1 mm intervals on the Vicker hardness tester. 100 gr. test load was applied in the hardness scannings (HV). While measuring the hardness; the base metal, joint area, thermomechanically affected area and weld metal values were scanned at equal intervals on both sides based on the center line of the weld.
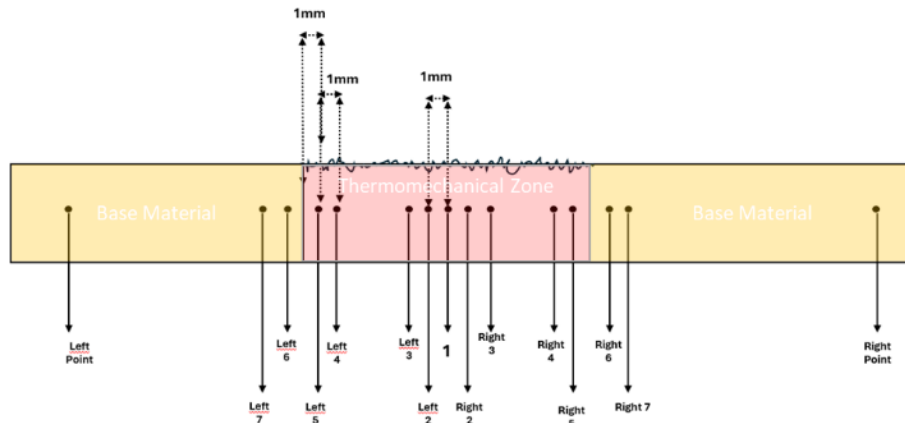
Figure 3. Hardness measurements.

Table 3. Friction stir welding joining parameters.

Base Material	Thickness (mm)	Tool Speed (mm/dak)	Revolutions Per (Rpm)	Tool Material	Tool Geometry	Tool Pin Diameter (d: mm)	Tool Height (h: mm)	Shoulder Diameter (D: mm)	D/d	Tool Angle (o)	Joining Position
AL 6016	2	400	600	2379	Conical	3	1.8	15	5	90	Butt Joint
AL 6016	2	400	1200	2379	Conical	3	1.8	15	5	90	Butt Joint
AL 6016	2	400	1800	2379	Conical	3	1.8	15	5	90	Butt Joint
AL 6016	2	400	2400	2379	Conical	3	1.8	15	5	90	Butt Joint
AL 6016	2	400	3000	2379	Conical	3	1.8	15	5	90	Butt Joint
AL 6016	2	400	3600	2379	Conical	3	1.8	15	5	90	Butt Joint

2.5. Tensile Test Specimens

Tensile tests were carried out on the main material according to TS 138 (EN 10002-1) standard, and on the joined parts.-For the samples, 3 samples for each test were prepared in accordance with TS 287 (EN 895) standard. The technical drawing of the prepared sample and the tensile device test are shown in Figure 4. While the upper and lower clamps perform the tensile process by holding the two ends of the sample, the extensometer shows the changes in the length of a sample, also known as strain measurement.
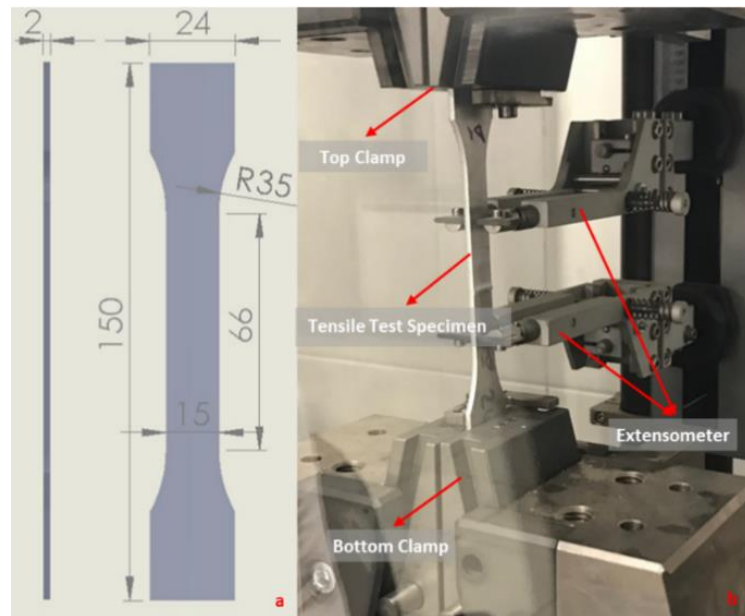
Figure 4. Sample technical drawing (a), Tensile test sample application (b).

2.6. Bending Test

Bending test aims to observe the cracks/breakages etc., that may occur in the weld area of the joined samples in the cold state. The bending test, which is applied according to the ISO 7438 standard, is performed by folding the plates with a thickness specified in Figure 5.a between two rounded supports with a pressure force by means of a bending mandrel of a certain diameter (d=2a). The data obtained in the bending tests were carried out by preparing 3 samples from the base metal and for each parameter of the friction stir welding for a one-time comparison. The schematic and application representation of this machine is given in Figure 5.
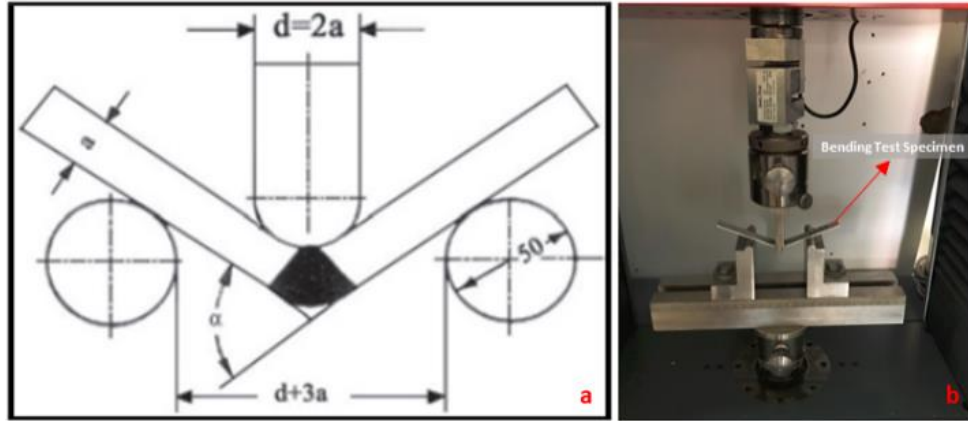
Figure 5. Schematic representation of bending test (a), Bending test specimen examples (b).

While the material is being folded during the bending process, after the first crack is seen, the load is removed and the bending angle of the piece is measured, or the cracks formed on the surface of the material folded 180° with a bending mandrel of a certain diameter and the appearance of its surface are examined.

3. RESULTS AND DİSCUSSİON

3.1. Heat Inputs and Tensile Test

The tensile test results of the joints made according to 6 different speeds, shown in Figure 6, were compared and it was seen that the highest strength was 214 MPa at 1800 rpm, the lowest strength was 83 MPa at 600 rpm. When compared with the base metal tensile strength, it was observed that the values were higher than the base metal at 1800, 2400 and 3000 rpm, but lower in other joints. Figure 6.a shows the images after the tensile test, and Figure 6.b shows the tensile strength (Rm (MPa)) values.
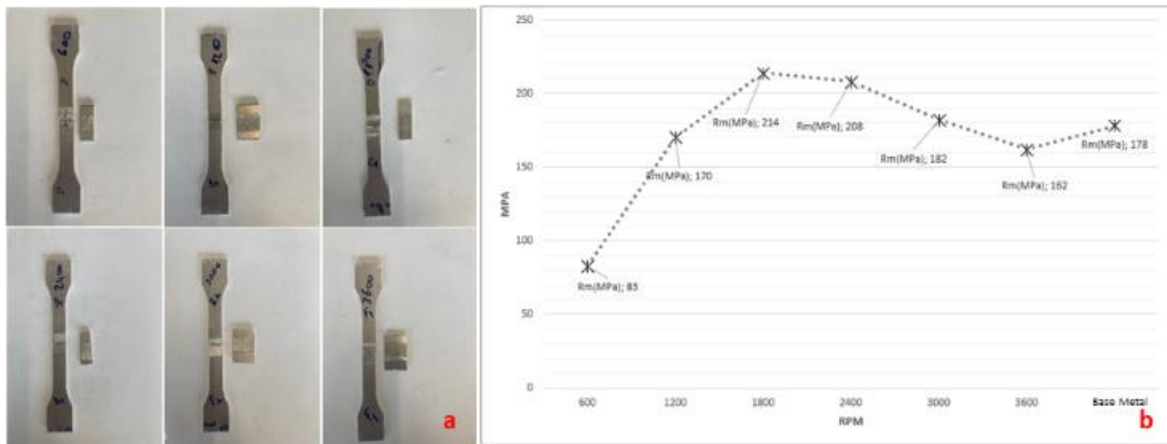
Figure 6. Tensile specimens and rupture zones (a), Rupture strength values graph (b).

Figure 7.a shows the heat input data for the joint at 6 different speeds. The heat inputs are calculated according to formula (1). In the FSW process, the weld heat input is affected by the tool rotation speed rather than the welding speed.

Tm : melting point of the base metal,
ω : rotation speed,
υ welding speed
α : (0.04~0.06) and K (0.65~0.75) are constant

$$T = K \left(\frac{w^2}{v \times 10^4}\right)^a T_m \tag{1}$$

As the speed of rotation increases on the fixed friction surface, the heat is observed to increase, the highest heat input is measured at 3600 rpm and 460 °C. Figure 7.b shows the instantaneous heat generation of the joints. The initial state is at room temperature, and the highest temperature values (375-460 °C) are observed between the 5th and 10th seconds. After the joint, a cooling curve is formed, reaching room temperature again at the 20th second. The highest temperature value is observed at 3600 rpm, while the lowest temperature value is observed at 600 rpm.
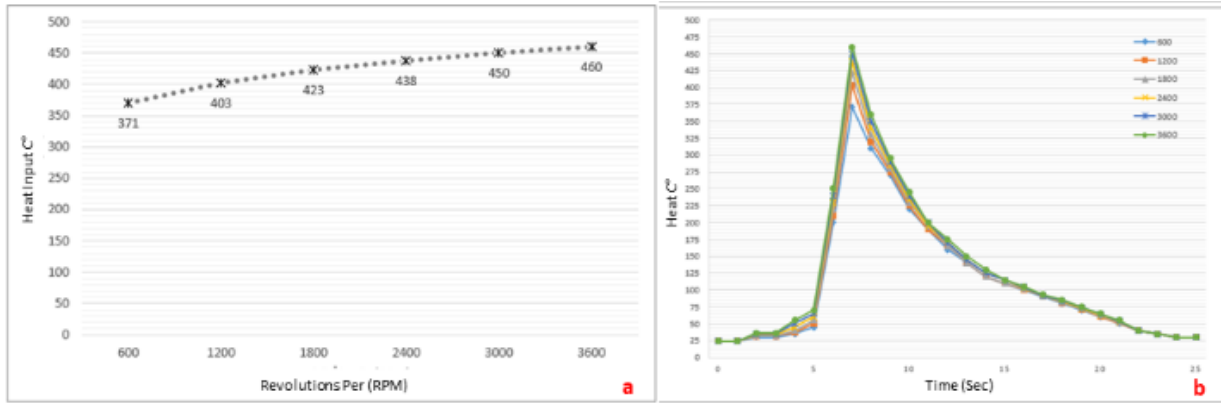
Figure 7. Heat input graph (a), Instantaneous heat generation (b).

The bending test results of the joints are shown in Table 4. The highest bending force was 3000 rpm and no fracture was observed in the weld area. Fractures were observed in the weld areas at 600, 1200, 1800 and 3600 rpm and it was determined that it was unsuccessful.

Table 4. Load and bending force of joints.

Sample	Type	E_f GPa	σ_{fC} MPa	σ_{fM} MPs	ε_M mm	L mm	h mm	b mm
1	3600	34.5	7.43	184	2.0	60	2	15.2
2	3000	33.2	254	310	12	60	2	15.2
3	2400	35.2	227	296	15	60	2	15.2
4	1800	40.9	228	269	7.7	60	2	15.2
5	1200	32.4	231	296	14	60	2	15.2
6	600	-1.3	6.99	65.3	0.32	60	2	15.2

Although the same bending force (296 MPa) was reached at 1200 and 2400 rpm, fractures occurred in the 1200 rpm weld zone, and fractures also occurred at 600, 1800 and 3600 rpm, but it was observed that there was no fracture in the 2400 and 3000 rpm weld zone and the result was successful. It was observed that the mixing and heat input changed in direct proportion to the tool rotation speed, and the fractures that occurred in joints other than 2400 and 3000 rpm were; jointing could not be achieved at 600 rpm, and partial joint areas were formed in joints at 1200 and 1800 rpm. It was observed that the heat input was maximum at 3600 rpm and it was determined that deteriorations (dimensional variation) occurred in the main material during cooling with heat input. It was determined that the fracture zones that progressed from the crack zone formed in the joint zone for all joints were brittle fractures. It was observed that the hardness values in all joint areas were close to each other. The bending forces of the joints are shown in Figure 8. a. The bending application is shown in Figure 8 (b).
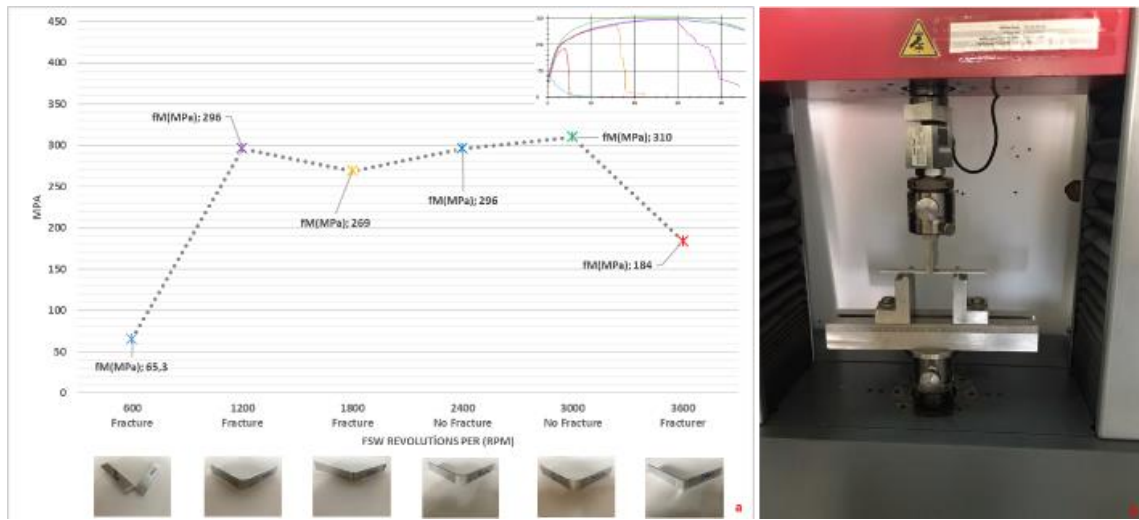
Figure 8. Bending force graph (a), Bending test application example (b).

3.2. Heat Inputs and Tensile Test

The current state of the base material to be joined affects the hardness behavior after FSW. In this study, the hardness line was determined along the cross-section of the weld zone and was monitored sequentially. Al6016 base metals have an average hardness value of 107 ± 2 HV for 2 mm sheet thickness. Figure 9 shows that the hardness of the weld zone of FSW joints decreases significantly at all applied rotation speeds due to the frictional heat generated during FSW processes causing annealing of the Al6016 base metal. For each butt welded joint between the weld zone, minimum hardness values were observed in the thermomechanical zone due to the grain structure and excessive aging effects. In contrast, Ahmed et al. reported that the presence of high hardness areas in the thermomechanical zone is mainly due to the dynamic recrystallized fine grain structure and the redeposition process that may occur during the cooling cycle [17]. It can be attributed to the high heat intensity generated as a result of plastic deformation during the FSW process. In addition, the variations in tensile shear are probably due to the increased thermal softening (changing hardness values) in the thermomechanical area due to the increased heat input and the decrease in the thickness of the layers under the shoulder with pressure. The hardness values after the joints were taken as rank hardness (HV) values from the main material, the joint area and the thermomechanically affected areas and are given in Table 5. The hardness data of all these joints were seen as the highest value of 105 HV in the main material. The hardness values decrease towards the joint area. The lowest value of the joint area was determined as 97.4 HV. The rank hardness values of 6 different joints are shown in Figure 9.

Table 5. Hardness (HV) values at reference points.

Rpm	Left Point	Left2	Left3	Left 4	Left 5	Left 6	Left 7	1	Right 2	Right 3	Right 4	Right 5	Right 6	Right 7	Right Point
600	105	86.4	91.5	90.2	86.2	97.4	96.8	92.1	83.7	96.3	85.9	91.8	102	106	103
1200	68.4	80.8	84.9	83.4	81.9	72.1	74	77.9	79.1	85	75.1	71	73.9	77.3	86.7
1800	90	75.6	77	71.6	71.5	71.3	74.8	74.4	77.2	79.4	71.9	73.8	81.9	83.9	86.4
2400	93.8	84	91.5	84.7	81.1	83.9	92.9	91.3	82.4	81.5	74.2	76	87.4	89.2	104
3000	85.4	78.7	86.6	76.7	73.6	76.5	82.5	77.8	86.9	82.5	86.2	85.8	74.7	78.2	94.4
3600	87.1	84.5	85.5	83.4	84.6	85	81.5	74.5	88.2	73	76.4	74	65.6	66.8	78.9
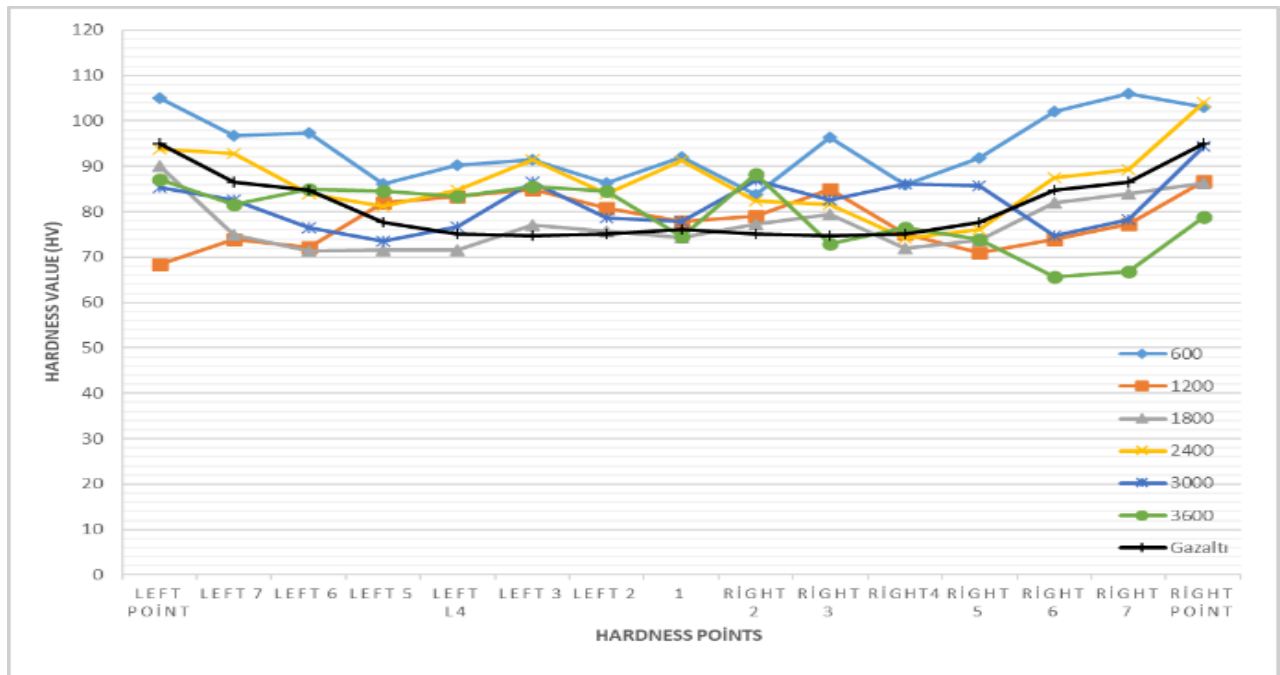
Figure 9. Hardness values.

3.3. Examination of Macro Structures

During friction stir welding of aluminum, the immersed stir tip in the welding region releases the mixing energy in the fusion region and ensures that two different aluminums are mixed together. Figure 10 shows macro images of 6 different joints. Material accumulation (mm), joint adequacy (mm), measurement variation (°), crack formation (mm) and penetration (mm) values are shown in the joint regions. Material accumulation and joint insufficiency were observed at 600 rpm. The joint with the highest measurement variation was 1800 rpm. Crack formation was observed in every joint and was observed most at 2400 rpm. It was observed that sufficient penetration levels occurred at all rpm speeds. While it was observed that the highest tensile strength value was at 1800 and 2400 rpm speeds, it was observed that the tensile strength decreased at other parameter values.

	Joining Area				
Tool Devir Hızı (Rpm)	Material Accumulation (mm)	Competence in Combining (mm)	Dimensional Variability (°)	Crack Formation (mm)	Penetration (mm)
600	0,10	0,10	1,27	2,14	0,38
1200	0,00	0,00	0,16	1,91	0,08
1800	0,00	0,00	0,37	1,81	0,07
2400	0,00	0,00	0,17	2,47	0,09
3000	0,00	0,00	0,17	2,01	0,06
3600	0,00	0,00	0,25	1,21	0,04
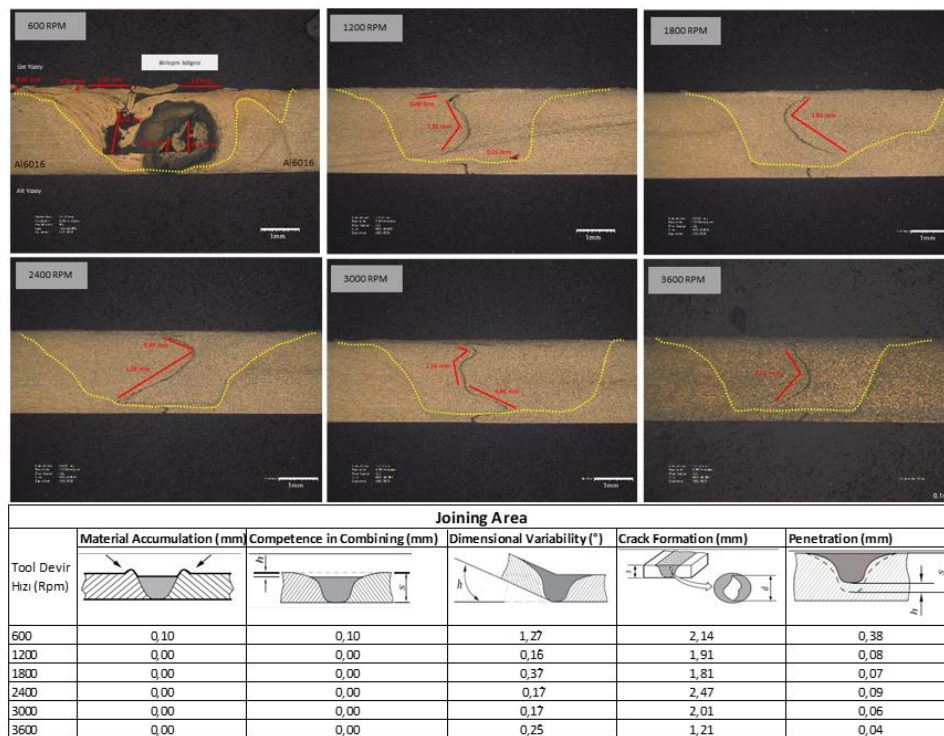
Figure 10. Macro images and joint region defects.

When the fracture surfaces are examined in Figure 11, it was determined that the mixer tip could not provide sufficient mixing during the joint and created thin film-shaped capillary cracks in the inner region of the joint. In addition, since the 600 rpm joint conditions could not be provided in the joints at 6 different speeds, it was not determined that the fracture was in an irregular line. For the joints at other speeds, the same geometry as the crack fault formed in the weld zone and the fracture progress were observed. It was determined that the fracture points occurred in the joint zone where there were micro cracks.
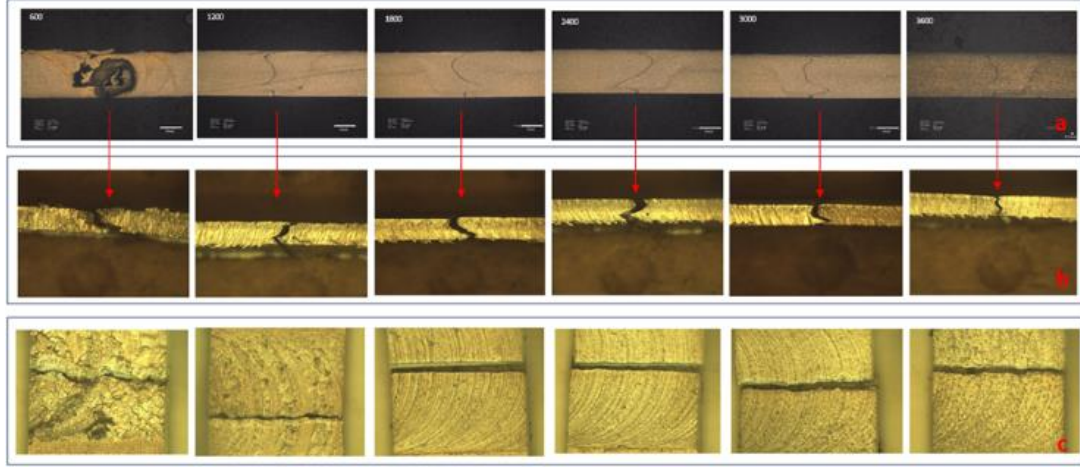
Figure 11. Joining zone microcrack (a), Joining zone front view after fracture (b), Joining zone top view after fracture (c).

3.4. Examination of Micro Structures

When the microstructures and grain sizes between the plates are examined, it shows the effect of heat input on the average thickness of the layer formed between the aluminum and the fusion zone during the friction stir welding process. The thickness of the layer has formed a coarse-grained layer at different speeds since the cooling rate of the FSW source changes in different regions with the change of the welding speed. Depending on the speed values of the mixer tip, the grain thickness is different, and the grain size changes not only with the mixer tip but also with the change of the speed. This affected the mechanical properties of the welded area between the samples after joining. The formation of high temperatures causes intense plastic deformation, which occurs in the material during joining. As a result, fine-structured recrystallized grains are formed. Thanks to the fine-grained microstructure formed, appropriate mechanical properties are obtained in the welding area [18].

Mixing tip, shoulder size and shape are important for mixing and heat input generation. The shoulder also provides compression of the material volume exposed to heat. Another function of the tool is to move the material by mixing it. Tool design and process loads affect the homogeneity of microstructure and properties. A concave shoulder and threaded cylindrical pins are often used. When the critical effect of tool geometry on metal flow is considered, the fundamental correlation between weld microstructure and material flow varies for each tool [19].

In Figure 12, micro images of the joints made at 2400 rpm were taken and it was determined that the grain structure became thinner from the base metal towards the joint area.
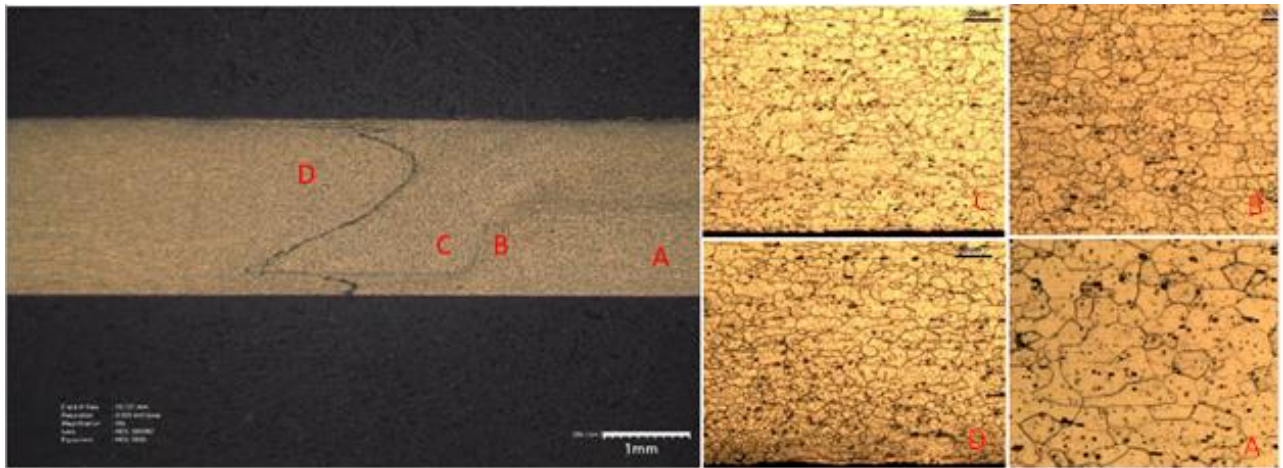
Figure 12. Comparison of micro images.

4. CONCLUSIONS

The joinability of 25% recycled Al6016 sheets by friction stir butt welding was investigated at 6 different tool speeds from 600 to 3600 rpm.

The highest tensile strength value was found to be 214 MPa at 1800 rpm and the lowest value was 83 MPa at 600 rpm at a feed rate of 400 mm/min.

No fracture was observed after the bending test of the specimens joined at 2400 and 3000 rpm. In the bending tests applied to the specimens joined at other rotational speeds, the weld failed by breaking from the weld seam.

The highest results of the joint hardness values were measured as 97.4 HV at 600 rpm rotational speed.

When the macrostructures were analysed, the joint with the highest measured change was 1800 rpm. Crack formation was observed at all joints, with the highest occurrence at 2400 rpm. Adequate penetration levels were found to occur at all rpm speeds.

When the micro images of the joints made at 2400 rpm were analysed, it was observed that the grain structure became thinner from the base metal to the joint region.

ACKNOWLEDGMENT

REFERENCES

[1]   E. Özdemir, B. Ercan, Avrupa Yeşil mutabakatının enerji sektörüne ve otomotiv endüstrisine etkileri ve sonuçları, EJOSAT, 190-202 (2023), https://doi: 10.31590/ejosat.1280352.
[2]   A.W. El-Morsy, M. Ghanem, H. Bahaitham, Effect of friction stir welding parameters on the microstructure and mechanical properties of AA2024-T4 Aluminum Alloy, Engineering, Technology & Applied Science Research, 8 (2018) 2493-2498, https://doi: 10.48084/etasr.1704.
[3]   S.S. Yılmaz, B.S. Ünlü, M. Uzkut, D. Ertürk, Alüminyum alaşımlarında sürtünme karıştırma kaynağı ve uygulamaları, Mühendis ve Makina, 57 (2016) 676.
[4]   C. Meran, M. Colak, Tool holder design for friction stir welding, Journal of the Faculty of Engineering and Architecture of Gazi University, 23 (2008) 671-679.
[5]   B. Çevik, Y. Ozcatalbas, I. Uygur, 7075 Alüminyum alaşımının sürtünme karıştırma kaynağı ile birleştirilmesi, International Conference on Welding Technologies and Exhibition, May 2012, 396-376.
[6]   I. Charit R.S. Mishra, Low temperature superplasticity in a friction-stir-processed ultrafine grained Al–Zn–Mg–Sc alloy, Acta Materialia, 53(15) (2005) 4211-4223.
[7]   J. Gronostajski, H. Marciniak, A. Matuszak, New methods of aluminium and aluminium-alloy chips recycling, Journal of Materials Processing Technology, 106(1) (2000) 34-39.
[8]   Y. Li, L.E. Murr, J.C. McClure, Flow visualization and residual microstructures associated with the friction-stir welding of 2024 aluminum to 6061 aluminum, Materials Science and Engineering: A, 271 (1999) 213-223.
[9]   Ş. Mert, S. Mert, Sürtünme karıştırma nokta kaynak yönteminin incelenmesi", Düzce University Journal Of Science And Technology, 2 (2013) 26-35.
[10] M. Peel, A. Steuwer, M. Preuss, P.J. Withers, Microstructure, mechanical properties and residual stresses as a function of welding speed in aluminium AA5083 friction stir welds, Acta Materialia, 51(16) (2003) 4791-4801, https://doi: 10.1016/S1359-6454(03)00319-7.

[11] S. Malopheyev, I. Vysotskiy, V. Kulitskiy, S. Mironov, R. Kaibyshev, Optimization of processing-microstructure-properties relationship in friction-stir welded 6061-T6 aluminum alloy, Materials Science and Engineering: A, 662 (2016) 136-143.

[12] Z. Barlas, The ınfluence of tool tilt angle on 1050 aluminum lap joint in friction stir welding process, Acta Physica Polonica A, 132(2017) 679-681.

[13] Z. Barlas, U. Ozsarac, Effects of FSW parameters on joint properties of AlMg3 alloy, Welding journal, 91 (2012) 16-22.

[14] D.De Caro et al., Effect of recycling on the mechanical properties of 6000 series aluminum-alloy sheet, Materials, 16 (2023) 6778, https://doi: 10.3390/ma16206778.

[15] H. Dawood et al., Effect of friction stir welding on microstructure and mechanical properties of the 6061 aluminium alloy/15vol % SiC p reinforcement, IOP Conference Series: Materials Science and Engineering, 870, (2020) 012162, https://doi: 10.1088/1757-899X/870/1/012162.

[16] G. Çam, Friction stir welding: A novel welding technique developed for al-alloys, 46 (2005) 30-39.

[17] M. Ahmed, B. Wynne, W. Rainforth, A. Addison, J. Martin, P. Threadgill, Effect of tool geometry and heat input on the hardness, grain structure, and crystallographic texture of thick-section friction stir-welded aluminium, Metallurgical and Materials Transactions A, 50 (2018) 271-284.

[18] A. Şik, İ. Ertürk, M. Önder, A study ınto effects of different parameters on mechanical properties in friction stir welding of AA 2024 aluminium alloy, Pamukkale University Journal of Engineering Sciences, 16(2) (2010) 139-147.

[19] Ç. Batuk, H. Demirtaş, Sürtünme karıştırma kaynağı ile birleştirilmiş 6061 alüminyum alaşımlı sacların mekanik özellikler yönünden incelenmesi, Manufacturing Technologies and Applications, 4(3) (2023) 167-178, https://doi: 10.52795/mateca.1393930.

Manufacturing Technologies and Applications
MATECA

MATECA

Effects of Aging on Charpy Notch Impact Test Results of Specimens Produced by SLA Method

Gizem Akdemir[1], * (ID), Gültekin Uzun[2] (ID)

[1]Department of Manufacturing Engineering, Institute of Science, Gazi University, Ankara, Türkiye
[2]Department of Manufacturing Engineering, Faculty of Technology, Gazi University, Ankara, Türkiye

ABSTRACT

Additive manufacturing is a computer-controlled manufacturing process that creates three-dimensional objects by depositing material in layers. Stereolithography (SLA), the oldest form of additive manufacturing, has attracted considerable interest in the industry due to the high dimensional accuracy and smooth surface quality of the printed parts. In this study, 3D polymer parts were printed using the SLA machine and aged at different temperatures (48, 60 and 72 ºC) and for different times (6, 9 and 12 hours) to investigate the effect of ageing on impact strength. As a result of the Charpy notch impact test, it was observed that the ageing process generally reduced the impact strength of the material and deformation was observed in the samples held above the glass transition temperature. When the change in size was examined over time, a decrease was observed up to 12 hours, while after 12 hours there was a sudden increase at all temperatures. In the measurements made as a result of the ageing process, it was observed that the results of the thickness and width measurements of the sample were in agreement with the results of the ageing process. Thanks to this study, knowledge about the usability, storage, durability and mechanical properties of the polymer material has been obtained and contributed to the literature in this sense.

Keywords: Stereolithography (SLA), Ageing, Charpy Notch Impact Test, Mechanical Properties, Additive manufacturing

SLA Yöntemi ile Üretilen Numunelerde Yaşlandırma İşleminin Charpy Çentik Darbe Test Sonuçlarına Etkileri

ÖZET

Eklemeli imalat katmanlar halinde malzeme biriktirirerek üç boyutlu nesneler oluşturan bilgisayar kontrollü bir üretim yöntemidir. Eklemeli imalatın en eski biçimi olan Stereolitografi (SLA) yöntemi yüksek boyutsal doğruluğu ve basılan parçaların pürüzsüz yüzey kalitesi nedeniyle endüstride oldukça ilgi görmektedir. Bu çalışmada, SLA cihazı kullanılarak 3B polimer parçalar basılmış, yaşlandırma işleminin darbe mukavemeti üzerine etkisini incelemek için farklı sıcaklıklarda (48,60 ve 72 ºC) ve farklı sürelerde (6,9 ve 12 saat) yaşlandırma işlemine maruz bırakılmıştır. Yapılan Charpy çentik darbe testi sonucunda yaşlandırma işleminin malzemenin darbe mukavemetini genel olarak azalttığı, camsı geçiş sıcaklığı üzerinde bekletilen numunelerde deformasyon olduğu gözlemlenmiştir. Süre açısından boyut değişimi incelendiğinde 12 saate kadar bir azalma gözlemlenirken 12. Saatte tüm sıcaklıklarda ani bir artış meydana gelmiştir. Yaşlandırma işlemi sonucunda yapılan ölçümlerde numunenin kalınlık ve genişlik ölçüleri sonuçlarının yaşlandırma işlemi sonucuna uygun olduğu görülmüştür. Yapılan bu çalışma sayesinde polimer malzemenin kullanılabilirliği, saklanması, raf ömrü ve mekanik özellikleriyle ilgili bulgular elde edilmiş ve literatüre bu anlamda katkı sağlanmıştır.

Anahtar Kelimeler: Stereolitografi (SLA), Yaşlandırma, Charpy Çentik Darbe Testi, Mekanik Özellikler, Eklemeli imalat

1. GİRİŞ

Eklemeli imalat, geometrik olarak karmaşık, kademeli malzeme bileşimlerine sahip ve özelleştirilebilen parçaların üretilebilmesine imkân tanıyan bir imalat yöntemidir. Eklemeli imalatın ardındaki ilke, geleneksel imalat süreçlerindeki çıkarmalı imalat yöntemlerinin aksine, üç boyutlu model verilerinden nesneler elde etmek amacıyla malzemelerin üst üste katmanlar halinde birleştirilmesi işlemine dayanmaktadır. Eklemeli imalat; otomotiv, mimarlık, tıp, savunma, doku mühendisliği vb. gibi gelişmekte olan birçok alanda kullanılmaktadır [1,2].

Teknolojinin gelişmesiyle birlikte eklemeli imalat uygulamaları çeşitli endüstrilerde hızla büyümüş ve farklı çalışmalara konu olmuştur. Sağlık alanında yapılan çalışmalar sayesinde, damarın tamamen eski haline dönmesinden 6–12 ay sonra biyolojik olarak parçalanabilen polimer stentler geliştirilmiş, biyolojik ve

nanoelektronik işlevlerin birleştirilmesiyle biyonik kulak elde edilmiştir [3,4]. Dr. Peckitt'in yaptığı kişiye özel implant tasarımı yardımıyla üst çene kemiğinden kesit parça alınması ve yeniden yapılandırılması işleminde standart yönteme göre yaklaşık 11 saat süre kazanılmıştır [5,6]. Savunma ve otomotiv endüstrisinde eklemeli imalatın kullanımıyla parçaların ağırlıkları ve operasyon süresi azaltılmış, üretim maliyetleri düşürülmüştür [7]. Akademik çalışmalarda prototip model üretimini kolaylaştırması, tasarım odaklı yaklaşım sağlamasıyla eğitim ve öğretim alanında da faydalanılmaktadır [8].

Eklemeli imalat yedi alt grupta sınıflandırılmıştır. Bunların arasında yüksek doğrulukta parçalar üretmek için kullanılan ve eklemeli imalatın en eski biçimi olan Stereolitografi (SLA) yöntemiyle, sıvı reçine bir fotopolimerizasyon reaksiyonuyla katılaştırarak üç boyutlu (3B) nesneler üretilir [9]. Bu yöntem yüksek boyutsal doğruluğu ve basılan parçaların pürüzsüz yüzey kalitesi sayesinde endüstride oldukça ilgi görmektedir [10]. Fakat bu avantajlarına rağmen SLA ile üretilen polimer malzemelerin yapısı beklenen mekanik performansı karşılamadığı için ileri proses işlemlerine ihtiyaç duyulmaktadır. Üretilen parçalara uygulanan polimerizasyon süresi; yapıların mekanik özelliklerini, yüzey kalitesini, boyut hassasiyetini vb. malzeme özelliklerini etkilemektedir [11].

Polimerler yüksek sıcaklığa uzun süre maruz kaldıklarında yapılarında fiziksel ve kimyasal değişiklikler meydana gelmektedir [12]. Polimerlerde yaşlanmanın en büyük sebebi ısı ve sıcaklık ile zincir yapısının bozunmasıdır. Bu nedenle maruz kalınan uygunsuz koşul altında malzemenin mekanik ve kimyasal dayanımını ölçmek için yaşlandırma testleri yapılır. Yaşlandırma testleri; ürünün kullanılabilirliğini, saklanmasını, raf ömrü ve geri dönüşümünü anlamak ve değerlendirmek için önemlidir.

Literatürde yaşlandırmanın malzemenin mekanik özelliklerine etkisiyle ilgili birçok çalışma yapılmıştır. SLA ile üretilen numuneleri, Mansour vd. [13] kontrollü (karanlık kap, %50 bağıl nem ve 20°C sıcaklık) ve kontrolsüz (rafta bekletilmiş) ortamda gözlemlerken; Tröger vd. [14] üç farklı reçineye önce farklı sürelerde kürleme işlemi yapmış daha sonra termal hava akışlı fırında yaşlandırma işlemine maruz bırakmıştır. Puebla vd. [15] ise numuneleri farklı yönlerde (düz, bir kenar üzerinde, dik), farklı yaşlandırma sürelerinde (4,30 ve 120 gün), farklı ön koşullandırma (ortam, kurutucu ve Uluslararası Amerikan Test ve Materyalleri Topluluğu (ASTM) ön koşullandırması) şartlarında bekleterek testlerini gerçekleştirmişlerdir. Bir diğer çalışmada [16] farklı sıcaklık ve sürelerde kürleme işlemi yapılan numuneler, ısıtma ve soğutma rampası kullanılarak yaşlandırmaya maruz bırakılırken, Wu vd. [17] çalışmasında epoksi ve vinil ester reçineleri kullanılarak termal, ultraviyole (UV) ve doğal yaşlanma koşullarında sararma mekanizmaları ve bunları etkileyen faktörler incelenmiştir.

Eriyik biriktirme yöntemi (FDM) ile üretilen numuneler için de farklı çalışmalar yapılmıştır. Arjun vd. [18] numuneleri dört farklı sıcaklık (65, 95, 125 ve 155 ºC) ve dört farklı süre (30, 60, 120 ve 240 dakika); Bhandari vd. [19] iki farklı sıcaklık (90 ve 110 ºC) ve 4 farklı süre (0, 30, 240 ve 480 dakika); Valvez vd. [20] üç farklı sıcaklık (90, 110 ve 130 ºC) ve üç farklı süre (30, 240 ve 480 dakika); Jayanth vd. [21] üç farklı sıcaklık (90, 100 ve 120 ºC) ve üç farklı süre (60, 120 ve 240 dakika) sıcak hava fırınında bekletmiştir. Yine benzer çalışmada [22] üretilen numuneler belirlenen üç farklı sıcaklık (100 °C, 150 °C, 200 °C) ve üç farklı sürede (30 dakika, 60 dakika, 90 dakika) sıcak hava fırınında bekletilmiştir.

Günümüzde yaşlandırma yöntemlerine ait değişkenlerin etkileri ve farklı yaşlandırma yöntemlerinin mekanik özelliklere etkisi önemli araştırma konuları olmaya devam etmektedir. SLA ile üretilen numunelerde doğal ve yapay yaşlandırma parametreleri üzerine yapılan çalışmalar sınırlıdır. Mevcut araştırmalarda kullanılan sıcaklık ve süre parametrelerinde önemli farklılıklar görülmekte bu da genelleme yapılmasını zorlaştırmaktadır. Buna karşın, FDM ile üretilen numunelerde sıcaklık ve süre parametreleri daha tutarlıdır.

Bu çalışmada, Anycubic Photon Mono X SLA 3B yazıcı ile Anycubic UV Gri Reçine kullanılarak polimerlerde yapay yaşlandırma işleminin malzemenin mekanik özelliklere etkileri incelenmek istenmiştir. Bunun için çentik darbe test numuneleri üretilmiş ve bu numuneler literatürdeki çalışmalar ve kullanılan malzemenin camsı geçiş sıcaklığı göz önüne alınarak, kararlaştırılan üç farklı sıcaklık (48,60 ve 72 ºC) ve üç farklı sürede (6,9 ve 12 saat) yapay yaşlandırma işlemine maruz bırakılmıştır.

2. MATERYAL VE YÖNTEM

2.1. Materyal

Çalışma kapsamında modellerin yazıcıda üretilmesi için Anycubic UV Gri Fotopolimer Reçine tercih edilmiştir. Bu malzemenin genel özellikleri Tablo 1'de verilmiştir. Üretici firmadan alınan bilgilere göre malzemenin camsı geçiş sıcaklığı (Tg) 60 °C'dir.

Tablo 1. UV sıvı reçinenin teknik özellikleri.

Dalga Boyu	Yoğunluk	Viskozite	Yüzey Sertliği	Çekme Mukavemeti	Raf Ömrü
355-410 *nm*	1.05-1.25 *g/cm3*	150-200 *mPa.s*	84 *HS*	36-45 *MPa*	1 *yıl*

2.2. Metot

Mekanik özellikleri değerlendirmek için SLA yöntemi ile charpy çentik darbe test numuneleri ASTM D6110 [23] standardına göre üretilmiştir. Elde edilen mekanik özellik değerlerinin güvenilir olduğundan emin olmak amacıyla her set için üç aynı numune hazırlanmıştır. Bu çalışmada kullanılan test numunesinin teknik çizimi Şekil 1'de verilmiştir.
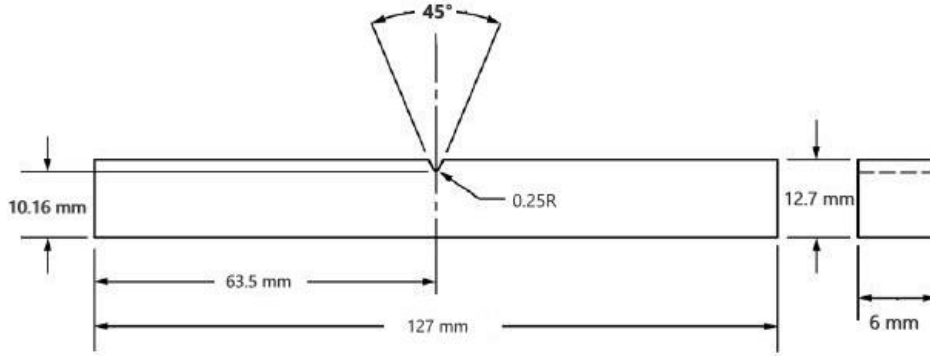
Şekil 1. Charpy testi numune boyutları-mm.

Solidworks bilgisayar destekli tasarım (CAD) programı kullanılarak Şekil 1'de gösterilen standart boyutlarına göre test numunesi modellenmiştir. CAD programında tasarlanan yapılar Photon_WorkShop programı kullanılarak STL dosyası formatında dışarı aktarılmıştır. Numunelerin basımında Anycubic Photon Mono X SLA yazıcısı kullanılmıştır. Her bir numune düz yapı yönelimi (0 °C) ile platformdan 8 mm yukarıda destek kullanılarak basılmıştır. Cihaz parametreleri 0.05 mm katman kalınlığı, 2 s normal pozlama süresi, 40 s alt pozlama süresi olacak şekilde ayarlanmıştır. Kullanılan 3B yazıcı ve üretilen test numuneleri Şekil 2'de gösterilmektedir. Basımı tamamlanan test numunelerinin yüzeyindeki reaksiyona girmemiş reçinelerin giderilmesi için numuneler, Şekil 2c'de verilen yıkama cihazında %99.9 saflıkta izopropil alkol kullanılarak 4 dk boyunca yıkandıktan sonra 2d'de verilen kürleme cihazıyla UV ışını altında 5 dk boyunca kürlenmiştir.
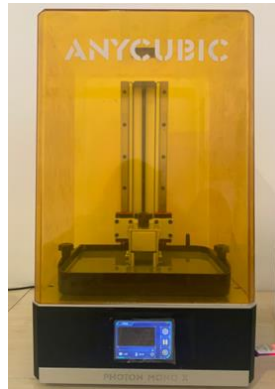
(a)

(b)
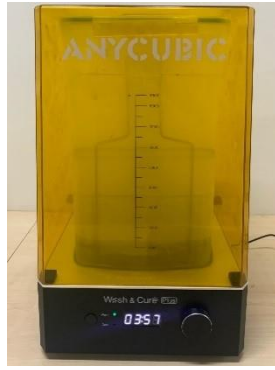
| (c) | (d) |

Şekil 2. a) Üretimde kullanılan SLA cihazı, b) Charpy test numunesi, c) Yıkama cihazı, d) Kürleme cihazı.

SLA cihazında üretilen numunelerin yaşlandırma işleminde Şekil 3'te yer alan Protherm Furnaces marka fırın kullanılmıştır.

Şekil 3. Protherm furnaces kamara fırını.

Tüm numuneler, her bir deney seti için, o setin sıcaklık değerinde ve test süresinde ısıl işleme maruz bırakıldıktan sonra aynı ortam koşullarında mekanik testlere tabi tutulmuştur. Tablo 2'de deney setlerinde yer alan değerler gösterilmiştir. Her deney üç tekrarlı test şeklinde gerçekleştirilmiştir.

Tablo 2. Deneysel Tasarım.

Deney No	Süre	Sıcaklık
D1		48 ^{o}C
D2	6 Saat	60 ^{o}C
D3		72 ^{o}C
D4		48 ^{o}C
D5	9 Saat	60 ^{o}C
D6		72 ^{o}C
D7		48 ^{o}C
D8	12 Saat	60 ^{o}C
D9		72 ^{o}C
Orj.	-	-

2.3. Charpy Çentik Darbe Testi

Charpy çentik darbe testleri, ASTM D6110 standardına göre Şekil 4'te verilen Alarge marka sarkaçlı darbe test cihazı ile yapılmıştır. Charpy darbe testi malzemenin kırılma sırasında emdiği enerji miktarını

belirlemek için gerçekleştirilmiştir. Emilen enerji, çarpmadan önce ve sonra sarkacın yükseklik farkı ile orantılıdır. Kullanılan cihazda bu değer otomatik olarak hesaplanmaktadır.
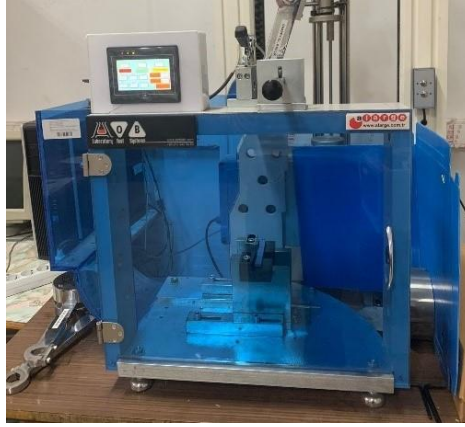
Şekil 4. Alarge darbe test cihazı.

Şekil 1b'de verilen ölçülere göre hazırlanan numuneler, Şekil 5'te gösterildiği gibi cihaza yerleştirilmiş ve 5 Joule çekiç kullanılarak test gerçekleştirilmiştir. Elde edilen veriler sonucunda yaşlandırma işleminin darbe dayanımına olan etkisi incelenmiştir.
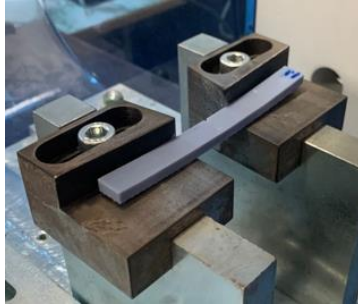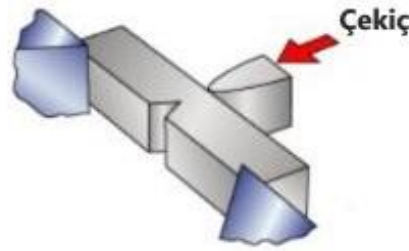
(a)　　　　　　　　　　　　　　　(b)

Şekil 5. a) Test numunesinin cihaza bağlanmış görseli, b) Test düzeneği.

3. DENEYSEL BULGULAR

3.1. Yaşlandırma İşlemi Sonrası Numune Ölçülerinin Geometrik Toleransında Meydana Gelen Değişiklikler

Numuneler, termal yaşlandırma işlemine maruz bırakılmadan önce ve sonra dijital kumpas ile ölçülmüş; 12.7 mm genişlik (Wo), 6 mm kalınlık (t) değerleri kaydedilmiştir. İşlem sonrası meydana gelen numune boyutlarındaki değişimin yüzdelik gösterimi Şekil 6'da yer almaktadır.

Buna göre yüzdesel değişimin en fazla olduğu değerin (%69) 12 saat 48 °C'de bekletilen numune olduğu; en düşük olduğu değerin ise (%16) 9 saat 72 °C'de bekletilen test numunesine ait olduğu gözlemlenmiştir. Max ve min değerler arasında yaklaşık %53'lük bir fark olduğu görülmüştür. Deneysel sonuçlar, numune ölçülerinde sıcaklık artışıyla birlikte boyut değişiminde azalma olduğunu göstermiştir. Süre açısından boyut değişimi incelendiğinde ise 12 saate kadar bir azalma gözlenmiş ancak 12. saatte tüm sıcaklıklarda ani bir artış meydana gelmiştir. Bu değerler, ASTM D6110 standardının belirlediği tolerans aralıkları içerisinde yer almaktadır (Wo = 12.7 ±0.15 / T=3-12.7 mm).
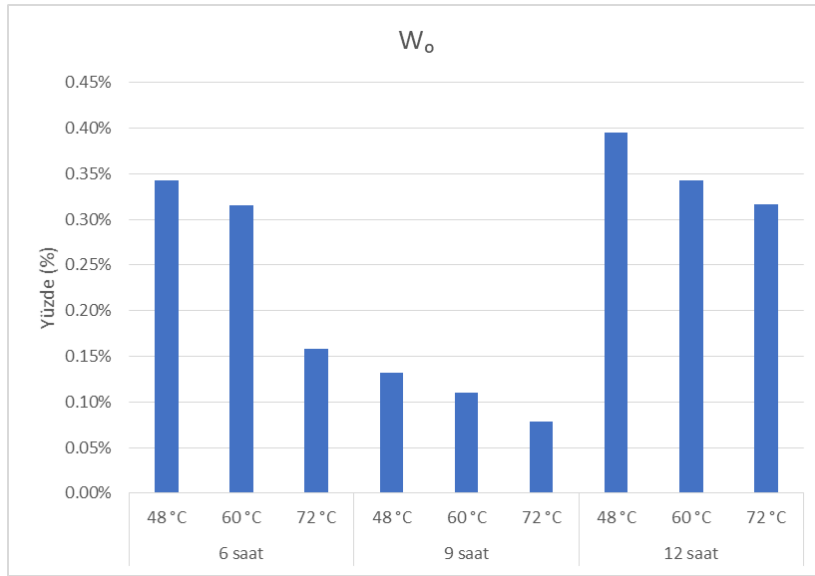
(a)
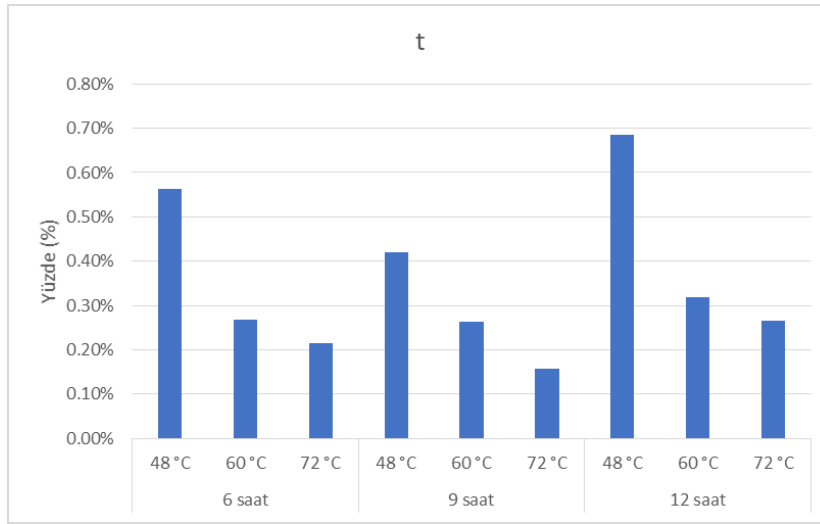
(b)

Şekil 6. Numune boyutlarındaki değişimin yüzdelik gösterimi a) Genişlik (W_o), b) kalınlık (t).

3.2. Charpy Çentik Darbe Testi Sonuçları

Bu çalışmada aynı üretim parametrelerine sahip numunelerin, aniden uygulanan bir strese nasıl tepki vereceğini belirlemek için tasarlanmıştır. Farklı sıcaklık ve sürelerde yaşlandırma işlemine maruz bırakılan numunelerin kırılma sırasında emdiği enerji miktarında gerçekleşen değişim incelenmiştir. Charpy test numuneleri SLA cihazında üretilirken çentikli olduğu için destekli olarak üretilmiştir. Şekil 7'de kırılan numunelerin tamamı yer almaktadır. Buna göre malzemelerin çoğu çentiğin bulunduğu orta noktadan kırılmıştır.
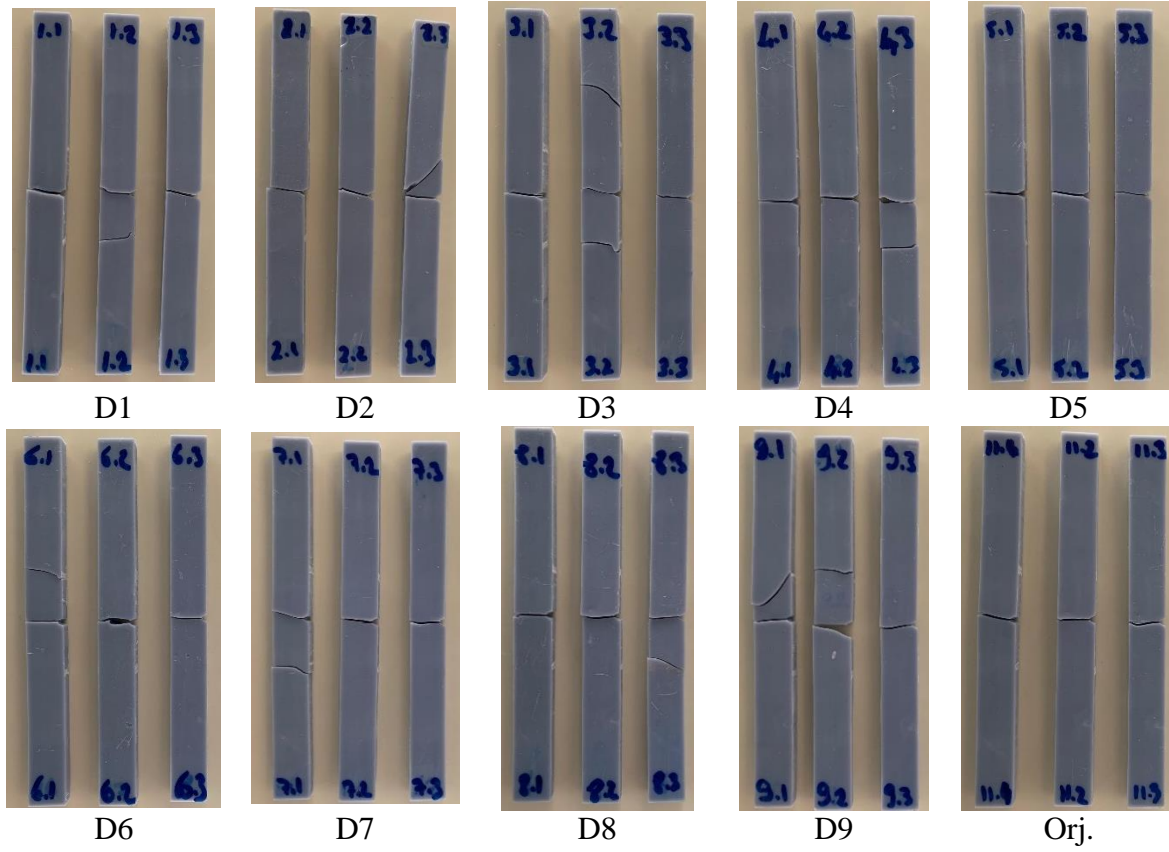
Şekil 7. Test edilen charpy numuneleri.

Yaşlandırma sonucunda malzemenin camsı geçiş sıcaklığı üzerinde sıcaklığa maruz bırakılan D3 (72 °C 6 saat), D6(72 °C 9 saat) ve D9 (72 °C 12 saat) numunelerin yüzeylerinde deformasyon gözlemlenmiştir (Şekil 8). Deneylerde kullandığımız reçine, termoset polimer özelliği göstermektedir ve malzemenin mekanik özelliklerinde belirttiğimiz üzere camsı geçiş sıcaklığı 60 °C'dir. Termoset malzemeler, camsı geçiş sıcaklığının (Tg) üstündeki bir sıcaklığa ısıtıldığında parçalanmakta ve ayrışma eğilimi göstermektedir [24]. Elde ettiğimiz bulgular, bu durumu doğrulamakta olup Tg'nin aşıldığı numunelerde belirgin deformasyonlar gözlemlenmiştir. Ayrıca, literatürde benzer çalışmalarda da yüksek sıcaklık etkisiyle malzemelerde geometrik tolerans kaybı, yüzey sararması gibi görsel deformasyonların meydana geldiği gözlenmiştir [17,25].
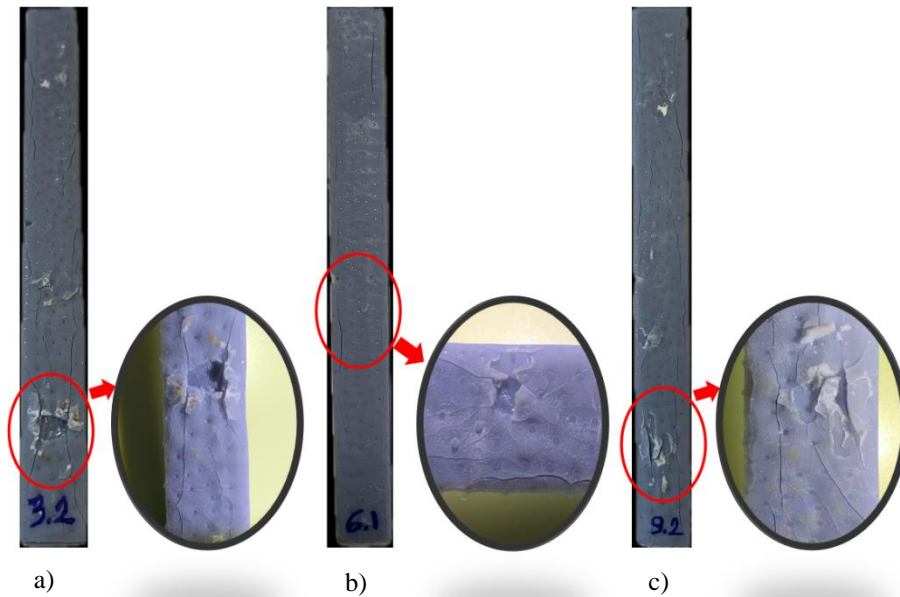
Şekil 8. Deforme olan test numunelerinin makroskobik görüntüsü; a) D3 ve b) D6 c) D9.

Yapılan testler sonucunda elde edilen verilerle Şekil 9'da yer alan grafik elde edilmiştir. Darbe sonucu açığa çıkan enerjinin en fazla olduğu değerin (0.769 J) 12 saat 60 °C'de bekletilen numune olduğu; en düşük olduğu değerin ise (0.499 J) 6 saat 60 °C'de bekletilen test numunesine ait olduğu gözlemlenmiştir. Max ve min değerler arasında yaklaşık %35.11'lik bir fark olduğu görülmüştür.
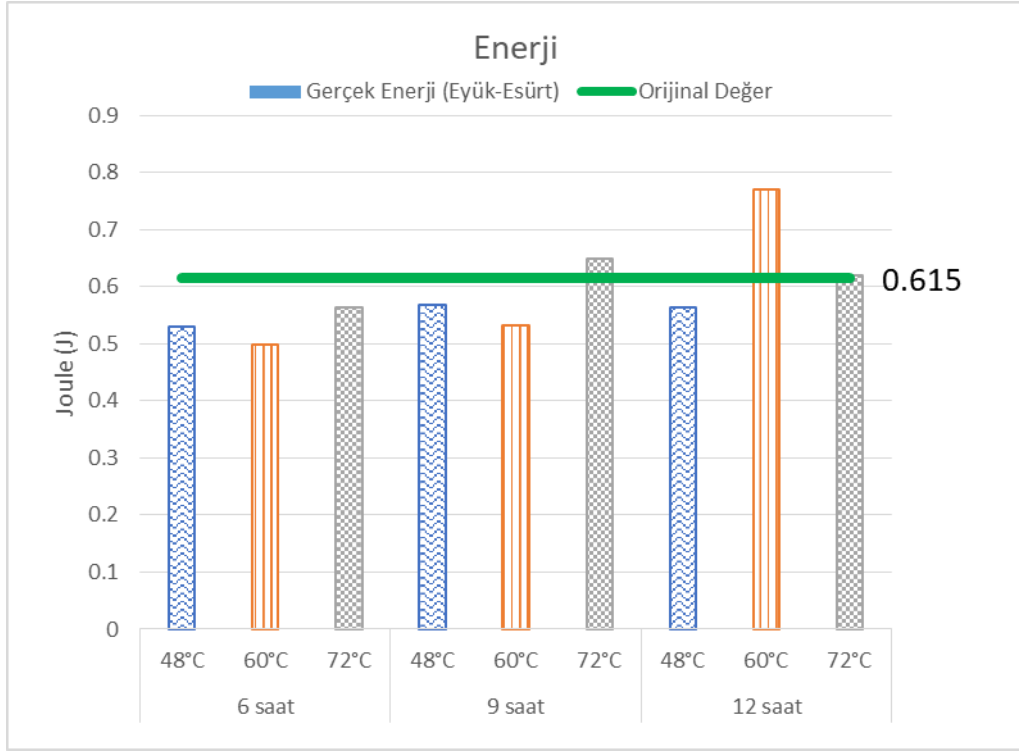
Şekil 9. Test numunelerinin darbe dayanımı kıyaslama grafiği.

48 °C'de bekletilen numunelerde süre ilerledikçe darbe mukavemetinde önce %7.37'lik bir artış olduğu daha sonra %0.71'lik azalış olduğu gözlenmiştir. Alınan bütün değerlerin sonucunda 48 °C'de bekletilen numunelerin yaşlandırılmamış olan numunelere kıyasla darbe mukavemetinde azalış olduğu görülmüştür.

60 °C'de bekletilen numunelerde süre ilerledikçe darbe mukavemetinde önce %6.81'lik daha sonra %44.2'lik bir artış olduğu gözlenmiştir. Alınan bütün değerlerin sonucunda 60 °C'de bekletilen numunelerde süre ilerledikçe darbe mukavemetinde artış olduğu gözlemlenmiştir. 60 °C'de bekletilen numuneler içerisinde 12 saat bekletilen numune hariç diğer numunelerin darbe mukavemetinin orijinal numuneyi geçemediği görülmüştür.

72 °C'de bekletilen numunelerde süre ilerledikçe darbe mukavemetinde önce %15.2'lik bir artış olduğu daha sonra %4.47'lik azalış olduğu gözlenmiştir. 72 °C'de bekletilen numuneler içerisinde 6 saat bekletilen numune hariç diğer numunelerin darbe mukavemetinin orijinal numuneyi geçtiği görülmüştür.

Yaşlandırma işlemi, özellikle yüksek sıcaklıklara maruz kalan termoset polimerlerin molekülleri arasında oluşan kovalent çapraz bağların yoğunluğunu artırarak malzemenin elastikiyetini arttırmaktadır. Ancak uzun süre devam eden yaşlandırma, bu kovalent bağların oksidasyonuna ve kopmasına yol açarak malzeme yapısında bozulmalara sebebiyet vermektedir. Bu süreç, malzemenin kırılgan hale gelmesine ve darbe dayanımı gibi mekanik özelliklerinin zamanla azalmasına sebep olmaktadır [26,27,28]. Yaptığımız çalışmanın sonuçları da bu bilgiyi desteklemektedir ve literatürde yapılan diğer çalışmalarda olduğu gibi yaşlandırma işlemi sonucunda malzemenin darbe mukavemetinde genel olarak azalma gözlemlenmiştir [11,29].

4. SONUÇLAR

Bu çalışmada, 3B SLA yazıcıda reçine ile üretilen charpy çentik darbe test numuneleri, aynı parametrelerde üretilmiş, farklı süre ve sıcaklıkta ısıl işleme maruz bırakılmış ve charpy çentik darbe testlerine tabi tutularak yaşlandırma şartlarının malzemenin darbe mukavemetine etkisi incelenmiştir. Elde edilen sonuçlar aşağıda kısaca özetlenmiştir:

1- SLA yöntemi literatürde kullanılmış olmakla birlikte, bu çalışmada ele alınan farklı parametre kombinasyonlarının daha önce detaylı bir şekilde incelenmediği görülmüştür. Bu bağlamda, çalışmanın literatüre özgün bir katkı sunduğu değerlendirilmektedir.

2- Malzemelerin camsı geçiş sıcaklığının üzerinde bir sıcaklığa maruz bırakılması durumunda yüzeylerinde deformasyon oluştuğu tespit edilmiştir. Literatürdeki diğer çalışmalar da bu durumu destekler nitelikte olup, yüksek sıcaklık etkisiyle geometrik tolerans kaybı ve yüzey sararması gibi görsel deformasyonların meydana geldiğini ortaya koymaktadır. Bu bağlamda, elde edilen bulgular literatürdeki mevcut verilerle uyum göstermektedir.

3- Darbe sonucu açığa çıkan enerjinin en fazla olduğu değerin (0.769 J) 12 saat 60 °C'de bekletilen numune olduğu; en düşük olduğu değerin ise (0.499 J) 6 saat 60 °C'de bekletilen test numunesine ait olduğu gözlemlenmiştir. Max ve min değerler malzemenin camsı geçiş sıcaklığında görülmüş olup arasılarında yaklaşık %35.11'lik bir fark olduğu görülmüştür.

4- Süre açısından boyut değişimi incelendiğinde; 12 saate kadar bir azalma gözlenmiş ancak 12. saatte tüm sıcaklıklarda ani bir artış meydana gelmiştir. Yüzdesel değişimde maksimum ve minimum değerler arasında yaklaşık %53'lük bir fark olduğu görülmüştür.

5- ASTM D6110 Standardına göre W_o = 12.7 ±0.15 / T=3-12.7 mm tolerans aralığı için 12.7 mm genişlik (W_o), 6 mm kalınlık (t) ölçüleri sonuçlarının yaşlandırma işlemi sonucuna uygun olduğu görülmüştür.

6- Yaşlandırma süresi ve sıcaklık artışının darbe mukavemetini arttırdığı söylenebilir. Sadece 9 saat 72 °C'de ve 12 saat 60 °C ile 72 °C'lerde orijinal numune değerinin üstünde mukavemet değeri ölçülmüştür.

7- Yaşlandırma işleminin malzemenin darbe mukavemetini genel olarak azalttığı gözlemlenmiştir.

Bu çalışma, polimer malzemelerin kullanılabilirliği, depolanması, raf ömrü ve geri dönüşüm süreçlerinin anlaşılması ve değerlendirilmesi açısından büyük önem taşımakta olup, literatüre bu doğrultuda değerli bir katkı sağlamaktadır. Geliştirilen çalışmalar sayesinde endüstride kullanılan polimer malzemelerde hem malzemelerin performansına hem de ürünlerin güvenilirliğine yönelik bilgiler elde edileceği öngörülmektedir. Gelecekteki araştırmalarda, camsı geçiş sıcaklığına kadar sıcaklık uygulamalarının gerçekleştirilmesi önerilmektedir; zira bu sıcaklık değerinin üzerinde meydana gelen ani artış ve azalışlar, malzemenin mekanik özelliklerindeki değişimlerin öngörülmesini zorlaştırmaktadır. Ayrıca, SLA (StereoLitografi) yöntemiyle üretilen reçinelerin üretim süreci, çevresel ışık, sıcaklık ve diğer birçok parametreden etkilenebilmekte olup, bu reçineler oldukça hassas bir yapı sergilemektedir. Literatürde SLA yöntemine ilişkin çalışmalar sınırlı sayıda bulunmakta ve üretim parametreleri ile farklı renk ve mekanik özelliklere sahip reçineler üzerine yeterli bulgu yer almamaktadır. Bu nedenle, gelecekteki araştırmalarda üretim parametrelerinin ve reçine çeşitliliğinin genişletilerek bu konulara dair literatüre daha kapsamlı katkılar sağlanması önerilmektedir.

TEŞEKKÜR

KAYNAKLAR

[1] D.W. Rosen, What are Principles for Design for Additive Manufacturing?, Proceedings of the 1st International Conference on Progress in Additive Manufacturing, 2014, Singapore.

[2] N. Guo, M.C. Leu, Additive manufacturing: technology, applications and research needs, Frontiers of Mechanical Engineering, 8(3) (2013) 215-243.

[3] A.A. Giannopoulos, D. Mitsouras, S. Yoo, P.P. Liu, Y.S. Chatzizisis, F.J. Rybicki, Applications of 3D printing in cardiovascular diseases, Nature Reviews Cardiology, 13(12) (2016) 701-718.

[4] M.S. Mannoor, Z. Jiang, T. James, Y.L. Kong, K.A. Malatesta, W.O. Soboyejo, N. Verma, D.H. Gracias, M.C. McAlpine, 3D Printed Bionic Ears, Nano Letters, 13 (2013) 2634-2639.

[5] S. Lohfeld, P. McHugh, D. Serban, D. Boyle, G. O'Donnell, N. Peckitt, A route for digital design and manufacturing of customised maxillofacial implants, Journal of Biomechanics, 39 (2006) 427.

[6] Y. Jun, K. Choi, Design of patient-specific hip implants based on the 3D geometry of the human femur, Advances in Engineering Software, 41 (2010) 537-547.

[7] R. Huang, M. Riddle, D. Graziano, J. Warren, S. Das, S. Nimbalkar, J. Cresko, E. Masanet, Energy and emissions saving potential of additive manufacturing: the case of lightweight aircraft components, Journal of Cleaner Production, 135 (2016) 1559-1570.

[8] H.K. Sürmen, Eklemeli imalat (3B baskı): teknolojiler ve uygulamalar, Uludağ Üniversitesi Mühendislik Fakültesi Dergisi, 24 (2) (2019) 373-392.

[9] F.P.W. Melchels, J. Feijen, D.W. Grijpma, A review on stereolithography and its applications in biomedical engineering, Biomaterials, 31 (2010) 6121-6130.

[10] M. Mukhtarkhanov, A. Perveen, D. Talamona, Application of stereolithography based 3D printing technology in investment casting, Micromachines,11 (2020) 946.

[11] İ. Aktitiz, K. Aydın, A. Topçu, Stereolitografi (SLA) tekniği ile basılan 3 boyutlu polimer yapılarda ikincil kürleme süresinin mekanik özelliklere etkisi, Çukurova Üniversitesi Mühendislik Mimarlık Fakültesi Dergisi, 35(4) (2020) 949-958.

[12] ASTM D3045, Standard practice for heat aging of plastics without load, ASTM International, 2018.

[13] S. Mansour, M. Gilbert, R. Hague, A study of the impact of short-term ageing on the mechanical properties of a stereolithography resin, Materials Science and Engineering, 447(2007) 277-284.

[14] C. Tröger, A.T. Bens, G. Bermes, R. Klemmer, J. Lenz, S. Irsen, Ageing of acrylate-based resins for stereolithography: thermal and humidity ageing behaviour studies, Rapid Prototyping Journal, 14(5) (2008) 305-317.

[15] K. Puebla, K. Arcaute, R. Quintana, R.B. Wicker, Effects of environmental conditions, aging, and build orientations on the mechanical properties of ASTM type I specimens manufactured via stereolithography, Rapid Prototyping Journal, 18(5) (2012) 374-388.

[16] E. Marin, F. Boschetto, M. Zanocco, H.N. Doan, T.P.M. Sunthar, K. Kinashi, D. Iba, W. Zhu, G. Pezzotti, UV-curing and thermal ageing of methacrylated stereo-lithographic resin, Polymer Degradation and Stability, 185, 2021.

[17] C. Wu, B.C. Meng, L. Tam, L. He, Yellowing mechanisms of epoxy and vinyl ester resins under thermal, UV and natural aging conditions and protection methods, Polymer Testing, 114 (2022).

[18] P. Arjun, V.K. Bidhun, U.K. Lenin, V.P. Amritha, R.V. Pazhamannil, P. Govindan, Effects of process parameters and annealing on the tensile strength of 3D printed carbon fiber reinforced polylactic acid, Materials Today: Proceedings, 62 (2022) 7379-7384.

[19] S. Bhandari, R.A. Lopez-Anido, D.J. Gardner, Enhancing the interlayer tensile strength of 3D printed short carbon fiber reinforced PETG and PLA composites via annealing, Additive Manufacturing, 30, 2019.

[20] S. Valvez, A.P. Silva, P.N.B. Reis, F. Berto, Annealing effect on mechanical properties of 3D printed composites, Procedia Structural Integrity, 37: 738-745, 2022.

[21] N. Jayanth, K. Jaswanthraj, S. Sandeep, N.H. Mallaya, S.R. Siddharth, Effect of heat treatment on mechanical properties of 3D printed PLA, Journal of the Mechanical Behavior of Biomedical Materials, 123 (2021).

[22] M. Coşkun, 3 boyutlu yazıcıda üretilmiş parçalara uygulanan ısıl işlemlerin mekanik özelliklere etkisi, Yüksek Lisans Tezi, Kastamonu Üniversitesi Malzeme Bilimi Mühendisliği Ana Bilim Dalı, Kastamonu, Türkiye, 2019.

[23] ASTM D6110, Standard test method for determining the charpy impact resistance of notched specimens of plastics, ASTM International, 2018.

[24] Knowledge in Practice Centre, Thermoset Polymers, https://compositeskn.org/KPC/A105, 24.01.2024.

[25] H.C. Özdemir, Eklemeli imalat yöntemi ile üretilmiş parçalara üretim sonrası yapılan işlemlerin yüzey kalitesine ve mekanik özelliklere etkisinin araştırılması, Yüksek Lisans Tezi, Gazi Üniversitesi Fen Bilimleri Enstitüsü, Ankara, Türkiye, 2023.

[26] M. Saçak, Polimer Kimyası, 10. Baskı, Gazi Kitabevi, Ankara, 2023.

[27] Unacademy, Thermosetting Polymers, https://unacademy.com/content/jee/study-material/chemistry/thermosetting-polymers/, 2024.

[28] Byju's, What is Thermosetting Polymer?, https://byjus.com/chemistry/thermosetting-polymers/, 2024.

[29] I. García-Moreno, M.A. Caminero, G.P. Rodríguez, J.J. López-Cela, Effect of thermal ageing on the ımpact and flexural damage behaviour of carbon fibre-reinforced epoxy laminates, Polymers, 11(1) (2019) 80.

Manufacturing Technologies and Applications
MATECA

A Comparative Evaluation of Dry-MQL Turning Applications for AISI 5115 Steel

Bahar Sayın Kul[1, *] [iD], Ayşe Sena Yamaner[1] [iD]

[1]*Department of Mechanical Engineering, Faculty of Technology, Selçuk University, Konya, Türkiye*

ABSTRACT

This study investigates the effect of various machining variables on cutting forces and surface roughness during turning of AISI 5115 steel in dry and MQL environments. While the experiments were carried out using two different feed rates, four different cutting speeds and constant depth of cut, the effects of them and their different levels on surface roughness and cutting forces were analyzed by reference to full factorial experimental design. The prominent findings of the research are as follows: The lowest surface roughness was obtained at 90 m/min cutting speed and 0.15 mm/rev feed rate in both mediums. The lowest cutting force was obtained at 135 m/min cutting speed, 0.15 mm/rev feed rate in dry environment and at 50 m/min cutting speed and 0.15 mm/rev feed rate in MQL environment. It was determined that there was an average 6.90% reduction in cutting force and an average 12.2% reduction in surface roughness in MQL condition. As a result, it was observed that machining in MQL conditions gave better results than dry conditions. These results show that the MQL method improves the machining performance compared to dry machining.

Keywords: Turning, MQL (minimum amount of lubrication), Dry Environment, Surface Roughness, Cutting Force

MQL Uygulaması ile AISI 5115 Çeliğinin Tornalama Performansının Değerlendirilmesi

ÖZET

Bu çalışma, AISI 5115 çeliğinin kuru ve MQL ortamlarında tornalanması sırasında çeşitli işleme değişkenlerinin kesme kuvvetleri ve yüzey pürüzlülüğü üzerindeki etkisini araştırmaktadır. Deneyler iki farklı ilerleme, dört farklı kesme hızı ve sabit kesme derinliği kullanılarak gerçekleştirilirken parametrelerin ve farklı seviyelerinin yüzey pürüzlülüğü ve kesme kuvvetleri üzerindeki etkisi tam faktöriyel deney tasarımı referans alınarak analiz edilmiştir. Araştırmanın öne çıkan bulguları aşağıdaki gibidir: En düşük yüzey pürüzlülüğü her iki ortamda da 90 m/dak kesme hızı ve 0,15 mm/dev ilerleme hızında elde edilmiştir. En düşük kesme kuvveti, kuru ortamda 135 m/dak kesme hızı ve 0.15 mm/dev ilerleme hızında, MQL ortamında ise 50 m/dak kesme hızı ve 0.15 mm/dev ilerleme hızında elde edilmiştir. MQL koşulunda kesme kuvvetinde ortalama %6,90 ve yüzey pürüzlülüğünde ortalama %12,2 azalma olduğu tespit edilmiştir. Sonuç olarak, MQL koşullarında işlemenin kuru koşullara göre daha iyi sonuçlar verdiği gözlemlenmiştir. Bu sonuçlar, MQL yönteminkuru işlemeye nazaran işleme performansını iyileştirdiğini göstermektedir.

Anahtar Kelimeler: Tornalama, MQL (minimum yağlama miktarı), Kuru Ortam, Yüzey Pürüzlülüğü, Kesme Kuvveti

1. INTRODUCTION

Machining is the process of removing chips from a workpiece to bring it to the desired dimensions. The main motivation in machining methods is to ensure the effectiveness of the process of turning materials into smaller pieces suitable for the purpose they will serve. The most widespread use of machining methods is the turning method due to its features such as its suitability for mass production, surface quality, precision processing, compatibility with technological developments and cost efficiency [1, 2]. Turning performance in hardened metals is a phenomenon that can be evaluated through parameters such as tool wear, tool life, surface roughness, cutting temperature, cutting force, etc. [3-7]. The increase in production speed due to the developments in the manufacturing industry necessitates a rise in the speed of cutting during the machining of the workpiece. However, the high temperatures associated with high cutting speed caused by friction during machining can damage the workpiece and cutting tool. This manifests itself with surface roughness, which is an undesirable surface quality indicator. To avoid these problems, it is essential to control the temperature in the machining area. Although the traditional cooling method is a very effective method in

*Corresponding author, e-mail: aysesena.yamaner@selcuk.edu.tr

heat control, it has a handicap in terms of cost and environmental effects caused by high fluid consumption. Although cryogenic cooling, which prioritizes tool life and surface quality, is a shining method in high precision applications, it returns as an extra cost in applications requiring special equipment. The use of cutting fluid reduces friction in the machining zone and removing heat along with the chips. Since the utilization of cutting fluid has disadvantages, such as requiring additional equipment and being costly, the use of dry processing conditions is still encountered in experimental studies. However, the dry environment machining method also has its negative aspects: it cannot sufficiently remove the chip from the environment, it causes rapid and high tool wear, and it cannot maintain surface integrity and it cannot provide sufficient heat control [8-11]. The MQL method, which has been widely utilized in recent years, is an application in which the cutting fluid is infused to the point where the machining is performed with compressed air. Although it relatively limits lubrication, it does not fall the traditional lubrication method in terms of machining. It has positive aspects such as increasing the material surface quality and improving processing performance [12-14]. It promotes environmental and industrial sustainability by minimizing cutting fluid and waste management problems. It also eliminates the cost and environmental burden of disposal of waste fluids by reducing the use of coolant.

Steels are impressive with their high mechanical properties, suitability for processes such as machining, forging, rolling and lower costs compared to their equivalents. Classified as a premium, low carbon, low alloy hardining steel, AISI 5115 offers a balanced combination of properties and generally serves to increase hardness and wear resistance [15-17].This steel, which is considered medium hardness, has a soft inner surface and a harder outer surface, and has a high ability to absorb impacts [17]. This special steel is widely used in many areas such as machine parts, shafts, gears, pulleys, bearings, chains and mechanical components. Studies on steel, which is seen in the literature using the abbreviation 16MnCr5 for the German Institute for Standardization (DIN), are summarized below. Baykara and Atik [17] conducted a study on how the wear resistance of 16MnCr5 steel would be affected by different heat treatments. Arunkumar, Chandrasekaran [18], carried out a detailed investigation of the properties of the 16MnCr5 steel at different hardness values such as 55 HRC, 45 HRC, 40 HRC by applying heat treatment to the material at 500 ℃, 450 ℃, and 250 ℃, respectively. After applying tensile tests to the material with various hardnesses, the shaft was analyzed at full load capacity to determine the stress of the design. Arrabiyeh, Setti [19] performed a study on the grinding of 16MnCr5 steel with micro pencil grinding tools, which they observed to be widely used on brittle materials with different hardnesses to create micro surfaces. Mouralova, Matousek [20] contributed to the literature with their study on the analysis of surface layer formation after machining of AISI 5115 steel with effective wire electrical charge. Saini, Goyal and Bhandari [21] used the multiple response optimization method to optimize 16MnCr5 steel by wire electrical charge machining. In their study, they carried out an optimization study to determine the influence of electrode types, pulse on time, pulse of time, peak current, pulse off time factors on metal removal rate and surface roughness. According to the findings of the study, they observed that the most influence factor for the studied parameters was pulse duration. Topography parameters of hard turned and ground 16MnCr5 steel surfaces were experimentally investigated, tribology maps were used to determine the optimum cutting parameters in the study belongs to Molnar [22]. The study conducted by Carrera Espinoza, Alvarez Vera [23] is another study examining the tribological behavior of 16MnCr5 steel, and the effects of the different surface treatments on tribology as well microstructural and mechanical properties are also included in the scope of the study. Jacob, Meurer and Bergs [24] focuses on the use of model ensemble approach to predict surface roughness in hard turning of 16MnCr5 steel in their research. In the study by Frölich, Magyar [25] AISI 5115 steel was evaluated for wear resistance in carburized, turned carburized and dry turned surface conditions. Molnar [26] performed a reseach on hard turning machining of hardened steel 16MnCr5. Utilizing regression analysis, full factorial experimental design, variance analysis and correlation analysis, the impacts of parameters such as, depth of chip, feed, cutting speed and cutting edge geometry on the topographical features of the part were studied by scanning the areas of the machined material surfaces. Balabanov, Balabanova and Agayev [27] presented a mathematical method for the estimation of cutting forces in machining of 16MnCr5 steel. The theoretical model, which allows the measurement of cutting forces and cutting parameters such as feed, spindle speed, chip depth, showed a deviation of not more than 4.72% compared to actual measurements. Mehmedoviü, Ekinoviü [28] analyzed the impacts of chip depth, feed and cutting speed parameters on the formation of white film in the machining of 16MnCr5 steel. The results showed that there is a close relationship between the white film thickness and the arithmetic deviation of the machined surface due to the differences the machining parameters in the machining of the workpiece. Szabó and Kundrák [29] studied the surface residual stresses during hard machining of 16MnCr5 steel with different rake angles. Molnar [30] investigated the changes in the asymmetric height distribution of the surfaces as a result of machining

16MnCr5 hardened steel with hard turning and grinding methods. The feed, chip depth and cutting speed emphasized in the hard turning method, while in the grinding method, evaluations were made specifically in terms of grinding feed rate and revolutions per minute. Magalhães, Ventura [31] deals with the experimental and numerical modelling of residual stresses, cutting forces and tool wear in hard machining of AISI 5115 workpieces. The ability of the numerical model to estimate cutting forces and residual stresses with relative errors below 20% and tool wear with relative errors below 10% is associated with the suitability of numerical modelling of hard turning operations with different edge geometries. Molnár [32] performed a study on the analysis of cutting, surface roughness and residual stress factors in hard machined 16MnCr5 steel. Meyer, Köhler and Denkena [33] studied the impact of tool nose radius on tool wear and cutting forces in hard machining of AISI 5115 steel. Mondal, Das [34] performed the effects of feed and cutting speed on machining of hardened AISI 5115 using different cutting tool tips. In the study, where flat and wide flute chipbreaker TiC coated carbide tips were used. the effects of machining conditions were compared. It was concluded that the mentioned tips exhibited satisfactory performance in MQL conditions even when dry machining conditions could not be achieved uniformly. Agarwal, Suman [16] carried out a study on the optimization of CNC processing of 16MnCr5 steel utilizing TiN coated cutting tools. The main objective of the study was to obtain the machining conditions that obtain the surface roughness with the highest metal removal value using the Taguchi method The parameters that have a considerable impact on metal removal rate and surface roughness are feed rate and depth of cut, respectively. Demirpolat [3] carried out a study on the machining of 16MnCr5 steel under MQL and dry mediums utilizing a carbide-coated insert. In the research where different variations of depth of chip, feed and cutting speed were tested as processing parameters, it was seen that cutting temperature, surface roughness and cutting force values gave better results in the MQL case. Choudhury and Dhar [35] evaluated the chip depth, feed rate and cutting speed as input parameters and the tool wear, cutting temperature, dimensional deviation, surface roughness as output parameters in the machining of 16MnCr5. Results of the research showed that there was a considerable development in surface quality and a decrement in tool wear in the event of machining in MQL mediums compared to dry machining. Rizvi and Ali [36], carried out the optimization of machining parameters in the machining of 16MnCr5 steel in their research. In their study, they observed that the most effective parameter in improving ANOVA results was the machining depth.

In the processing of AISI 5115 hardened steel, judging by the literature review, it has been seen that the focus is on methods such as grinding, hard turning, wire electric discharge. Research on the turning of the material is relatively more limited. The goal of this article is to study the impact of various machining parameters on cutting forces and surface roughness in the machining of AISI 5115 steel by turning method in dry and MQL mediums. In the present research, the influences of cutting speed and feed parameters at different levels were examined as per a full factorial experimental design and (S/N) ratios were utilized to determine the best turning mediums.

2. MATERIAL AND METHOD

2.1. Experimental Setup

In Figure 1, there is a visual of the general schematic of experiment for study including highlights. For this study, AISI 5115 (DIN 16MnCr5) workpiece was provided, and the material was cylindrical in shape with a diameter of 45 mm and a length of 600 mm. Additionally, each experiment was carried out with a machining length of 400 mm. The properties of the material, which is one of the hardened steel types, is given in Table 1. Machining parameters were selected by examining the studies in existing literature and according to the hypothesis established in accordance with the purpose of the experiment, taking into account both material properties and the recommendations of the cutting tool company. The full factorial experimental design, which is preferred because it is an optimum approach since it includes all possible combinations of different machinability parameters [37], was used to specify the feed rate and cutting speed values with their levels. The machining parameters and their levels mentioned above are shown in Table 2.
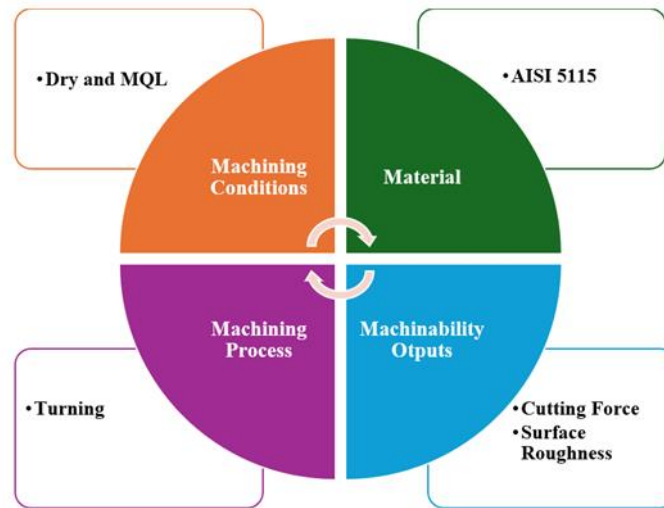
Figure 1. General schematic of experiment.

Table 1. Chemical composition-AISI 5115 [3].

Element (weight %)	P %	C %	Mn%	Si%	Cr%	Fe%
AISI 5115	0.02	0.16	1.20	0.40	1.10	Bal.

Table 2. Machinability parameters/levels.

Exp. No.	Cutting speed (m/min)	Feed rate (mm/rev)	Cutting depth (mm)
1	50	0.15	0.2
2	60	0.15	0.2 0.2
3	90	0.15	0.2
4	135	0.15	0.2
5	50	0.3	0.2
6	60	0.3	0.2
7	90	0.3	0.2
8	135	0.3	0.2

2.2. Cutting Tool, Cutting Conditions and Experiments

Machine tool specifications are presented in Table 3. Cutting tool and tool holder selection was made according to the applications commonly used in the manufacturing sector. As can be found in the literature [38], TiN coated cutting tool was used in accordance with ISO 3685. Machining experiments were carried out in dry and MQL cutting conditions by changing the cutting tools in each experiment. Cutting tool clearance angle was 7°, cutting edge length was 9 mm, cutting tip thickness was 4.97 mm and corner radius was 0.8 mm. STN 15 Micro Lubrication System, the specifications of which are presented in Table 4, environmentally friendly sunflower oil obtained from renewable resources was used. Sunflower oil is a safe oil because it does not contain harmful compounds, so it is a favourable choice among environmentally friendly lubricants [39]. In the MQL system, oil lubricating fluid was sprayed to the machining area from 20 mm and used at 6 bar pressure and 45° nozzle angle. In the study, the influence of two different parameters and levels on surface roughness and cutting force were reseached by the turning method. A total of 16 machining experiments, designed with the full factorial method, were carried out on De Lorenzo S547-8899 lathe. Cutting force signals measured with Kistler 9275 dynamometer were recorded in the computer environment. After processing, surface roughness values were measured from three different points using Mahr Perthometer M1 device and evaluated by taking the averages. Roughness taken into consideration was determined by taking the differences of the highest/lowest values from the roughness measurements and taking the average of the three. Surface roughness measurements were customized according to DIN EN ISO 4287. Figure 2 shows the experimental setup.

Table 3. Machine tool specification.

Maximum workpiece diameter, mm	460
Distance between chuck and tailstock, mm	1500
Spindle speed range, rev/min	25-1800
Spindle speed number, piece	12
Feed range, mm	0.04-2.46
Number of feeds, piece	122
Maximum tool holder size, mm	25x25
Motor power, kW	5.5

Table 4. Micro lubrication system specification.

Supply voltage, V	230-24 AC/DC
Operating voltage, V	24 AC/DC
Power consumption, Watt	5
Air pressure,bar	4-6
Oil quantity, stages	24
Oil quantity min.,ml	0.0012
Oil quantity max.,ml.	0.028
Oiling interval, sec	0.1-10
Operating temperature, °C	-15-70
Reservoir, L	1.5
Viscosity range, cst.	2-30
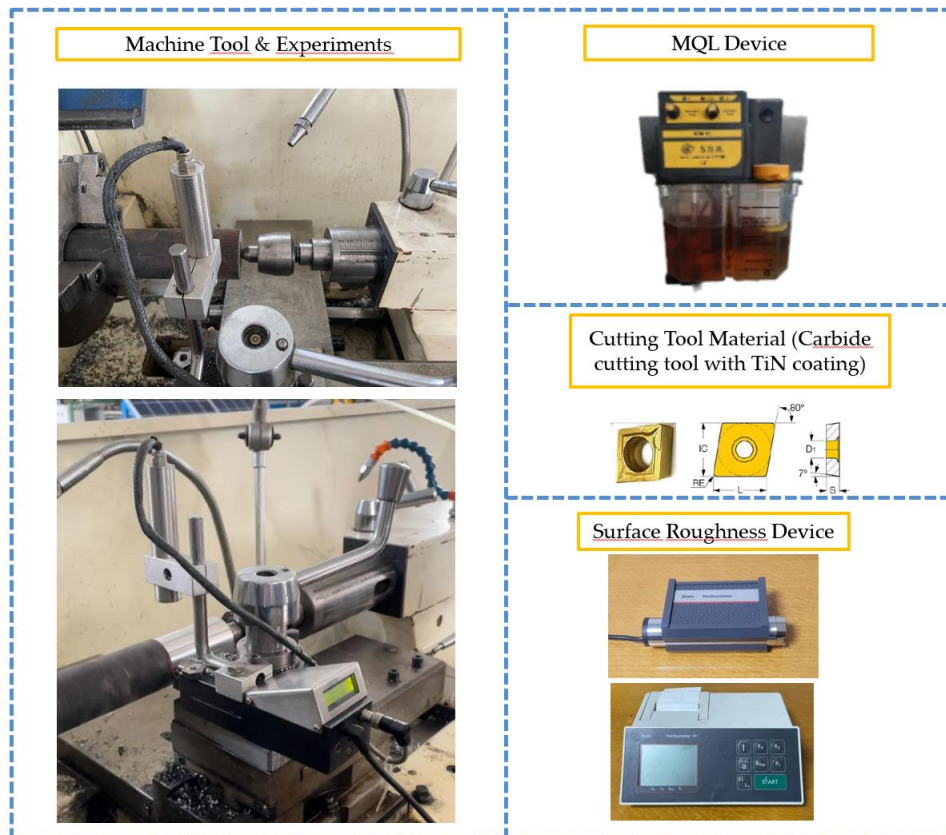
Figure 2. Experimental setup.

3. RESEARCH FINDING

3.1. Surface Roughness

In machining, chip accumulation is seen as a significant problem during the processing of materials. The reason for this is that the accumulated chip formed during the machining of the part negatively affects the surface quality due to the adhesion of the cutting tool [21]. It is thought that the cutting speeds should be increased in order to prevent the formation of accumulated chips. When Figure 3 is given, which shows the average surface roughness varying according to machining parameters and cutting environments, increasing cutting speeds generally affected the surface roughness values (except for high feed and cutting speed values). With the increase of the cutting speed and the feed movement caused by the cutting tool movement, a reduction in the walls occurs. Therefore, during machining, the cutting tool removes chips from the workpiece more easily and better quality surfaces are produced. Since the increase in machining speeds makes the machinability relatively easier, it increases the surface quality of the part, as in [22-24]. The same was observed in the machining of AISI 5115 hardened steel, in dry machining, the worst surface finish was obtained for the combination of 60 m/min cutting speed and 0.15 mm/rev feed rate respectively, while the best surface finish was obtained at 90 m/min cutting speed and 0.15 mm/rev feed rate respectively. Replacing dry environment with MQL did not change the experimental combinations that gave the worst and best surface properties. However, it is clear that the surface roughnesses for MQL environments are in all cases lower than those under dry conditions. This can be explained by the oil film layer formed between the workpiece and the cutting tool interface in the MQL environment, which allows the chips generated during machining to be more easily removed from the cutting medium [40-42]. Rising the feed positively affected the surface quality for the cutting speed values of 50 m/min and 90 m/min in both dry and MQL machining mediums.
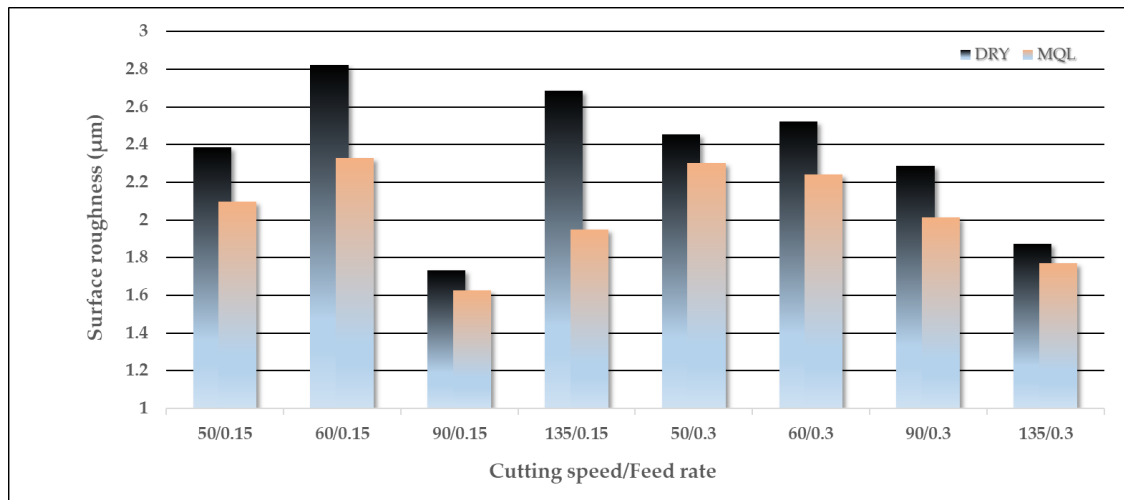
Figure 3. Surface roughness variation vs. cutting speed and feed rate.

S/N (Signal/Noise) ratio is main criterion for analyzing experimental data. This ratio expresses the ratio of a signal to the background noise factor, exemplified by humidity and ambient temperature [43, 44]. According to the smallest-best approach in Taguchi experimental design method, S/N ratios for surface roughness in dry and MQL mediums are given in Figure 4, respectively. According to the graph, the change in cutting speed in dry and MQL mediums corresponds to the S/N worth of surface roughness in the graph. In addition, it can be seen that high feeding level is more effective in experiments conducted in dry conditions, while low level is more effective in MQL results.
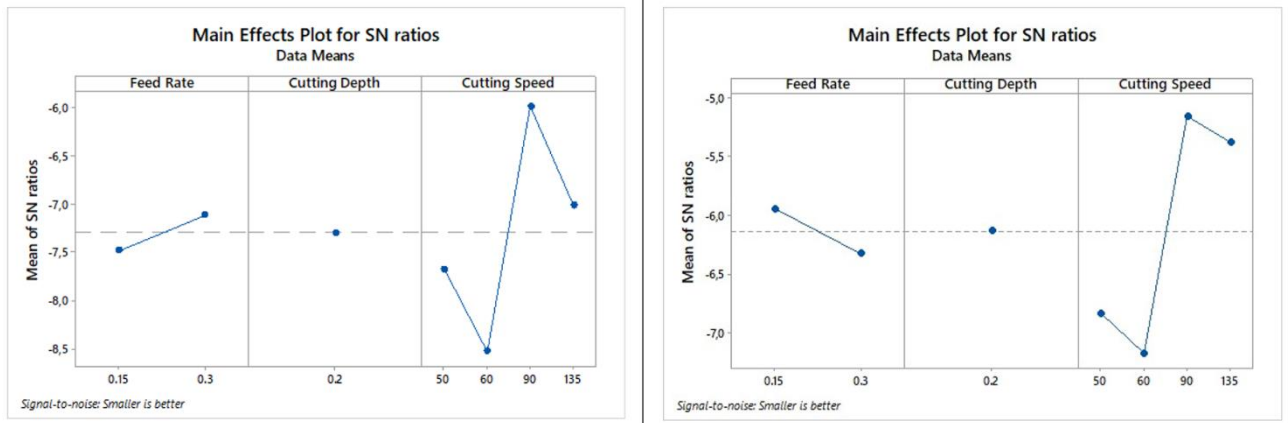
Figure 4. S/N ratio plot for average surface roughness under dry and MQL conditions, respectively.

Chip depth, feed rate and cutting speed are as important as cutting angle and cutting tool geometry for chip angle and control in workpiece machining [45]. As the chip depth increases, rougher surfaces are obtained, while improvements in surface quality occur as the depth decreases [46]. The cutting tool geometry chosen in this study had a significant effect on the removal of surface roughness. Considering the comparison between dry machining and machining with MQL application in the study carried out with constant chip depth, more favorable results were obtained in machining in MQL environment.

3.2. Cutting Force

The assortment in the machining force according to the processing parameters and cutting mediums are given in Figure 5. In general, it is possible to say that the cutting force values increase with the increase in cutting speeds in both cutting conditions. It is well recognized from the literature that the heat in the machining zone rises with growing cutting speeds and therefore the chip is more easily removed from the part [47, 48]. The growing in cutting forces with rising cutting speeds is consistent with the results of studies in literature [5, 49] and it can be said that the reason for the raise is tool wear. It is observed that the cutting force increases with increasing feed rate both dry and MQL environments. In both machining environments, it is also seen that the cutting force rises with increasing progress. At higher feed speeds, since the chip section increases with higher resistance to processing, more force is needed in cutting [50]. It is an expected result that lower cutting force is obtained in MQL conditions than in dry conditions due to the decrease in the temperature formed at the tool-chip interface in MQL environment machining and therefore easier chip removal from the part [51]. In a more general sense, it can be said that in almost all experimental conditions, the cutting force values obtained in machining in MQL environment are lower than those obtained in dry machining. Maximum cutting force values were found in dry machining with 0.3 mm/rev feed and 135 m/min cutting speed and in MQL machining with 0.3 mm/rev and 60 m/min cutting speed.
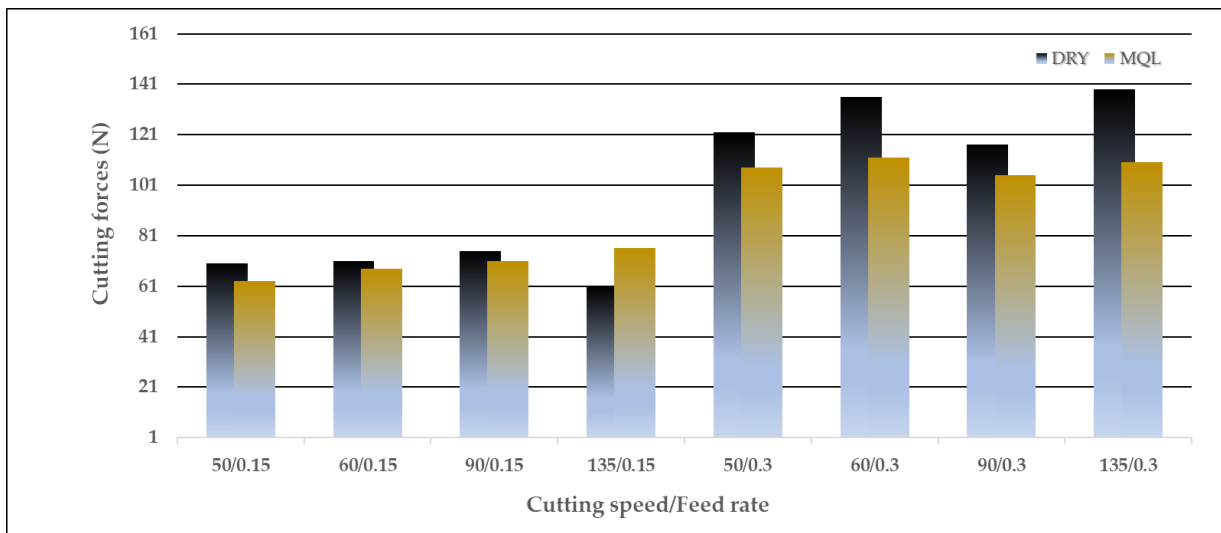
Figure 5. Cutting force variation vs. cutting speed and feed rate.

S/N ratios for cutting force in MQL and dry conditions are given in Figure 6 respectively. While the cutting speed value that minimizes the cutting forces is 50 m/min, keeping the feed at 0.15 mm/rev serves the purpose of reducing the cutting force. Although there are no significant differences between MQL and dry mediums, it can be said that the machining situation in the MQL condition also indicates a cutting speed of 50 m/min and a feed of 0.15 mm/rev.
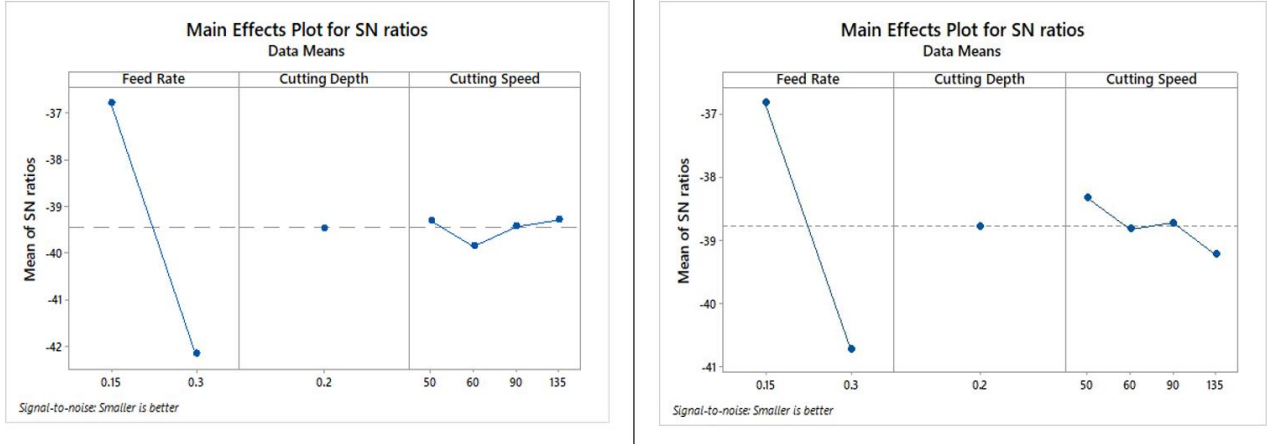
Figure 6. S/N ratio plot for average cutting forces under dry and MQL conditions, respectively.

4. CONCLUSIONS AND DISCUSSIONS

This paper focuses on the machinability of AISI 5115 steel by turning in MQL conditions compared to dry conditions. The fact that there is no satisfactory information yet about the machinability of this material in the MQL environment reveals the originality of the study. The study characterizes the effects of various cutting parameters on surface roughness and cutting force.

The major findings of the research results are summarized below ;

- When all the variables within the scope of the experiment are evaluated together, it is seen that the cooling environment is the most influential of all variables. So much so that, with all other parameters remaining the same, it was observed that there was a significant decrease in the surface roughness value by changing the cooling environment from dry environment to MQL environment. It is also seen that there is a crucial decrease in cutting force values in the MQL method because cutting fluid penetrates well between the workpiece and the cutting tool. When the comparison of machining under the two working conditions is made, it is seen that machining under MQL mediums gives better results. In MQL conditions, an average 6.90% reduction in cutting force and 12.2% reduction in surface roughness occurred. In addition, it can be said that MQL is an effective option in terms of environmental impacts and cost effectiveness compared to dry conditions

Although the fact that the study does not address the impact of cutting tool geometry on the experimental parameters does not prevent it from contributing to science, it is anticipated that its evaluation will provide opportunities for future research. By taking this study as a reference, which provides a framework that will form the basis for more comprehensive studies, studies can be conducted in which the effects of cutting parameters/levels on more parameters can be evaluated interactively and the process can be optimized.

REFERENCES

[1] H. Akkuş, AISI 1040 çeliğinin işlenebilirliği sırasında oluşan yüzey pürüzlülüğü değerlerinin farklı tahmin modelleri ile araştırılması, Kahramanmaraş Sütçü İmam Üniversitesi Mühendislik Bilimleri Dergisi, 24(2) (2021) 84-92.

[2] M. Yaka, AISI 1040 çeliğinin tornalanmasında yüzey pürüzlülüğünün istatistiksel incelenmesi, Amasya Üniversitesi Fen Bilimleri Enstitüsü, Amasya, 2019.

[3] H. Demirpolat, Evaluation of the turning parameters of AISI 5115 steel in dry and MQL cutting environments with the use of a coated carbide cutting insert: An experimental study, Journal of Materials and Mechatronics: A, 5(1) (2024) 168-182.

[4]   R. Binali, M. Kuntoğlu, An in-depth analysis on the surface roughness variations during turning of GGG50 ductile cast iron, Doğu Fen Bilimleri Dergisi, 5(2) (2022) 41-49.

[5]   M. Kuntoğlu, et al., Parametric optimization for cutting forces and material removal rate in the turning of AISI 5140, Machines, 9(5) (2021) 90.

[6]   İ. Asiltürk, A comprehensive analysis of surface roughness, vibration, and acoustic emissions based on machine learning during hard turning of AISI 4140 steel, Metals, 13(2) (2023) 437.

[7]   M. Kuntoğlu, Measurement and analysis of sustainable indicators in machining of Armox 500T armor steel. Proceedings of the Institution of Mechanical Engineers, Part C: Journal of Mechanical Engineering Science, 236(13) (2022) 7330-7349.

[8]   E. Salur, The effects of MQL and dry environments on tool wear, cutting temperature, and power consumption during end milling of AISI 1040 steel, Metals, 11(11) (2021) 1-16.

[9]   P. Sivaiah, D. Chakradhar, Effect of cryogenic coolant on turning performance characteristics during machining of 17-4 PH stainless steel: A comparison with MQL, wet, dry machining, CIRP Journal of Manufacturing Science and Technology, 21(2018) 86-96.

[10] M. Kuntoğlu, K. Kaya, R. Binali, Investigation of surface roughness changes in the machining of carbon steel under sustainable conditions, In Int. Conf. Pioneer Innov. Stud. of Conferenc, 163-167.

[11] D.Y. Pimenov, et al., A comprehensive review of machinability of difficult-to-machine alloys with advanced lubricating and cooling techniques, Tribology International, (2024) 109677.

[12] S. Yağmur, AISI 1050 çeliğinin tornalanmasında minimum miktarda yağlamanın (MMY) kesme kuvvetleri ve yüzey pürüzlüğü üzerindeki etkisinin araştırılması, Gazi University Journal of Science Part C: Design and Technology, (2023) 1-1.

[13] R. Binali, Experimental and machine learning comparison for measurement the machinability of nickel based alloy in pursuit of sustainability, Measurement, 236 (2024) 115142.

[14] R. Binali, et al., Energy saving by parametric optimization and advanced lubri-cooling techniques in the machining of composites and superalloys: A systematic review, Energies, 15(21) (2022) 8313.

[15] İ. Yeğen, M. Usta, The effect of salt bath cementation on mechanical behavior of hot-rolled and cold-drawn SAE 8620 and 16MnCr5 steels, Vacuum, 85(3) (2010) 390-396.

[16] S. Agarwal, et al., Optimisation of cutting parameters during turning of 16MnCr5 steel using Taguchi technique, International Journal on Interactive Design and Manufacturing (IJIDeM), 18(4) (2024) 2055-2066.

[17] C. Baykara, E. Atik, The effect of surface roughness and carburized depth on wear resistance in 16MnCr5 case hardening steel, Industrial Lubrication and Tribology, (2024).

[18] S. Arunkumar, et al., Study properties and mechanical behavior of the shaft material 16MnCr5, Materials Today: Proceedings, 37 (2021) 2458-2461.

[19] P. Arrabiyeh, et al., Micro grinding 16MnCr5 hardened steel using micro pencil grinding tools with diameters∼ 50 μm, CIRP J Manuf Sci Technol; 27(2019) 1–10.

[20] K. Mouralova, et al., Analyzing the surface layer after WEDM depending on the parameters of a machine for the 16MnCr5 steel, Measurement, 94 (2016) 771-779.

[21] T. Saini, K. Goyal, D. Bhandari, Multi-response optimization of WEDM parameters on machining 16MnCr5 alloy steel using Taguchi technique. Multiscale and Multidisciplinary Modeling, Experiments and Design, 2 (2019) 35-47.

[22] V. Molnar, Experimental Investigation of Tribology-Related Topography Parameters of Hard-Turned and Ground 16MnCr5 Surfaces, Lubricants, 11(6) (2023) 263.

[23] R. Carrera Espinoza, et al., Study on the Tribological Properties of DIN 16MnCr5 Steel after Duplex Gas-Nitriding and Pack Boriding, Materials, 17(13) (2024) 3057.

[24] J. Jacob, M. Meurer, T. Bergs, Surface Roughness Prediction in Hard Turning (Finishing) of 16MnCr5 Using a Model Ensemble Approach, Procedia CIRP, 126:(2024) 504-507.

[25] D. Frölich, et al., Investigation of wear resistance of dry and cryogenic turned metastable austenitic steel shafts and dry turned and ground carburized steel shafts in the radial shaft seal ring system, Wear, 328 (2015) 123-131.

[26] V. Molnar, Influence of cutting parameters and tool geometry on topography of hard turned surfaces, Machines, 11(6) (2023) 665.

[27] I.P. Balabanov, Y. Balabanova, A. Agayev, Development of a parametric model for calculating cutting forces in external cylindrical turning of 16MNCR5 Steel, Key Engineering Materials, 979:(2024) 11-18.

[28] M. Mehmedoviü, et al. Influence of operating regime parameters on white layer formation during a turning process of hardened 16MnCr5 steel, In Proceedings of 10th International Research/Expert Conference "Trends in the Development of Machinery and Associated Technology" TMT.

[29] G. Szabó, J. Kundrák, Investigation of residual stresses in case of hard turning of case hardened 16MnCr5 Steel, Key Engineering Materials, 581 (2014) 501-504.

[30] V. Molnar, Asymmetric height distribution of surfaces machined by hard turning and grinding. Symmetry, 14(8) (2022) 1591.

[31] F. Magalhães, et al., Experimental and numerical analysis of hard turning with multi-chamfered cutting edges, Journal of Manufacturing Processes, 49 (2020) 126-134.

[32] Molnár, V., Analyzing surface integrity elements of hard turned 16mncr5 steel. Cutting & Tools in Technological System, 98 (2023) 49-58.

[33] R. Meyer, J. Köhler, B. Denkena, Influence of the tool corner radius on the tool wear and process forces during hard turning, The International Journal of Advanced Manufacturing Technology, 58:(2012) 933-940.

[34] K. Mondal, et al., An investigation on turning hardened steel using different tool inserts, Materials and Manufacturing Processes, 31(13) (2016) 1770-1781.

[35] S. Choudhury, N. Dhar, Study of the behavior of the minimum quantity lubrication (mql) in turning 16MnCr5 steel, Proceedings of the All India Conference on Recent Developments in Manufacturing & Quality Management, India, (2007) 167-177.

[36] S.A. Rizvi, W. Ali, Integration of grey-based Taguchi technique for the optimization of process parameters during the turning operation of 16MnCr5 steel, Int J Ind Eng Prod Res, 30(2019) 245-254.

[37] J.D. Kechagias, et al., A comparative investigation of Taguchi and full factorial design for machinability prediction in turning of a titanium alloy, Measurement, 151(2020) 107213.

[38] ISO 3685: Tool-life Testing with Single-point Turning Tools. 1993: International Organization for Standardization (ISO): Geneva, Switzerland.

[39] M.A. Makhesana, et al., Evaluation of drilling and hole quality characteristics in green machining aluminium alloys: A new approach towards green machining, Journal of Manufacturing Processes, 129 (2024) 176-186.

[40] R.H. Namlu, et al., An experimental study on surface quality of Al6061-T6 in ultrasonic vibration-assisted milling with minimum quantity lubrication, Procedia CIRP, 108 (2022) 311-316.

[41] O. Öndin, et al., Investigation of the influence of MWCNTs mixed nanofluid on the machinability characteristics of PH 13-8 Mo stainless steel, Tribology International, 148 (2020) 106323.

[42] A.K. Sharma, A.K. Tiwari, A.R. Dixit, Effects of Minimum Quantity Lubrication (MQL) in machining processes using conventional and nanofluid based cutting fluids: A comprehensive review, Journal of cleaner production, 127 (2016) 1-18.

[43] S. Neşeli, S. Yaldız, E. Türkeş, Optimization of tool geometry parameters for turning operations based on the response surface methodology, Measurement, 44(3) (2011) 580-587.

[44] R. Binali, Parametric optimization of cutting force and temperature in finite element milling of AISI P20 steel. Journal of Materials and Mechatronics: A, 4(1) (2023) 244-256.

[45] F. Kafkas, H. Gürbüz, U. Şeker, Analysis of the effect of tool geometry and machining parameters on surface integrity properties in turning of AISI 316L stainless steel by Taguchi method, Gazi Üniversitesi Fen Bilimleri Dergisi Part C: Tasarım ve Teknoloji, 10(3) (2022).

[46] M. Pul, H.B. Özerkan, Al 6061 alaşımının işlenmesinde kesme derinliği ve kesici takım geometrisinin yüzey pürüzlülüğüne ve takım aşınma davranışına etkisi. Gazi Üniversitesi Mühendislik Mimarlık Fakültesi Dergisi, 37(4):(2022) 2013-2024.

[47] B. Özlü, H. Demir, M. Türkmen, The effect of mechanical properties and the cutting parameters on machinability of AISI 5140 steel cooled at high cooling rates after hot forging, Politeknik Dergisi, 22(4) (2019) 879-887.

[48] Demirpolat, H., et al., AISI 52100 Rulman Çeliğinin Tornalanmasında İşleme Parametrelerinin Yüzey Pürüzlülüğü, Kesme Sıcaklığı ve Kesme Kuvveti Üzerindeki Etkilerinin İncelenmesi. İmalat Teknolojileri ve Uygulamaları, 4(3)179-189.

[49] R. Binali, S. Yaldız, S. Neşeli, Finite element analysis and statistical investigation of S960ql structure steel machinability with milling method, Journal of the Brazilian Society of Mechanical Sciences and Engineering, 46(5) (2024) 260.

[50] H. Demirpolat, et al., Comparison of tool wear, surface roughness, cutting forces, tool tip temperature, and chip shape during sustainable turning of bearing steel, Materials, 16(12) (2023) 4408.

[51] R. Binali, et al., Machinability investigations based on tool wear, surface roughness, cutting temperature, chip morphology and material removal rate during dry and MQL-assisted milling of Nimax mold steel, Lubricants, 11(3)(2023) 101.

Manufacturing Technologies and Applications
MATECA

Alternative Approach to Charging Stations: Hybrid Renewable Energy System Design

Samet Yavuz[1] [iD], Selim Sayın[1] [iD], Emre Çakır[1] [iD], Kübra Keser[1, *] [iD]

[1] Kutahya Dumlupinar University, Simav Technical Faculty, Department of Electrical and Electronics Engineering, 43500 Simav/Kutahya, Turkey

ABSTRACT

Solar and wind energy are among the renewable energy sources and are green energy types that do not create polluting waste. Integrating renewable energy into power systems is one of the most popular approaches today. By combining the two types of energy, the effects of energy sources can be understood, a safe and economical system can be created. Hybrid renewable energy systems can provide energy sustainability. The aim of this study is to present an innovative system that feeds Arduino and creates a mini mobile phone charging station by using the voltage values obtained from solar panels and wind turbines together. The system optimizes the supply and demand balance by synchronizing both energy sources. Thanks to the system, the energy produced by the solar panel and wind turbine is collected and combined with an energy management system. Arduino is integrated with the energy management system to monitor energy, control the charging process and provide a user interface. The most important features of the study are to contribute to the use of renewable energy sources with the developed method and to increase environmental awareness, as well as to provide awareness and skills in electronics and energy systems. The study provides the user with a practical and environmentally friendly charging solution, while serving as an example to demonstrate the potential of renewable energy sources.

Keywords: Solar panel, Wind turbine, Green energy, Arduino, Renewable energy

Şarj İstasyonlarına Alternatif Yaklaşım: Hibrit Yenilenebilir Enerji Sistemi Tasarımı

ÖZET

Güneş ve rüzgâr enerjisi yenilenebilir enerji kaynakları arasında yer almakta olup, kirletici atık oluşturmayan yeşil enerji türüdür. Yenilenebilir enerjiyi güç sistemlerine entegre etmek günümüzde en popüler yaklaşımlardan biridir. İki enerji türünü birleştirerek enerji kaynaklarının etkisi anlaşılabilir, güvenli ve ekonomik bir sistem oluşturulabilir. Hibrit yenilenebilir enerji sistemleri enerji sürdürülebilirliğini sağlayabilir. Bu çalışmanın amacı, güneş panellerinden ve rüzgâr türbinlerinden elde edilen voltaj değerlerini birlikte kullanarak Arduino'yu besleyen ve mini bir cep telefonu şarj istasyonu oluşturan yenilikçi bir sistem sunmaktır. Sistem, her iki enerji kaynağını senkronize ederek arz ve talep dengesini optimize eder. Sistem sayesinde güneş paneli ve rüzgâr türbini tarafından üretilen enerji toplanır ve bir enerji yönetim sistemi ile birleştirilir. Arduino, enerjiyi izlemek, şarj sürecini kontrol etmek ve bir kullanıcı arayüzü sağlamak için enerji yönetim sistemi ile entegre edilmiştir. Çalışmanın en önemli özellikleri, geliştirilen yöntemle yenilenebilir enerji kaynaklarının kullanımına katkıda bulunmak ve çevre bilincini artırmak, ayrıca elektronik ve enerji sistemleri konusunda farkındalık ve beceri kazandırmaktır. Çalışma kullanıcıya pratik ve çevre dostu bir şarj çözümü sunarken, yenilenebilir enerji kaynaklarının potansiyelini göstermek için bir örnek teşkil etmektedir.

Anahtar Kelimeler: Güneş paneli, Rüzgâr türbini, Yeşil enerji, Arduino, Yenilenebilir enerji

1. INTRODUCTION

Fossil fuel resources are used to meet energy needs in Turkey and the world. While these resources are among the exhaustible energy resources, they have increased the need for alternative energy resources due to their harm to human health [1-3] and the environment (soil, water, air pollution, etc.) [4,5]. Clean, reliable, sustainable energy that will overcome negativities, reduce dependency on other countries, and make maximum use of energy produced with renewable resources is of great importance here.

Solar energy is a type of energy with high potential for widespread use due to its advantages such as being environmentally friendly, renewable, the cleanest and inexhaustible energy source, and reducing carbon dioxide emissions in the atmosphere [6,7]. Solar energy can be used in three ways: photovoltaic (PV), photothermal and photocatalytic [7]. PV panels convert sunlight directly into electricity, while thermal

systems are used to heat water or air using solar energy [6]. Solar energy is converted into electrical energy in PV panels, where monocrystalline and polycrystalline silicon materials are commonly used. This panel structure has a built-in electric field. When photons with an energy greater than the band gap energy of the semiconductor material of the panels come from the sun, if these photons are absorbed, electrons move towards the conduction band. DC power is generated by the flow of this electron-hole structure in opposite directions [8]. In addition to the increasing interest in PV cells worldwide, the increasing trend in installed capacity, their ease of installation, not causing waste, not affecting living things and lower costs make them preferred [9,10]. Wind energy stands out with its development in the last decade, its low energy costs, its high-power generation capacity, its sustainable clean energy source, and its public health protection due to the fact that it does not produce gas that will cause environmental and air pollution [11,12]. In addition, although the annual cumulative wind energy capacity is constantly increasing, it is stated in various studies that generating power from wind energy reduces greenhouse gas (GHG) emissions by 330-590 tons of CO_2 per Gigawatt (GW) hour [12].

Both types of energy are green energy types as they are among the renewable energy sources and do not create waste that pollutes the environment. However, the use of renewable energy sources separately increases the capital cost due to the variability and intermittency of some energies and decreases the system reliability [13]. In this case, hybrid renewable energy systems, where energy is produced by bringing at least two energy sources together, are one of the most popular approaches.

PV-wind energy systems are among the examples that can be given to different types of hybrid renewable energy systems. Although the sun's rays decrease towards the end of the day, there is more intense solar radiation in certain seasons. Wind, on the other hand, blows continuously, although it has different speeds. Bringing these two energies together can bring about a hybrid system that complements each other [13]. Turkey has much more advantage than many countries in terms of both solar energy and wind energy potential due to its location in the middle belt with its geographical location.

When looking at the literature, it is seen that there is a review of the final dimensioning methodologies of hybrid renewable energy systems [13], where information is presented and evaluations are made about different types of hybrid renewable energy systems, as well as another comprehensive review that aims to present a review of the latest developments in the field of optimization of different hybrid renewable energy systems (HRES) using various optimization techniques based on classical methods, artificial intelligence (AI), hybrid algorithms and software-based optimization tools [14]. In a study where solar energy is used for battery charging systems, it is reported that an Arduino-based solar battery charging system is designed and implemented, and it is stated that the system consists of a solar panel, Arduino microcontroller and battery [15]. In the study, where it is aimed to propose the preliminary design of a small Arduino-based wind energy production system, it is stated that the data can be used for further analysis to determine the wind energy potential in the field [16]. Another study, titled A review of hybrid renewable energy systems: Solar and wind-powered solutions: Challenges, opportunities, and policy implications, addresses key challenges such as system optimization, energy storage, and seamless power management, as well as discussing technological innovations such as machine learning algorithms and advanced inverters that have the potential to overcome these hurdles. It also emphasizes that the study's results show that hybrid renewable energy systems have the potential to not only meet but also exceed future energy demands in a sustainable manner [17]. Another study examining the latest studies published in hybrid renewable energy systems focuses on the four basic categories of hybrid energy systems: dimensioning, optimization, control and energy management. The advantages and disadvantages of these methods are discussed comparatively [18]. In a study where a grid-connected solar-wind hybrid system was presented to meet the electrical load demand of a small shopping complex and an electric vehicle charging station was included in the grid, it was stated that a cost-effective and reliable system could be designed by appropriately managing renewable power generation and load demands. In this study, a solar-wind hybrid system is proposed, the working methodology, mathematical model, objective function and constraints of the system as well as various optimization algorithms are included [19]. In the study titled Techno-economic analysis of a hybrid solar wind electric vehicle charging station in highway roads, it is stated that 17 electric vehicles can be charged during the day from 6:00 in the morning to 6:00 in the evening with the designed system [20].

When these studies are examined, it is seen that there are generally studies on the dimensioning, optimization, modeling and examination of hybrid renewable energy systems; review articles presenting information on different hybrid renewable energy systems; and studies on hybrid energy systems for electric vehicles. In the study on Arduino-based systems, it is seen that solar or wind energy is included separately, and most of them do not aim to charge electronic devices such as phones.

Based on all these shortcomings, this study aims to design and develop an Arduino-based charging station to charge mobile phones using solar and wind energy together. PV-wind hybrid systems were considered and focused on obtaining higher power, and an innovative system was presented that uses the voltage values obtained from solar panels and wind turbines together to power the Arduino and create a mini charging station.

With the created system, both energy sources are synchronized and the supply and demand balance is optimized. Thanks to the system, the energy produced by the solar panel and wind turbine is collected and combined with an energy management system. Arduino is integrated with the energy management system to monitor the energy, control the charging process and provide the user interface. A wind energy system consisting of a wind turbine, charge controller and batteries is added. The wind turbine produces electricity from the blowing wind and this electricity is processed by the charge controller and stored in the battery.

The developed method contributes to the use of renewable energy sources and the increase of environmental awareness, while also raising awareness about electronics and energy systems. The original and special aspect of the study is the ability to charge portable devices such as mobile phones without being dependent on the electrical grid and the provision of a clean and reliable hybrid renewable energy source to power small electronic devices. Another unique aspect is that devices can be charged even when there is little or no sunlight. This study can be developed and used more widely in larger power systems in the future.

2. MATERIAL AND METHOD

2.1. Materials

Solar panels, wind turbine, Arduino microcontroller, DC-DC charging module, voltage regulator, 3 diodes (1N4007), 6 resistors, 2 coils (750 nH), 4 capacitors (2350 uF/1410 uF) were used in the creation of the system. The basic features of the elements used are given in Table 1.

Table 1. Basic properties of the elements used

Element used	Basic properties
Solar panels	12 V, 300 mA, 5 W; dimension: 110 cmx220 cm; 30° inclined (for optimal light reception)
Wind turbine	16 V, 310 mA, 5W, horizontal vertical axis, hard plastic
Arduino microcontroller	5 V, uno, 14 digital I/O pins and 6 analog inputs
DC-DC charging module	Input voltage 6-24V, output current 3A
Voltage regulator	LM2596 adjustable DC-DC regulator, 4-35V input voltage, 1-30V output voltage

2.2. System Design

In order to equalize the frequencies of the voltage values coming from the wind turbine and solar panel, to ensure synchronous operation and to prevent possible frequency fluctuations from damaging the Arduino and other electronic materials to be used, a rectifier circuit was installed and connected to the outputs of each energy source. In order to prevent feedback to the outputs of the motor used in the wind turbine, 2 diode connections were made, one for input and one for output. The output of these diodes was connected to the positive and negative ends of the 2350 μF capacitor, and then the LM2596 adjustable DC-DC regulator was connected to the ends of the 1410 μF capacitor. The same process was applied to the solar panel. The positive and negative poles of the solar panel were connected as inputs by the 2350 μF capacitor of the second circuit we created from the capacitors and coils, and the LM2596 adjustable DC-DC regulator was connected to the ends of the 1410 μF capacitor as outputs. In order to increase the current value of the circuit, the outputs of the LM2596 adjustable DC-DC regulators were connected in parallel.

The rotor blades of the wind turbine are made of lightweight materials and are designed to start rotating even at low wind speeds, then mounted to capture maximum wind (Figure 1.a). For the turbine's electricity production efficiency, the turbine outputs are regularly monitored and necessary adjustments are made.

Solar panels, which are one of the energy types in the system and are used in solar energy production, are mounted to receive the sun's rays at the steepest angle in order to obtain the highest energy efficiency (Figure 1.b). After the panel connections were made in parallel and series configurations to provide the voltage and

current values obtained in the simulation program and required for the operation of the system, the voltage measurements were verified using digital multimeters.

After the installation of solar panels and wind turbine is completed, the DC motor used in the wind turbine must be able to reach the desired speed with the help of the wing connected to the motor. For this, calculations were made and a gearbox design was created that would allow the motor to make 25 turns with one turn of the wing due to the effect of the wind. The spur gears to be used in the gearbox design phase were drawn in the AutoCAD program and printed on a 3D printer. The assembly of these printed spur gears was compressed between two transparent plexiglas and the gearbox design was completed. In order to minimize the wear of the gears in the wind turbine mechanism, the gear sizes were kept thick and the minimum wearable material was used (Figure 1.c-e).
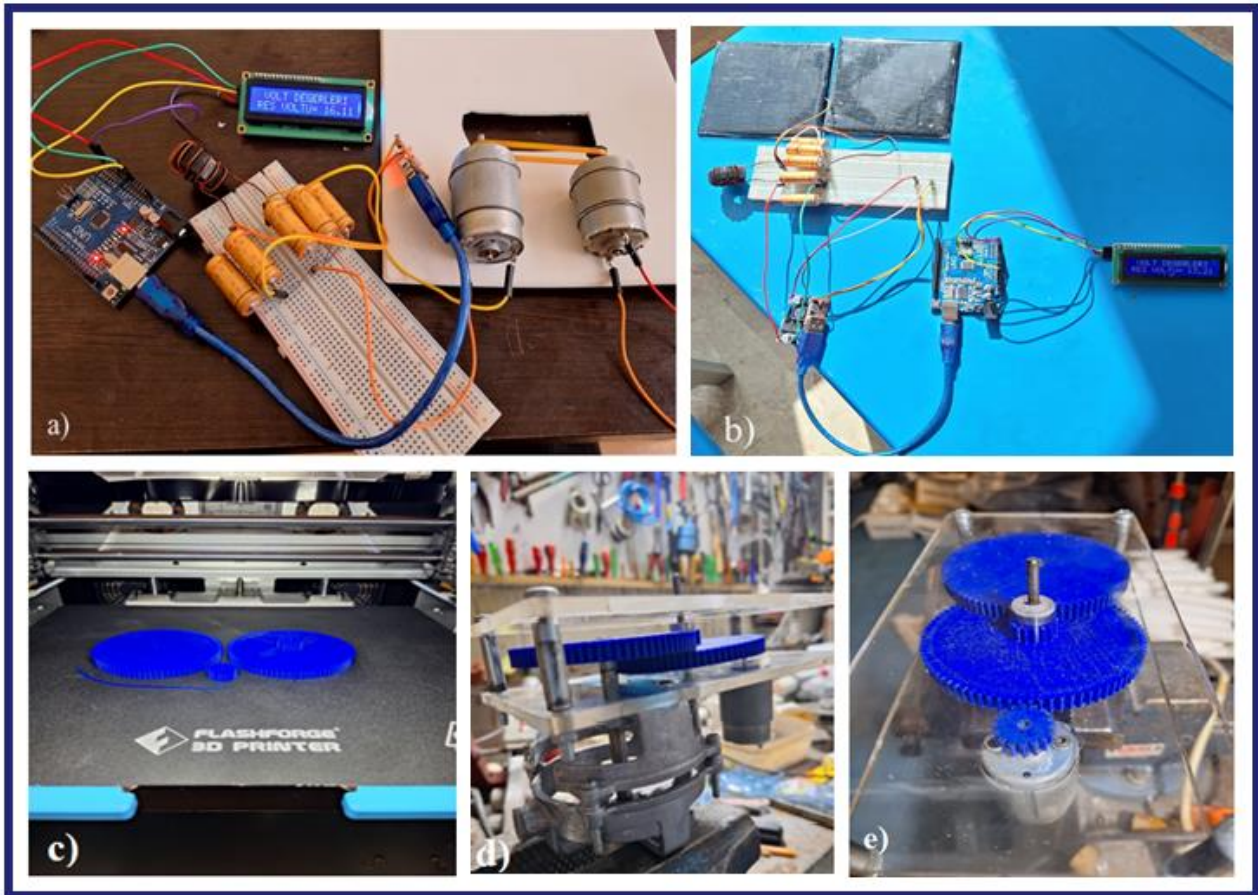
Figure 1. Design of hybrid renewable energy system a) Wind energy system circuit b) Solar energy system circuit c-e) Gear box

In the next stage, the Arduino was properly connected to the microcontroller and the analog pins were used for the connections of the loads (phone charger). The connection diagram was drawn in detail and tested on the breadboard.

By integrating Arduino with the energy management system, it is possible to monitor energy, control the charging process and stop the solar panel and wind turbine if necessary. Following this process, an interface software was developed that will monitor energy levels, manage the charging process and provide information to the user.

In order to feed the Arduino, the parallel connected outputs of the LM2596 adjustable DC-DC regulators were connected to the DC-DC charging module and the Arduino was fed from the output of this module. In addition, a second DC-DC charging module to be used for phone charging was connected in parallel to this DC-DC charging module.

A circuit design was made on the perforated plate so that the voltage values produced by the power sources could be displayed on the LCD screen via the Arduino. The terminals coming from the output of the rectifier circuit consisting of the capacitors and coils connected to the output of the solar panel with the 10K and 1K resistors connected in series were connected ((+) terminal to the 10K resistor, (-) terminal to the 1K

resistor). Then, the connection was made from the serially connected terminals of the 1K and 10K resistors to the A1 analog pin on the Arduino.

In order to measure the voltage value generated in the wind turbine, a simple circuit consisting of a series connection of a separate 10 K and 1 K resistor was connected to the plus and minus poles coming from the output of the rectifier circuit consisting of a capacitor and a coil ((+) end to the 10 K resistor, (-) end to the 1 K resistor). Afterwards, the DC motor used in the wind turbine was associated with these circuit connections and a connection was made from the series-connected ends of the two resistors to the A2 analog pin on the Arduino.

In order to measure the output voltage of the parallel connection of the LM2596 adjustable DC-DC regulators, the series connection of the 10K and 1K resistors was connected to the ends, the (+) of the parallel connection was connected to the 10K resistor and the (-) to the 1K resistor, and then this series resistor structure was connected to the analog A0 pin on the Arduino.

For the LCD screen connection, the SCL pin on the LCM1602 module outputs connected to the LCD screen is connected to the Arduino's analog A5 pin; the SDA pin is connected to the Arduino's analog A4 pin, while the VCC pin is connected to the Arduino's 5 Volt pin and the GND pin is connected to the Arduino's GND pin (Figure 2).
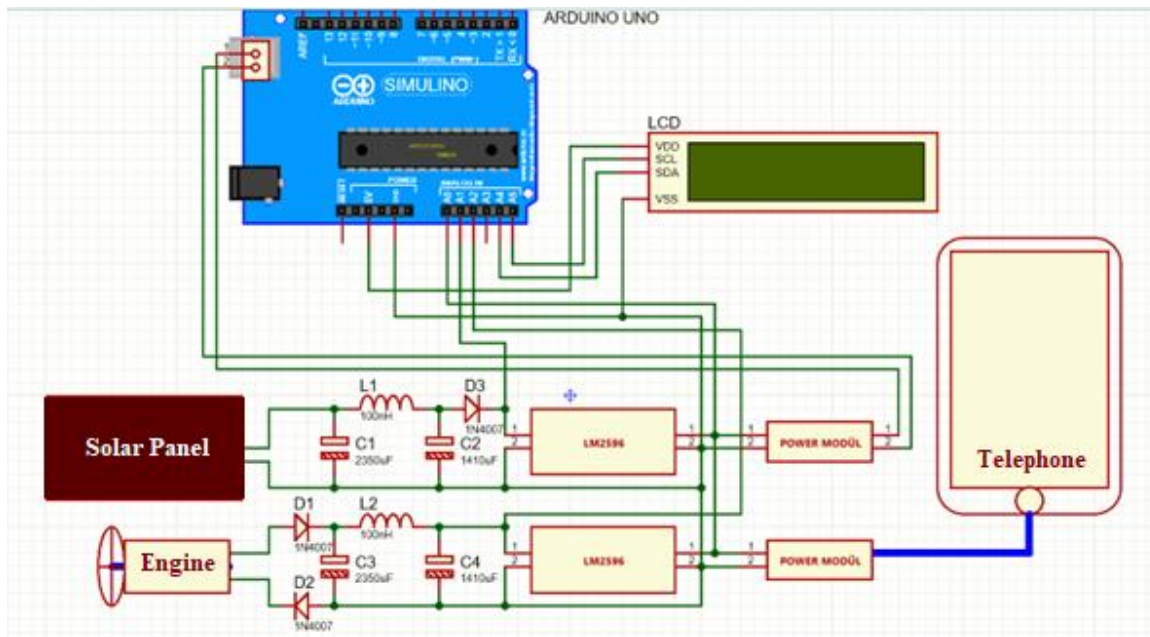
Figure 2. Proteus circuit simulation of hybrid system (for single voltmeter)

2.3. System Testing and Calibration

After the system design was completed, the power data obtained from the solar panel and wind turbine were tested in various weather conditions. Charge and discharge performances were monitored and the overall efficiency of the system was evaluated. Percentage error values were calculated from the data obtained by using the equation in Equation 1.

$$\text{Percentage Error} = [(\text{Observed value} - \text{True value})/(\text{True value})] \times 100 \tag{1}$$

3. EXPERIMENT AND OPTIMIZATION RESULTS

In addition to the importance of the separate design of circuits in hybrid renewable energy systems, another of the most important issues is that the installed systems can be operated without problems when they are integrated. In the final stage of this study, a power box was created in which the solar panel and wind turbine, which were designed separately, were brought together. The power box view of the created hybrid renewable energy system is given in Figure 3.

Separate buttons were placed on the box to cut the energy of the LCD screen, wind turbine and solar panel, and a separate button was installed to cut the energy of the modules used for Arduino supply and phone charging.
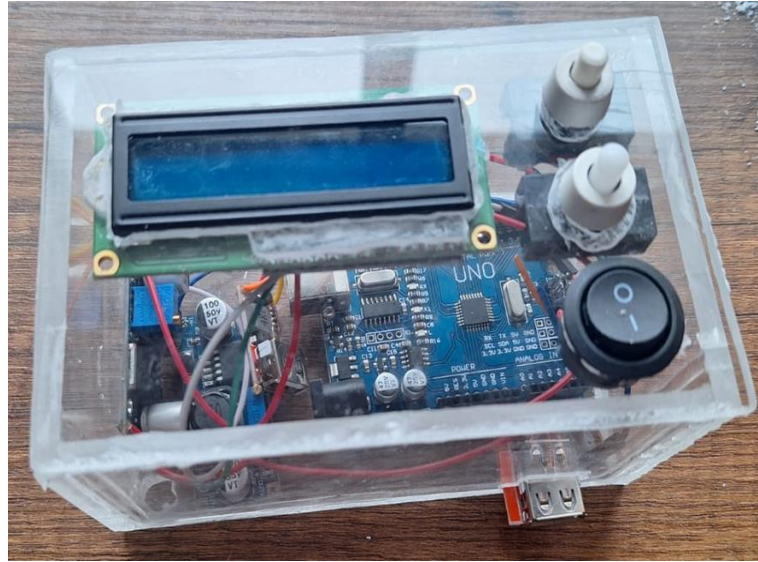
Figure 3. Electronic hardware of the designed hybrid system

The structure where the solar panel is placed on the wing, DC motor and gearbox is connected to the wooden floor via an aluminum pipe.
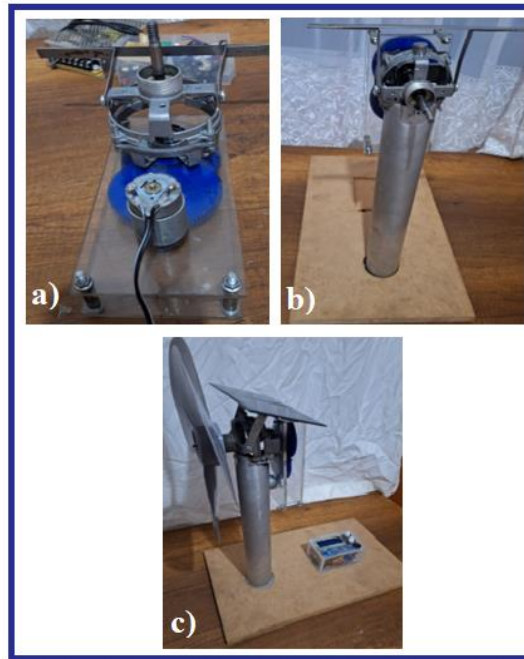
Figure 4. Combining wind and solar energy systems
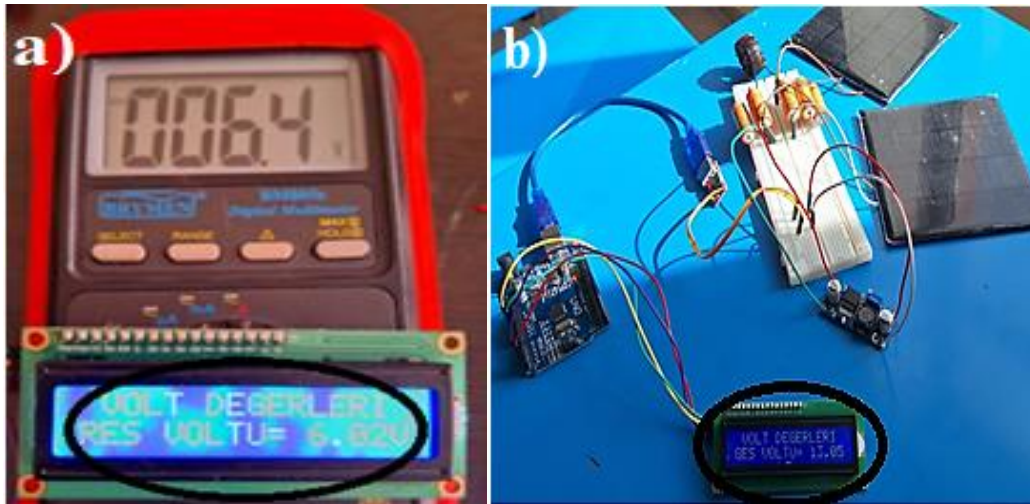
Figure 5. Obtained test results a) Wind energy system result b) Solar energy system result

When looking at Figure 5.a, it is seen that the voltage value obtained from the system created with the wind energy system is 6.4 V when read with a voltmeter, while it is 6.02 V when read from the LCD screen on the power box. When looking at Figure 5.b, the voltage value read on the LCD screen in the system created with the solar energy system is 13.02 V.

When these data are evaluated, it is confirmed that measurements can be made with a 6% error with the wind energy system with RES, that synchronous measurements can be made, and that the energy produced by the solar panel and wind turbine is collected and used correctly.

In addition, the voltage measurements of all modules were calibrated by testing whether energy management was done properly. After this stage, the study was concluded when it was seen that Arduino controlled the feeding process correctly and the phone charging process could be done successfully and without any problems.

4. CONCLUSIONS

In this study, an innovative system that feeds Arduino and creates a mini charging station using the voltage values obtained from a hybrid renewable energy system where solar panels and wind turbines are used together, which has not been used in other studies in the literature, is presented.

With the work presented,

- Having a structure that optimizes the supply and demand balance by synchronizing both energy sources and combining them with an energy management system,

- In addition to being able to make synchronous measurements, measurements can be made with a 6% error with the wind energy system,

- Verifying that the energy produced by the solar panel and wind turbine is collected and used correctly are the most important outputs presented.

It has been tested in the experimental stages that the phone charges successfully with the designed system, but studies need to be done on increasing the charging efficiency and shortening the charging time.

REFERENCES

[1] J. Kotcher, E. Maibach, WT. Choi, Fossil fuels are harming our brains: identifying key messages about the health effects of air pollution from fossil fuels. BMC Public Health, 19 (2019) 1079, https://doi.org/10.1186/s12889-019-7373-1.

[2] F. Perera, Pollution from fossil-fuel combustion is the leading environmental threat to global pediatric health and equity: Solutions exist, Int. J. Environ. Res. Public Health, 15 (1) (2018) 16.

[3] M. Romanello et al.*,* The 2022 report of the *Lancet* Countdown on health and climate change: health at the mercy of fossil fuels, The Lancet, 400, 10363, 1619 – 1654.

[4] F. Martins, C. Felgueiras, M. Smitkova, N. Caetano, Analysis of fossil fuel energy consumption and environmental ımpacts in european countries, Energies, 12 (2019) 964, https://doi.org/10.3390/en12060964.

[5] A. Kavoosi, Environmental pollution caused by the use of fossil fuels in architecture and the need for renewable energy, Science and Technology of the Day, 2(4) (2021) 314-319.

[6]   E. Kabir, P. Kumar, S. K Kumar, A. A. Adelodun, K. Kim, Solar energy: Potential and future prospects, Renewable and Sustainable Energy Reviews, 82(2018) 894-900, https://doi.org/10.1016/j.rser.2017.09.094.

[7]   J, Gong, C. Li, M.R. Wasielewski, Advances in solar energy conversion, Chemical Society Reviews, 48 (2019) 1862. https://doi.org/10.1039/C9CS90020A.

[8]   M.M. Fouad, L.A. Shihata, E.I. Morgan, An integrated review of factors influencing the perfomance of photovoltaic panels, Renewable and Sustainable Energy Reviews, 80 (2017) 1499-1511.

[9]   M. Tawalbeh, A. Al-Othman, F. Kafiah, E. Abdelsalam, F. Almomani, M. Alkasrawi, Environmental impacts of solar photovoltaic systems: A critical review of recent progress and future Outlook, Science of The Total Environment, 759 (2021) 143528, https://doi.org/10.1016/j.scitotenv.2020.143528.

[10]   M.B. Hayat, D. Ali, K.C. Monyake, L. Alagha, N. Ahmed, Solar energy—A look into power generation, challenges, and a solar-powered future, International Journal of Energy Research, 43 (2018) 1049–1067, https://doi.org/10.1002/er.4252.

[11] F. M. Guangul, G.T. Chala, SWOT analysis of wind energy as a promising conventional fuels substitute, 2019 4th MEC International Conference on Big Data and Smart City (ICBDSC), Maskat, Umman, 2019, ss. 1-6, 10.1109/ICBDSC.2019.8645604.

[12]   K. Adeyeye, N. Ijumba, J. Colton, Exploring the environmental and economic impacts of wind energy: a cost-benefit perspective, International Journal of Sustainable Development & World Ecology, 27(8) (2020) 718–731.

[13]   J. Lian, L., Y. Zhang, C. Ma, Y. Yang, E. Chaima, A review on recent sizing methodologies of hybrid renewable energy systems, Energy Conversion and Management, 199 (2019) 112027.

[14]   M. Thirunavukkarasu, Y. Sawle, H. Lala, A comprehensive review on optimization of hybrid renewable energy systems using various optimization techniques, Renewable and Sustainable Energy Reviews, 176 (2023) 113192, https://doi.org/10.1016/j.rser.2023.113192.

[15]   A. Muthyala, Solar Powered Battery Charging System by Using Arduino: Experimental design, International Transactions on Electrical Engineering and Computer Science, 2(2) (2023) 52-59, https://doi.org/10.62760/iteecs.2.2.2023.49

[16]   G. Al Mubarok, W. Djatmiko, M. Yusro, Design of Arduino-based small wind power generation system, E3S Web of Conferences, 67 (2018) 01006,. https://doi.org/10.1051/e3sconf/20186701006.

[17]   Q. Hassan, S. Algburi, A. Z. Sameen, H.M. Salman, M. Jaszczur, A review of hybrid renewable energy systems: Solar and wind-powered solutions: Challenges, opportunities, and policy implications, Results in Engineering, 20 (2023) 101621.

[18]   Ammari, D. Belatrache, B. Touhami, S. Makhloufi, Sizing, optimization, control and energy management of hybrid renewable energy system—A review, 3 (4) (2022) 399-411. https://doi.org/10.1016/j.enbenv.2021.04.002.

[19]   S. Singh, P. Chauhan, N. J. Singh, Feasibility of Grid-connected Solar-wind Hybrid System with Electric Vehicle Charging Station, Journal of Modern Power Systems and Clean Energy, 9(2) (2021) 295-306.

[20]   J. Nishanthy, S.C Raja, T. Praveen, J.J.D. Nesamalar, P. Venkatesh, Techno-economic analysis of a hybrid solar wind electric vehicle charging station in highway roads, International Journal of Energy Research, 46 (2022) 7883–7903, https://doi.org/10.1002/er.7688.

Manufacturing Technologies and Applications MATECA

Ultra High Frequency Induction System Sintering of Nano Boron Nitride Reinforced Powder Aluminum

Hıdır Sercan Çubuk [1, *] (ID), Alper Mutlu[2] (ID), Uğur Çavdar[3] (ID)

*[1]Dokuz Eylül Üniversitesi, Fen Bilimleri Enstitüsü, Konstrüksiyon ve İmalat Anabilim Dalı, İzmir, Türkiye, hsercancubuk@gmail.com
[2]Dokuz Eylül Üniversitesi, Meslek Yüksekokulu, Elektronik Otomasyon Biyomedikal Cihaz Teknolojisi Alanı, İzmir, Türkiye, alper.mutlu@deu.edu.tr
[3]İzmir Demokrasi Üniversitesi, Mühendislik Fakültesi, Makine Mühendisliği Bölümü, İzmir, Türkiye, ugur.cavdar@idu.edu.tr

ABSTRACT

In the study, powder sintering of Nano Boron Nitride reinforced Aluminum powders was applied with a 2.8 kW power, 900 kHz Ultra High Frequency Induction System. Nano Boron Nitride reinforced aluminum matrix powder compositions were compressed by a cold press in a uniaxial single-acting mold under 20 bar pressure, afterwards sintered with the given parameters. Five different compositions which are 0.1 wt.%, 0.5 wt.%, 1 wt.%, 2 wt.% and 5 wt.% Nano Boron Nitride reinforced aluminum composites were processed. In order to sinter these 5 different compositions, temperatures of 600°C, 650°C and 700°C were determined. These optimizations were carried out separately by subjecting them to Induction Sintering for 3, 5 and 10 minutes. The resulting samples are approximately 16.00 mm in diameter and 4.75 mm in height with a coin-like structure. After the production of 45 samples determined by temperature, time and additive ratio; hardness, density, energy efficiency and SEM results of these samples were compared among themselves and the effects of Nano Boron Nitride reinforcement on Induction Sintering were revealed.

Keywords: Alumınıuim, Nano boron nitride, Induction sintering, Penetration depth, Powder metallurgy

Nano Bor Nitrür Takviyeli Alüminyum Tozlarının Ultra Yüksek Frekanslı İndüksiyon Sistemi ile Sinterlenmesi

ÖZET

Yapılan çalışmada, Nano Bor Nitrür takviyeli Alüminyum tozlarına; 2.8 kW güç ve 900 kHz'lik Ultra Yüksek Frekanslı İndüksiyon Sistemi'yle toz sinterlenmesi işlemi yapılmıştır. Nano Bor Nitrür katkılı alüminyum matrisli toz kompozisyonları; 20 bar basınç altında tek eksenli tek tesirli bir kalıp içerisinde soğuk pres ile sıkıştırılmış, ardından belirlenen parametreler ile sinterlenmiştir. %0.1, %0.5, %1, %2 ve %5 Nano Bor Nitrür takviyeli alüminyum kompozitleri olmak üzere 5 farklı kompozisyonda işlem yapılmıştır. Bu 5 farklı kompozisyonun sinterleme sıcaklığı olarak 600°C, 650°C ve 700°C sıcaklık belirlenmiştir. Bu optimizasyonlar ayrı ayrı olmak üzere 3, 5 ve 10 dakika İndüksiyon Sinterleme işlemine tabi tutulmuştur. Oluşan numuneler, yaklaşık olarak 16.00 mm çapında ve 4.75 mm yüksekliğinde bozuk para benzeri yapıdadır. Sıcaklık, süre ve katkı oranı ile belirlenen 45 adet numunenin üretiminin ardından; bu numunelerin sertlik, yoğunluk, enerji verim ve SEM sonuçları kendi arasında karşılaştırılmış, Ultra Yüksek Frekanslı sinterlemenin Nano Bor Nitrür takviyeli Alüminyum malzeme üzerine etkileri araştırılmıştır.

Anahtar Kelimeler: Alüminyum, Nano bor nitrür, İndüksiyon sinterleme, Penetrasyon derinliği, Toz metalurjisi

1. GİRİŞ

Alüminyum (Al) hafif ve kolay şekil verilebilen, diğer metallere kıyasla mukavemet özellikleri düşük bir elementtir. Bu element ulaşımdan inşaat sektörüne kadar mühendislik uygulamalarında sıklıkla kullanılmaktadır. Bu yüzden Al'a mukavemet ve mekanik iyileştirmeler yapılması ile alakalı birçok çalışma bulunmaktadır [1-4]. Al'a yapılan iyileştirmelerde sıklıkla seramik takviyelerden yararlanılır. Bu takviyeler, seramik malzemelerin mekanik, termal ve kimyasal özelliklerini alüminyum matrisine transfer ederek malzemenin özelliklerini geliştirmektedir. Çünkü seramik takviyeler; yüksek sertlik ve mukavemet, düşük yoğunluk, uzun süreli sıcaklık dayanımı, iyi aşınma ve korozyon direnci gibi birçok avantaj sağlar. Bunun yanı sıra bu takviyeyi fiziksel ve kimyasal olarak daha etkili sonuçlar verdiği bilinen 'nano' boyutta yapmak; yeni ve gelişmeye açık çalışmaların da önünü açabilmektedir [5-11].

Nano Bor Nitrür (NBN), matris elementine iyi bağlanma özellikleri gösterebilen nano boyutta bir seramik türüdür. Bu malzeme yarı iletkendir. Oksidasyona karşı direnci olup, mekanik ve termal özellikleri ile dikkat

çekmekte ve toz metalürji (TM) tekniklerinde kullanılabilmektedir. Malzemenin nano boyutta taneciklere sahip olması özelliklerini geliştirmiştir [12,13]. NBN, alüminyum matrisle kompozit oluşturulduğunda oluşan yapı iyi mekanik ve termal iletkenlik sağlayabilmektedir [13,14].

Bu ve buna benzer kompozit malzemeler üretilirken indüksiyon sinterleme tekniğinin kullanıldığı görülmüştür. İndüksiyonla sinterlemede, indüksiyon bobinleri yüksek frekanslı elektromanyetik alan üreterek malzemelere ısıl işlem uygular ve nihai parça elde edilir [15-17]. Bu yöntem, kısa süreli yüksek sıcaklık oluşturmasıyla hızlı ve etkili bir sinterleme süreci sağlamaktadır. İşlem; homojen ısıtma, düşük enerji tüketimi, kontrol edilebilir ısıtma hızı ve daha kısa işlem süreleri gibi avantajlar sağlar. Ek olarak, indüksiyon sinterleme yöntemi, özellikle yüksek sıcaklıklarda hızlı sinterleme gerektiren durumlar için kullanılır [18,19].

Bu çalışmada; Saf Al tozuna, ağırlıkça %0.1, %0.5, %1, %2 ve %5 NBN katkısı eklenerek Ultra Yüksek Frekanslı İndüksiyon Sistemi (UYFIS) ile sinterlemesi sağlanmıştır. Sinterleme yoluyla elde edilen numunelerin sertlik, SEM, yoğunluk ve elektrik kullanımı sonuçları kendi arasında karşılaştırılmıştır.

2. MATERYAL VE YÖNTEM

2.1. Deney Düzeneği

Çalışmada malzeme olarak Saf Al ile NBN tozları kullanılmıştır. Kullanılan Al tozları %98.50-98.85 saflığa sahip 15 mikron boyutunda küresel ve pul görünüme sahip tozlardır. Tozun yoğunluğu 1.25 gr/cm^3 – 1.45 gr/cm^3 arasında değişmektedir (Nanokar, İstanbul). Takviye elemanı olarak ise NBN kullanılmıştır. Bu malzemenin saflığı %99.8 ve boyutu 65-75 nm'dur. Yapısı Hegzagonal (h-BN) 'dir. Gaz atomizasyonu yöntemi ile üretilmiştir (Nanografi, Ankara). NBN'ün diğer özellikleri Tablo 1'de verilmiştir.

Tablo 1. NBN özellikleri.

Nano Bor Nitrür (NBN) Parametreleri	Değeri	Birimi
Gerçek Yoğunluk	2.3	*g/cm^3*
Moleküler Ağırlık	24.82	*g*
Kristalite	Hegzagonal	-
Termal İletkenlik	29 ila 60	*W/m*
Termal Genleşme	0.54 ila 18	*μm/m*
Gencin Modülü	14 ila 60	*GPa*
Tam Kütle	25.0124	*g*
Monoizotropik Kütle	25.012	*g*

2.2. Deney Yöntemi

Bu çalışmada üretim; TM yöntemiyle gerçekleştirilmiştir. Şekil 1'de numunelerin üretim yöntemi gösterilmektedir.

(1) Saf Al, Saf Nano BN Tozları Temini ve Optimizasyon
(2) Tozların V Tipi Mikserde Karıştırılması
(3) Karışımların Tek Eksenli, Tek Tesirli Kalıp ile Soğuk Preslenmesi
(4) Belirlenen Sürelerde ve Sıcaklıklarda UYFIS Sinterlemesi ve Doğal Soğuma
(5) Analiz ve Değerlendirme (Sertlik Taraması, Mikroyapısal Analiz,Yoğunluk Değişimi ve Enerji Kullanımı)
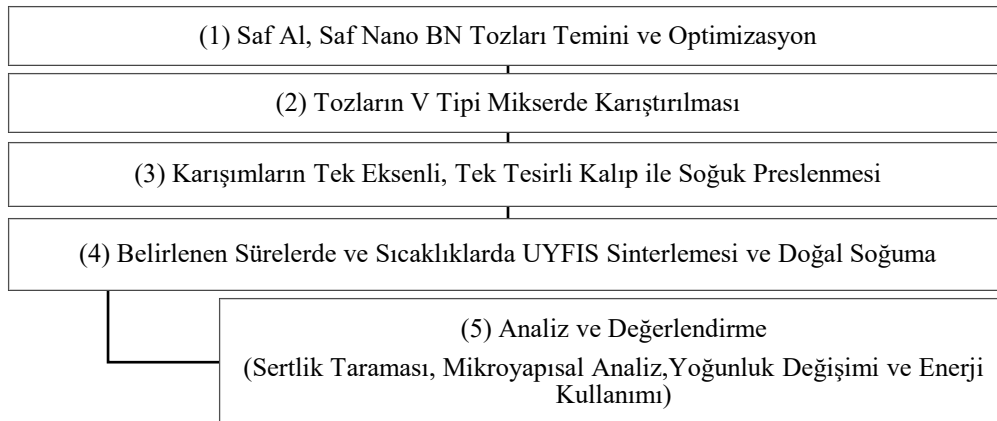
Şekil 1. Saf Al matrisli, NBN katkılı kompozitlerin üretim aşamaları.

Çalışma; yüzdece katkı, sıcaklık ve süre optimizasyonu ile başlamıştır. Yüzdece katkı için Al'a eklenen NBN katkı oranları %0.1, %0.5, %1, %2 ve %5 olarak belirlenmiştir. Bu 5 farklı NBN katkılı Al matrisli toz kompozitlerinin oluşması için İzmir Demokrasi Üniversitesi Laboratuvarında bulunan Weightlab Instruments marka WSA-224T model 0.0001 g hassasiyetli elektronik terazi kullanılmıştır. Hazırlanan tozlar, sızdırmaz V-Tipi bir karıştırıcıda 1 saat boyunca 40 devir/dakika olacak şekilde homojen olarak karıştırılmıştır.

Ardından sıcaklık optimizasyonu için 600°C, 650°C ve 700°C sıcaklıklar belirlenmiştir. Her sıcaklık için 5 farklı katkı oranına sahip Al matrisli NBN tozları hazırlanmıştır. Farklı sıcaklıklardaki sinterleme için hazırlanan bu 15 farklı toz karışımının süre optimizasyonu belirlenmiştir. Ayrı ayrı 3, 5 ve 10 dakika bekleme süreleriyle toplam 45 adet toz karışımı hazır hale getirilmiştir. Hazırlanan bu karışımlar ortalama 2.5 gramdır. Al matrisli NBN toz karışımlarının sıkıştırılması için tek eksenli tek tesirli kalıp kullanılmıştır. Sıkıştırma, 20 bar basınç altında Hidropir marka pres kullanılarak yapılmıştır. Kullanılacak kalıp ise alaşımlı sertleştirilmiş çelik silindirdir. Kalıbın dış çapı 56 mm, yüksekliği 61 mm'dir. İçeriye giren zımbanın dış çapı 16 mm'dir. Sıkıştırma sonrası oluşan numune 16 mm çap (±2%)) ve 4.96 (±2%)) kalınlığa sahiptir. Şekil 2'de (a) karıştırılmış ve tartılmış Al matrisli NBN toz kompoziti (2.55gr (±2%)), (b) karıştırılan tozun kalıp içine doldurulması, (c) pres sonrası elde edilen ham malzeme gösterilmektedir.
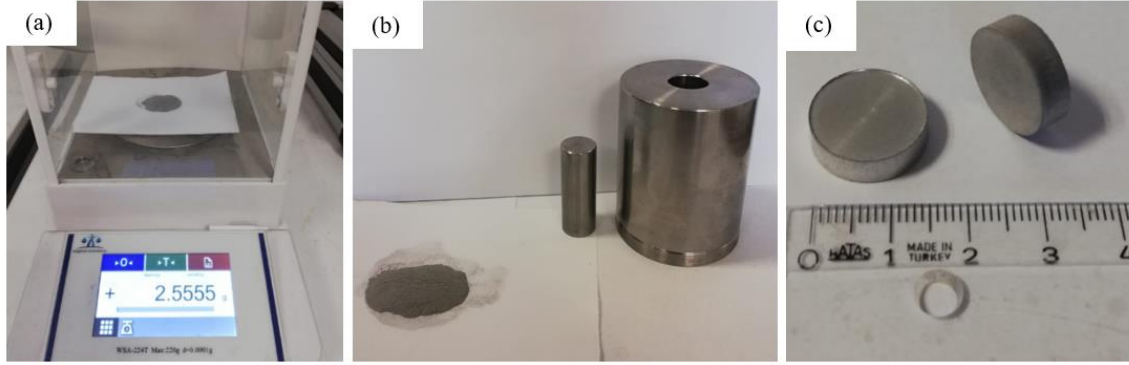
Şekil 2. a) %0.5 NBN katkılı Al tozu (2.55gr (±1%)), b) karıştırılan tozun kalıp içine doldurulması, c) pres sonrası elde edilen ham numune paketi.

Elde edilen 45 adet ham silindir paketleri, belirlenen sıcaklık ve sürelerde UYFIS kullanılarak sinterlenmiştir. İndüksiyon cihazı 2.8 kW güç, 900 kHz'lik Ultra Yüksek Frekanslı İndüksiyon cihazıdır. Işıma hızı ~20 0C/s'dir. Cihazın indüksiyon bobini tek sarımlıdır. Bobinin dış çapı 26 mm, et kalınlığı 0.5 mm'dir. Sinterlemeden sonra doğal soğumaya bırakılan numunelerin yüzeyleri, mekanik ve mikroyapısal analizin yapılabilmesi için Metkon Forcipol 202 marka cihazla 100'den 2500 kuma kadar SiC zımparası ile zımparalanmış ardından 6μ ve 1μ elmas süspansiyon çuha ile parlatılmıştır. Şekil 3' de 600°C, 5 dk'da %1 NBN katkılı Al kompozitinin (8 numaralı numune) UYFIS ile sinterlemesi verilmiştir. Şekil 4'te ise UYFIS Sinterlemesi sonrası hazır hale getirilmiş tüm numuneler gösterilmektedir. Harflendirilen her satır farklı NBN katkı oranına sahip numuneleri sunmaktadır.

Şekil 3. 600°C 5 dk'da %1 NBN katkılı Al kompozitinin (8) UYFIS sinterlemesi işlemi.
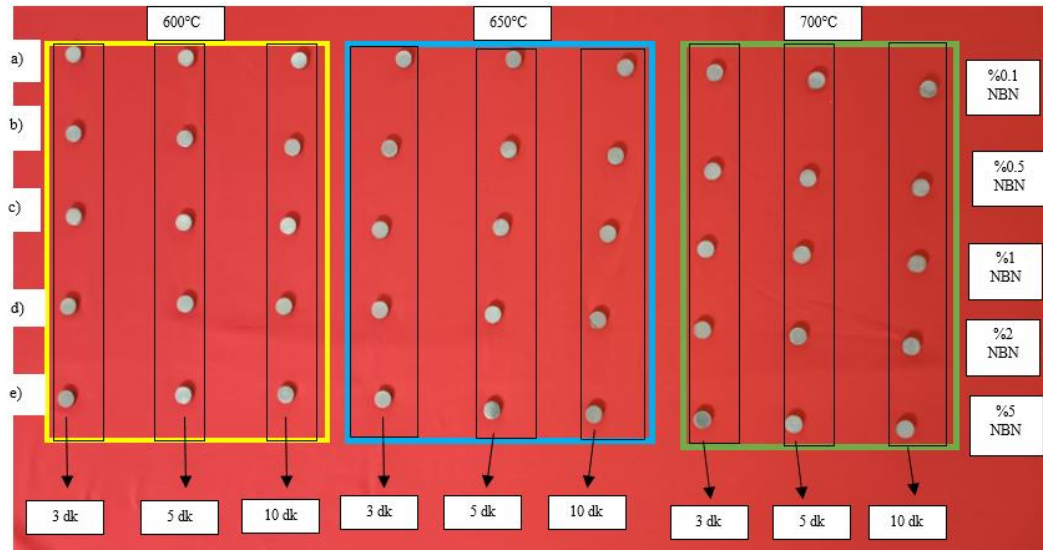
Şekil 4. Özellikleri ile birlikte 45 adet numune.

2.3. Analiz

NBN taktiyeli Saf Al kompozitlerin sertlik deneyleri, Metkon Duroline-LV Vickers Hardness Tester (HV) sertlik ölçme cihazında ASTM E92 standardına uygun olarak 10 saniye süre ve 3 kgf yükte gerçekleştirilmiştir. Sertlik ölçümleri numunenin dıştan içeri doğru 5 farklı noktasından yapılmıştır. Her noktada ise 5 kez ölçüm yapılmıştır. Bu anlamda; her noktada kabul edilen sertlik değeri, o noktadan alınan 5 sertlik değerinin ortalamasıdır. Bu da hata payını (Error Range: E.R.) en aza indirmiştir. Her bir kompozisyon için malzemenin yüzeyinde belirlenen noktalardan sertlik taraması 45 numunenin tamamında gerçekleştirilmiştir. Sertlik taraması penetrasyon derinliğinden (ısıl işlem bölgesi), yani malzemenin en dışından 2 nokta (1.ve 2.nokta), ardından malzemenin merkezine doğru sırasıyla 3 noktadan (3,4 ve 5.nokta) alınmasıyla yapılmıştır. Numunenin 1.noktası çapı, 5. noktası merkezidir. Ayrıca analizlerdeki E.R. gösterilmektedir. Şekil 5'te numune üzerinden ölçülen sertlik noktalarının şematik gösterimi verilmektedir.
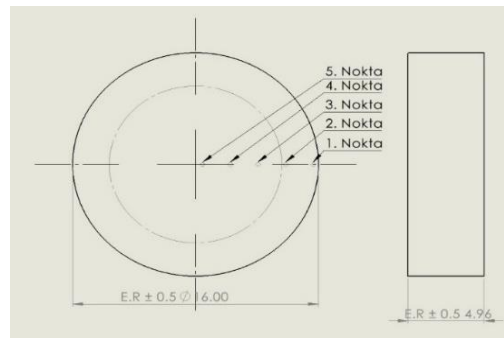
Şekil 5. Numune üzerinden ölçülen sertlik noktalarının şematik gösterilmiş hali.

Numunelerden SEM görüntüleri alınmadan önce %1 hidroflüorik asit; %1.5 klorhidrik asit; %2.5 nitrik asit ve %95 saf su içeriğine sahip Keller sıvısıyla 4 saniye boyunca dağlanmıştır. Ardından mikro yapı analizleri SEM ile incelenmiştir. SEM incelemeleri İzmir Yüksek Teknoloji Enstitüsü Malzeme Araştırma Merkezi Laboratuvarı'nda bulunan FEI marka QUANTA FEG 250 model cihaz ile yapılmıştır.

%0.1, %0.5, %1, %2 ve %5 NBN takviyeli Saf Al kompozitlerin deneysel yoğunlukları ASTM B962-17 standardına uygun olarak Arşimet Prensibine göre yapılmıştır. Öncelikle, 0.0001 gr hassasiyete sahip dijital terazi yardımıyla kompozitlerin ağırlıkları (mA) ölçülmüştür. Ardından su içerisinde bekletilen kompozitlerin suya doymuş ağırlıkları (mD) ölçülmüştür. Sonrasında 40°C sıcaklıkta etüv fırını içerisinde kurutulan kompozitlerin kuru ağırlıkları (mK) dijital terazi ile belirlenmiş ve deneysel yoğunluklar hesaplanmıştır.

Çalışmada UYFIS sinterlerlemesi yapılırken enerji verileri kaydedilmiştir. Buna göre her bir numunenin indüksiyon sinterlemesi sırasında harcadıkları enerji kWh cinsinden yazılmıştır. Elektrik maliyetinin hesaplanması amacıyla güç kalite analizörü kullanılmıştır.

3. DENEY VE OPTİMİZASYON SONUÇLARI

3.1. Sertlik Bulguları

600°C, 650°C ve 700°C'de yapılan;%0.1, %0.5, %1, %2 ve %5 NBN takviyeli Saf Al kompozitlerinin UYFIS sinterlemesi sonucu sertlik ölçümleri yapılmıştır. Sertlik alınan noktalar dış çaptan merkeze doğru sırasıyla 1,2,3,4 ve 5. noktayı göstermektedir. En yüksek sertlik tüm numunelerde 1. noktada (çap) ; en düşük sertlik ise 5.noktada (merkez) görülmektedir. Numunelerdeki E.R.± %2.28 olarak belirlenmiştir. HV cinsinden yapılan ölçüm sonuçları Şekil 6'da verilmektedir.
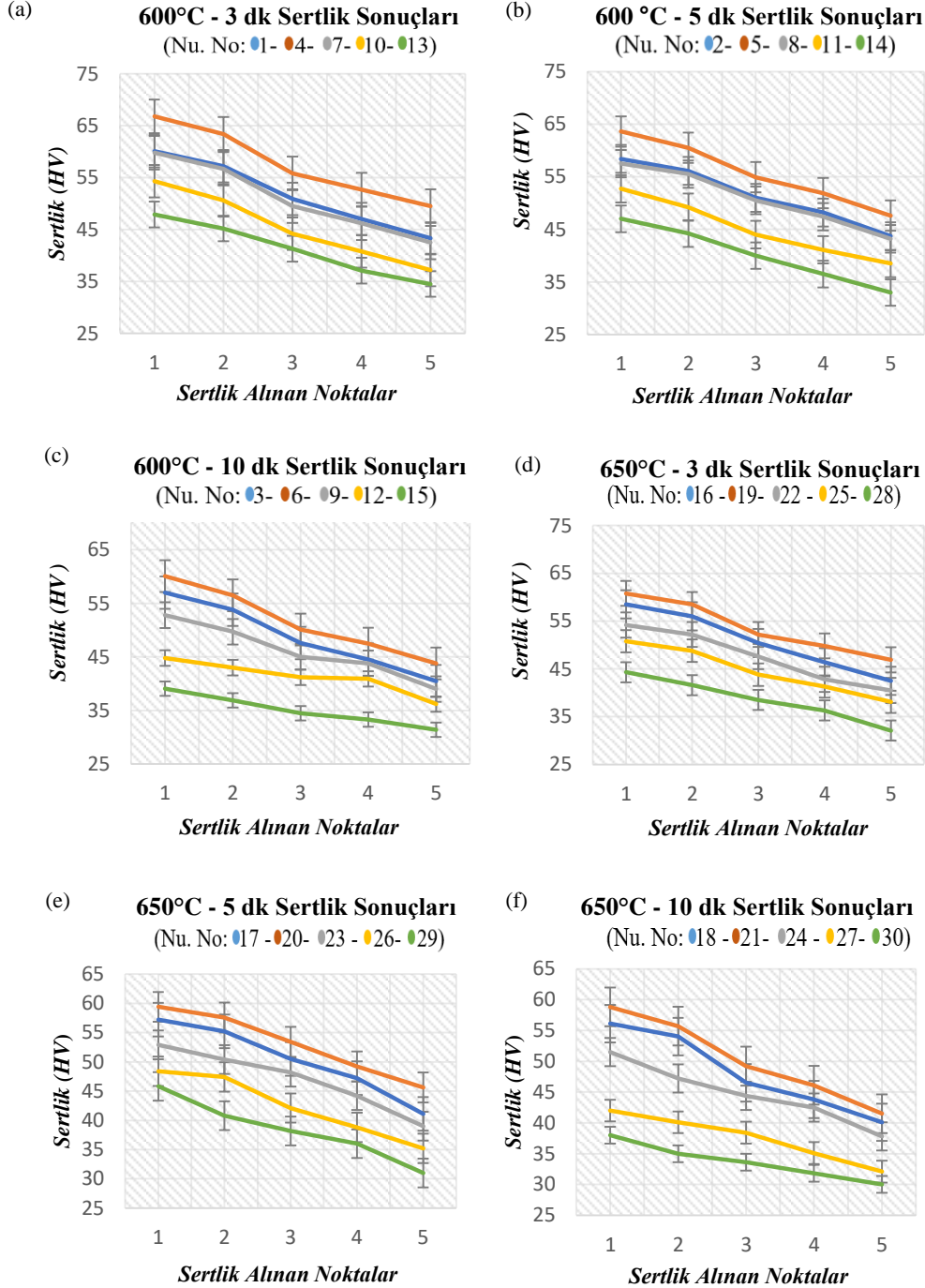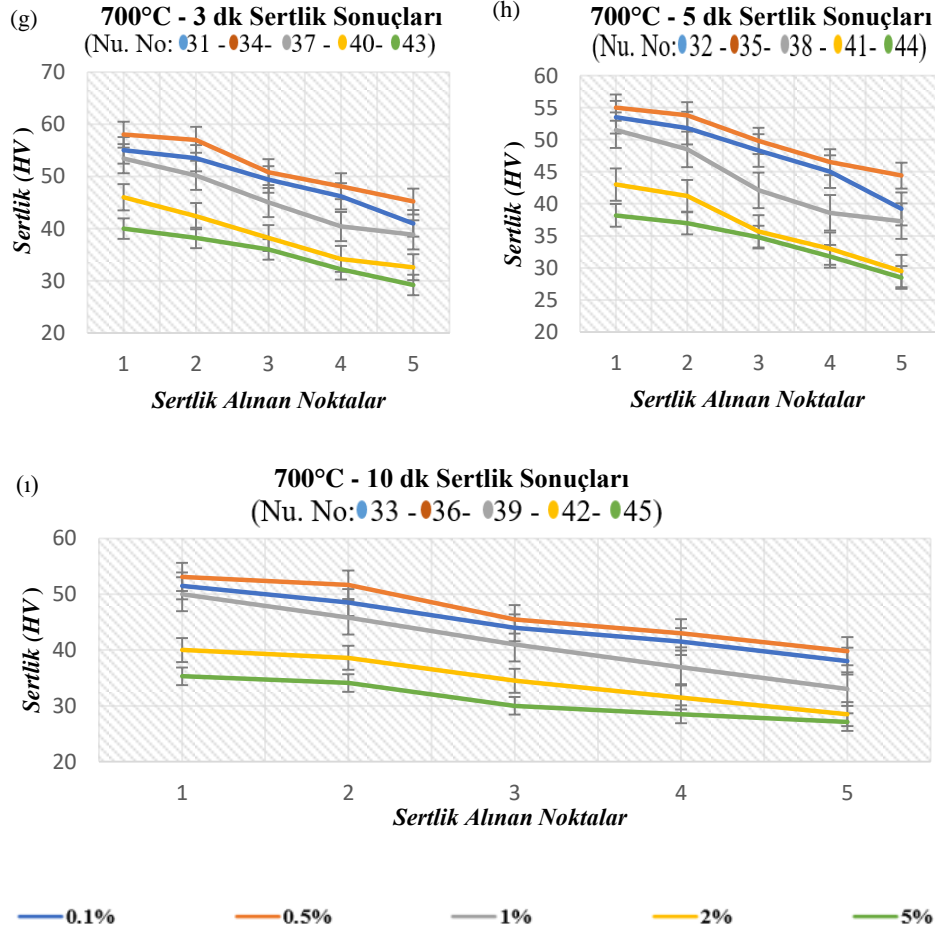
Şekil 6. 600°C'de a) 3 dakika (1-4-7-10-13), b) 5 dakika (2-5-8-11-14), c) 10 dakika (3-6-9-12-15); 650°C d) 3 dakika (16-19-22-25-28), e) 5 dakika (17-20-23-26-29), f) 10 dakika (18-21-24-27-30) ve 700°C'de g) 3 dakika (31-34-37-40-43), h) 5 dakika (32-35-38-41-44), ı) 10 dakikadaki (33-36-39-42-45) HV sertlik sonuçları.

3.2. SEM Bulguları

Keller sıvısı ile dağlanan numuneler SEM yardımıyla incelenmiştir. Numuneler 10x – 1000x arası değerlerde büyütülmüştür. Şekil 7, Şekil 8 ve Şekil 9'da bazı numunelere dair SEM görüntüleri verilmektedir.
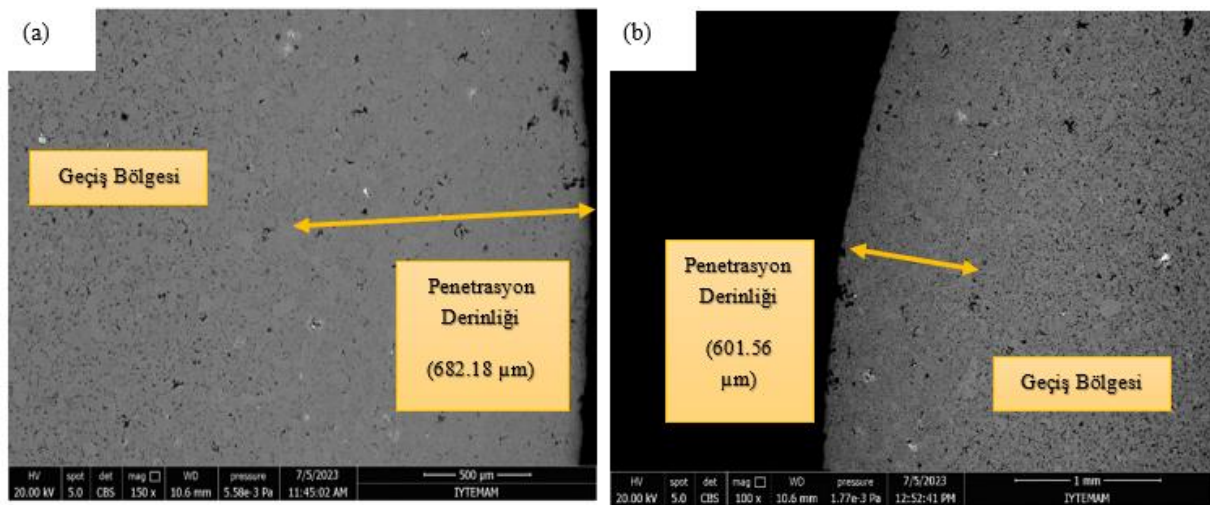
Şekil 7. a) 600°C - 3 dk- %0.5 NBN katkılı indüksiyon ile sinterlenmiş numunenin (4) penetrasyon derinliğinden alınmış 500 μm boyutunda SEM görüntüsü, b) 600°C - 3 dk- %1 NBN katkılı indüksiyon ile sinterlenmiş numunenin (7) penetrasyon derinliğinden alınmış 1 mm boyutunda SEM görüntüsü.
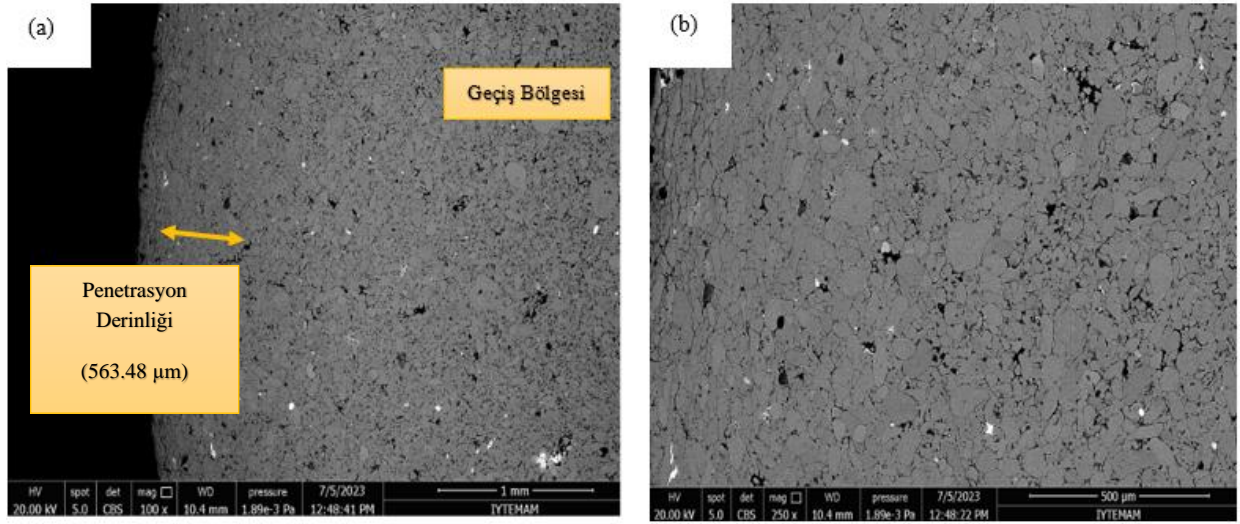
Şekil 8. 650°C - 10 dk- %2 NBN katkılı indüksiyon ile sinterlenmiş numuneden (27) a) penetrasyon derinliğinden 1 mm ölçeğinde ve b) merkezinden 500 μm ölçeğinde alınmış SEM görüntüsü.
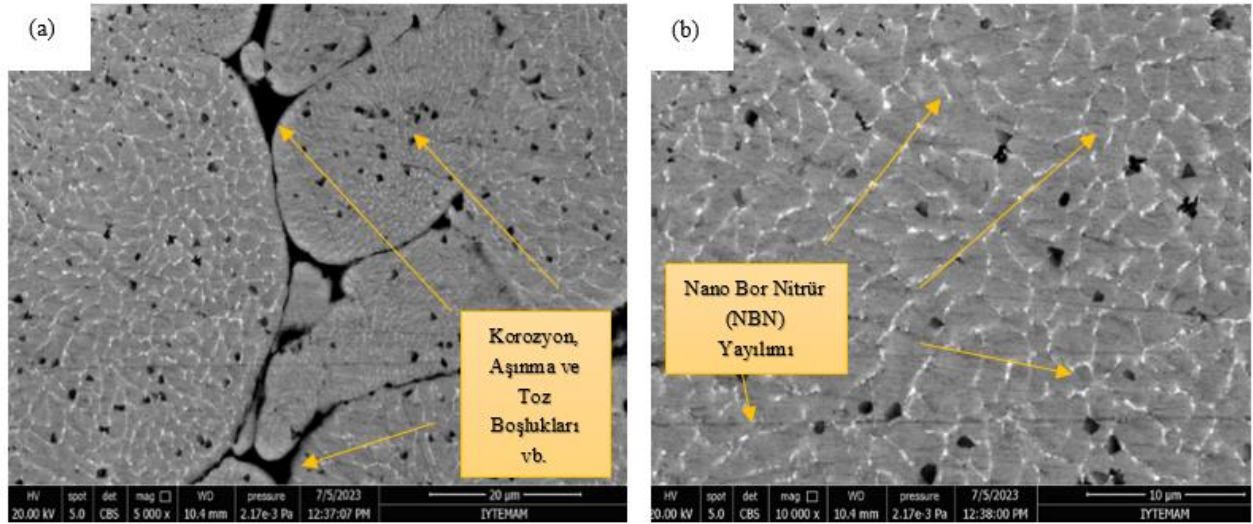
Şekil 9. 700°C- 3 dk- %1 NBN katkılı indüksiyon ile sinterlenmiş numuneden (37) alınmış NBN takviyesinin, Al malzeme matrisindeki penetrasyon bölgesinde iyi yayıldığını gösteren (a) 20 μm, (b) 10 μm'den SEM görüntüsü.

3.3. Yoğunluk Bulguları

600°C, 650°C ve 700°C'de yapılan;%0.1, %0.5, %1, %2 ve %5 NBN takviyeli Saf Al kompozitlerinin UYFIS sinterlemesi sonucu yoğunluk deneyleri yapılmıştır. Hata payı ortalama E.R. ± 0.254 olarak Tablo 2'de verilmektedir.

Tablo 2. NBN katkılı Al numumelerinin yoğunluk sonuçları.

Num. No	Sıcaklık (°C)	Saf Al'a Eklenen NBN Katkı Oranı (%)	Süre (dakika)	Ham Yoğunluk (g/cm³)	Sinterleme Sonrası Yoğunluk (g/cm³)	Yüzdece Değişim (%-g/cm³)
1	600°C	0.1	3	2.561	2.586	0.976
2	600°C	0.1	5	2.551	2.575	0.940
3	600°C	0.1	10	2.585	2.604	0.735
4	600°C	0.5	3	2.575	2.608	1.281
5	600°C	0.5	5	2.554	2.584	1.174
6	600°C	0.5	10	2.56	2.589	1.132
7	600°C	1	3	2.575	2.608	1.281
8	600°C	1	5	2.568	2.600	1.246
9	600°C	1	10	2.584	2.614	1.160

10	600°C	2	3	2.555	2.579	0.939
11	600°C	2	5	2.594	2.617	0.886
12	600°C	2	10	2.584	2.601	0.657
13	600°C	5	3	2.531	2.568	1.145
14	600°C	5	5	2.562	2.589	1.053
15	600°C	5	10	2.561	2.583	0.859
16	650°C	0.1	3	2.561	2.605	1.718
17	650°C	0.1	5	2.564	2.601	1.443
18	650°C	0.1	10	2.574	2.591	0.660
19	650°C	0.5	3	2.588	2.624	1.391
20	650°C	0.5	5	2.575	2.608	1.281
21	600°C	0.5	10	2.584	2.614	1.160
22	650°C	1	3	2.558	2.599	1.602
23	650°C	1	5	2.579	2.614	1.357
24	650°C	1	10	2.575	2.608	1.281
25	650°C	2	3	2.594	2.627	1.272
26	650°C	2	5	2.584	2.621	1.431
27	650°C	2	10	2.573	2.619	1.787
28	650°C	5	3	2.561	2.598	1.444
29	650°C	5	5	2.561	2.593	1.249
30	650°C	5	10	2.552	2.581	1.136
31	700°C	0.1	3	2.547	2.577	1.177
32	700°C	0.1	5	2.594	2.622	1.079
33	700°C	0.1	10	2.589	2.615	1.004
34	700°C	0.5	3	2.58	2.619	1.511
35	700°C	0.5	5	2.564	2.598	1.326
36	700°C	0.5	10	2.555	2.579	0.939
37	700°C	1	3	2.573	2.609	1.399
38	700°C	1	5	2.601	2.634	1.268
39	700°C	1	10	2.579	2.594	0.581
40	700°C	2	3	2.572	2.607	1.360
41	700°C	2	5	2.594	2.627	1.272
42	700°C	2	10	2.584	2.601	0.657
43	700°C	5	3	2.597	2.625	1.078
44	700°C	5	5	2.538	2.559	0.827
45	700°C	5	10	2.555	2.575	0.782

3.4. Enerji Verim Bulguları

Çalışmanın her aşamasında enerji kullanım verileri kaydedilmiştir. Buna göre her bir numunenin indüksiyon sinterlemesi sırasında harcadıkları enerji verileri bulunmuştur. Elektrik maliyetinin hesaplanması amacıyla güç kalite analizörü kullanılmıştır. Ortalama E.R. % ± 4'dür. 600°C, 650°C ve 700°C'de yapılan; %0,1, %0,5, %1, %2 ve %5 NBN takviyeli Saf Al kompozitlerinin UYFIS sinterlemesi sonucu oluşan elektrik verim sonuçları kWh cinsinden Tablo 3'te verilmektedir.

Tablo 3. NBN katkılı Al numumelerinin elektrik verim sonuçları.

Num. No	Sıcaklık (°C)	Saf Al'a NBN Katkı Oranı (%)	Süre (dakika)	Enerji Sonuçları (kWh)
1	600°C	0.1	3	361
2	600°C	0.1	5	506
3	600°C	0.1	10	1086
4	600°C	0.5	3	358
5	600°C	0.5	5	510.3
6	600°C	0.5	10	1090
7	600°C	1	3	363
8	600°C	1	5	503.7
9	600°C	1	10	1088
10	600°C	2	3	357
11	600°C	2	5	509
12	600°C	2	10	1091
13	600°C	5	3	354

14	600°C	5	5	508
15	600°C	5	10	1092
16	650°C	0.1	3	292
17	650°C	0.1	5	662
18	650°C	0.1	10	1270
19	650°C	0.5	3	300
20	650°C	0.5	5	670
21	600°C	0.5	10	1280
22	650°C	1	3	288
23	650°C	1	5	660
24	650°C	1	10	1267
25	650°C	2	3	282
26	650°C	2	5	670
27	650°C	2	10	1276
28	650°C	5	3	279
29	650°C	5	5	667
30	650°C	5	10	1278
31	700°C	0.1	3	419
32	700°C	0.1	5	718.7
33	700°C	0.1	10	1448
34	700°C	0.5	3	423
35	700°C	0.5	5	722.7
36	700°C	0.5	10	1460
37	700°C	1	3	430
38	700°C	1	5	730
39	700°C	1	10	1502
40	700°C	2	3	445
41	700°C	2	5	742.2
42	700°C	2	10	1592
43	700°C	5	3	452
44	700°C	5	5	792.3
45	700°C	5	10	1623.3

4. SONUÇLAR

Bu çalışmada %98.85 saflığa sahip alüminyum tozuna; farklı sıcaklıkta ve sürelerde, yüzdece %0.1, %0.2 %0.5, %1 ve %5 NBN eklenerek UYFIS sinterlemesi yapılmıştır. Sinterlemeden elde edilen sertlik, SEM, yoğunluk ve elektrik verim sonuçları aşağıda verilmektedir;

- Al esaslı toz metal kompozitler için en yüksek sertlik değeri 66.1 HV ile 600°C, 3 dakika ve %0.5 NBN katkılı 4 numaralı numunede bulunmaktadır.
- En düşük sertlik 700°C'de 10 dakika sinterlenen %5 NBN katkılı 45 numaralı numunede 27.1 HV olarak ölçülmüştür.
- İndüksiyonla sinterlenen Al matrisli toz metal numunelerde, katkı oranı arttıkça penetrasyon derinliğinde azalma görülmektedir. İncelenen SEM görüntülerinde; %0.5 katkı oranına sahip 4 numaralı numunede ortalama 682.18 µm uzunluğunda penetrasyon derinliği ölçülürken, %2 NBN katkılı 7 numaralı numunede ortalama uzunluğu 563.48 µm penetrasyon derinliği ölçülmüştür. Bu da "katkı oranının penetrasyon derinliğiyle doğrudan ilişkili olduğu" sonucunu vermektedir.
- Penetrasyon bölgesindeki tane yapıları diğer bölgelere göre iri ve büyüktür.
- Üretilen tüm kompozitlerde yüksek sertlik için en uygun NBN katkı oranı %0.5 ve 3 dakika indüksiyon sinterleme süresi olarak bulunmaktadır.
- SEM görüntülerinde ağırlıkça %0.1, %0.5 ve %1 NBN takviyesinin, malzeme matrisindeki penetrasyon bölgesinde iyi yayıldığı görülmüş ve bunun sonucunda malzemenin mukavemetinin arttığı anlaşılmıştır.
- Sertlik değerinin %0.5 NBN takviyesine kadar arttığı görülmektedir. Bu katkı oranı, kompozit için sertlik değerindeki tepe noktadır. %0.5 NBN katkısından sonra katkı oranı arttıkça sertlik azalmıştır.
- Aynı kimyasal kompozisyona sahip malzemelerde sıcaklık veya sinterleme süresi arttıkça sertliğin düştüğü saptanmıştır.
- İndüksiyonla sinterleme sonrası tüm numunelerde yoğunluk artmaktadır. İndüksiyon süresi arttıkça yüzdece yoğunluk değişimi azalmaktadır. En yüksek yüzdece yoğunluk değişimi %1.787g/cm^3 ile 27

numaralı numunede, en düşük yüzdece yoğunluk değişimi ise %0.581 g/cm^3 ile 39 numaralı numunede görülmektedir.
- En düşük elektrik enerjisi kullanımı 279 kWh ile 28 numaralı numunede, en yüksek elektrik enerjisi kullanımı ise 1623.3 kWh ile 45 numaralı numunede gerçekleşmiştir.

Bu çalışmasının devamında aşağıda belirtilen çalışmaların yapılması önerilmektedir.

• NBN katkılı Saf Alüminyum kompozitlerin üretilebilirliği bakımından %0.1 ila %0.5 NBN katkı aralığı ile (%0.2; %0.3; %0.4) ; %0.5 ila %1 NBN katkı aralığında (%0.6; %0.7; %0.8; %0.9) farklı kompozit alaşımlar oluşturularak mekanik özelliklere etkisi araştırılabilir. Bu durum sıcaklık optimizasyonun netleşmesinde de önemli parametreler sağlayabilir.

• Üretilen kompozitlere sıcak pres yoluyla indüksiyon sinterleme yapılarak mekanik özelliklere etkisi araştırılabilir. Bu durum mekanik özelliklerin, malzemenin her yerine homojen bir şekilde yayılmasını sağlayabilir mi sorusunun cevabını verebilir.

• Kompozitlerin preste sıkıştırılması sağlanırken uygulanan basınç için bir optimizasyon yapılarak mekanik özelliklere etkileri incelenebilir.

• Matris malzemesine, ısıl iletkenliği daha yüksek olan bakır ve çelik gibi başka metal malzemeler eklenip hibrit kompozit üretimi yapılarak mekanik özelliklere etkisi araştırılabilir.

• Üretilen kompozitlerin işlenebilirlik, aşınma ve korozyon özellikleri saptanabilir.

• İndüksiyon Sinterleme esnasında oluşan penetrasyon derinliğinin malzemelere ve katkı oranına bağlı matematiksel modellemesi çıkarılabilir.

• Yapılan bu çalışmayla ilgili mühendislik disiplinleriyle alakalı bir optimizasyon çalışması yapılabilir.

TEŞEKKÜR

KAYNAKLAR

[1] M. Sekmen, M. Günay, U. Şeker, Alüminyum alaşımlarının işlenmesinde kesme hızı ve talaş açısının yüzey pürüzlülüğü, yığıntı talaş ve yığıntı katmanı oluşumu üzerine etkisi, Politeknik Dergisi, 18(3) (2015) 141-148.

[2] V. Guerra, C. Wan, T. McNally, Thermal conductivity of 2D nanostructured boron nitride (BN) and its composites with polymers, Progress in Materials Science, 100 (2019) 170-186.

[3] M. Loeblein, S. H. Tsang, M.Pawlik, E.J.R. Phua, H. Yong, X.W. Zhang & E.H.T. Teo, High-density 3D-boron nitride and 3D-graphene for highperformance nano–thermal interface material. ACS Nano, 11(2), 2017, 2033-2044.

[4] M. K. Gupta, M.E. Korkmaz, M. Sarıkaya, G.M. Krolczyk, M. Günay, S. Wojciechowski, Cutting forces and temperature measurements in cryogenic assisted turning of AA2024-T351 alloy: An experimentally validated simulation approach, Measurement, 188 (2022) 110594.

[5] H. Ateş, E. Bahçeci, Nano malzemeler için üretim yöntemleri, Gazi University Journal of Science Part C: Design and Technology, 3(2) (2015) 483-499.

[6] İ.A. Karamanlı, M. Günay, Seramik malzemelerin işlenmesinde uygulanan alışılmamış imalat yöntemleri, Konya Journal of Engineering Sciences, 10(4) (2022) 1061-1082.

[7] M. Pul, Karbon nanotüp (cnt) ve nano grafen (g) takviyeli al 2024 kompozitlerin vorteks yöntemiyle üretilerek aşınma ve işlenebilme özelliklerinin incelenmesi, International Journal of Engineering Research and Development, 11(1), 2019, 370-382.

A. Kaçal, F. Yıldırım, M. Koyunbakan, Sac malzeme yüzey pürüzlülüğünün fiber-metal tabakalı kompozitlerin mekanik özelliklerine olan etkisi, El-Cezeri, *8*(3) (2021) 1215-1228.

[8] P.L. Niu, W.Y. Li, N. Li, Y.X. Xu, D.L. Chen, Exfoliation corrosion of friction stir welded dissimilar 2024-to-7075 aluminum alloys, Materials Characterization, 147 (2019) 93-100.

[9] S.T. Mavhungu, E.T. Akinlabi, M.A. Onitiri, F.M. Varachia, Aluminum matrix composites for industrial use: advances and trends, Procedia Manufacturing, 7 (2017) 178-182.

[10] H. Dedeakayoğulları, A. Kaçal, Eklemeli imalat teknolojileri ve kullanılan talaşlı imalat yöntemleri üzerine yapılan çalışmaların değerlendirilmesi, İmalat Teknolojileri ve Uygulamaları, 1(1), 2020, 1-12.

[11] Arenal, A. Lopez-Bezanilla, Boron nitride materials: an overview from 0D to 3D (nano) structures. wiley ınterdisciplinary reviews: Computational Molecular Science, 5(4) (2024) 299-309.

[12] H. Aydın, Nanoyapılı Hegzagonal bor nitrür üretimi ve karakterizasyonu, Fırat Üniversitesi Mühendislik Bilimleri Dergisi, 30(2) (2018) 269-275.

[13] M. Clausi, M. Zahid, A. Shayganpour, I.S. Bayer, Polyimide foam composites with nano-boron nitride (BN) and silicon carbide (SiC) for latent heat storage, Advanced Composites and Hybrid Materials, 5(2), 2022, 798-812.

[14] B. Karaca, U. Çavdar, Saf ve bor karbür takviyeli alüminyum tozlarının ultra yüksek frekanslı indüksiyon jeneratörü ile sinterlenmesi, Mühendis ve Makina, 55 (2014) 59-64.

[15] C. Çivi, E. Atik, Bakır ve grafit içeren demir esaslı malzemelerin indüksiyon ile sinterlenmesinde sinterleme sıcaklığının malzeme dayanımına etkisi, Celal Bayar University Journal of Science, 13(2) (2017) 467-473.

[16] E. Atik, C. Çivi, C. Kökey, G. Eyici, Toz metal parçalar ile çelik parçaların indüksiyon ile sinterleme yöntemiyle birleştirilmesi, Çukurova Üniversitesi Mühendislik-Mimarlık Fakültesi Dergisi, 31 (2016) 117-122.

[17] M. Ortega Varela de Seijas, M, A. Bardenhagen, T. Rohr, & E. Stoll, Indirect induction sintering of metal parts produced through material extrusion additive manufacturing, Materials, 16(2), (2023) 885.

[18] B. Gül, U. Gezici, M. Ayvaz, U. Çavdar, The comparative study of conventional and ultra-high frequency induction sintering behavior of pure aluminum, International Advanced Researches and Engineering Journal, 4(3) (2020) 173-179.

Manufacturing Technologies and Applications
MATECA

Effects of Al₂O₃ Based Nanofluids with Different Particle Sizes on Machining Performance in Milling of Hastelloy X Superalloy

Ahmet Gemci[1] , Emine Şirin[2] , *, Turgay Kıvak[3]

¹Duzce University, Graduate School of Education, Duzce, Türkiye
²Duzce University, Gumusova Vocational School, Duzce, Türkiye
³Duzce University, Faculty of Engineering, Duzce, Türkiye

ABSTRACT

In recent years, due to the increasing demand in the space and aviation sector, serious developments have been experienced. The increasing acceleration in the light of the developments has contributed to the development of superior materials that will meet the requirements. In addition to the superior fatigue and creep properties of these materials namely superalloys, there may be difficulties in shaping them with machining methods. In order to overcome these difficulties, researchers have accelerated their study to develop sustainable manufacturing methods. In this study, Hastelloy X superalloy material, which is frequently preferred in the space and aviation areas, was milled under sustainable cooling/lubrication conditions. It was aimed to investigate the effects of particle sizes of nanofluids on machining performance in the milling process. For this purpose, dry, minimum quantity lubrication (MQL), 4 nm sized Al_2O_3, 48 nm sized Al_2O_3 and 136 nm sized Al_2O_3 nanofluid cooling/lubrication conditions were preferred. In order to investigate the effects of cooling/lubrication conditions, the cutting speed, feed rate, and cutting depth parameters were taken as 50 m/min, 0.10 mm/rev, and 0.5 mm, respectively. Surface roughness Ra, cutting temperature, power consumption, and tool flank wear values were determined as performance characteristics. According to the results obtained from milling experiments, 4 nm sized Al_2O_3 nanofluid exhibited superior performance compared to other conditions. 4 nm sized Al_2O_3 nanofluid condition showed decrease of 37.43%, 36.02%, 8.33%, and 66.66%, respectively, in surface roughness, cutting temperature, power consumption, and tool flank wear results compared to dry condition.

Keywords: Hastelloy X, Milling, Nanofluid, MQL, Al₂O₃

Hastelloy X Süperalaşımının Frezelenmesinde Farklı Parçacık Boyutlu Al₂O₃ Esaslı Nanoakışkanların İşleme Performansı Üzerindeki Etkileri

ÖZET

Uzay ve havacılık sektörüne artan taleple birlikte son yıllarda ciddi gelişmeler yaşanmıştır. Gelişmeler ışığında artan ivmelenme, gereksinimleri karşılayacak özellikle üstün malzemelerin geliştirilmesine katkıda bulunmuştur. Süperalaşım adı verilen bu malzemelerin üstün yorulma ve sürünme özelliklerinin yanında, talaşlı imalat yöntemleriyle şekillendirilmesinde zorluklar yaşanabilmektedir. Yaşanan bu zorlukların üstesinden gelebilme adına araştırmacılar sürdürülebilir imalat yöntemlerin geliştirilmesi için çalışmalarına hız vermiştir. Bu çalışmada uzay ve havacılık alanında sıklıkla tercih edilen, Hastelloy X süperalaşım malzemesi sürdürülebilir soğutma/yağlama koşulları altında frezeleme işlemi uygulanmıştır. Frezeleme işleminde nanoakışkanların parçacık boyutlarının işleme performansı üzerindeki etkilerinin incelenmesi amaçlanmıştır. Bu amaç doğrultusunda, kuru, minimum miktarda yağlama (MMY), 4 nm boyutlu Al_2O_3, 48 nm boyutlu Al_2O_3 ve 136 nm boyutlu Al_2O_3 nanoakışkan soğutma/yağlama koşulları tercih edilmiştir. Soğutma/yağlama koşullarının etkilerini inceleme adına kesme hızı, ilerleme ve kesme derinliği parametreleri, sırasıyla 50 m/dak, 0.10 mm/dev ve 0.5 mm sabit alınmıştır. Performans karaktersitiği olarak yüzey pürüzlülüğü Ra, kesme sıcaklığı, güç tüketimi ve takım yanak aşınma değeri belirlenmiştir. Frezeleme deneylerinden elde edilen sonuçlara göre, diğer koşullara kıyasla 4 nm boyutlu Al_2O_3 nanoakışkanı daha üstün performans sergilemiştir. 4 nm boyutlu Al_2O_3 nanoakışkan koşulu kuru koşula göre, yüzey pürüzlülüğü, kesme sıcaklığı güç tüketim ve takım yanak aşınması sonuçlarına göre sırasıyla % 37.43, %36.02, %8.33 ve %66.66 oranında düşüş göstermiştir**.**

Anahtar Kelimeler: Hastelloy X, Frezeleme, Nanoakışkan, MMY, Al₂O₃

1. GİRİŞ

Uzay ve havacılık sektöründe sıklıkla kullanılan malzemelerden biri de Nikel esaslı süperalaşımlardır. İçeriğindeki elementler (nikel (Ni), krom (Cr), demir (Fe) ve molibden (Mo)) sayesinde üstün özellikler

göstermektedir. Nikel esaslı süperalaşımlar, yüksek mukavemet, yüksek korozyon direnci, tokluk, yüksek sıcaklık direnci gibi özelliklere sahiptir [1]. Bazı malzemelerin davranışları yüksek sıcaklık aralığında değişmektedir. Malzeme davranışlarının kararlılığı açısından, yüksek çalışma sıcaklıklarına dayanabilen malzemelere olan ihtiyaç her geçen gün artmaktadır [2]. Özellikle nikel esaslı malzemelerin alaşım elementlerinden olan Mo ve Cr elementleri bu malzemenin yüksek çalışma sıcaklıklarında kararlı yapı sergilemesine olanak tanımaktadır. Bu sebeple özellikle yüksek sıcaklık gerektiren uygulamalarda kullanım alanı gün geçtikçe yaygınlaşmaktadır. Hastelloy X, nikel esaslı süperalaşım grubundaki malzemelerden biridir. Gaz türbini motor yanma odaları, egzoz boruları, itme ters çeviriciler ve art yakıcılar gibi uçak uygulamalarında yaygın olarak kullanılır. Bu üstün özelliklerinin yanında düşük ısı iletkenliği ve ısıl yayılma, yüksek sıcaklık direnci, işleme sırasında sertleşme eğilimi gibi özellikleri bu malzemeyi işlenmesi zor malzemeler sınıfına koyar [3,4]. Zor malzemelerin işlenmesi sırasında işleme verimliliğini artırmak için kesme bölgesine soğutma/yağlama yöntemleri uygulanmaktadır.

Ekolojik işleme yöntemlerinden biri de kuru işlemedir. Kuru işlemede kesme bölgesine herhangi bir soğutucu ve yağlayıcı uygulanmamaktadır. Düşük işleme koşullarında uygun bir işleme koşulu olarak görünse de orta ve ağır işleme koşullarında işleme verimliliği açısından uygun bir işleme koşulu değildir. Kuru işleme koşuluna alternatif olan yöntemlerden biri de minimum miktarda yağlama (MMY) yöntemidir. MMY, az miktarda yağın (10−100 mL/saat) basınçlı hava ile karıştırılarak aerosol şeklinde kesme bölgesine uygulandığı ekolojik bir yöntemdir [5]. MMY yöntemi etkili bir yağlama sağlayarak hem kesme bölgesini soğutmakta hem de parçanın yüzey kalitesini artırmaktadır. MMY yönteminin etkinliğini artırmak amacıyla baz sıvı içerisine farklı özelliklerde nanoparçacıklar eklenerek nanoakışkanlar elde edilmektedir. Baz sıvı içerisine bakır oksit (CuO), alüminyum oksit (Al$_2$O$_3$), bakır (Cu), çok duvarlı karbon nanotüp (MWCNT), hekzagonal bor nitrür (hBN), molibden sülfür (MoS$_2$) ve grafen gibi nanoparçacıklar eklenmektedir. Eklenen bu nanoparçacıklar nanoakışkanların tribolojik özelliklerini iyileştirmektedir [6]. Genel olarak, bu özellikleri nanoparçacıkların boyutu, şekli ve katkı oranı etkilemektedir [7]. Nanoakışkanlar kesme bölgesinde etkili bir yağlama sağlayarak kesme bölgesinde oluşan sıcaklığı düşürüp kesici takım ömrünü artırmaktadır. Ayrıca kesme bölgesinde etkili bir tribofilm tabakası oluşturarak yüzey kalitesini artırmaktadır. Yapılan çalışmalarda nanoakışkan kullanımının kesme işleminde verimliliği artırdığı konusunda çok sayıda çalışmalar bulunmaktadır. Günan ve arkadaşları yaptıkları çalışmada Hastelloy C276 süperalaşım malzemenin kuru, MMY ve Al$_2$O$_3$ ilaveli nanoakışkan koşulları altında frezelenmesi sonucunda yüzey pürüzlülüğü ve takım aşınması kriterlerini incelemişlerdir. Nanoakışkan kullanımının yüzey kalitesini ve takım aşınmasını önemli ölçüde iyileştirdiğini tespit etmişlerdir [8]. Vasu ve arkadaşları Inconel 600 süperalaşım malzemesinin kuru, MMY ve Al$_2$O$_3$ nanoparçacık ilaveli nanoakışkan koşullarında işlenmesinde yüzey kalitesi, kesme sıcaklığı, kesme kuvveti ve takım aşınma değerlerini incelemişlerdir. Nanoakışkan koşulunda sıcaklık, kesme kuvveti ve takım aşınması değerinin düştüğü ve yüzey kalitesinin iyileştiğini ifade etmişlerdir [9]. Venkasetan ve arkadaşları Incoloy 800H malzemeye Hindistan yağı içerisine ağırlıkça % 0.25-0.50 ve 1 oranında Al$_2$O$_3$ ilaveli nanoakışkan koşulunda tornalayarak kesme kuvveti, yüzey pürüzlülüğü ve takım aşınmasını incelemişlerdir. Ağırlıkça % 0.25 nanoparçacık ilavesinin incelenen çıktılarda daha iyi sonuç verdiğini tespit etmişlerdir [10]. Eltaggas ve arkadaşları östemperlenmiş küresel grafitli dökme demir malzemeyi MMY ve Al$_2$O$_3$ ilaveli nanoakışkan koşullarında tornalayarak takım aşınması değerini incelemişlerdir. Al$_2$O$_3$ ilaveli nanoakışkan koşullarında en iyi takım ömrü değerini elde ettiklerini ifade etmişlerdir [11]. Hadi ve Atefi AISI D3 çelik malzemeyi MMY ve Al$_2$O$_3$ ilaveli MMY koşullarında frezeleyerek yüzey pürüzlülüğü değerini incelemişlerdir. Deneysel çalışma sonucunda MMY koşuluna göre nanoakışkan koşulunda yüzey pürüzlülüğü değerlerinde % 25 oranında azalma olduğunu vurgulamışlardır [12]. Yıldırım ve arkadaşları Waspaloy süperalaşım malzemeyi kuru, MMY ve Al$_2$O$_3$ ilaveli nanoakışkan koşullarında frezeleyerek takım aşınması değerini incelemişlerdir. Deneysel çalışma sonucunda takım aşınma değerinde nanoakışkan koşulunda kuru koşula göre %44.4 oranında bir iyileşme sağlandığını tespit etmişlerdir [13]. Lee ve arkadaşları SK41-C malzeme iş parçasını kuru, MMY ve farklı oranlarda (hacimce %2-%4) ve farklı boyutlarda (30-150 nm) Al$_2$O$_3$ ve nanoelmas ilaveli nanoakışkan koşullarında taşlayarak kesme kuvveti ve yüzey pürüzlülüğü parametrelerini incelemişlerdir. Deneysel sonuçlardan elde edilen verilere göre kesme kuvveti ve yüzey pürüzlülüğü sonuçlarında küçük oranlarda ve küçük boyutlarda nanoparçacık ilavesi ile yapılan nanoakışkan karışımlarının daha iyi performans gösterdiğini tespit etmişlerdir. Ayrıca yüzey pürüzlülüğü açısından 30 nm boyutlu Al$_2$O$_3$ ilaveli karışımların en iyi performans gösterdiğini vurgulamışlardır [14].

Yapılan literatür çalışmaları değerlendirildiğinde, MMY ve nanoakışkanların kullanıldığı çevreci yöntemler üzerine çalışmaların yoğunlaştığı görülmektedir. Genel olarak parçacık şekli, boyutu ve nanoakışkan katkı oranının nanoakışkanının tribolojik özelliklerinini etkilediği bilinmektedir. Ancak yapılan

çalışmalarda farklı boyutlardaki nanoparçaçıkların etkisinin incelenmesi üzerine çalışmaların kısıtlı olduğu bilinmektedir. Bu noktadan hareketle bu çalışmada kuru, MMY ve 3 farklı boyutta (4-48-136 nm) Al_2O_3 parçaçık ilaveli nanoakışkanın kullanıldığı soğutma/yağlama koşullarının işleme çıktıları üzerine etkileri incelenmiştir. Hastelloy X süper alaşımının frezelenmesi üzerine soğutma/yağlama koşullarının etkisini görmek amacıyla deneylerde kesme hızı 50 m/dak, ilerleme 0.10 mm/dev ve kesme derinliği 0.5 mm olarak belirlenmiştir. Al_2O_3 nanoparçaçık boyutunun etkisinin belirlenmesi için kesme sıcaklığı, yüzey pürüzlülüğü, güç tüketimi ve takım yanak aşınma değerleri incelenmiştir.

2. MATERYAL VE YÖNTEM

2.1. İş Parçası, Kesici Takım ve Takım Tezgâhı

Deneysel çalışmada, 100x150x13.5 mm ölçülerinde Hastelloy X süperalaşım malzemesi kullanılmıştır. Hastelloy X süperalaşım malzemesine ait kimyasal bileşim Tablo 1'de ve mekanik özellikleri Tablo 2'de verilmiştir.

Tablo 1. Hastelloy X süperalaşımının kimyasal içeriği (%) [15].

Ni	Cr	Fe	Mo	Ti	Al	Mn	Si	C	Cu	Co	Diğer
46.7	22.6	18.72	8.98	0.02	0.14	0.51	0.30	0.05	0.14	0.67	1.17

Tablo 2. Hastelloy X süperalaşımının fiziksel ve mekanik özellikleri [15].

Erime Sıcaklığı (°C)	Elastikiyet Modülü (GPa)	Özgül Isı (J/kg-K)	Sertlik (HRB)	Çekme Dayanımı (MPa)	Akma Dayanımı (MPa)	Termal İletkenlik (W/m-K)	Yoğunluk (gr/cm^3)	Uzama (%)
1260-1355	207	486	87.1	732.2	319.2	9.1	8.22	54.4

Frezeleme deneylerinde Sandvik marka ISO 490R-08T30-8E ML S30T kodlu, TiAlN PVD kaplamalı sementit karbür kesici takımlar kullanılmıştır. Kesici takımların rijit bir şekilde bağlanmasında Sandvik marka ISO 490-025A20-08L kodlu takım tutucu kullanılmıştır.

Frezeleme deneyleri, maksimum devri 10000 dev/dak, motor gücü 11 kW olan DELTA SEIKI CNC-1050 A marka CNC freze tezgâhında gerçekleştirilmiştir. Çalışmada kullanılan tezgah ve diğer ekipmalar Şekil 1'de verilmektedir. Soğutma/yağlama koşullarının etkilerini incelemek için kesme parametreleri kesici takım firmasının tavsiye etttiği değerler arasından seçilmiştir. Kesme parametresi olarak, kesme hızı 50 m/dak, ilerleme 0.10 mm/dev ve kesme derinliği 0.5 mm olarak belirlenmiştir.

Tablo 3. Deney parametreleri.

Tezgâh	DELTA SEIKI CNC-1050 A
İş Parçası	Hastelloy X (100x150x13.5 mm)
Kesici Takım	Sandvik marka ISO 490R-08T30-8E MLS30T
Kesme Parametreleri	Kesme hızı 50 m/dak, İlerleme 0.10 mm/dev, Kesme derinliği 0.5 mm
Kesme Koşulları	Kuru, MMY, Al_2O_3-4 nm, Al_2O_3-48 nm, Al_2O_3-136 nm
Kesme Yağı	Werte Fastcut (Kinematik viskozite 18 cSt)
MMY	SKF LubriLean Vario, Basınç 8 bar, Debi 80 mL/saat, Nozul çapı 2 mm
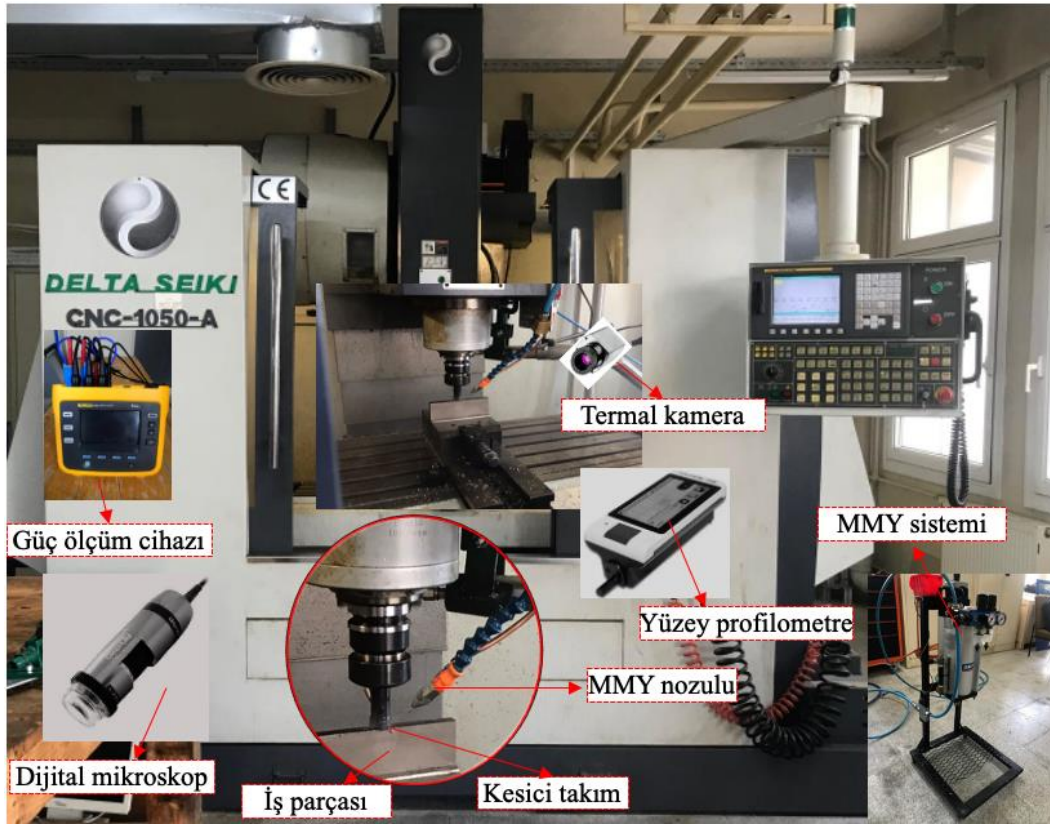
Şekil 1. CNC freze tezgâhı ve deneysel ekipmanlar.

2.2. Nanoakışkan Karışımlar ve Karışım Prosesi

MMY soğutma/yağlama koşulunda, SKF LubriLean Vario model MMY cihazı kullanılmıştır. MMY cihazı içerisine, atmosfere ve insan sağlığına zararsız kimyasal bilişime sahip Werte Fastcut bitkisel esaslı sentetik yağ kullanılmıştır. MMY sisteminin çalışma debisi 80 mL/saat ve çalışma basıncı 8 bar olarak ayarlanmıştır. MMY sistemi içerisinde pülverize hale getirilen ve basınç kazandırılan yağ, kesme bölgesine 2 mm çapında bir nozul yardımıyla 30 mm mesafeden 30° açı ile gönderilmiştir. Literatürde yer alan çalışmalarda nanoakışkan karışımlarda hacimce %0.5~0.75 nanoparçaçık karışım oranının uygun aralık olduğu ifade edilmiştir [16]. Bu çalışmada baz yağın içerisine hacimce %0.6 oranında farklı boyutlarda (4-48-136 nm) Al_2O_3 nanoparçaçık (Nanografi/Türkiye) eklenerek nanoakışkanlar hazırlanmıştır. Al_2O_3 nanoparçaçık özellikleri Tablo 4'te verilmiştir.

Tablo 4. Al_2O_3 nanoparçaçık özellikleri [17].

Boyut	Saflık	Özgül yüzey alanı	Renk	Şekil
(nm)	*(%)*	*(m^2/g)*		
4	99.99	>20	Beyaz	Küresele yakın
48	99.90	>30	Beyaz	Küresele yakın
136	99.95	>20	Beyaz	Küresele yakın

Nanoakışkan hazırlamak için kolaylığı ve ekonomik olması bakımından genellikle iki adım yöntemi tercih edilmektedir [18]. Bu çalışmada da nanoakışkanların hazırlanmasında iki adım yöntemi kullanılmıştır. Karıştırma prosesi üç aşamada gerçekleştirilmiştir. Birinci aşamada Al_2O_3 nanoparçaçıkları baz yağa eklendikten sonra Daihan HS100D mekanik karıştırıcıda 750 rpm'de 60 dakika boyunca karıştırılmıştır. İkinci aşamada mekanik karıştırma işleminden sonra, nanoakışkanlar Bandelin Sonopuls HD 320020 ultrasonik bir homojenizatörde 20 kHz frekansta 30 dakika boyunca karıştırılmıştır. Son aşamada, Termal N1115 manyetik karıştırıcı ile 60 dakika boyunca 1500 rpm'de karıştırılarak karışımlar hazır hale getirilmiştir. Nanoakışkan hazırlama prosesi Şekil 2'de verilmektedir. Hazırlanan nanoakışkanlar homojenliğini kaybetmeden hemen kullanılarak frezeleme deneyleri gerçekleştirilmiştir.
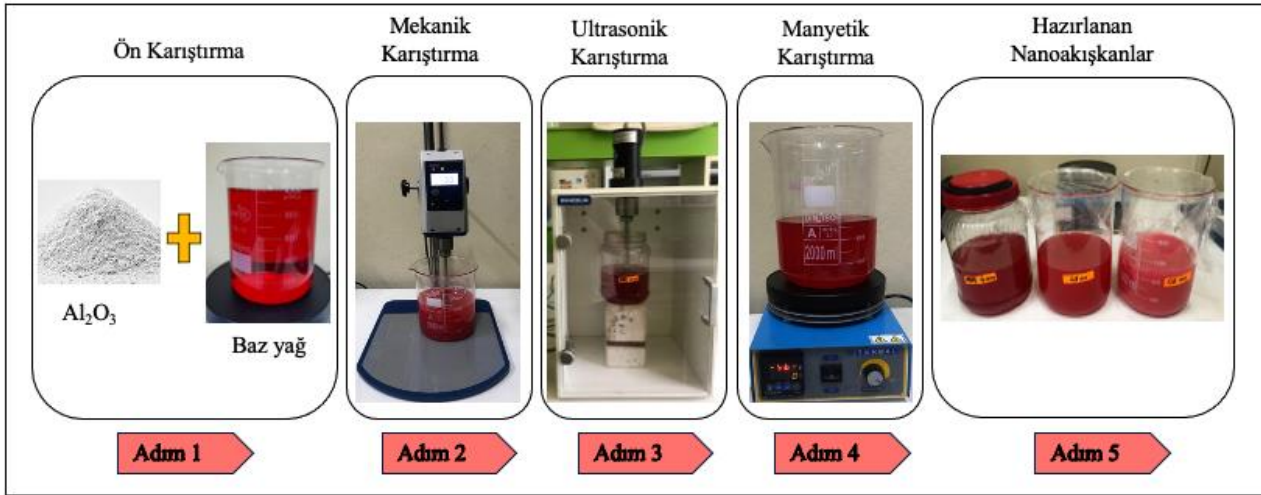
Şekil 2. Nanoakışkan hazırlama prosesi.

2.3. Deneysel Ölçümler

İşlenen parçaların yüzey kalitesinin belirlenmesi için parçaların yüzey pürüzlülük ölçümleri yapılmıştır. Yüzey pürüzlülük ölçümlerinde Mahr Marsurf PS10 taşınabilir yüzey pürüzlülük ölçüm cihazı kullanılmıştır. Yüzey pürüzlülük ölçümleri ISO 4287 standardına göre yapılmıştır. Ölçüm sırasında ölçme uzunluğu 4 mm ve örnekleme uzunluğu 0.8 mm olarak belirlenmiştir. İşlenen yüzeyin üç farklı bölgesinden alınan Ra değerlerinin aritmetik ortalaması alınarak yüzey pürüzlülük değerleri belirlenmiştir. İşleme esnasında kesme bölgesinde oluşan maksimum sıcaklık değerinin tespiti için Optris marka PI450 kızılötesi termal kamera kullanılmıştır. Anlık olarak alınan sıcaklık görüntüleri Optris PI Connect yazılımı üzerinden okunmuştur. Termal kamera üretici tavsiyesi ve katalog değerleri esas alınarak Hastelloy X süperalaşım malzemesi için emisivite değeri 0.5 olarak alınmıştır. İşleme sırasında, tezgâh güç tüketimini ölçmek için Fluke 1732 A, B ve C üç fazlı güç tüketim ölçüm cihazı kullanılmıştır. Güç tüketim ölçüm cihazı CNC freze tezgahının ana giriş güç trafosuna bağlanmış ve yazılım yardımıyla ölçüm sonuçları kaydedilmiştir. Cihaz her deneyden önce kalibre edilerek kullanılmıştır. Kesici takım yanak aşınma miktarının tespit edilmesinde DinoLite marka AM791MZT dijital mikroskop kullanılmıştır. Mikroskoptan elde edilen görüntüler DinoLite yazılımı ile alınarak kontrol edilmiştir. Her deney için yeni bir kesici uç kullanılmış olup deney seti Şekil 1'de verilmiştir.

3. BULGULAR VE TARTIŞMA

3.1. Yüzey Pürüzlülük Değerlendirmesi

Yüzey pürüzlülüğü talaşlı imalatta ürün kalitesini belirleyen en önemli kalite göstergelerinden biridir. Özellikle hassasiyetin ve kalitenin ön planda olduğu havacılık sektörünün vazgeçilmez bir unsurudur. Yüzey pürüzlülüğü, bitmiş ürünün yorulma dayanımı, korozyon direnci, sürtünme katsayısı gibi birçok özelliğini doğrudan etkilemektedir [19–22]. Bu nedenle yüzey pürüzlülüğünün iyileştirilmesi büyük önem arz etmektedir. Bu amaçla havacılık sektöründe yaygın kullanımı olan Hastelloy X süperalaşımının frezelenmesinde farklı soğutma/yağlama koşullarının ortalama yüzey pürüzlülüğü üzerindeki etkilerini ortaya koymak için bir dizi deney yapılmıştır. Deneysel çalışmadan elde edilen sonuçlar Şekil 3'te verilmiştir. En yüksek Ra değeri 0.406 µm olup beklendiği gibi kuru kesme koşulunda elde edilmiştir. Takım/talaş temas alanında herhangi bir yağlayıcı ajanın olmayışı sürtünmenin artmasına neden olmaktadır. Buda kuru kesme koşulunun düşük yüzey kalitesi ile sonuçlanmasına yol açmaktadır. Kuru kesme çevreci bir üretim yöntemi olmakla birlikte süperalaşım gibi üstün mekanik özelliklere sahip malzemelerin işlenmesinde düşük yüzey kalitesi, düşük takım ömrü ve işleme verimliliği açısından dezavantajlara sahiptir [23,24]. Bu noktada bitkisel kesme yağının kullanıldığı MMY yöntemi alternatif olarak karşımıza çıkmaktadır. Çalışmada MMY kesme koşulunun yüzey pürüzlülüğünde kuru kesmeye göre %22.66 iyileşme sağladığı görülmüştür. Bu yöntemde kesme bölgesine sis buharı şeklinde gönderilen kesme yağı etkin bir yağ filmi oluşturarak sürtünmenin azalması noktasında önemli bir rol üstlenmiştir. Kesme yağının etkinliğini daha da artırmak amacıyla nanoparçacıklar ile hazırlanan nanoakışkanlar üstün yağlayıcılık özellikleri ile ön plana çıkmaktadırlar [25]. Nitekim yapılan çalışmada en düşük Ra değerleri Al_2O_3 nanoakışkan kesme koşullarında elde edilmiştir. Kesme yağına katılan nanoparçacıklar sahip oldukları üstün özellikleri ile kesme yağının

termal iletim katsayısını artırmanın yanı sıra yağlayıcılık özelliklerini de önemli ölçüde iyileştirmektedirler. Ayrıca tamir, parlatma ve yuvarlanma mekanizmaları ile takım/talaş ve takım/iş parçası arasında bariyer oluşturarak etkin film tabakası ile sürtünmenin azaltılmasını sağlamaktadırlar [26]. Tüm sayılan bu özellikler en düşük Ra değerlerinin nanoakışkan kesme koşullarında elde edilmesinde önemli bir rol üstlenmiştir. Nanoparçacık boyutunun Ra üzerindeki etkisi incelendiğinde ise nanoparçacık boyutunun küçülmesiyle Ra değerlerinde belirgin bir düşüş olduğu görülmüştür. Öyle ki Al_2O_3-136 nm kesme koşulunda 0.292 µm olan Ra değeri Al_2O_3-4 nm nanoakışkan kesme koşulunda %13.01 düşüş ile 0.254 µm olmuştur. Tüm kesme koşulları içerisinde en düşük Ra değeri ise Al_2O_3-4 nm nanoakışkan ile elde edilmiş olup kuru ve saf MMY koşuluna göre sırasıyla %37.43 ve %23.26 düşüş sağlanmıştır. Bu durum nanoparçacık boyutunun küçülmesiyle nanoparçacık takım/talaş arayüzeyine daha iyi nüfuz etmesi ve daha ince bir film tabakası oluşturarak yağlayıcılığı önemli ölçüde artırmasına atfedilmiştir. Özelikle 100 nm'den daha küçük nanoparçacıklar ile hazırlanan nanoakışkanların performanslarının daha büyük boyutlulara göre önemli ölçüde daha yüksek olduğu söylenebilir.
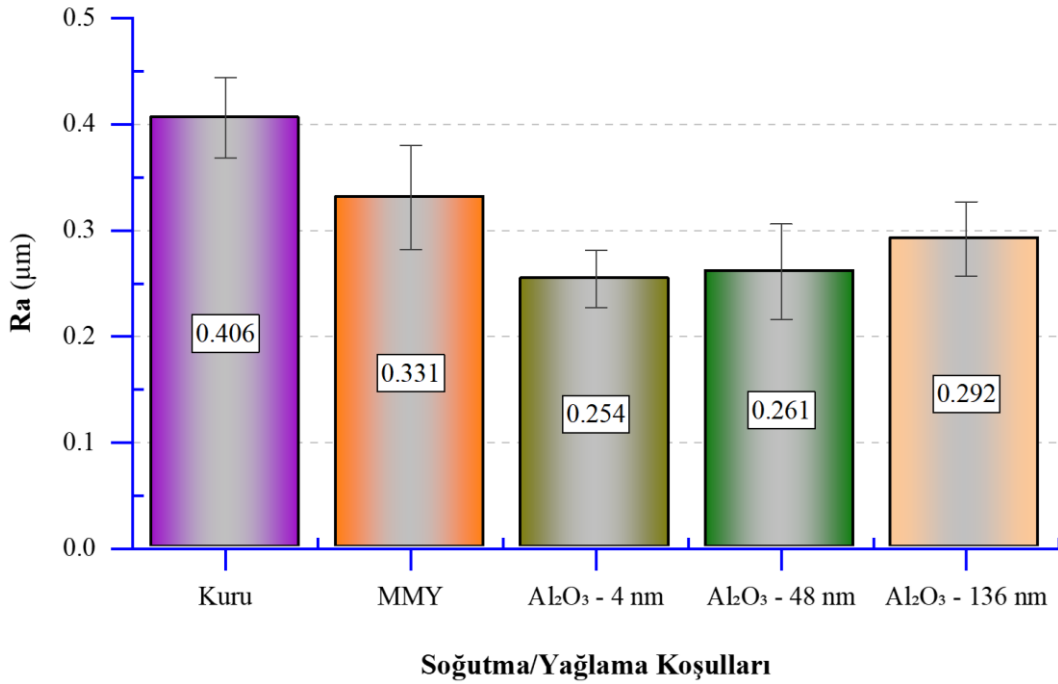
Şekil 3. Farklı soğutma/yağlama koşulları altında yüzey pürüzlülük Ra sonuçları.

3.2. Kesme Bölgesindeki Sıcaklığın Değerlendirilmesi

Metal kesmede malzemenin deformasyonu için gerekli olan mekanik enerjinin tamamına yakını ısı enerjisine dönüşmektedir. Kesme bölgesinde oluşan yüksek sıcaklıklar ise kesici takımın ömrünü önemli ölçüde azaltarak işleme verimliliğinin düşmesine neden olmaktadır [27,28]. Bu nedenle özellikle üstün mekanik özelliklere sahip süperalaşım gibi malzemelerin işlenmesinde kesme sıcaklığının kontrol edilmesi büyük önem arz etmektedir. Çalışmanın bu kısmında farklı soğutma/yağlama yöntemlerinin kesme sıcaklığı üzerindeki etkilerini irdelemek amacıyla kesme esnasında ölçümler gerçekleştirilmiş olup sonuçları Şekil 4'te verilmiştir. Beklenildiği gibi en yüksek kesme sıcaklığı 257.3 ^oC ile kuru kesme koşulunda elde edilmiştir. Bu durum takım/talaş temas alanındaki yüksek sürtünmenin bir tezahürü olarak değerlendirilmiştir. Saf kesme yağının MMY ile sis bulutu şeklinde kesme bölgesine tatbik edilmesinin sürtünmeyi azaltma ve kesme sıcaklığını düşürmede etkin olduğu görülmüştür. Öyle ki bu kesme koşulunda kuru kesme koşuluna göre %23.70'lik bir düşüş kaydedilmiştir. Literatürdeki yapılan birçok çalışmada benzer düşüşleri görmek mümkündür [29,30]. Yüzey pürüzlülüğünde olduğu gibi kesme sıcaklığının düşürülmesinde de nanoakışkanların önemli bir çarpan olduğunu söylemek mümkündür. En düşük kesme sıcaklığı değerleri nanoakışkan kesme koşulları altında gerçekleşmiştir. Nanoparçacıkların yüksek termal iletim katsayısına sahip olmaları katıldıkları yağın termal iletim özelliğini önemli ölçüde iyileştirdiği bilinmektedir [16]. Bu özelliği ile kesme bölgesinde oluşan sıcaklığı önemli ölçüde tahliye etmesinin kesme sıcaklığının düşmesinden sorumlu olduğu düşünülmektedir. Nanoparçacık boyutunun kesme sıcaklığı üzerindeki etkisi irdelendiğinde ise 100 nm'nin altındaki nanoparçacıklar hazırlanan nanoakışkanların kesme sıcaklığının değişimi üzerinde çok fazla bir etkisi olmazken nanoparçacık boyutunun 100 nm'nin üzerine

çıkmasının kesme sıcaklığının önemli ölçüde artmasına neden olduğu görülmüştür. Öyle ki Al_2O_3-136 nm nanoakışkan kesme koşulu kuru ve MMY kesme koşuluna göre kesme sıcaklığında sırasıyla %29.10 ve %7.08 düşüş sağlarken bu oranlar Al_2O_3-4 nm nano akışkan kesme koşulunda %36.02 ve %16.14 olarak gerçekleşmiştir. Buradan hareketle nanoparçacık boyutunun nanoakışkanların soğutma özelliği üzerinde önemli bir etkiye sahip olduğunu söylemek mümkündür. Burada nanoakışkandaki termo-fiziksel değişimlerin kesmeye olan etkilerinin yanı sıra daha küçük parçacıklara sahip nanoakışkanın takım/talaş alanına daha iyi nüfuz etmesinin göz ardı edilmemesi gerektiği düşünülmektedir.
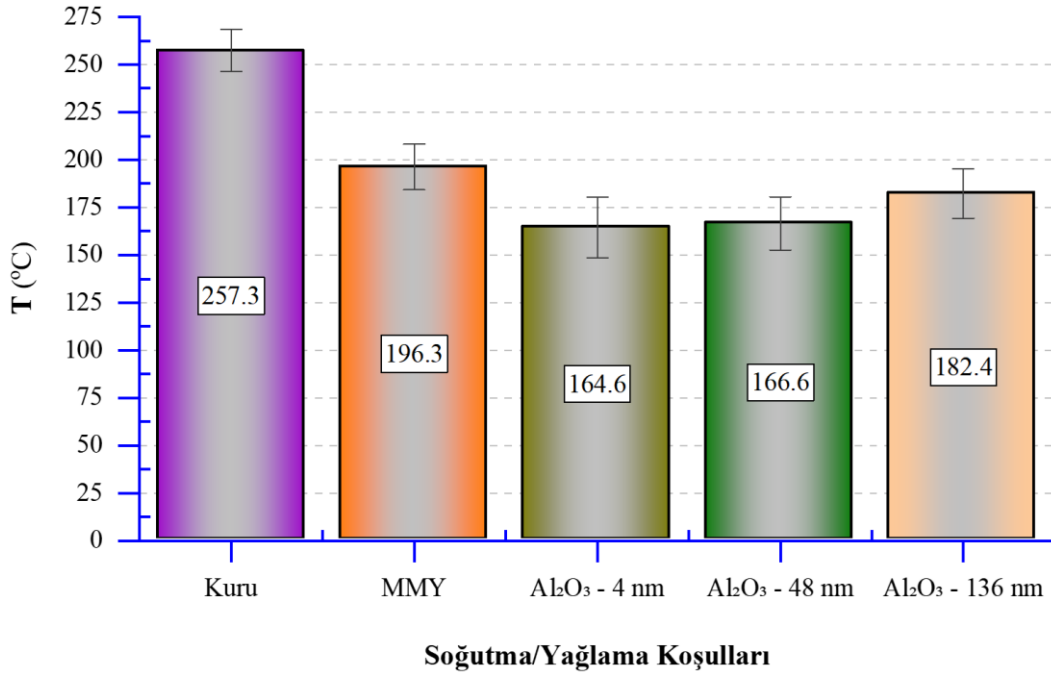
Şekil 4. Farklı soğutma/yağlama koşulları altında kesme sıcaklığı sonuçları.

3.3. Güç Tüketiminin Değerlendirilmesi

Günümüz dünyasında artan enerji maliyetleri ve çevreci üretim gereklilikleri imalat endüstrisinde enerji verimliliğinin önemini her geçen gün artırmaktadır [31]. Talaşlı imalat endüstrisinde ise sürdürülebilir üretimin temel gerekliliklerinin başında enerji sarfiyatını azaltmak ve çevreci üretim tekniklerini kullanmak gelmektedir. Enerji sarfiyatını azaltmanın yolu ise tezgâh güç tüketimini azaltacak kesme koşullarının tespiti ile mümkün olabilmektedir [32]. Bu amaçla çevreci soğutma/yağlama koşullarının tezgâh güç tüketimi üzerindeki etkilerini belirlemek amacıyla bir dizi deney yapılmış olup sonuçlar Şekil 5'te verilmiştir. Kuru kesme koşulu her ne kadar çevreci bir yöntem olarak değerlendirilse de süperalaşım gibi malzemelerin işlenmesinde güç tüketiminin önemli ölçüde artmasına neden olmaktadır. Yapılan çalışma da 480 Watt güç tüketimi ile en yüksek güç tüketen kesme koşulu kuru kesme olmuştur. Diğer işleme çıktılarında olduğu gibi güç tüketimi üzerinde de kuru sürtünmenin sonucu olarak malzemenin yüksek mekanik yükler altında deformasyonunun güç tüketiminin artmasına neden olduğu düşünülmektedir. Saf MMY kesme koşulunda yağlayıcı ajanın varlığı, sürtünmenin azaltılması dolayısıyla tezgâh güç tüketiminin %6.25 kadar düşmesini sağlamıştır. Literatürde de yapılan benzer çalışmalarda kuru kesme koşulunda kesme bölgesinde yüksek sürtünme ve kesme kuvvetlerinin olduğu gözlemlenmiştir. Yağlamanın etkisiyle azalan sürtünme ve kesme kuvvetlerine bağlı olarak güç tüketiminde de düşüşler görülmüştür [33],[34]. Nanoakışkan kesme koşulları MMY kesme koşuluna göre güç tüketiminde her ne kadar düşüş sağlasa da diğer işleme çıktılarındaki kadar etkin bir rol oynamadığı söylenebilir. Hatta nanoparçacık boyutu 136 nm olduğunda MMY kesme koşuluna göre bir miktar güç tüketiminin arttığı görülmüştür. Bu da nanoparçacık boyutunun belli bir değerin üzerinde olması nanoakışkanın dar alanda gerçekleşen kesme bölgesine efektif bir şekilde ulaşamadığının bir göstergesi olarak değerlendirilebilir. Boyut farkına bağlı nanoakışkanlar arasındaki farklar göz ardı edilebilecek kadar az olmakla birlikte en düşük güç tüketimine (440 Watt) yine Al_2O_3-4 nm nanoakışkan kesme koşulunda ulaşılmıştır. Al_2O_3-4 nm nanoakışkan kesme koşulunda güç tüketim değeri kuru koşula göre %8.33 ve MMY koşuluna göre %2.22 düşüş göstermiştir. Genel olarak değerlendirildiğinde 4 nm ve 48 nm boyutlu nanoakışkanların kullanımının sonuçları çok belirgin derecede değiştirmediği görülmektedir. Nanoakışkanlar arasında en büyük değişim 4 nm ve 136 nm boyutlu nanoakışkan kullanımı arasında

görülmektedir. Bu durum özellikle büyük boyutlu nanoparçacıkların (100 nm üstü) kesme bölgesine direk etki edemediğinin bir göstergesidir. Küçük boyutlu nanoparçacık ilaveli nanoakışkanların takım-talaş-iş parçası arasına daha iyi nüfuz etmesine bağlı olarak daha etkili yağlama yaptığı sonucuna ulaşılmaktadır.
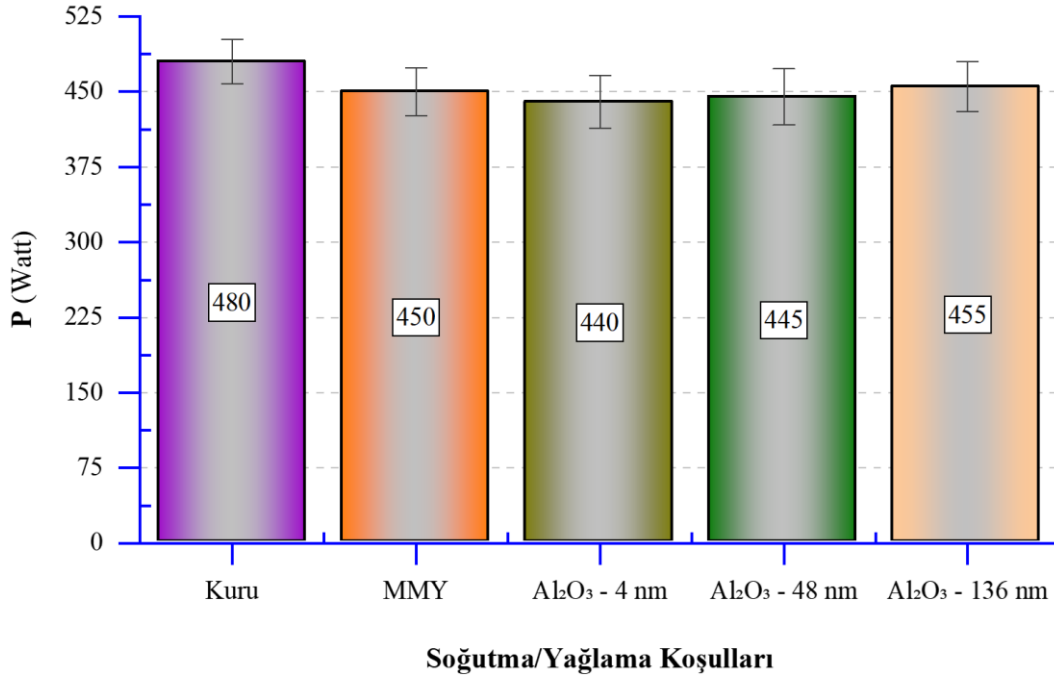
Şekil 5. Farklı soğutma/yağlama koşulları altında güç tüketimi sonuçları.

3.4. Takım Yanak Aşınmasının Değerlendirilmesi

Takım aşınması/ömrü üretim maliyetlerini ve ürün kalitesini doğrudan etkileyen en önemli işlenebilirlik kriterlerinden biridir [16,23,27]. Çalışmanın bu kısmında soğutma/yağlama koşullarının takım aşınması üzerindeki etkilerini belirlemek amacıyla hacme bağlı olarak kesici takım yanak aşınması ölçümleri yapılmış olup değişimleri gösterir grafik Şekil 6'da verilmiştir. En ağır işleme koşulu olan kuru kesme koşulunda takım aşınması kriteri olan 3 µm değerine 10000 cm^3 talaş hacminde ulaşıldığından bu talaş hacmi diğer kesme koşullarında sabit tutularak ölçümler gerçekleştirilmiştir. Tüm kesme koşullarında artan talaş hacmi ile takım aşınmasının arttığı ancak kuru kesme koşulunda aşınma artış hızının çok daha yüksek olduğu görülmüştür. Süperalaşım malzemenin kuru kesme ile işlenmesi işleme verimliliğini son derece olumsuz etkileyen bir durum olarak karşımıza çıkmaktadır. Aynı kesme koşulunda yüzey kalitesinin bozulması ve güç tüketiminin de artması bu durumu doğrular niteliktedir. Bu durumun oluşmasında temel sebep yüksek sürtünme ve buna bağlı olarak ortaya çıkan yüksek sıcaklıkların kesici takımın aşınmasını son derece hızlandırması olduğu söylenebilir. En yüksek kesme sıcaklığının bu kesme koşulunda elde edilmiş olması bu durumu teyit etmektedir (Bkz Bölüm 3.2). MMY kesme koşulunda 10000 cm^3 talaş hacminde yanak aşınması değeri 156 µm ölçülmüş olup kuru kesmeye göre %48'lik ciddi bir iyileşme kaydedilmiştir. Bu da süperalaşım malzemelerin işlenmesinde soğutma/yağlamanın önemini açık bir şekilde ortaya koymaktadır. Yağlayıcı ajanın varlığı ile hem sürtünmenin azaltılması hem de sürtünme kaynaklı ısının azaltılması takımın daha uzun süre çalışmasına zemin hazırladığı düşünülmektedir. Diğer deney çıktılarında olduğu gibi takım aşınmasının azaltılması noktasında da nanoakışkan yağlayıcıların kilit rol oynadığı söylenebilir. Özellikle 100 nm'den daha küçük parçacık ihtiva eden nanoakışkanların takım aşınmasında kayda değer iyileşmeler sağladığı görülmüştür. Öyle ki en küçük parçacıklı Al$_2$O$_3$-4 nm nanoakışkan kesme koşulu takım aşınmasında Al$_2$O$_3$-136 nm nanoakışkan, MMY ve kuru kesme koşuluna göre sırasıyla %23.66, %35.89 ve %66.66 iyileşme sağlamıştır. Kesme yağına katılan Al$_2$O$_3$ nanoparçacıklarının yağın yağlayıcılık özelliğini iyileştirmenin yanı sıra termal iletkenliğini de önemli ölçüde iyileştirdiği birçok çalışmada dile getirilmiştir [8,11,13]. Yağlayıcılık özelliği sürtünmenin azaltılması, dolayısıyla sürtünme kaynaklı ısı oluşumunun azaltılmasına katkı sunarken termal iletkenliğindeki artış ise kesme bölgesinde oluşan ısının hızla tahliyesini sağlamaktadır. Ayrıca nanoakışkan içerisindeki parçacıklar sürtünme bölgesinde yuvarlanma, parlatma gibi mekanizmalar sayesinde ara yüzeyde ince bir yağ filmi ile bariyer oluşturmaktadır [26]. Bu sayede kesici takımın aşınmasına sebep olan mekanik yük faktörlerinin yanı sıra termal ve aşındırıcı yük faktörlerinin de

azalmasına imkân sağlamaktadır. Nanoparçacık boyutunun küçülmesi ise nanoparçacıkların daha dar alanlara ulaşabilmesini böylece yukarıda bahsedilen mekanizmaların etkinliğinin artmasına katkı sunduğu düşünülmektedir. Sonuç olarak Hastelloy X alaşımın işlenmesinde kuru kesmenin işleme verimliliği açısından son derece verimsiz bir yöntem olduğu MMY'in ise işleme verimliğini önemli ölçüde artırdığı söylenebilir. Nanoakışkan yağlayıcıların ise tüm işleme çıktılarında sağladığı önemli iyileşmeler ile en verimli işleme yöntemi olduğu görülmüştür.
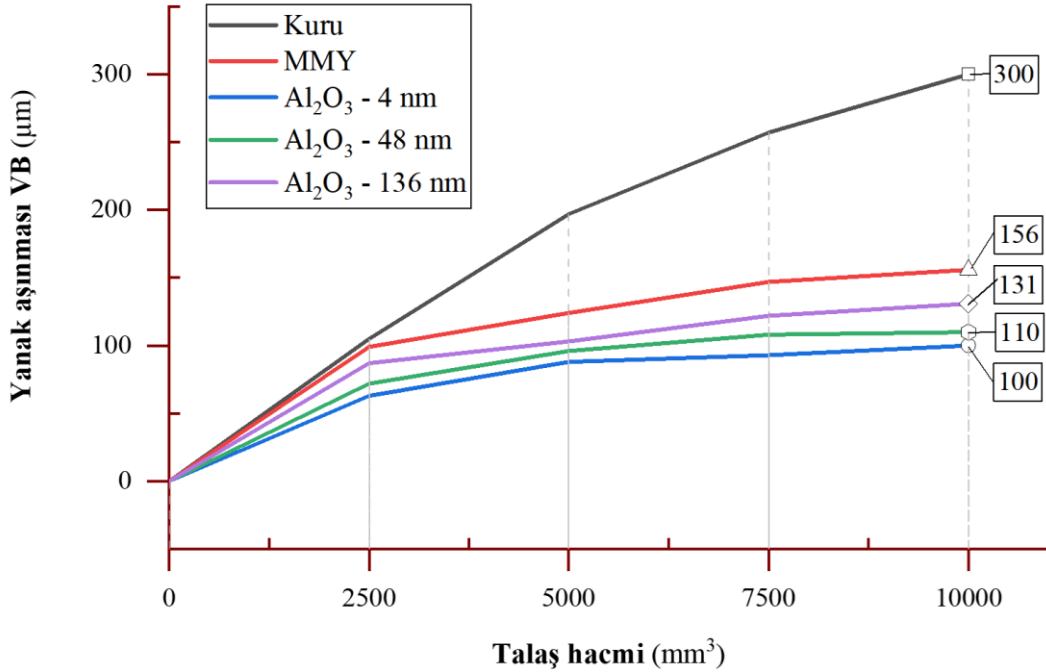
Şekil 6. Farklı soğutma/yağlama koşulları altında takım yanak aşınma.

4. SONUÇLAR

Bu çalışmada süperalaşım Hastelloy X alaşımının frezelenmesinde farklı parçacık boyutlu Al_2O_3 esaslı nanoakışkan yağlayıcıların işleme performansları kuru ve saf MMY kesme koşulları ile karşılaştırılmıştır. Performans kriterleri olarak yüzey pürüzlülüğü, kesme sıcaklığı, tezgâh güç tüketimi ve takım aşınması dikkate alınmıştır. Nanoakışkan parçacık boyutları ise 4 nm, 48 nm ve 136 nm olarak belirlenmiştir. Yapılan çalışma sonucunda elde edilen bulgular ve sonuçlar aşağıda maddeler halinde özetlenmiştir.

✓ Ra değerleri üzerinde soğutma/yağlama koşullarının önemli etkileri olduğu görülmüştür. En yüksek Ra değeri 0.406 µm ile kuru kesme koşulunda elde edilmiştir. MMY kesme koşulu kuru kesmeye göre Ra değerinde %22.66 iyileşme sağlamıştır. Tüm kesme koşulları içerisinde en düşük Ra değeri ise Al_2O_3-4 nm nanoakışkan ile elde edilmiş olup kuru ve saf MMY koşuluna göre sırasıyla %37.43 ve %23.26 düşüş sağlanmıştır.

✓ Kuru kesmede 257 ^{o}C olan kesme sıcaklığı, MMY kesme koşulunda %23.70'lik bir düşüşle 196.3 ^{o}C olmuştur. Nanoakışkanlar kesme sıcaklığının düşmesinde önemli bir rol oynamış olup en düşük sıcaklık değerlerinin elde edilmesini sağlamıştır. Öyle ki Al_2O_3-4 nm nanoakışkan kesme koşulu kuru ve MMY kesme koşuna göre kesme sıcaklığında sırasıyla %36.02 ve %16.14 düşüş sağlamıştır.

✓ Tezgâh güç tüketiminde MMY kesme koşulu kuru kesme koşuluna göre %6.25'lik bir düşüş sağladığı görülmüştür. Güç tüketimi üzerinde parçacık boyut farkına bağlı farklar göz ardı edilebilecek kadar az olmakla birlikte en düşük güç tüketimine (440 Watt) yine Al_2O_3-4 nm nanoakışkan kesme koşulunda ulaşılmıştır.

✓ Süperalaşım malzemenin işlenmesinde takım aşınması üzerinde soğutma/yağlamanın dramatik bir etkiye sahip olduğu görülmüştür. Aynı talaş hacminde kuru kesme koşulunda 3 µm olan yanak aşınması bir yağlayıcı ajanın varlığı ile MMY kesme koşulunda %48'lik düşüş ile ciddi bir iyileşme kaydedilmiştir. Parçacık boyutundaki azalma nanoakışkanların takım aşınmasını azaltma etkisini belirgin bir şekilde artırmıştır. Al_2O_3-4 nm nanoakışkan kesme koşulu MMY ve kuru kesme koşuluna göre takım aşınmasında sırasıyla %23.66 ve %35.89 iyileşme sağlamıştır.

Yapılan çalışma neticesinde elde edilen bulgular dikkate alındığında süperalaşım gibi işlenmesi zor olan malzemelerde işleme verimliliği açısından soğutma/yağlamanın son derece önemli olduğu söylenebilir. Parçacık boyutlarının ise nanoakışkanların performansı üzerinde önemli etkiye sahip olduğu parçacık boyutunun küçülmesi ile nanoakışkanların kendisinden beklenen etkiyi daha efektif bir şekilde gösterebildiği çıkarımı yapılabilir.

KAYNAKLAR

[1] T. M. Pollock, S. Tin, Nickel-based superalloys for advanced turbine engines : chemistry , microstructure , and properties, J Propuls Power 22 2 (2006) 361–374.

[2] R. Demirsöz, M. Boy, Measurement and evaluation of machinability characteristics in turning of train wheel steel via CVD coated-RCMX carbide tool, İmalat Teknol ve Uygulamaları 3 1 (2022) 1–13.

[3] Q. Han, R. Mertens, M. L. Montero-Sistiaga, S. Yang, R. Setchi, K. Vanmeensel, B. V. Hoorewe, S. L. Evans, H. Fan, Laser powder bed fusion of Hastelloy X: Effects of hot isostatic pressing and the hot cracking mechanism, Mater Sci Eng A 732 (2018) 228–239.

[4] H. U. Hong, I. S. Kim, B. G. Choi, H. W. Jeong, C. Y. Jo, Effects of temperature and strain range on fatigue cracking behavior in Hastelloy X, Mater Lett 62 28 (2008) 4351–4353.

[5] O. Pereira, P. Català, A. Rodríguez, T. Ostra, J. Vivancos, A. Rivero, L.N. López-de-Lacalle, The use of hybrid CO2+MQL in machining operations, Procedia Engineering 132 (2015) 492–499.

[6] N. Zadafiya, K. Shah, P. Shokrani, A. Khanna, Recent advancements in nano-lubrication strategies for machining processes considering their health and environmental impacts, J Manuf Process 68 (2021) 481-511.

[7] N. S. Veeranna, S. Lakshmi, Al2O3-based nanofluids: a review, Nanoscale Res Lett, 6 (2011) 456–471.

[8] F. Gunan, T. Kıvak, C. V. Yıldırım, M. Sarıkaya, Performance evaluation of MQL with Al2O3 mixed nanofluids prepared at different concentrations in milling of Hastelloy C276 alloy, J Mater Res Technol 9 5 (2020) 10386–10400.

[9] G. Vasu, V. Pradeep Kumar Reddy, Effect of minimum quantity lubrication with Al2O3 nanoparticles on surface roughness, tool wear and temperature dissipation in machining Inconel 600 alloy, Proc Inst Mech Eng Part N J Nanoeng Nanosyst 225 1 (2011) 3-16.

[10] T. Venkatesan, K. Devendiran, S. Ghazaly, N. M., Rahul, R.Mughilan, Optimization of cutting parameters on turning of Incoloy 800h using Al2O3 nanofluid in coconut oil, Procedia Manuf 30 (2019) 268-275.

[11] H. A. Eltaggaz, A. Hegab, H. Deiab, I. Kishawy, Hybrid nano-fluid-minimum quantity lubrication strategy for machining austempered ductile iron (ADI), In . J Interact Des Manuf 12 (2018) 1273–1281.

[12] R. Hadi, M. Atefi, Effect of minimum quantity lubrication with gamma-Al2O3 nanoparticles on surface roughness in milling AISI D3 steel, Indian J Sci Technol 8 3(2015) 130–135.

[13] Ç. V. Yıldırım, Ş. Şirin, T. Kıvak, Waspaloy süper alaşımının frezelenmesinde nanopartikül katkılı yağlamanın takım aşınması üzerindeki etkisinin araştırılması, Düzce Üniversitesi Bilim ve Teknol Dergisi 7 1 (2019) 466–476.

[14] S. W. Lee, P. H. Nam, J. S. Li, C. Lee, An experimental study on micro-grinding process with nanofluid minimum quantity lubrication (MQL), Int J Precis Eng Manuf 13 (2012) 331-338.

[15] E. Şirin, Hastelloy X süper alaşımının delinmesinde nano partikül katkılı kesme yağlarının işleme performansı üzerindeki etkilerinin incelenmesi, Doktora Tezi, Düzce Üniversitesi Fen Bilimleri Enstitüsü, 2021.

[16] Ş. Şirin, T. Kıvak, Performances of different eco-friendly nanofluid lubricants in the milling of Inconel X-750 superalloy,Tribol Int 137 (2019) 180–192.

[17] Nanografi, Al$_2$O$_3$ Aluminum Oxide, https://www.nanografi.com.tr/, 10.11.2024.

[18] M. Suresh, S. Venkitaraj, K. P. Selvakumar, P. Chandrasekar, Synthesis of Al2O3–Cu/water hybrid nanofluids using two step method and its thermo physical properties, Colloids Surfaces A Physicochem Eng Asp 388 1 (2011) 41-48.

[19] G. Pramanik, A. Dixit, A. R. Chattopadhyaya, S. Uddin, M. S. Dong, Y. Basak, A. K. Littlefair, Fatigue life of machined components, Advances in Manufacturing 5 (2017) 59-76.

[20] Ş. Şirin, S. Akıncıoğlu, M. K. Gupta, T. Kıvak,N. Khanna, A tribological performance of vegetable-based oil combined with GNPs and hBN nanoparticles on the friction-wear tests of titanium grade 2, Tribol Int 181 (2023) 108314.

[21] Y. Ye, C. Zhang, C. Zhao, J. Dong, Effects of post-processing on the surface finish, porosity, residual stresses, and fatigue performance of additive manufactured metals: a review, J Mater Eng Perform 30 (2021) 6407-6425.

[22] O. Öndin, T. Kıvak, M. Sarıkaya, Ç. V. Yıldırım, Investigation of the influence of MWCNTs mixed nanofluid on the machinability characteristics of PH 13-8 Mo stainless steel, Tribol Int 148 (2020) 106323.

[23] E. Şirin, Ç. V. Yıldırım, Ş. Şirin, T. Kıvak, M. Sarıkaya, Comprehensive analysis of cutting temperature, tool wear, surface integrity and tribological properties in sustainable milling of Ti6Al4V alloy: LN2, nanofluid and hybrid machining, J Manuf Process 131 (2024) 1360-1371.

[24] Ç. V. Yıldırım, M. Sarıkaya, T. Kıvak, Ş. Şirin,The effect of addition of hBN nanoparticles to nanofluid-MQL on tool wear patterns, tool life, roughness and temperature in turning of Ni-based Inconel 625, Tribol Int 134 (2019) 443–456.

[25] P. Chinchanikar, S. Kore, S. S. Hujare, A review on nanofluids in minimum quantity lubrication machining, J Manuf Process 68 (2021) 56–70.

[26] Y. Wang, Z. Wan, L. Lu, Z. Zhang, Y. Tang, Friction and wear mechanisms of castor oil with addition of hexagonal boron nitride nanoparticles, Tribol Int 124 (2018) 10–22.

[27] E. Şirin, Evaluation of tribological performance of MQL technique combined with LN_2, CO_2, N_2 ecological cooling/lubrication techniques when turning of Hastelloy C22 superalloy, Tribol Int 188 (2023) 108786.

[28] M. A. Abukhshim, N. A. Mativenga, P. T. Sheikh, Heat generation and temperature prediction in metal cutting: A review and implications for high speed machining, Int J Mach Tools Manuf 46 7 (2006) 782-800.

[29] A.Yücel, Ç. V. Yıldırım, M. Sarıkaya, Ş. Şirin, T. Kıvak, M. K.Gupta, İ. V. Tomaz, Influence of MoS2 based nanofluid-MQL on tribological and machining characteristics in turning of AA 2024 T3 aluminum alloy, J Mater Res 15 (2021) 1688–1704.

[30] Ş. Şirin, M. Sarıkaya, Ç. V. Yıldırım, T. Kıvak, Machinability performance of nickel alloy X-750 with SiAlON ceramic cutting tool under dry, MQL and hBN mixed nanofluid-MQL,Tribol Int 153 (2021) 106673.

[31] A. Aramcharoen S. K. Chuan, An experimental ınvestigation on cryogenic milling of Inconel 718 and its sustainability assessment, Procedia CIRP 14 (2014) 529–534.

[32] E. Şirin, E. Uysal, N. Khanna, Ş. Şirin, An investigation of deep wear status assessment of AISI 329 material under green nanofluid conditions, Arab. J Sci Eng (2014) 1–20.

[33] Ç. V. Yıldırım, Ş. Şirin, S. Dağlı, H. Salvi, N. Khanna, Analysis of machinability and sustainability aspects while machining Hastelloy C4 under sustainable cutting conditions, Sustain Mater Technol 38 (2023) 00781.

[34] M. Ö. Ayhan, E. Şirin, Ç. V. Yildirim, The effect of environmentally friendly cooling techniques in hard turning: comparison of nanofluid, vortex, GQDs and hybrid cooling methods, Arab J Sci Eng (2024) 1–22.

Manufacturing Technologies and Applications
MATECA

Optimization of Drilling Parameters and Tool Geometry for Enhanced Performance and Hole Quality in AISI 1050 Steel

M.Alperen Çoban[1] [ID], Çiğdem Çiçek[2] [ID], İbrahim Baki Şahin[3,*] [ID]

[1] Gazi University, Graduate School of Natural and Applied Sciences, Department of Manufacturing Engineering, Ankara, Turkey

[2] Gazi University, Faculty of Technology, Department of Wood Products Industrial Engineering, Ankara, Turkey

[3*] Kirsehir Ahi Evran University, Faculty of Engineering and Architecture, Department of Mechanical Engineering, Kırşehir, Turkey

ABSTRACT

This study presents a comprehensive statistical analysis of the effects of drilling parameters on cutting forces and hole quality in AISI 1050 steel, utilizing Analysis of Variance (ANOVA) to evaluate the significance of various factors. The research employs a full factorial experimental design to systematically investigate the influence of drill geometry, cutting speed, and feed rate on thrust force, torque, and several metrics of hole quality. The ANOVA results indicate that drill geometry is the predominant factor, accounting for a significant portion of the variance in thrust force and torque, with statistically significant F-values, thereby confirming its critical role in drilling performance optimization. Moreover, cutting speed and feed rate also demonstrate substantial contributions to the variance in cutting forces and hole quality metrics. These findings highlight the importance of these parameters in enhancing drilling efficiency and minimizing defects such as burr formation and surface roughness. The interaction between these parameters is essential for achieving optimal drilling conditions, as evidenced by the statistical modeling approaches employed in the study. In addition to ANOVA, the study incorporates Taguchi method's signal-to-noise ratio analysis to further validate the findings. This method underscores the superior performance of specific drill geometries in minimizing variability in drilling outcomes, thereby reinforcing the significance of drill design in achieving high-quality holes. The insights derived from this research provide a robust foundation for optimizing drilling processes in industrial applications, particularly for medium-carbon steels like AISI 1050, and offer valuable guidance for future research endeavors aimed at enhancing machining efficiency and quality. The implications of this study extend to practical applications in manufacturing, where understanding the interplay of drilling parameters can lead to improved operational efficiencies and product quality. The findings contribute to the existing body of knowledge by elucidating the critical factors influencing drilling performance, thus serving as a reference point for further investigations in the field of machining and materials processing.

Keywords: AISI 1050 Steel, Drilling Parameters, ANOVA, Taguchi Method

AISI 1050 Çeliğinde Kesme Verimliliği ve Delik Kalitesini Artırmak için Delme Parametrelerinin Optimizasyonu

ÖZET

Bu çalışma, AISI 1050 çeliğinde delme parametrelerinin kesme kuvvetleri ve delik kalitesi üzerindeki etkilerini kapsamlı bir istatistiksel analizle sunmaktadır. Çalışmada, çeşitli faktörlerin önemini değerlendirmek için Varyans Analizi (ANOVA) kullanılmıştır. Araştırma, matkap geometrisi, kesme hızı ve ilerleme hızının itme kuvveti, tork ve delik kalitesinin çeşitli metrikleri üzerindeki etkisini sistematik olarak incelemek amacıyla tam faktöriyel deney tasarımı kullanmaktadır. ANOVA sonuçları, matkap geometrisinin itme kuvveti ve torktaki varyansın önemli bir kısmını açıklayan baskın faktör olduğunu ve istatistiksel olarak anlamlı F-değerleri ile delme performansının optimizasyonundaki kritik rolünü doğruladığını göstermektedir. Ayrıca, kesme hızı ve ilerleme hızı da kesme kuvvetleri ve delik kalitesi metriklerindeki varyansa önemli katkılar sağlamaktadır. Bu bulgular, bu parametrelerin delme verimliliğini artırmada ve çapak oluşumu ile yüzey pürüzlülüğü gibi kusurları en aza indirmede önemini vurgulamaktadır. Bu parametreler arasındaki etkileşim, çalışmada kullanılan istatistiksel modelleme yaklaşımlarıyla kanıtlandığı üzere, optimal delme koşullarının elde edilmesi için esastır. ANOVA'ya ek olarak, çalışma bulgularını daha da doğrulamak için Taguchi'nin sinyal-gürültü oranı analizini içermektedir. Bu yöntem, belirli matkap geometrilerinin delme sonuçlarındaki değişkenliği en aza indirmedeki üstün performansını vurgulamakta ve yüksek kaliteli delikler elde etmede matkap tasarımının önemini pekiştirmektedir. Bu araştırmadan elde edilen içgörüler, özellikle AISI 1050 gibi orta karbonlu çelikler için endüstriyel uygulamalarda delme süreçlerinin optimize edilmesi için sağlam bir temel sağlamakta ve işleme verimliliği ve kalitesini artırmayı amaçlayan gelecekteki araştırma çabalarına değerli rehberlik sunmaktadır. Çalışmanın etkileri, delme parametrelerinin etkileşimini anlamanın operasyonel verimlilikleri ve ürün kalitesini artırabileceği üretim alanındaki pratik uygulamalara kadar uzanmaktadır. Bulgular, delme performansını

etkileyen kritik faktörleri açıklayarak, işleme ve malzeme işleme alanındaki daha ileri araştırmalar için bir referans noktası olarak mevcut bilgi birikimine katkıda bulunmaktadır.

Anahtar Kelimeler: AISI 1050 Çeliği, Delme Parametreleri, ANOVA, Taguchi Yöntemi

1. INTRODUCTION

Drilling is a fundamental material removal process, integral to numerous manufacturing sectors, constituting a substantial portion of machining operations [1]. This process is essential for creating precise holes in a variety of materials, such as metals, polymers, and composites. The efficiency and quality of drilling operations are influenced by numerous factors, including the type of cutting tool, its geometry, hole diameter, machine rigidity, cutting fluids, and cutting parameters. A comprehensive understanding of these dynamics is critical for optimizing process efficiency and ensuring product quality, especially in high-precision applications where tolerances are critical [2, 3]. Despite its critical importance, drilling poses several challenges that can adversely affect the quality of the drilled holes. Variability in cutting forces and material removal rates often lead to complications such as tool jamming and excessive wear [4, 5]. Additionally, the use of suboptimal spindle and drill chuck configurations can introduce geometric errors, resulting in circular deviations and axial misalignments-collectively referred to as cylindrical deviation-between entry and exit holes. Such deviations risk compromising the integrity of the final product by exceeding acceptable tolerance limits [6].

The demand for high-precision machining has intensified with technological advancements, necessitating stringent control over key parameters that affect hole quality, including dimensional accuracy, circularity, cylindrical deviation, and surface finish. Achieving these quality indicators often necessitates secondary operations, such as reaming, which enhance precision but also increase machining time and production costs [7]. Literature indicates that surface roughness is significantly impacted by drilling parameters like cutting speed and feed rate, which can cause thermal softening and subsequent surface damage [8, 9]. Extensive research has explored a variety of factors impacting drilling performance. Studies highlight the significant influence of cutting tool type on surface roughness and tool wear [10, 11]. Investigations reveal that coated tools often outperform uncoated ones in surface finish and longevity [12, 13]. Furthermore, the geometry of the drill bit, including its diameter and point angle, is crucial for determining drilling efficiency and hole quality [14]. Additionally, the application of cutting fluids can enhance drilling performance by mitigating friction and heat, thereby improving surface finish and extending tool life [15]. Minimum Quantity Lubrication (MQL) techniques are particularly noteworthy for offering effective cooling solutions with minimal environmental impact [16]. The effectiveness of these strategies, however, varies with the material and specific operational conditions [17].

The complexities associated with drilling operations necessitate ongoing investigation to develop robust models and strategies for optimization. This is especially true for materials like AISI 1050 steel, which present unique challenges due to their specific metallurgical properties [18]. Research suggests that optimizing parameters such as feed rate and cutting speed can significantly improve surface finish and dimensional accuracy [19]. Moreover, integrating advanced technologies like fuzzy logic and artificial intelligence enhances the predictive capabilities of drilling models, enabling real-time process adjustments [20]. In summary, while drilling is a cornerstone of modern manufacturing, it poses challenges that can compromise quality. A thorough understanding of drilling dynamics is essential to optimizing process efficiency and achieving high-quality outcomes. Continued research in this domain is critical to addressing the complexities of drilling operations and developing innovative solutions to enhance precision and reliability.

This study aims to systematically investigate the individual and interactive effects of cutting speed, feed rate, and drill geometry on thrust force and torque during the drilling of AISI 1050 steel. By employing a full factorial experimental design and rigorous statistical analysis, the research seeks to elucidate the impact of these parameters on critical hole quality metrics. The findings will contribute to the development of empirical models and optimization strategies, ultimately enhancing the efficiency and quality of drilling operations in industrial applications.

2. MATERIAL AND METHOD

2.1. Experimental Setup

The drilling experiments were conducted on a CNC vertical machining center (Johnford VMC-850 model). Drilling was performed directly on the chamfered surface without prior spot-facing, simulating real-world manufacturing conditions where preparatory operations are often impractical. This study aimed to assess the performance of cutting tools and process parameters under these challenging conditions. A full factorial experimental design was utilized to systematically analyze the effects of drilling parameters—cutting speed, feed rate, and drill geometry—on cutting forces and torque during the machining of AISI 1050 steel. This material, widely used in gear manufacturing, was selected for its mechanical strength and moderate machinability. The test samples, crafted from AISI 1050 steel, were prepared to replicate the industrially relevant thickness and curvature of a 16-B sprocket. The chemical composition of the workpiece material is detailed in Table 1.

Table 1. Chemical composition of AISI 1050 manufacturing steel

% C	% Si (Max)	% Mn	% P (Max)	% S (Max)
0.45-0.55	0.40	0.6-0.9	0.035	0.035

The cutting speed (Vc, m/min) was varied across three distinct levels: Low (20 m/min), Medium (40 m/min), and High (60 m/min). This range was chosen to encompass typical operational conditions, allowing for a thorough assessment of its influence on cutting forces and surface integrity. The feed rates (f, mm/rev) selected for the study were set at 0.11, 0.13, and 0.15 mm/rev. These levels were specifically chosen based on preliminary tests to cover a broad spectrum of material removal rates, from conservative to aggressive, thus enabling the identification of optimal feed conditions that maximize efficiency without compromising quality. Three different drill geometries were investigated: the U-Drill, a standard drill with a 180° point angle, and a 140° point angle drill. These geometrical variations were selected to discern their respective impacts on the drilling dynamics and resultant hole quality, as tool geometry is a critical determinant of cutting performance. The experimental design's full factorial nature ensures comprehensive coverage of parameter combinations, thus allowing for robust statistical analysis of main effects and interactions. This approach not only facilitates the identification of optimal drilling conditions but also enhances the understanding of the underlying mechanical processes influencing hole quality in AISI 1050 steel. The specific cutting parameters and tool specifications are presented in Table 2. In Figure 1, the technical drawing of the 16B chain sprocket and the experimental specimen are shown.

Table 2. Control factors and their levels

Control Factors	Level 1	Level 2	Level 3
Cutting Speed (Vc, m/min)	Low(20 m/min)	Medium(40 m/min)	High(60 m/min)
Feed Rate (f, mm/rev)	0.11	0.13	0.15
Drill Geometry	U-Drill	180°	140°
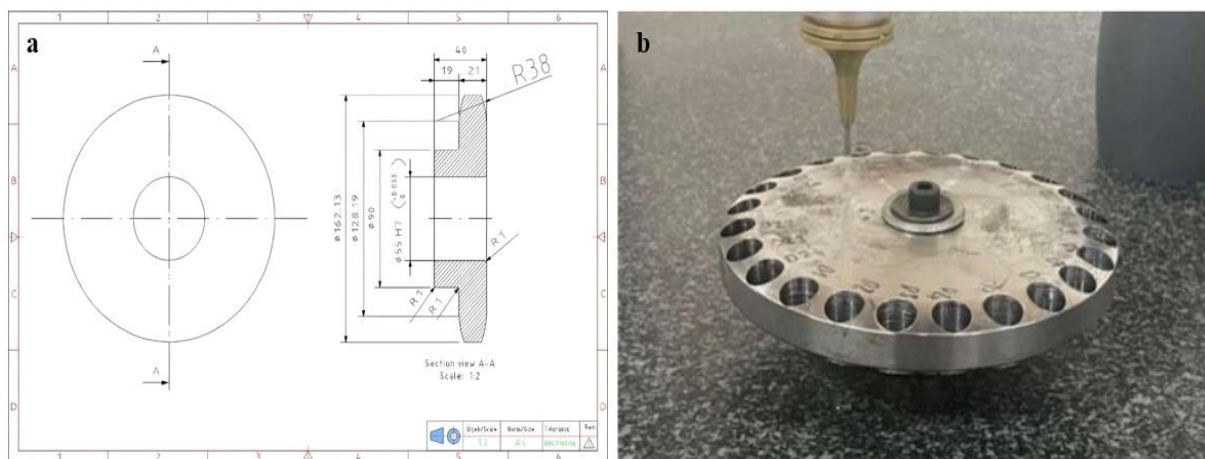
Figure 1. 16B chain sprocket techinal drawaing (a) and Test spicemen (b)

Cutting forces and torque were meticulously recorded using a Kistler 9272-A 4-component dynamometer paired with a Kistler 5070-A multi-channel amplifier, ensuring precision in data acquisition. Post-drilling evaluations involved measuring hole diameters, circular deviations, and cylindrical deviations using a coordinate measuring machine (CMM) for high precision.
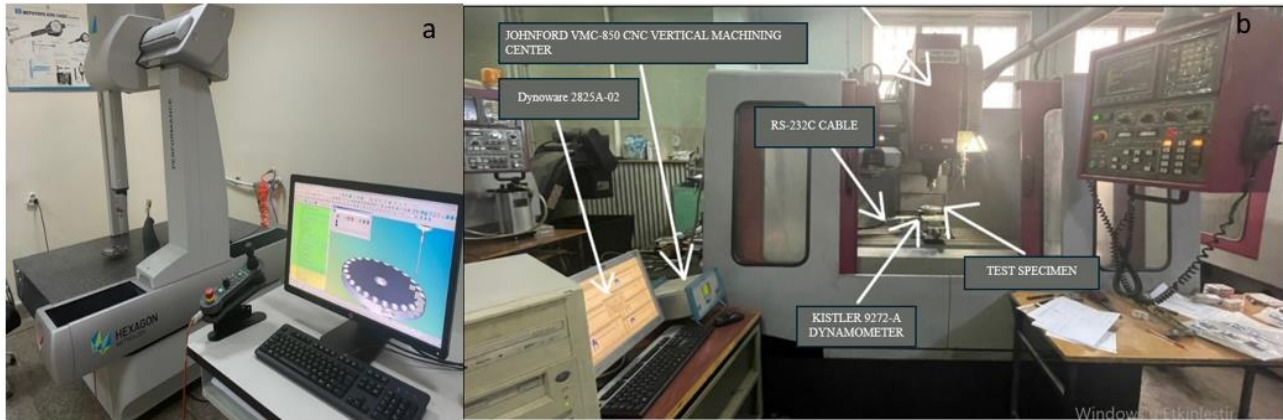
Fig.2 Experimental setup of the CMM (a) and JOHNFORD VMC-850 CNC vertical machining center with integrated Kistler 9272-A dynamometer, (b) Kistler 5070-A signal amplifier, and Dynoware 2825A-02 data acquisition system for machining force measurement.

A full factorial experimental design was implemented, allowing thorough investigation of the effects of three primary parameters-drill diameter, feed rate, and cutting speed-across three levels, and drill type across two levels. This approach enabled analysis of individual and interaction effects of control parameters, resulting in a total of 27 experimental trials (Table 3).

Table 3. Taguchi design

Experiment No	Drill Geometry	Cutting Speed (Vc, m/min)	Feed Rate (f, mm/rev)
1	U-Drill	Low(20 m/min)	0.11
2	U-Drill	Low(20 m/min)	0.13
3	U-Drill	Low(20 m/min)	0.15
4	U-Drill	Medium(40 m/min)	0.11
5	U-Drill	Medium(40 m/min)	0.13
6	U-Drill	Medium(40 m/min)	0.15
7	U-Drill	High(60 m/min)	0.11
8	U-Drill	High(60 m/min)	0.13
9	U-Drill	High(60 m/min)	0.15
10	180°	Low(20 m/min)	0.11
11	180°	Low(20 m/min)	0.13
12	180°	Low(20 m/min)	0.15
13	180°	Medium(40 m/min)	0.11
14	180°	Medium(40 m/min)	0.13
15	180°	Medium(40 m/min)	0.15
16	180°	High(60 m/min)	0.11
17	180°	High(60 m/min)	0.13
18	180°	High(60 m/min)	0.15
19	140°	Low(20 m/min)	0.11
20	140°	Low(20 m/min)	0.13
21	140°	Low(20 m/min)	0.15
22	140°	Medium(40 m/min)	0.11
23	140°	Medium(40 m/min)	0.13
24	140°	Medium(40 m/min)	0.15
25	140°	High(60 m/min)	0.11
26	140°	High(60 m/min)	0.13
27	140°	High(60 m/min)	0.15

3. EXPERIMENT AND OPTIMIZATION RESULTS

The experimentation conducted using the L27 orthogonal design represents a robust and well-established methodology for analyzing the effects of various drilling parameters on critical machining outcomes. The L27 orthogonal array facilitates a systematic exploration of multiple factors and their interactions, which is essential for optimizing drilling processes. This methodological approach has been effectively employed in numerous studies to evaluate the influence of parameters such as spindle speed, feed rate, and drill point angle on drilling performance [21, 22].

In this context, the analysis of variance (ANOVA) table serves as a fundamental analytical tool, enabling the determination of the significance of each parameter's contribution to the variability in response variables. For instance, empirical studies have demonstrated that factors like cutting speed and feed rate significantly influence the quality of drilled holes and surface finish [23, 24]. The integration of ANOVA with the L27 orthogonal design enhances the reliability of the findings and supports the derivation of robust conclusions regarding optimal drilling conditions.

Moreover, response curves play a pivotal role in visualizing the relationship between drilling parameters and their corresponding responses. The larger-the-better and smaller-the-better approaches are frequently employed in the analysis of signal-to-noise (S/N) ratios, which are crucial for optimizing the drilling process [21, 24]. This methodological framework not only facilitates an understanding of the effects of individual parameters but also aids in making informed decisions regarding the selection of optimal machining conditions. In summary, the integration of the L27 orthogonal design, ANOVA provides a comprehensive and effective framework for analyzing the effects of drilling parameters.

3.1. Taguchi Analysis

3.2. Fz (N) and M (N.cm) versus Drill Geometry; Cutting Speed (Vc, m/min); Feed Rate (f, mm/rev)

The Taguchi method is a powerful statistical tool widely utilized for optimizing drilling parameters, particularly in the context of composite materials and various drilling geometries. The method employs orthogonal arrays to systematically analyze the influence of multiple factors, such as cutting speed (Vc), feed rate (f), and drill geometry, on performance metrics like thrust force (Fz) and surface roughness. For instance, studies have shown that the selection of optimal drilling parameters can significantly reduce surface roughness and thrust force, thereby enhancing the overall quality of drilled holes [25-27]. The outcome of procedure parameters on Fz(N) and M(N.cm) was found as given below Table 4.

Table 4. Fz (N) and M (N.cm) results

Experiment no	Fz(N)	M(N.cm)	S/N Ratio (Fz)	S/N Ratio (M(N.cm)
1.	1340	7432	-62.5421	-77.4221
2.	1611	8125	-64.1419	-78.1965
3.	1340	8105	-62.5421	-78.1751
4.	1229	8984	-61.7910	-79.0694
5.	1405	8968	-62.9535	-79.0539
6.	1304	7696	-62.3056	-77.7253
7.	1204	7656	-61.6125	-77.6800
8.	1492	8567	-63.4754	-78.6566
9.	1404	7895	-62.9473	-77.9470
10.	967	8551	-59.7085	-78.6403
11.	1047	8767	-60.3989	-78.8570
12.	1133	9055	-61.0846	-79.1378
13.	112	113	-40.9844	-41.0616
14.	112	113	-40.9844	-41.0616
15.	112	113	-40.9844	-41.0616
16.	107	5578	-40.5877	-74.9296
17.	1107	5564	-60.8830	-74.9077
18.	1107	5564	-60.8830	-74.9077
19.	807	5733	-58.1375	-75.1676
20.	1142	5568	-61.1533	-74.9140
21.	1142	5568	-61.1533	-74.9140
22.	532	5565	-54.5182	-74.9093
23.	1148	5615	-61.1988	-74.9870

24.	1148	5615	-61.1988	-74.9870
25.	532	5565	-54.5182	-74.9093
26.	1148	5615	-61.1988	-74.9870
27.	1148	5615	-61.1988	-74.9870

When Figure 3 is examined, the analysis reveals that the 180° drill geometry exhibits the highest S/N ratio, indicating its superior performance in minimizing variability in thrust force. Additionally, a medium cutting speed is identified as optimal, yielding the best S/N ratio and suggesting its effectiveness in reducing variability. Furthermore, a feed rate of 0.11 mm/rev achieves the highest S/N ratio, demonstrating its efficacy in minimizing thrust force variability.
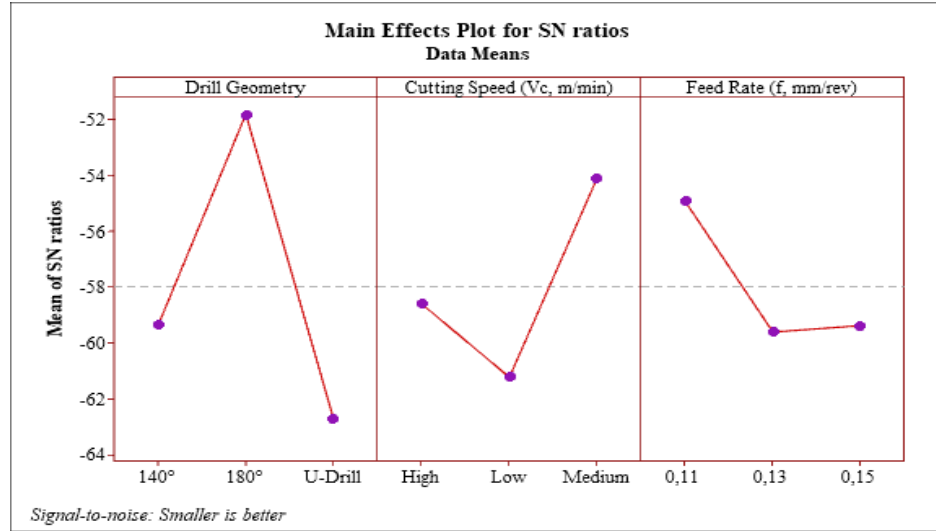
Figure 3. Effect of essential parameters Fz (N) S/N Ratio.

The analysis indicates that the 180° drill geometry achieves the highest S/N ratio, highlighting its superior performance in minimizing variability in torque (M). A medium cutting speed is optimal, yielding the best S/N ratio and effectively reducing variability. Additionally, a feed rate of 0.11 mm/rev results in the highest S/N ratio, demonstrating its efficacy in minimizing torque variability (Figure 4).
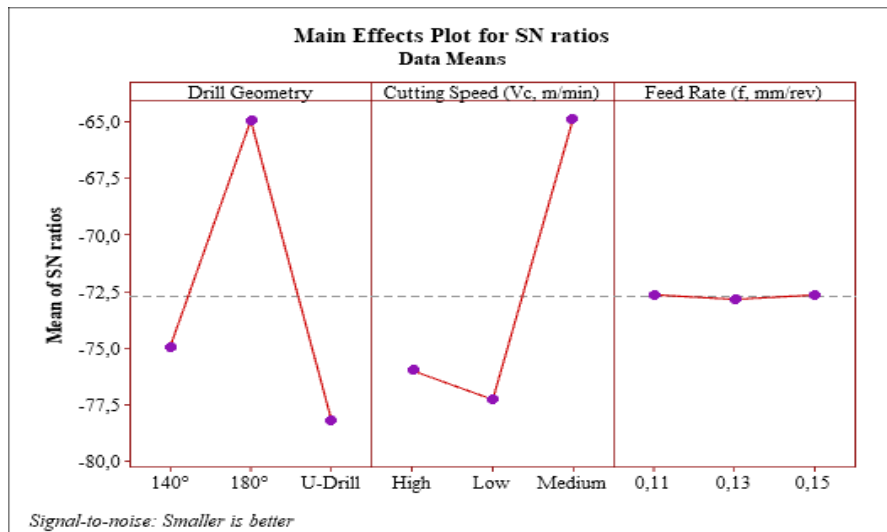
Figure 4. Effect of essential parameters M (N.cm) S/N Ratio.

3.3. Taguchi Analysis of Hole Diameter Deviation (mm), Center Distance Difference (mm), Ovality Deviation (mm) and Parallelism Deviation (%)

The Taguchi analysis was conducted to evaluate the impact of various factors on four critical dimensional parameters in the manufacturing process: hole diameter deviation (mm), center distance difference (mm),

ovality deviation (mm), and parallelism deviation (%). This robust design methodology aims to optimize process parameters while minimizing variability in the output. Table 5 presents the signal-to-noise (S/N) ratios for these parameters, which are crucial indicators of process stability and product quality. The S/N ratios, calculated using Taguchi's "smaller-is-better" characteristic, provide valuable insights into the relative influence of each factor on the respective deviations. By analyzing these S/N values, it becomes possible to identify the optimal combination of process parameters that simultaneously minimizes all four types of deviations, thereby enhancing the overall quality and precision of the manufactured components.

Table 5. Hole Diameter Deviation (HDD) (mm), Center Distance Difference (CDD) (mm), Ovality Deviation (OD) (mm) and Parallelism Deviation (PD) (%) results

Experiment no.	HDD (mm)	CDD (mm)	OD (mm)	PD (%)	SNRA3	SNRA4	SNRA5	SNRA6
1.	0.110	31	21	5	19.1721	-29.827	-26.444	-13.979
2.	0.099	36	26	6	20.0873	-31.126	-28.299	-15.563
3.	0.145	197	36	8	16.7726	-45.889	-31.126	-18.061
4.	0.175	36	26	6	15.1392	-31.126	-28.299	-15.563
5.	0.135	136	26	6	17.3933	-42.670	-28.299	-15.563
6.	0.109	36	26	6	19.2515	-31.126	-28.299	-15.563
7.	0.105	36	26	6	19.5762	-31.126	-28.299	-15.563
8.	0.107	36	26	6	19.4123	-31.126	-28.299	-15.563
9.	0.109	36	26	6	19.2515	-31.126	-28.299	-15.563
10.	0.105	36	26	6	19.5762	-31.126	-28.299	-15.563
11.	0.107	36	26	6	19.4123	-31.126	-28.299	-15.563
12.	0.109	36	26	6	19.2515	-31.126	-28.299	-15.563
13.	0.112	36	26	6	19.0156	-31.126	-28.299	-15.563
14.	0.112	36	26	6	19.0156	-31.126	-28.299	-15.563
15.	0.112	36	26	6	19.0156	-31.126	-28.299	-15.563
16.	0.107	36	26	6	19.4123	-31.126	-28.299	-15.563
17.	0.107	36	26	6	19.4123	-31.126	-28.299	-15.563
18.	0.107	36	26	6	19.4123	-31.126	-28.299	-15.563
19.	0.092	36	26	6	20.7242	-31.126	-28.299	-15.563
20.	0.092	36	26	6	20.7242	-31.126	-28.299	-15.563
21.	0.092	36	26	6	20.7242	-31.126	-28.299	-15.563
22.	0.092	36	26	6	20.7242	-31.126	-28.299	-15.563
23.	0.092	36	26	6	20.7242	-31.126	-28.299	-15.563
24.	0.092	36	26	6	20.7242	-31.126	-28.299	-15.563
25.	0.092	36	26	6	20.7242	-31.126	-28.299	-15.563
26.	0.092	36	26	6	20.7242	-31.126	-28.299	-15.563
27.	0.092	36	26	6	20.7242	-31.126	-28.299	-15.563

The analysis shows (in Figure 5) that the 140° drill geometry achieves the highest S/N ratio, indicating its superior performance in minimizing hole diameter deviation. A high cutting speed is optimal, yielding the best S/N ratio and effectively reducing variability. Additionally, a feed rate of 0.13 mm/rev results in the highest S/N ratio, demonstrating its efficacy in minimizing hole diameter deviation.

The analysis in Figure 6 indicates that the 140° drill geometry achieves the highest S/N ratio, highlighting its superior performance in minimizing center distance difference. A high cutting speed is optimal, yielding the best S/N ratio and effectively reducing variability. Additionally, a feed rate of 0.11 mm/rev results in the highest S/N ratio, demonstrating its efficacy in minimizing center distance difference.

The analysis shows (in Figure 7) that the 140° drill geometry achieves the highest S/N ratio, indicating its superior performance in minimizing ovality deviation. A medium cutting speed is optimal, yielding the best S/N ratio and effectively reducing variability. Additionally, a feed rate of 0.11 mm/rev results in the highest S/N ratio, demonstrating its efficacy in minimizing ovality deviation.

The analysis shows in Figure 8 that the 140° drill geometry achieves the highest S/N ratio, indicating its superior performance in minimizing parallelism deviation. A medium cutting speed is optimal, yielding the best S/N ratio and effectively reducing variability. Additionally, a feed rate of 0.11 mm/rev results in the highest S/N ratio, demonstrating its efficacy in minimizing parallelism deviation.
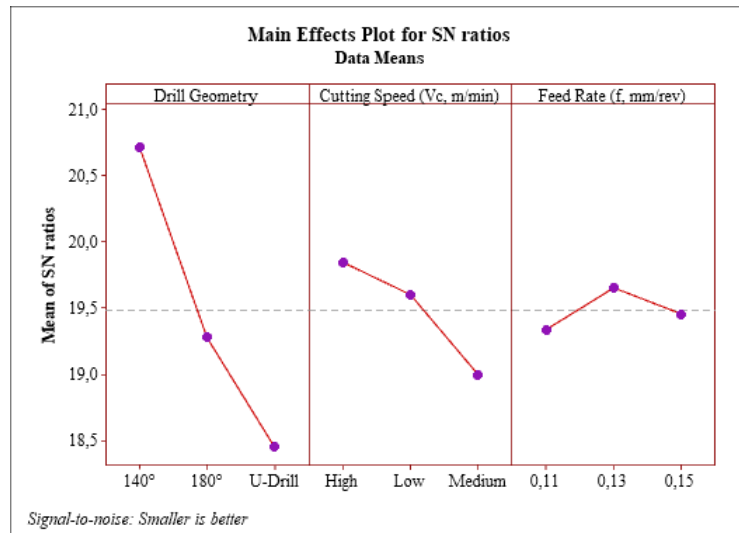
Figure 5. Effect of essential parameters of hole diameter deviation S/N ratio.
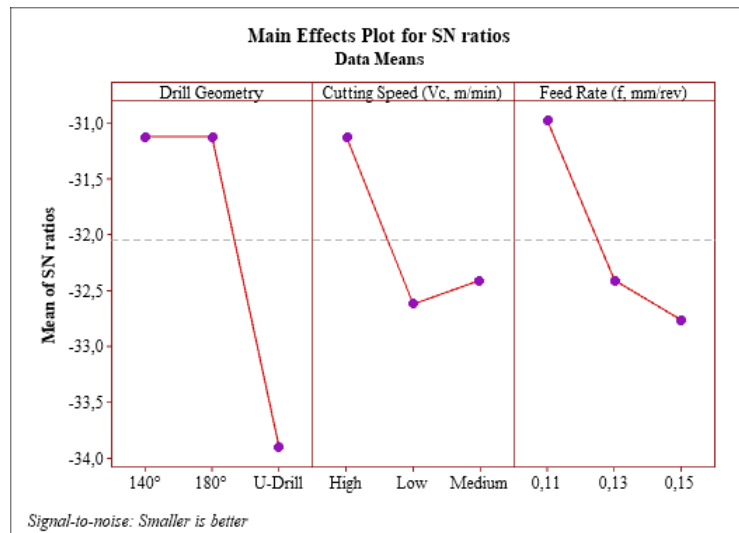

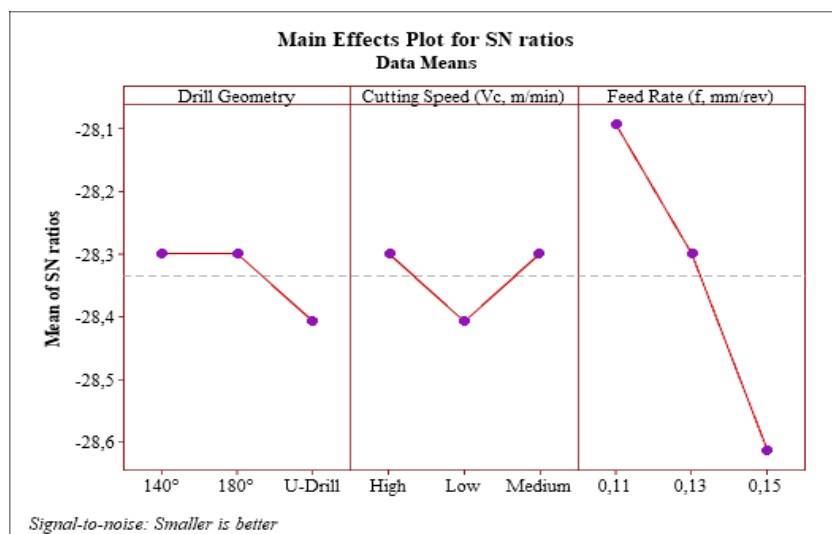Figure 6. Effect of essential parameters center distance difference S/N ratio.

Figure 7. Effect of essential parameters ovality deviation S/N ratio.

3.4. Analysis of variance

The ANOVA results in Table 6 indicate that drill geometry is the most significant factor affecting the variance, contributing 45.90% to the total variance with a highly significant F-value of 17.36 (p = 0.000). Cutting speed also plays a notable role, contributing 12.89% with an F-value of 4.88 (p = 0.019). The feed rate contributes 14.78% to the variance, with an F-value of 5.59 (p = 0.012). The error accounts for 26.44% of the total variance. These findings highlight the critical influence of drill geometry on the process, followed by feed rate and cutting speed, in determining the overall.
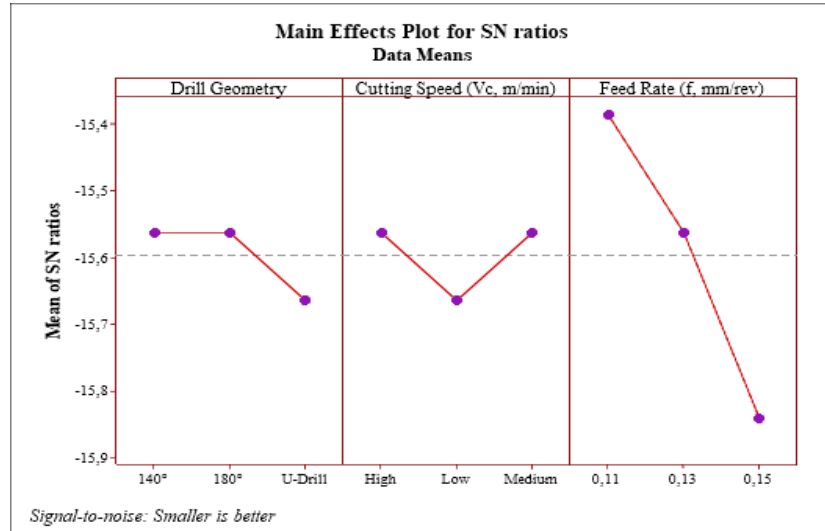
Figure 8. Effect of essential parameters parallelism deviation (%) S/N ratio.

Table 6. Fz variance analysis results.

Source	DF	Adj SS	Adj MS	F	P	Contribution (%)
Drill Geometry	2	2372874	1186437	17.36	0.000	45.8972223
Cutting Speed (Vc, m/min)	2	666383	333191	4.88	0.019	12.889487
Feed Rate (f, mm/rev)	2	763921	381960	5.59	0.012	14.776112
Error	20	1366795	68340			26.4371787
Total	26	5169973				100

ANOVA results in Table 7 demonstrate that drill geometry significantly influences the variance, contributing 31.65% with an F-value of 6.43 (p = 0.007). Cutting speed also has a notable impact, contributing 19.03% with an F-value of 3.97 (p = 0.038). The feed rate shows minimal influence, contributing only 0.12% with an F-value of 0.03 (p = 0.975). The error accounts for 49.20% of the total variance. These results underscore the importance of optimizing drill geometry and cutting speed to enhance performance.

Table 7. M variance analysis results

Source	DF	Adj SS	Adj MS	F	P	Contribution (%)
Drill Geometry	2	54731509	27365754	6.43	0.007	31.6533841
Cutting Speed (Vc, m/min)	2	32896988	16448494	3.87	0.038	19.0256219
Feed Rate (f, mm/rev)	2	214333	107167	0.03	0.975	0.1239572
Error	20	85066040	4253302			49.1970363
Total	26	172908871				100

The ANOVA results in Table 8 reveal that drill geometry is the most significant factor affecting hole diameter deviation, contributing 43.71% to the total variance with a highly significant F-value of 9.38 (p = 0.001). Cutting speed contributes 8.30% with an F-value of 1.78 (p = 0.194), while the feed rate has a

minimal impact, contributing only 1.36% with an F-value of 0.29 (p = 0.750). The error accounts for 46.62% of the total variance. These findings emphasize the critical role of drill geometry in controlling hole diameter deviation.

Table 8 Hole diameter deviation variance analysis results

Source	DF	Adj SS	Adj MS	F	P	Contribution (%)
Drill Geometry	2	0.003952	0.001976	9.38	0.001	43.7119788
Cutting Speed (Vc, m/min)	2	0.000750	0.000375	1.78	0.194	8.29554253
Feed Rate (f, mm/rev)	2	0.000123	0.000061	0.29	0.750	1.36046897
Error	20	0.004215	0.000211			46.620949
Total	26	0.009041				100

The ANOVA results in Table 9 indicate that drill geometry contributes 14.48% to the variance in center distance difference, with an F-value of 1.89 (p = 0.177). Cutting speed contributes 4.14% with an F-value of 0.54 (p = 0.591), and feed rate contributes 4.67% with an F-value of 0.61 (p = 0.553). The error accounts for 76.70% of the total variance. These results suggest that while drill geometry has some influence, the majority of the variance is attributed to error, indicating potential variability in the process.

Table 9. Center distance difference variance analysis results

Source	DF	Adj SS	Adj MS	F	P	Contribution (%)
Drill Geometry	2	4855	2427.3	1.89	0.177	14.4843223
Cutting Speed (Vc, m/min)	2	1388	693.9	0.54	0.591	4.14093499
Feed Rate (f, mm/rev)	2	1567	783.4	0.61	0.553	4.67496047
Error	20	25710	1285.5			76.7027656
Total	26	33519				100

The ANOVA results in Table 10 show that feed rate is the most influential factor on ovality deviation, contributing 7.49% to the variance with an F-value of 1.21 (p = 0.320). Drill geometry and cutting speed each contribute 1.08% with an F-value of 0.17 (p = 0.843). The error accounts for 90.43% of the total variance. These findings suggest that feed rate has a minor impact, while most of the variance is due to error.

Table 10. Ovality deviation variance analysis results

Source	DF	Adj SS	Adj MS	F	P
Drill Geometry	2	1.852	0.9259	0.17	0.843
Cutting Speed (Vc, m/min)	2	1.852	0.9259	0.17	0.843
Feed Rate (f, mm/rev)	2	12.963	6.4815	1.21	0.320
Error	20	107.407	5.3704		
Total	26	172908871			

The ANOVA results in Table 11 indicate that feed rate is the most significant factor affecting parallelism deviation, contributing 10.44% to the variance with an F-value of 1.21 (p = 0.320). Drill geometry and cutting speed each contribute 1.49% with an F-value of 0.17 (p = 0.843). The error accounts for 86.58% of the total variance. These results highlight that feed rate has a slight influence, with the majority of the variance attributed to error.

A more in-depth analysis of the ANOVA results reveals the nuanced impact of each factor on the drilling process outcomes. For thrust force (Fz), drill geometry emerged as the most influential factor, with a remarkably high F-value of 17.36 (p = 0.000), accounting for 45.90% of the total variance. This substantial effect size, as indicated by the partial eta squared ($\eta^2 p$) of 0.459, underscores the critical role of drill geometry in optimizing thrust force. Cutting speed and feed rate also demonstrated significant effects, with F-values of 4.88 (p = 0.019) and 5.59 (p = 0.012), respectively. Their contributions to the variance were

12.89% ($\eta^2 p = 0.129$) for cutting speed and 14.78% ($\eta^2 p = 0.148$) for feed rate, indicating moderate but meaningful influences on thrust force variability.

Table 11. Parallelism deviation (%) variance analysis results

Source	DF	Adj SS	Adj MS	F	P
Drill Geometry	2	0.07407	0.03704	0.17	0.843
Cutting Speed (Vc, m/min)	2	0.07407	0.03704	0.17	0.843
Feed Rate (f, mm/rev)	2	0.51852	0.25926	1.21	0.320
Error	20	4.29630	0.21481		
Total	26	4.96296			

In the case of torque (M), drill geometry again exhibited the strongest effect, with an F-value of 6.43 (p = 0.007), explaining 31.65% of the variance ($\eta^2 p = 0.317$). Cutting speed showed a notable impact with an F-value of 3.87 (p = 0.038), contributing 19.03% to the variance ($\eta^2 p = 0.190$). Interestingly, the feed rate's influence on torque was minimal, with a negligible F-value of 0.03 (p = 0.975) and a contribution of merely 0.12% to the variance ($\eta^2 p = 0.001$).

For hole diameter deviation, drill geometry once more demonstrated its paramount importance, with an F-value of 9.38 (p = 0.001), accounting for 43.71% of the total variance ($\eta^2 p = 0.437$). The effects of cutting speed and feed rate were less pronounced in this case, with F-values of 1.78 (p = 0.194) and 0.29 (p = 0.750), respectively, contributing 8.30% ($\eta^2 p = 0.083$) and 1.36% ($\eta^2 p = 0.014$) to the variance.

These detailed ANOVA results elucidate the hierarchical influence of drilling parameters, with drill geometry consistently emerging as the most critical factor across multiple outcome measures. The varying effect sizes and significance levels for cutting speed and feed rate across different outcomes highlight the complex interplay of these factors in the drilling process, emphasizing the need for careful optimization strategies tailored to specific performance metrics.

3.5. Regression Analysis

In machining processes, regression analysis is employed to examine and establish the relationship between process parameters and their outcomes [28]. The thrust force (Fz) during drilling operations was modeled using multiple linear regression analysis. The regression equation, incorporating the effects of drill geometry (DG), cutting speed (CS), and feed rate (FR). The regression model derived from this study is presented below (Eq.1):

$$Fz = \beta_0 + \beta_1(DG) + \beta_2(CS) + \beta_3(FR) + \varepsilon \tag{1}$$

Where:
- Fz is the thrust force in Newtons (N)
- β_0 is the intercept (baseline thrust force)
- β_1, β_2, β_3 are the regression coefficients for drill geometry, cutting speed, and feed rate, respectively
- ε is the error term

The fitted regression model is (Eq.2):

$$Fz = 767 + \beta_1(DG) + \beta_2(CS) + \beta_3(FR) + \varepsilon \tag{2}$$

The coefficients for each factor level are as follows (Table 12):

Table 12. Coefficeints level of drilling parameters for Fz.

Drill Geometry (DG)	Cutting Speed (CS)	Feed Rate (FR)
140°: $\beta_1 = 0$ (reference level)	High: $\beta_2 = 0$ (reference level)	0.11 mm/rev: $\beta_3 = 0$ (reference level)
180°: $\beta_1 = -327$	Medium: $\beta_2 = -239$	0.13 mm/rev: $\beta_3 = +376$
U-Drill: $\beta_1 = +398$	Low: $\beta_2 = +142$	0.15 mm/rev: $\beta_3 = +334$

This regression model allows for the prediction of thrust force based on the selected drilling parameters. The coefficients indicate the change in thrust force relative to the reference level for each factor. For instance, using a 180° drill geometry is expected to decrease the thrust force by 327 N compared to the 140° geometry, while the U-Drill is expected to increase it by 398 N. The model's intercept ($\beta_0 = 767$ N) represents the baseline thrust force when all factors are at their reference levels (140° drill geometry, high cutting speed, and 0.11 mm/rev feed rate). The inclusion of the error term (ε) acknowledges that the model may not account for all sources of variation in thrust force. Similarly, the torque (M) during drilling operations was modeled using multiple linear regression analysis. The regression equation for torque, incorporating the effects of drill geometry (DG), cutting speed (CS), and feed rate (FR), is expressed as follows (Eq.3):

$$M = \beta_0 + \beta_1(DG) + \beta_2(CS) + \beta_3(FR) + \varepsilon \tag{3}$$

Where:
- M is the torque in Newton-centimeters (N.cm)
- β_0 is the intercept (baseline torque)
- β_1, β_2, β_3 are the regression coefficients for drill geometry, cutting speed, and feed rate, respectively
- ε is the error term

The fitted regression model for torque is(Eq.4):

$$M = 5746 + \beta_1(DG) + \beta_2(CS) + \beta_3(FR) + \varepsilon \tag{4}$$

The coefficients for each factor level are as follows (Table 13):

Table 13. Coefficeints level of drilling parameters for M.

Drill Geometry (DG)	Cutting Speed (CS)	Feed Rate (FR)
140°: $\beta_1 = 0$ (reference level)	High: $\beta_2 = 0$ (reference level)	0.11 mm/rev: $\beta_3 = 0$ (reference level)
180°: $\beta_1 = -782$	Medium: $\beta_2 = -1649$	0.13 mm/rev: $\beta_3 = +192$
U-Drill: $\beta_1 = +2552$	Low: $\beta_2 = +1032$	0.15 mm/rev: $\beta_3 = +5$

This regression model allows for the prediction of torque based on the selected drilling parameters. The coefficients indicate the change in torque relative to the reference level for each factor. For example, using a 180° drill geometry is expected to decrease the torque by 782 N.cm compared to the 140° geometry, while the U-Drill is expected to increase it by 2552 N.cm. The model's intercept ($\beta_0 = 5746$ N.cm) represents the baseline torque when all factors are at their reference levels (140° drill geometry, high cutting speed, and 0.11 mm/rev feed rate). As with the thrust force model, the inclusion of the error term (ε) acknowledges that the model may not account for all sources of variation in torque. Comparing the two models, we can observe that the factors affect thrust force and torque differently. For instance, while the U-Drill geometry increases both thrust force and torque, its effect on torque (2552 N.cm increase) is proportionally larger than its effect on thrust force (398 N increase). This highlights the importance of considering multiple performance metrics when optimizing drilling parameters.

3.6. Enhanced Statistical Analysis

The Taguchi method and ANOVA employed in this study have facilitated a profound examination of the effects of various parameters in the drilling process of AISI 1050 steel. In this section, we delve further into the statistical significance of the obtained results and the impact of each parameter on variance.

The ANOVA results demonstrate that the influence of drill geometry on thrust force (Fz) is highly significant ($F = 17.36$, $p = 0.000$). This parameter accounts for 45.90% of the total variance, indicating that optimizing drill geometry may considerably enhance drilling performance. Cutting speed ($F = 4.88$, $p = 0.019$) and feed rate ($F = 5.59$, $p = 0.012$) also exhibit statistically significant effects, explaining 12.89% and 14.78% of the variance, respectively. These results emphasize the critical importance of jointly optimizing these three parameters for effective thrust force control. For torque (M), ANOVA analysis again identifies drill geometry as the most influential factor ($F = 6.43$, $p = 0.007$), accounting for 31.65% of the total variance. The influence of cutting speed is also significant ($F = 3.87$, $p = 0.038$), explaining 19.03% of the variance. These findings underscore the importance of optimizing drill geometry and cutting speed in torque control. The relative impact of various drilling parameters on thrust force (Fz) and torque (M) is visually represented in Figure 10.

In the analysis of hole diameter deviation, the effect of drill geometry is once more prominent (F = 9.38, p = 0.001), explaining 43.71% of the total variance. This result highlights the critical importance of selecting appropriate drill geometry in precision drilling operations. Signal-to-noise (S/N) ratio analyses obtained via the Taguchi method corroborate these ANOVA results. For example, the 180° drill geometry exhibited the highest S/N ratios for both thrust force and torque, indicating its effectiveness in minimizing variability for these parameters. Similarly, the 140° drill geometry achieved the highest S/N ratios for hole quality parameters, demonstrating its superiority in optimizing hole quality.

This enhanced statistical analysis underscores the significance of a multifactorial approach in the optimization of drilling parameters. Understanding the interactive effects of drill geometry, cutting speed, and feed rate is crucial for optimizing both cutting forces and hole quality in the drilling of AISI 1050 steel. These findings provide valuable guidance for improving the efficiency and quality of drilling operations in industrial applications.
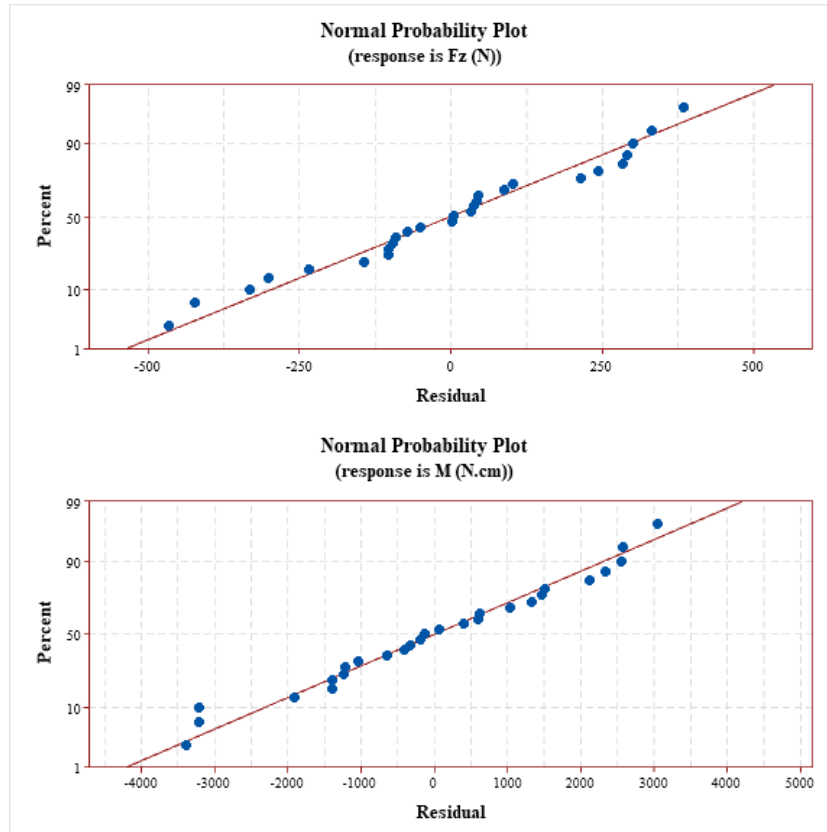

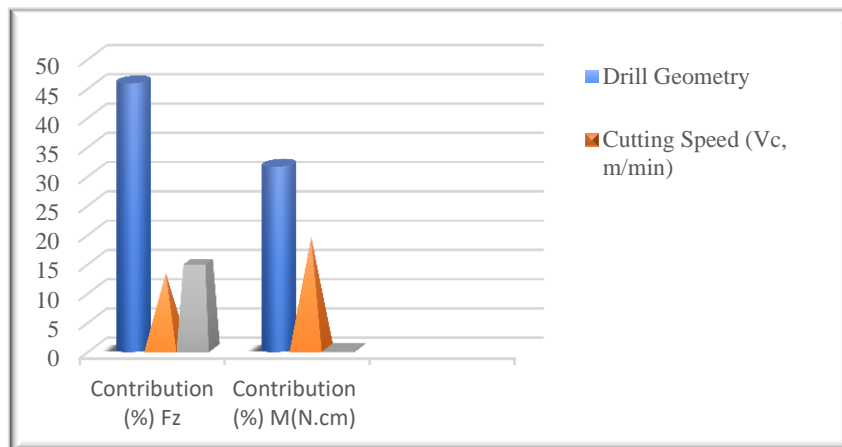Figure 9. Normal probability plots of residuals for (a) Fz and (b) M.

Figure 10. Contribution of drilling parameters on Fz and M

3.7. Discussion

The experimental investigation into the drilling parameters of AISI 1050 steel has yielded critical insights into the interplay between drill geometry, cutting speed, and feed rate, particularly concerning thrust force, torque, and hole quality. The findings align with existing literature, underscoring the importance of these parameters in enhancing drilling performance.

The study identifies drill geometry as the most significant factor influencing thrust force, torque, and hole diameter deviation. Specifically, the 180° drill geometry exhibited superior performance in minimizing thrust force and torque variability. This observation is consistent with the work that highlighted the pivotal role of cutting tool geometry in drilling operations [29, 30]. Conversely, the 140° drill geometry proved optimal for minimizing hole diameter deviation, corroborating the findings of Rajendra Singh et al. and Fernández-Pérez et al., who emphasized the influence of tool geometry on dimensional accuracy [31, 32].

In terms of cutting speed, the study found that medium cutting speeds were generally optimal for reducing variability in thrust force and torque. This conclusion is supported by Ellenberger et al. (2022) and Scarano et al., 2020, who reported significant impacts of cutting speed on drilling performance and surface quality. The results suggest that medium cutting speeds strike a balance between efficient material removal and minimal thermal damage, thereby enhancing overall drilling performance [33, 34].

The investigation also revealed that a feed rate of 0.11 mm/rev was most effective in minimizing thrust force and torque variability. This finding aligns with the research conducted by Maleki et al., who identified feed rate as a crucial parameter in optimizing drilling processes [35]. Lower feed rates contribute to maintaining stability during drilling, which reduces the likelihood of tool deflection and improves hole quality.

Drill geometry was found to significantly influence hole diameter deviation, accounting for a substantial portion of the total variance. This finding is consistent with the observations of Fernández-Pérez et al., who reported the importance of process parameters in achieving dimensional accuracy and surface quality in drilled holes [31]. The results emphasize the necessity of selecting appropriate drill geometries to ensure high-quality outcome.

The analysis of variance (ANOVA) conducted in this study revealed that drill geometry, cutting speed, and feed rate exert varying degrees of influence on different aspects of the drilling process. This multi-factorial influence is corroborated by the findings of Hale & Ng, who employed statistical analyses to explore the complex interplay of drilling parameters [36]. The ANOVA results underscore the importance of a comprehensive approach to parameter optimization, considering the interactions between different factors to achieve optimal drilling performance.

4. CONCLUSIONS

In this study, the experimental investigation into the drilling parameters of AISI 1050 steel has illuminated the critical impact various factors have on cutting forces and hole quality. A systematic analysis was conducted to understand how drill geometry, cutting speed, and feed rate affect drilling efficacy and efficiency. The impact of drill geometry on thrust force and torque was unmistakable. Specifically, a drill with a 180° geometry was found to maximize the signal-to-noise ratio for thrust force, validating its use as a key influence on cutting efficiency. Mid-range cutting speeds emerged as optimal, reflecting a balance between performance and stability, while a feed rate of 0.11 mm/rev proved effective in achieving minimal variability in thrust force. Regarding the quality of drilled holes, parameters such as hole diameter deviation, centering accuracy, ovality, and parallelism were assessed. The 140° drill geometry excelled, significantly minimizing diameter deviations. This finding highlights the need for precise control of both geometry and cutting conditions—high cutting speeds and a feed rate of 0.13 mm/rev were found to yield the best results, ensuring high-quality hole production. The statistical analysis underscored the predominance of drill geometry in affecting thrust force variability, contributing nearly half of the observed variation and reaffirming its statistical significance. Contributions from cutting speed and feed rate, though less pronounced, were still substantial, indicating their role in refining the drilling process. For torque considerations, drill geometry maintained its critical role, emphasizing the necessity of selecting optimal geometries alongside suitable cutting speeds for effective drilling. Similarly, deviations in hole diameter due to drill geometry were significant, underscoring the pressing need for exacting tool geometry to maintain dimensional precision. Finally, feed rate was identified as a strong influencer in managing parallelism deviations, highlighting the importance of accurately controlling operational parameters to ensure quality. Thus, the outcomes of this study contribute significantly to our understanding of the dynamics involved in drilling operations.

In summary, this research offers a thorough understanding of the interdependencies between various drilling parameters and their combined effects on cutting forces and hole quality in AISI 1050 steel. The insights provided herein are invaluable for optimizing drilling practices, enhancing both performance and quality in industrial applications.

REFERENCES

[1]   G. Kannan, R. Thangaraju, Effect of industrial waste fly ash on the drilling characteristics of banana fiber residue reinforced polymer composites, Journal of Industrial Textiles, 51(2), (2022) 2665-2687.

[2]   M.F. Ghazali, et al., Tool wear and surface evaluation in drilling fly ash geopolymer using HSS, HSS-Co, and HSS-TiN cutting tools, Materials, 14(7), 2021, 1628.

[3]   R. Pramod, S. Basavarajappa, G.B.V. Kumar, Investigation on surface roughness of drilled holes in nanoparticle filled polymer matrix composites, Advances in Science and Technology, 105 (2021) 68-76.

[4]   K. Giasin, et al., Evaluation of the Surface Defects and Dimensional Tolerances in Multi-Hole Drilling of AA5083, AA6061, and AA2024. Applied Sciences, 11(9), 2021, 4285.

[5]   N.K. Kamble, V.S. Jatti, Optimization of drilling process parameter during of drilling of AISI 317L stainless steel, Engineering Research Express, 1(2), 2019, 025021.

[6]   N. Mandal, S. Hloch, and A.K. Das, Comparison of maraging steel surface integrity in hybrid and conventional micro-ecdm processes, Materials, 15(13), 2022, 4378.

[7]   D. Deepak, B.V. Rajendra, The effect of process parameters on material removal rate in drilling of Al 6061-SiC composite, Matec Web of Conferences, 144, 2018, 03009.

[8]   S. Juneja, et al., Impact of process variables of acetone vapor jet drilling on surface roughness and circularity of 3D-printed ABS parts: Fabrication and Studies on Thermal, Morphological, and Chemical Characterizations. Polymers, 14(7), 2022, 1367.

[9]   M. Yusof, H. Harun, R. Bahar, Experimental investigation of minimum quantity lubrication in meso-scale milling with varying tool diameter. IOP Conference Series Materials Science and Engineering, 290, 2018, 012035.

[10]   A. Mohammed, et al., Sustainable machining of Mg-9Al-1.4Zn foam used for temporary biomedical implant using cryogenic cooling, Materials, 15(19), 2022, 6678.

[11]   P. Saraswat, Experimental Investigation of Surface roughness and MRR in rotary-ultrasonic machining of float glass, Evergreen, 10(4), 2023, 2675-2682.

[12]   R. Sahoo, et al., Fabrication of micro-hole using novel maglev EDM, Journal of Micromanufacturing, 6(2), 2022, 141-150.

[13]   V.K. Singh, D. Joshi, P. Saraswat, A review on effect of process parameters on machining characteristics of rotary ultrasonic machine, Skit Research Journal, 10(2) 2020, 78.

[14]   P. Chaitanya, Optimization of hole quality parameters using TOPSIS method in drilling of GFRP composite. International Journal of Science and Research Archive, 9(2), 2023, 030-038.

[15]   M. Mudhukrishnan, et al., Optimization and sensitivity analysis of drilling parameters for sustainable machining of carbon fiber–reinforced polypropylene composites, Journal of Thermoplastic Composite Materials, 32(11), 2018, 1485-1508.

[16]   Zhou, H., et al., Experimental research on new hole-making method assisted with asynchronous mixed frequency vibration in TiBw/TC4 composites, The International Journal of Advanced Manufacturing Technology, 125(1-2), 2022, 543-561.

[17]   R. Shanmugam, et al., Machining temperature, surface integrity and burr size investigation during coolant-free hole milling in Ti6Al4V titanium alloy, Lubricants, 11(8), 2023, 349.

[18]   J.U. Prakash, et al., Optimization of machining parameters in drilling of LM6/ C/Fly ash hybrid composites. Manufacturing Review, 9, 2022, 28.

[19]   H.A Al-Tameemi, et al., Evaluation of cutting-tool coating on the surface roughness and hole dimensional tolerances during drilling of Al6061-T651 alloy, Materials 14(7), 2021, 1783.

[20]   J.M. Susai, B.H. Sai, D. Dinakaran, Prediction and geometric adaptive control of surface roughness in drilling process. Fme Transaction, 47(3), 2019, 424-429.

[21]   İ.B. Şahin, Urtekin, L., Genç, A., Özerkan, H. B., Optımızatıon of machining parameters for boron alloy steel by plunge electro erosion by taguchi technique, Journal of Scientific Reports-A, 50, (2022), 169-180.

[22]   K.L. Kala, K.P. Rao, Experimental investigation on drilling of fiber metal laminates using grey based taguchi approach. Journal of Mines Metals and Fuels, 2022, 200-206.

[23]   J.S.S. Babu, M. Heo, C.G. Kang, Study of machining parameter optimization in drilling of magnesium based hybrid composites reinforced with SiC/CNT, Key Engineering Materials, 846, 2020, 42-46.

[24]   C.L.Tan, A.I. Azmi, N. Muhammad, Surface roughness analysis of carbon/glass hybrid polymer composites in drilling process based on taguchi and response surface methodology, Advanced Materials Research, 1119, 2015, 622-627.

[25]   M. Aamir, et al., Optimization and modeling of process parameters in multi-hole simultaneous drilling using taguchi method and fuzzy logic approach. Materials, 13(3), 2020, 680.

[26] S. Arunachalam, S. Perumal, Investigation of effect of graphite particles on drillability of metal matrix composite, Materials Science, 22(3), 2016, 390-396.

[27] Ç. Bolat, Effect of drilling parameters and tool geometry on the thrust force and surface roughness of aerospace grade laminate composites. Micromachines 14 (7), (2023), 1427.

[28] R.J. Brook, G.C. Arnold, Applied regression analysis and experimental design, 2018: CRC Press.

[29] V. Alevizakos, R. Mosch, C.V. See, Influence of multiple used implant drills on their cutting performance and fracture resistance, Materials, 16(15), 2023, 5271.

[30] M.G. Fard, H. Baseri, A. Zolfaghari, Experimental Investigation of the effective parameters and performance of different types of structural tools in drilling CFRP/AL alloy stacks, Journal of Composite Materials, 56(29), 2022, 4461-4471.

[31] J. Fernández-Pérez, et al., Hybrid composite-metal stack drilling with different minimum quantity lubrication levels. Materials, 12(3), 2019, 448.

[32] H. Singh, B. Dewangan, P.K. Jain, Experimental study on drilling characteristics of the hybrid sisal–jute fibre epoxy composites, Journal of Micromanufacturing, 4(2), 2021, 157-168.

[33] A. Ellenberger, et al., Drilling of natural fiber-reinforced based polyurethane foam composite. Journal of Composite Materials, 56(6), 2022, 899-909.

[34] A. Scarano, F. Lorusso, S. Noumbissi, Infrared thermographic evaluation of temperature modifications induced during implant site preparation with steel vs. zirconia implant drill, Journal of Clinical Medicine, 9(1), 2020, 148.

[35] H.R. Maleki, et al., Experimental study on drilling of jute fiber reinforced polymer composites, Journal of Composite Materials, 53(3), 2018, 283-295.

[36] P. Hale, E. Ng, 3D Finite element model on drilling of CFRP with numerical optimization and experimental validation, Materials, 14(5), 2021, 1161.

Manufacturing Technologies and Applications
MATECA

Optimization of the Effect of Processing Parameters on Boring Torque in Boring of 1.2738 Material by Using Response Surface Method

Aslan Akdulum[1,*] , Mehmet Süzgünol[2] , Yunus Kayır[3]

¹ Hacettepe Üniversitesi, Başkent OSB Meslek Yüksekokulu, Makine ve Metal Teknolojileri Bölümü, Ankara, Türkiye

² Yeşilevler Mesleki ve Teknik Anadolu Lisesi, Adana, Türkiye

³ Gazi Üniversitesi, Teknoloji Fakültesi, İmalat Mühendisliği Bölümü, Ankara, Türkiye

ABSTRACT

1.2738 material is used extensively in the mold industry because it offers long-lasting use due to its high polishability. Quality holes are needed for long-lasting molds. Quality holes can mostly be obtained through boring operations. In addition, the boring operation is heavily preferred in the machining of engine cylinder bores in the automotive industry. However, due to limitations such as working in a hole, a long and thin boring bar, dynamic rigidities, geometric deviations, increased cutting forces, and poor surface quality may occur. To overcome these disadvantages, optimization of processing parameters is required. This study aims to investigate the effect of processing parameters on the cutting torque occurring in the boring process of workpieces produced from 1.2738 material and to optimize it by using the response surface method. The Taguchi L36 experimental design method was used to reduce the number of experiments. A two-factor interactive (2FI) model was proposed, and the R² value of the model was calculated as 0.9456, while the standard deviation value was calculated as 10.68. It was determined that the parameters that have the most significant effect on the cutting torque are the radial depth of cut and the feed rate. High agreement was achieved between the experimental results and the values predicted by the model, and important findings were obtained for optimizing the cutting torque in machining processes.

Keywords: Regression analysis, Response surface method Taguchi, Optimization, Boring torque

1.2738 Malzemesinin Baralanmasında İşleme Parametrelerinin Baralama Torkuna Etkisinin Yanıt Yüzey Yöntemi ile Optimizasyonu

ÖZET

1.2738 malzemesi, yüksek parlatılabilme özelliği dolayısıyla uzun ömürlü kullanım imkânı sunduğu için kalıp sektöründe yoğun bir şekilde kullanılmaktadır. Uzun ömürlü kalıplar için kaliteli deliklere ihtiyaç bulunmaktadır. Kaliteli delikler ise çoğunlukla baralama operasyonları ile elde edilebilmektedir. Ayrıca otomotiv sektöründe motor silindir yuvalarının işlenmesinde baralama operasyonu yoğun bir şekilde tercih edilmektedir. Ancak delik içinde çalışma, bara çubuğunun uzun ve ince olması, dinamik rijitsizlikler gibi kısıtlılıklardan dolayı geometrik sapmalar, kesme kuvvetlerinde artış ve kötü yüzey kalitesi meydana gelebilmektedir. Bu olumsuzlukların üstesinden gelmek için işleme parametrelerinin optimizasyonu gerekmektedir. Bu çalışmada, 1.2738 malzemesinden üretilen iş parçalarının baralanması işleminde meydana gelen kesme torku üzerinde işleme parametrelerinin etkisinin incelenmesini ve yanıt yüzey yöntemi ile optimizasyonunu amaçlamıştır. Deney sayısını azaltmak için Taguchi L36 deney tasarım yöntemi kullanılmıştır. İki faktör etkileşimli (2FI) model önerilmiş ve modelin R² değeri 0,9456 olarak hesaplanırken standart sapma değeri 10,68 olarak hesaplanmıştır. Kesme torku üzerinde en önemli etkiye sahip parametrelerin radyal kesme derinliği ve ilerleme miktarı olduğu belirlenmiştir. Deneysel sonuçlar ile modelin tahmin ettiği değerler arasında yüksek uyum sağlanmış ve talaşlı imalat süreçlerinde kesme torkunu optimize etmeye yönelik önemli bulgular elde edilmiştir.

Anahtar Kelimeler: Regresyon analizi, Yanıt yüzey yöntemi, Taguchi, Optimizasyon, Baralama torku

1. GİRİŞ

1.2738 malzemesi, dış katmandan çekirdeğine kadar mükemmel bir sertlik dengesi göstererek nitrasyona ve krom kaplamaya müsait, parlatılabilme özelliği oldukça iyi olan plastik kalıp çeliğidir [1]. Plastik kalıp çeliği sektöründe en yoğun kullanılan malzemelerden biridir [2]. Plastik ürünlerin kullanımının artmasıyla birlikte, plastik enjeksiyon kalıplarına olan talep de giderek artmaktadır [3]. Ürün kalitesini sürekli olarak

---

yüksek tutmak için kalıpların yüksek tekrarlı çalışmaya dayanıklı ve uzun ömürlü olması gerektiğinden bu kalıplarda kaliteli delikler arzulanmaktadır [4]. Bu kaliteyi sağlamak için son işlem olarak baralama operasyonları uygulanmaktadır [5]. Otomotiv sektöründe özellikle motor bloğundaki silindir deliğinin genişletilmesinde baralama işlemi kritik bir rol oynamaktadır [6]. Brezilya'da yapılan bir çalışmada içten yanmalı motorların valf yuvalarının baralanması işleminin yılda yaklaşık 25 milyon kez yapıldığı, işlemin düzgün bir şekilde yapılmadığında ise yanma odasının sızdırmazlığının bozulduğu, bu durumunda güç kaybına ve daha fazla kirletici gaz emisyonuna neden olarak çevreye zarar verdiği ifade edilmiştir [7]. Dolayısıyla baralama operasyonlarının ve işleme parametrelerinin dikkatlice analiz edilerek optimizasyonu oldukça önemlidir.

İşleme merkezlerinde gerçekleştirilen baralama operasyonlarında nihai delik kalitesi bara takımları ile elde edilebilmektedir. Bu takımlar çeşitli yöntemler ile elde edilmiş deliklerin yüksek kalite ve dar tolerans aralıklarında işlenmesi amacıyla kullanılmaktadır [8]. Kesici takımın yeterince rijit olmaması, delik içinde çalışma, bara çubuğunun uzun ve ince olması, delik içine tek noktada temas gibi olumsuzluklardan dolayı çeşitli problemler ortaya çıkabilmektedir [9]. Bu problemlerin başında kötü yüzey kalitesi, geometrik sapmalar, dengesiz kuvvetler, tırlama ve kesici uç kırılması gelmektedir [8]. Bu problemlerin üstesinden gelebilmek için baralama parametrelerinin optimize edilmesi gerekmektedir [6]. Delik ekseni ve bara çubuğu ekseni birbirinden kaçık olduğu için merkezkaç kuvvetleri bu işlemde daha etkindir [10]. Tek noktada delik içi yüzeyine temas olduğu için en yüksek kesme kuvveti olarak kesme torku öne çıkmaktadır [11]. Dolayısıyla baralama torku üzerinde işleme parametrelerinin etkilerinin açığa çıkarılması arzulanan delik kalitesinin elde edilebilmesi açısından son derece önemlidir.

Dik işleme tezgahlarında baralama işleminin incelenmesi üzerine çeşitli çalışmalar yapılmıştır. Yapılan bir çalışmada kesici uç tipi, soğutma sıvısı, iş mili hızı ve ilerleme oranının deliklerin boyutsal tamlığı, daireselliği, silindirikliği ve yüzey kalitesi üzerindeki etkileri ele alınmıştır [12]. Kesme hızı, ilerleme miktarı ve kesme derinliğinin baralama sonucu elde edilen deliğin dikliğine etkileri deneysel olarak incelenmiştir [13]. Soğutma yöntemlerinin kesme kuvvetlerine, sıcaklığa ve takım aşınmasına etkileri araştırılmıştır [14]. Baralama işlemi sırasında meydana gelen titreşimler [15], dinamik kararlılık [16] ve form hataları [17] ile ilgili çeşitli araştırmalar bulunmaktadır. Kesme kuvvetlerinin radyal kesme derinliği, ilerleme miktarı ve takım geometrisi ile analitik olarak modellenmesi yapılmıştır [9, 18]. Ayrıca, baralama işlemi sonucunda deliğin boyutsal hataları üzerinde merkezkaç kuvvetlerinin etkisi incelenmiştir [10]. Lazer kılavuzlu sistemler kullanılarak delik derinliğine bağlı kesici uç sapması ve delik çapı sapması incelenmiştir [19]. Literatür incelendiğinde, baralama işlemi sırasında meydana gelen kesme torku üzerinde işleme parametrelerinin etkisi yeterince derinlemesine araştırılmamıştır. Oysa kesme torkundaki bir olumsuzluk geometrik sapmalara, yüzey pürüzlülüğünün artmasına ve titreşimlerin meydana gelmesine neden olarak delik kalitesinin olumsuz etkilenmesine neden olabilir. Bu nedenle kesme torkunun detaylı bir şekilde incelenerek optimizasyonu, işlem planlaması ve verimlilik açısından büyük önem taşımaktadır.

İşleme parametrelerinin optimizasyonu için çeşitli çalışmalarda Yanıt Yüzey Yöntemi (Response Surface Methodology, RSM) tercih edilmiştir. Bu yöntem, karmaşık sistemlerde bağımlı ve bağımsız değişkenler arasındaki ilişkileri modellemek ve optimize etmek için etkili bir araçtır [1]. Diğer optimizasyon yöntemlerine kıyasla etkili bir şekilde ikinci dereceden (kuadratik) modeller oluşturabilmesi nedeniyle avantajlıdır. Ayrıca, faktörler arasındaki etkileşimlerin kolaylıkla değerlendirilmesine olanak tanır ve süreç değişkenlerinin optimum kombinasyonlarını belirlemede yüksek doğruluk sağlar. Literatürde ses seviyesi ve yüzey pürüzlülüğü üzerinde kesme parametrelerinin etkilerinin incelenmesi amacıyla kullanılmıştır [1]. Diğer bir çalışmada esas kesme kuvvetlerinin incelenmesi amacıyla tercih edilmiştir [2]. Frezelemede meydana gelen yüzey pürüzlülüğünün araştırılması için uygulanmıştır [3].

Bu çalışmada, 1.2738 malzemesinin baralanması sürecinde işleme parametrelerinin baralama torku üzerindeki etkilerinin araştırılarak optimizasyonu için yanıt yüzey yönteminin kullanılması amaçlanmıştır. Literatürdeki önemli etkilerinden ve kesme süreci üzerindeki önemlerinden dolayı baralama parametreleri olarak radyal kesme derinliği, kesme hızı, kesici uç radüsü, ilerleme miktarı ve kaplama tipi belirlenmiştir. Baralama parametrelerinin etkileri yanıt yüzey yöntemi, ortalama etki grafiği, Taguchi ve Anova yöntemleri ile analiz edilmiştir. Kurulan matematiksel model ile regresyon eşitlikleri elde edilmiştir. Elde edilen sonuçların işlem planlaması, malzeme ve takım seçimi gibi aşamalarda kullanılabileceği öngörülmektedir.

2. MATERYAL VE YÖNTEM

Deneysel düzenek, 1.2738 malzemesinin dik işleme tezgahında baralanması ve bu işlem sırasında kesme torkunun gerçek zamanlı olarak ölçülmesi amacıyla oluşturulmuştur. 1.2738 malzemesine sahip iş parçası, 60 × 60 × 35 mm boyutlarında hazırlanmış ve deneylerde kullanılmıştır. İş parçasının kimyasal bileşimi ile

mekanik özellikleri Tablo 1'de sunulmuştur. Mekanik özellikler, çekme testi ve sertlik ölçümü ile elde edilmiş olup, her test üç kez tekrarlanarak ortalama değerler hesaplanmıştır.

Tablo 1. 1.2738 malzemesinin temel özellikleri.

Mekanik Özellikler		Kimyasal Bileşim, %	
Sertlik, Rockwell C	35.5 HRC	C	0.4
Uzama	%8.15	Mo	0.2
Akma dayanımı	807 MPa	Cr	1.9
Çekme dayanımı	975 MPa	Mn	1.5
		Si	0.3
		Ni	1.0
		Fe	Kalan

Taramalı elektron mikroskobu ile elde edilen mikroyapı, Şekil 1'de gösterilmiştir. Şekilde gösterilen yapın martenzittir. Baralama işlemine başlamadan önce, uygun radyal kesme derinliği sağlamak amacıyla farklı çaplarda normal helisel matkaplar kullanılarak delikler boydan boya delinmiştir. Daha sonra delik genişletme işlemi olarak bilinen baralama, deliklerin tamamı boyunca yukarıdan aşağı gerçekleştirilmiştir.
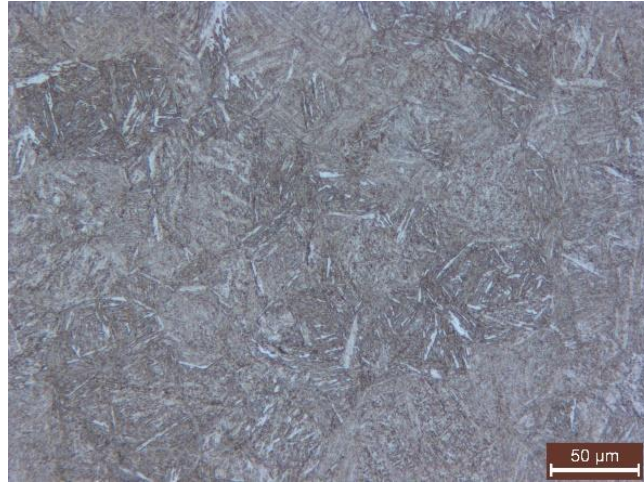
Şekil 1. 1.2738 malzemesinin mikroyapı görseli.

Bu çalışmada, deney tasarımı olarak Taguchi L36 (2^2 3^3) yöntemi kullanılmıştır. Taguchi yöntemi, daha az deneyle optimum kesme parametrelerini belirlemek için yaygın olarak tercih edilmektedir [4]. Ayrıca işleme parametrelerinin optimizasyonu için yanıt yüzey yöntemi kullanılmıştır [5]. Bu yaklaşım, optimizasyon ve parametreler arasındaki ilişkileri modelleme açısından güçlü bir yöntemdir. Literatürde Taguchi tasarımı ile elde edilen verilerin Yanıt Yüzey Yöntemi veya benzeri yöntemlerle analiz edildiğine dair örnekler bulunmaktadır [6]. Özellikle, endüstriyel uygulamalarda sıkça karşılaşılan çoklu faktörlü problemlerde hem zamandan hem de maliyetten tasarruf sağlaması, yöntemin tercih edilmesinde önemli bir rol oynamıştır. Bu bağlamda, çalışmanın amacı doğrultusunda Yanıt Yüzey Yönteminin sağladığı güçlü analiz yetenekleri, kullanılan yöntemin uygunluğunu ortaya koymaktadır.

Mevcut çalışmada, toplam beş baralama parametresi yer almakta olup, bu parametrelerden ikisi ikişer seviyeye, üçü ise üçer seviyeye sahiptir. Tam faktöriyel bir deney tasarımında 2x2x3x3x3=108 deney yapılması gerekirken, Taguchi yöntemi sayesinde bu sayı 36'ya indirilmiştir. İşlenebilirlik deneylerindeki maliyet ve zaman kısıtlamaları göz önüne alındığında, bu yöntemin avantajlı olduğu görülmektedir. Taguchi L36'ya ait parametreler ve seviyeleri Tablo 2'de sunulmuştur.

Bilgisayar kontrollü bir dik işleme tezgâhı ile delik baralama operasyonları gerçekleştirilmiştir. Tezgâhın markası Johnford VMC-550'dir. İş mili motoru 5.5 KW, maksimum iş mili hızı ise 8000 rpm'dir. Tezgâhın kontrol paneli Fanuc olup, ölçüm hassasiyeti 0.001 mm'dir. Baralama işlemi için Dandrea marka baralama çubuğu, baralama başlığı ve kesici uçlar kullanılmıştır. Baralama parametreleri, kesici takım katalog önerileri ve literatür referans alınarak belirlenmiştir. Baralama torkunu ölçmek amacıyla üç farklı ilerleme miktarı (0.09 – 0.06 ve 0.04 mm/dev), üç farklı radyal kesme derinliği (0.5 – 0.3 ve 0.2 mm) ve üç farklı kesme hızı (203, 162 ve 130 m/dak) seçilmiştir. İki tür sermet (cermet) kesici uç, kaplamalı ve kaplamasız olarak

kullanılmıştır. Kesici uçların burun radüsü ise 0.4 mm ve 0.2 mm olarak belirlenmiştir. Baralama parametreleri ve elde edilen deneysel Tork değerleri Tablo 3'te sunulmuştur.

Tablo 2. Faktörler ve seviyeleri

Seviye	Faktörler				
	Uç radüsü (*UR*), mm	Kaplama Tipi (*KT*)	Kesme Derinliği (*KD*), mm	İlerleme Miktarı (*f*), mm/dev	Kesme Hızı (*Vc*), m/dak
1	0.4	Kaplamalı	0.5	0.09	203
2	0.2	Kaplamasız	0.3	0.06	162
3			0.2	0.04	130

Tablo 3. Baralama parametreleri ve elde edilen Tork değerleri.

| Deney No	UR	Vc	f	KD	KT	Tork	Deney No	UR	Vc	f	KD	KT	Tork
L1	0.2	130	0.04	0.2	1	20.34	L19	0.2	130	0.06	0.2	2	32.45
L2	0.2	162	0.06	0.3	1	68.04	L20	0.2	162	0.09	0.3	2	67.18
L3	0.2	203	0.09	0.5	1	104.8	L21	0.2	203	0.04	0.5	2	85.9
L4	0.2	130	0.04	0.2	1	23.99	L22	0.2	130	0.06	0.3	2	39.07
L5	0.2	162	0.06	0.3	1	64.13	L23	0.2	162	0.09	0.5	2	157.8
L6	0.2	203	0.09	0.5	1	89.02	L24	0.2	203	0.04	0.2	2	20.49
L7	0.2	130	0.04	0.3	1	40.68	L25	0.2	130	0.09	0.3	2	62.38
L8	0.2	162	0.06	0.5	1	110.7	L26	0.2	162	0.04	0.5	2	82.32
L9	0.2	203	0.09	0.2	1	42.94	L27	0.2	203	0.06	0.2	2	38.15
L10	0.4	130	0.04	0.5	1	43.37	L28	0.4	130	0.09	0.3	2	81.72
L11	0.4	162	0.06	0.2	1	42.48	L29	0.4	162	0.04	0.5	2	89.17
L12	0.4	203	0.09	0.3	1	57.84	L30	0.4	203	0.06	0.2	2	36.59
L13	0.4	130	0.06	0.5	1	68.01	L31	0.4	130	0.09	0.5	2	169.7
L14	0.4	162	0.09	0.2	1	57.65	L32	0.4	162	0.04	0.2	2	34.17
L15	0.4	203	0.04	0.3	1	52.95	L33	0.4	203	0.06	0.3	2	69.36
L16	0.4	130	0.06	0.5	1	84.02	L34	0.4	130	0.09	0.2	2	43.73
L17	0.4	162	0.09	0.2	1	55.39	L35	0.4	162	0.04	0.3	2	55.37
L18	0.4	203	0.04	0.3	1	58.29	L36	0.4	203	0.06	0.5	2	121.9

Deneylerde iş parçası sabit, kesici takım ise döner pozisyondadır. Deneyler kuru ortamda gerçekleştirilmiş olup, soğutma sıvısı kullanılmamıştır. Deneysel düzenek Şekil 2'de gösterilmiştir. Delik barası ile deliği genişletirken, baralama torkunu gerçek zamanlı ölçmek ve kaydetmek için Kistler 9272 dinamometre ve Kistler 5070A amplifier kullanılmıştır. Toplanan sinyal verileri, Dynoware programı ile işlenerek ortalama baralama torku hesaplanmıştır.

14 mm delik çapını elde etmek amacıyla uygun bara başlığı ve bara çubuğu seçilmiştir. Uygun çapı elde edebilmek için Dandrea takım setinde B 3.11 (Ø11- Ø17 mm) kodlu kesici takımlar seçilmiştir. Belirtilen radyal kesme derinliklerini elde edebilmek için Ø13 - Ø13,4 ve Ø13,6 normal helisel matkaplar ile ön delme işlemi gerçekleştirilmiştir. Şekil 3'te kullanılan kesici uçların geometrik özellikleri ve boyutları verilmiştir. Kesici uçların geometrisi TPGX090204L ve TPGX090202L'dir. Kaplamalı kesici ucun kodu DC100T, kaplamasız kesici ucun kodu ise DC100'dür.

3. DENEY VE OPTİMİZASYON SONUÇLARI

Bu çalışmada 1.2738 malzemeden üretilmiş iş parçasının baralanması işleminde meydana gelen baralama torku üzerinde işleme parametrelerinin etkisinin incelenerek yanıt yüzey yöntemi ile optimizasyonu amaçlanmıştır. Deney sayısının azaltılması amacıyla Taguchi L36 deney tasarım yöntemi kullanılmıştır. Deney sırasında meydana gelen gerçek zamanlı baralama torku değerleri bir dinamometre yardımıyla gerçek zamanlı olarak kaydedilmiştir. Daha sonra dinamometrenin kendi yazılımı olan dynoware ile sinyal bilgileri analiz edilmiştir. Sinyallerin ortalamaları alınarak baralama torku değerleri belirlenmiştir. Baralama torku

üzerinde baralama parametrelerinin etkilerini incelemek ve optimize etmek için Design Expert 13 programı ve yanıt yüzey yöntemi tercih edilmiştir. Yanıt yüzey yöntemi, ikinci dereceden bir polinom fonksiyonu kullanılarak doğrusal olmayan olguları yaklaşık olarak hesaplamak için etkili ve basit bir araçtır [7].
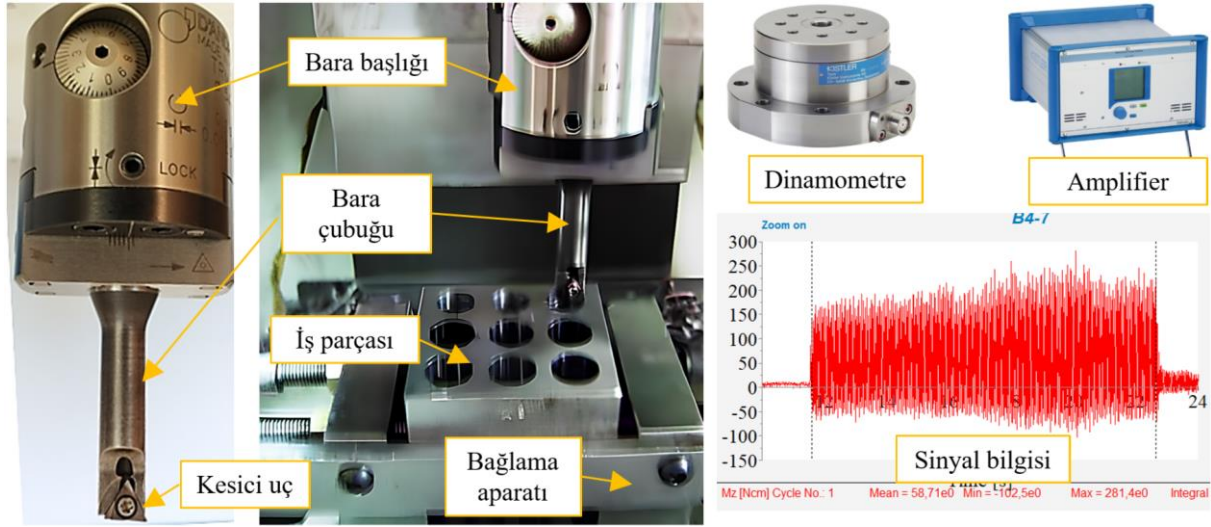
Şekil 2. Baralama operasyonu ve kesme torku test düzeneği.
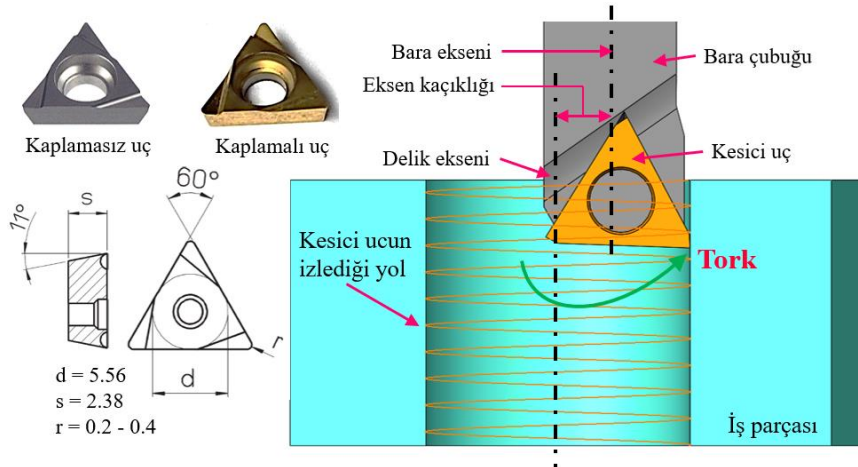
Şekil 3. Kullanılan bara çubuğu ve kesici uçlar.

İşleme parametrelerinin optimizasyonu amacıyla program tarafından çeşitli modeller incelenerek en uygun olanları Tablo 4'te verilmiştir. En düşük göstergeler lineer model ile elde edilmişken en yüksek göstergeler kuadratik model ile hesaplanmıştır. Ancak program tarafından iki faktör etkileşimi (2FI) ile elde edilen model önerilmiştir. Kuadratik model ise doğrusal bağımlı (aliased) yani modelin bazı katsayılarının ya da terimlerinin diğerleri ile tam bir doğrusal bağımlılık içinde olduğunu ve bu nedenle modelin kararsız veya hatalı sonuçlar üretebileceğini göstermektedir. Dolayısıyla etkili bir parametre analizi ve optimizasyon gerçekleştirebilmek için iki faktör etkileşimli model dikkate alınmıştır. Standart sapma değerinin daha küçüğü iyiyken, R^2 değerinin 1'e yaklaşması daha iyi sonucu temsil etmektedir [8]. Belirlenen modelin standart sapma değeri 10,68 ve R^2 değeri ise 0,9456 olarak hesaplanmıştır. 0,8013'lük tahmini R^2 değeri, 0,9047'lik düzeltilmiş R^2 değeriyle makul ölçüde uyumludur; yani fark 0,2'den küçüktür.

Tablo 4. Modelin özet istatistikleri

Kaynak	Standart Sapma	R^2	Düzeltilmiş R^2	Tahmin edilen R^2	
Lineer	17.99	0.7682	0.7295	0.6507	
2FI	**10.68**	**0.9456**	**0.9047**	**0.8013**	**Önerilen**
Kuadratik	8.91	0.9678	0.9336	0.8173	Model uyuşmazlığı

Baralama parametrelerinin sinyalinin gürültüye oranları (S/N) Tablo 5'te verilmiştir. Taguchi analizi, kesme torkuna baralama parametrelerinin etkilerini incelemek için çıktı yanıtlarını S/N oranlarına dönüştürmektedir [9]. Baralama torku değerinin daha az olması hedeflenen bir amaçtır. Dolayısıyla küçük daha iyidir prensibine göre Taguchi analizi gerçekleştirilmiştir. Taguchi analizinde S/N oranlarının ve delta değerlerinin daha yüksek olması daha kabul edilebilir sonuçlar üretmektedir. Daha yüksek delta değerine sahip olan faktörün önem derecesi daha yüksektir. Dolayısıyla önem derecesine göre faktörler sıralandığında en önemli faktör radyal kesme derinliğiyken en az öneme sahip faktör kaplama tipi olarak sonuçlanmıştır.

Tablo 5. Baralama parametreleri S/N oranlarının yanıt tablosu.

Level	KT	UR	Vc	f	KD
1	-34.75	-34.81	-34.32	-33.46	-31.01
2	-35.74	-35.88	-36.83	-35.10	-35.30
3			-34.89	-37.48	-39.73
Delta	0.99	1.07	2.51	4.02	8.73
Rank	5	4	3	2	1

Analiz sonucunda elde edilen ortalama etki grafiği Şekil 4'te bulunmaktadır. Faktörlerin daha büyük S/N oranları daha iyi olarak kabul edilmektedir [10]. Daha büyük S/N oranlarına sahip faktör seviyeleri kesme derinliği için 0.2 mm, ilerleme miktarı için 0.04 mm/dev, kesme hızı için 130 m/dak, uç radüsü değeri için 0.2 mm ve kaplama tipi için kaplamalı kesici uç olarak belirlenmiştir.
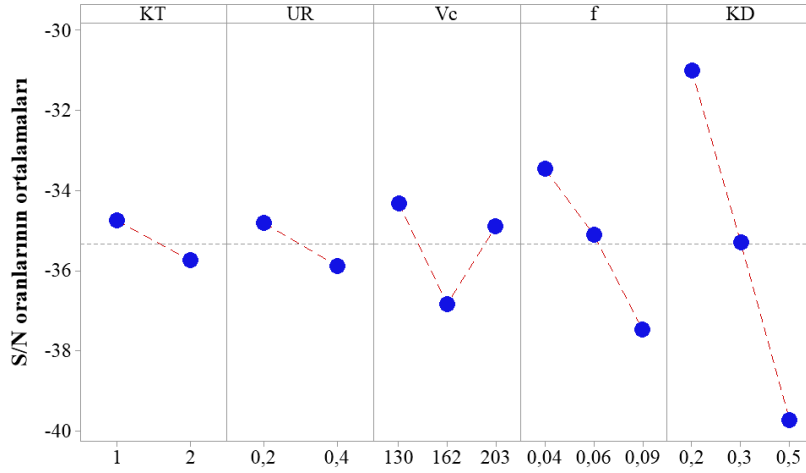

Şekil 4. S/N oranlarının ortalamaları

Önerilen modelin Anova sonuçları Tablo 6'da bulunmaktadır. Kurulan modelin f değerinin 23,16 olması modelin önemli olduğunu göstermektedir. Gürültü nedeniyle bu kadar büyük bir F değerinin oluşma olasılığı ise yalnızca %0,01'dir. Baralama faktörlerinin kareler toplamı ve F değerinin daha büyük olanı çıktı yanıtı üzerinde daha yüksek etkiye sahiptir. Ayrıca P değerinin 0,05'den küçük olması model terimlerinin önemli olduğunu göstermektedir [4]. Bu durumda önemli model terimleri C (ilerleme miktarı), D (radyal kesme derinliği), AE (Uç radyusu x kaplama tipi), BC (kesme hızı x ilerleme miktarı), CD (ilerleme miktarı x radyal kesme derinliği), DE (kesme derinliği x kaplama tipi) olmuştur. 0,1'den daha büyük değerler, model terimlerinin önemli olmadığını göstermektedir. Kesme hızı, uç radyusu ve kaplama tipi gibi bireysel faktörlerin baralama torku üzerinde istatistiksel olarak anlamlı bir etkisinin olmaması, bu parametrelerin mevcut değerlendirme aralıklarıyla süreç optimizasyonunda önceliklendirilmesine gerek olmadığına işaret etmektedir. Bu bulgular Anova analizi sonucunda elde edilmiştir. Anova'nın varsayımları doğrusal ilişkilere dayanır. Ancak Şekil 4 incelenirse Vc ile Tork arasında doğrusal olmayan bir ilişki mevcuttur. Bu durumun bireysel parametreler açısından istatistiksel olarak anlamsız olmasına neden olduğu değerlendirilmiştir. Kesme hızı, uç radyusu ve kaplama tipinin kombinasyonları dikkate alındığında ise istatistiksel açıdan daha önemli hale gelmektedirler.

Tablo 6. İki faktör etkileşimine göre kurulan modelin Anovası

Kaynak	Kareler Toplamı	Df	Ort. Kare	F-değeri	p-değeri	
Model	39604,41	15	2640,29	23,16	< 0,0001	Önemli
A-UR	0,2832	1	0,2832	0,0025	0,9607	
B-Vc	46,25	1	46,25	0,4057	0,5314	
C-f	4766,46	1	4766,46	41,81	< 0,0001	
D-KD	21920,98	1	21920,98	192,29	< 0,0001	
E-KT	153,22	1	153,22	1,34	0,2600	
AB	130,29	1	130,29	1,14	0,2978	
AC	2,86	1	2,86	0,0251	0,8757	
AD	158,58	1	158,58	1,39	0,2521	
AE	836,12	1	836,12	7,33	0,0135	
BC	937,11	1	937,11	8,22	0,0095	
BD	437,67	1	437,67	3,84	0,0642	
BE	45,72	1	45,72	0,4010	0,5337	
CD	1763,69	1	1763,69	15,47	0,0008	
CE	20,00	1	20,00	0,1755	0,6798	
DE	2755,50	1	2755,50	24,17	< 0,0001	
Artıklar	2279,99	20	114,00			
Uyum eksiği	1995,90	14	142,56	3,01	0,0912	Önemli değil
Saf Hata	284,10	6	47,35			
Toplam	41884.40	35				

Baralama parametreleri ile kesme torku arasındaki ilişkinin grafikleri Şekil 5'te bulunmaktadır. İlerleme miktarının artışı ile kesme torku artma eğilimindedir. İlerleme miktarının artışı, talaş kaldırma sürecinde daha fazla talaş kalınlığına sahip malzeme kesilmesine neden olur ve bu da kesme bölgesinde daha yüksek kesme kuvvetleri ve tork gereksinimi oluşturabilmektedir [11]. İlerleme arttıkça kesici uç, daha büyük bir hacimde malzemeyi deforme eder ve sürtünmeyi artırır, bu da torkun artışına katkıda bulunmaktadır [12]. Yüksek ilerleme ve kesme hızlarında, talaş oluşumu ve kesme bölgesindeki deformasyon daha belirgin hale gelmiştir. Radyal kesme derinliğinin artışı ile kesme torku artma eğilimindedir. Radyal kesme derinliğinin artması, kesici ile iş parçası arasındaki temas yüzeyini genişleterek kesme torkunu artırır [13]. Kesme derinliği yükseldikçe, kesme kuvvetlerinin doğrudan torka olan etkisi büyür, çünkü daha geniş bir kesme alanında enerji harcanmaktadır [14]. Küçük kesici uç radyusu kesme torkunun artmasına neden olmuştur. Küçük kesici uç radyusu, kesici kenarın kesme bölgesindeki etkisini artırarak kesme kuvvetlerinin daha yoğun bir bölgeye odaklanmasına neden olarak malzeme üzerinde daha fazla gerilme ve tork artışı ile sonuçlanmış olabilir. Ayrıca daha küçük sürtünme alanı ile beraber sıcaklığın artması sonucu kesici aşınması artmış olabilir [15]. Kesici aşınmasının artması ise kesme torkunu artırmış olabilir. Yüksek ilerleme miktarlarında ve büyük radyal kesme derinliklerinde, kesme hızı arttıkça torkta bir azalma gözlemlenebilir [16]. Bu durum, yüksek kesme hızlarında takımın yüzeyle temas süresinin azalması ve sıcaklığın artması sonucu takım talaş arayüzeyine sıvanan malzeme kayma dayanımının azalmasıyla ifade edilebilir [17]. Ayrıca, yüksek ilerleme ve büyük radyal kesme derinliklerinde, malzemenin işlenmesi sırasında oluşan aşırı ısı birikimi de takımın performansını düşürebilir, bu da tork ve kesme hızında bir dengesizlik yaratabilir [18]. Buna ek olarak 1.2738 malzemesinin mikroyapısı martenzittir. Bu mikroyapı yüksek sertliği nedeniyle kesici takımın malzemeye nüfuz etmesini zorlaştırmaktadır [19]. Dolayısıyla kesme kuvvetlerini ve baralama torkunu artırır. Yüksek sürtünme ve ısı üretimi, takım aşınmasını hızlandırarak torkun zamanla artmasına sebep olabilir. Bu etkiler, özellikle ilerleme miktarı ve radyal kesme derinliği gibi işleme parametrelerinin yüksek seviyelerde olduğu durumlarda daha belirgin hale gelir. Martenzitik mikro yapının torka olan bu özgün etkileri, malzemenin işlenebilirliğini doğrudan şekillendirerek hem kesici takım seçiminde hem de işleme parametrelerinin optimizasyonunda dikkate alınması gereken kritik bir faktör haline gelmektedir. Sonuç olarak, bu parametrelerin kesme torku üzerindeki etkileri, talaşlı imalat süreçlerinde dikkatle optimize edilmesi gereken kritik faktörlerdir. İlerleme, kesme derinliği ve kesici uç geometrisi gibi parametrelerin optimizasyonu işleme kalitesi, takım ömrü ve enerji verimliliği açısından önemli rol oynamaktadır.
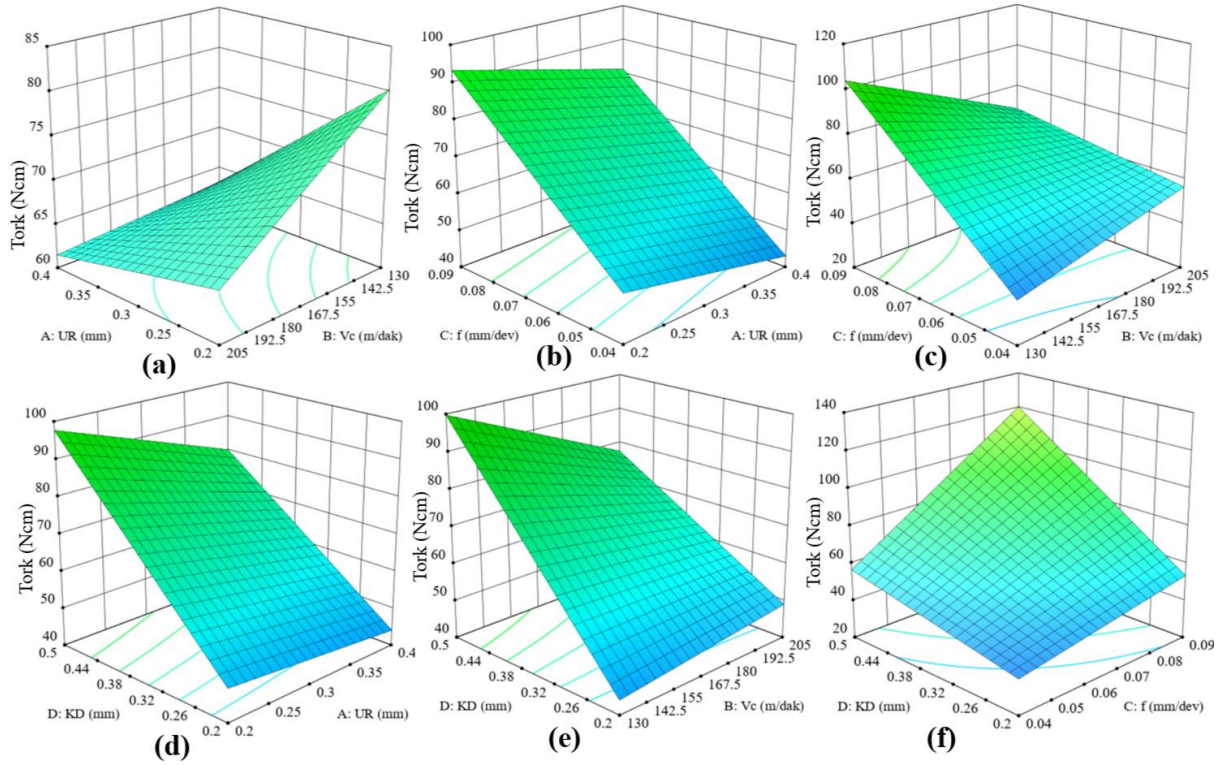
Şekil 5. Baralama parametreleri ile kesme torkunun ilişkisi (a) UR-Vc, (b) f-UR, (c) f-Vc, (d) KD-UR, (e) KD-Vc, (f) KD-f

Kurulan matematiksel modele göre kaplama tipi için regresyon eşitlikleri Eşitlik 1 ve 2'de bulunmaktadır. İki faktör etkileşimi ile kurulan modellerde kaplama tipi kategorik değişken olarak tanımlanmıştır. Model için elde edilen 0,9456'lık R^2 değeri dikkate alındığında kaplamalı ve kaplamasız kesici uçlar ile elde edilmesi muhtemel baralama torku başarı ile hesaplanabilir.

$$\text{Tork}_{\text{kaplamasız}} = -132,4 - 111,9.\text{UR} + 0,97.\text{Vc} + 2081,2.\text{f} + 200.\text{KD} + 0,85.\text{UR.Vc}$$
$$- 177,6.\text{UR.f} - 207,4.\text{UR.KD} - 14,07.\text{Vc.f} - 1,2.\text{Vc.KD} + 3156,4.\text{f.KD} \qquad (1)$$

$$\text{Tork}_{\text{kaplamalı}} = -225,5 - 1,03.\text{UR} + 1.07.\text{Vc} + 1964,4.\text{f} + 360,4.\text{KD} + 0,85.\text{UR.Vc}$$
$$- 177,62.\text{UR.f} - 207,4.\text{UR.KD} - 14.07.\text{Vc.f} - 1,2.\text{Vc.KD} + 3156,4.\text{f.KD} \qquad (2)$$

Deneysel sonuçlar ile yanıt yüzey yöntemi ile elde edilen tahmini değerlerin karşılaştırılması Şekil 6'da bulunmaktadır. Gerçek ve tahmini değerlerin oldukça uyumlu olduğu anlaşılmaktadır.
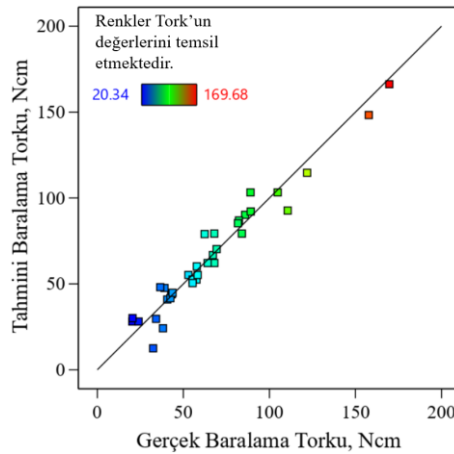
Şekil 6. Baralama torkunun gerçek ve tahmini değerlerinin kıyaslanması

Şekil 7'de kurulan modeller için kalan değerlerin grafikleri bulunmaktadır. Kalan değerler bir gözlemin model üzerindeki etkisini değerlendirmek için kullanılmaktadır [5]. Özellikle, bir veri noktasının çıkarıldığı

durumda modelin ne kadar değiştiğini gösterir ve böylece uç değerlerin ve etki eden noktaların belirlenmesine yardımcı olmaktadır. Standart artıklar, bir modelin gözlemler ile tahmin edilen değerler arasındaki farklardır. Kalan değerler ise, bir gözlem çıkarıldığında, çıkarılan gözlem için kalan verilerle hesaplanan artıkların, bu gözlemle güncellenmiş varyansı kullanılarak normalize edilmesiyle elde edilir. İki kırmızı yatay çizgi arasında kalan gözlemler normal hatalar aralığında yer alır. Kırmızı yatay çizgiler genellikle kritik sınırları temsil eder. Bu sınırların dışında kalan gözlemler ise potansiyel uç değerler veya model üzerinde büyük etkisi olan gözlemler olarak değerlendirilir. Şekil 7(a)'da tahmini baralama torku için kalan değerler yer almaktadır. Tüm veri noktaları kırmızı çizgilerin arasında yer almaktadır. Dolayısıyla kurulan model için gözlemlerin modelle iyi bir uyum sağladığı söylenebilir. Şekil 7b'de deney veri noktaları ile kalan değerlerin grafiği yer almaktadır. Tüm gözlemler model tarafından iyi bir şekilde açıklanmıştır. Deneylerden elde edilen sonuçlar, model tarafından tahmin edilen değerlere yakın olup, herhangi bir deneyin model üzerindeki etkisinin aşırı olmadığını göstermektedir. Dolasıyla hem modelin uygunluğu hem de verilerin sağlamlığının kabul edilebilir sınırlar içinde olduğu söylenebilir.
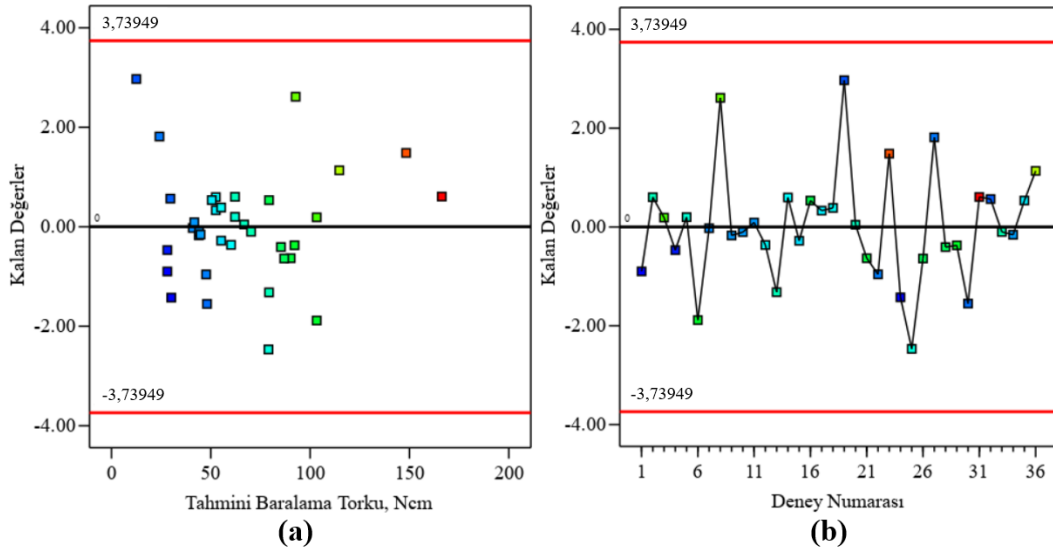
Şekil 7. Kalan değerlerin grafiği (a) Tahmini baralama torku, (b) Deney numarası

4. SONUÇLAR

Çalışmanın sonucunda, 1.2738 malzemesinden üretilmiş iş parçasının baralanması işlemi sırasında meydana gelen baralama torku değerleri üzerinde işleme parametrelerinin etkisi başarılı bir şekilde analiz edilmiştir. Taguchi L36 deney tasarımı ve yanıt yüzey yöntemi kullanılarak yapılan bu çalışma, deney sayısını azaltırken optimum işleme koşullarının elde edilmesini amaçlamıştır. Deneylerden elde edilen veriler ve yapılan analizler sonucunda, işleme parametrelerinin kesme torku üzerinde belirgin bir etkiye sahip olduğu anlaşılmıştır. Özellikle radyal kesme derinliği ve ilerleme miktarının kesme torkunu artırıcı etkisi, deneysel sonuçlarla desteklenmiş ve optimizasyon çalışmaları sonucunda en uygun parametreler belirlenmiştir. İki faktör etkileşimli modelin tercih edilmesi, modelin daha kararlı ve güvenilir sonuçlar vermesini sağlamıştır. Ayrıca, modelin yüksek R^2 değeri (0,9456) ve düşük standart sapma (10,68) değerleri, modelin doğruluğunu ve güvenilirliğini ortaya koymuştur. Analizler sonucunda, kesme torku üzerindeki en önemli parametrenin radyal kesme derinliği olduğu saptanmıştır. Son olarak, modelin tahmin ettiği tork değerleri ile deneysel veriler arasında yüksek bir uyum sağlandığı, modelin işleme koşullarını doğru bir şekilde yansıttığı görülmüştür.

TEŞEKKÜR

KAYNAKLAR

[1] S. Albayrak, F. Yeşildal,C. Yıldırım, SAE 4140 Çeliğin Tornalanmasında Kesme Parametrelerinin Ses Seviyesi ve Yüzey Pürüzlüğüne Etkileri: Parametrelerin Optimizasyonu, Journal of the Institute of Science and Technology,10(4), (2020), 2759-2769, https://doi.org/10.21597/jist.714810

[2] N. Eren, F. Hayat,M. Günay, Sertleştirilmiş 1.2367 takım çeliğinin işlenmesinde enerji tüketiminin analizi ve modellenmesi, İmalat Teknolojileri ve Uygulamaları, 1(3) (2020) 41-49.

[3] L. Uğur, 7075 Alüminyum Malzemesinin Frezelenmesinde Yüzey Pürüzlülüğünün Yanıt Yüzey Metodu İle Optimizasyonu, Erzincan University Journal of Science and Technology, 12(1) (2019) 326-335. https://doi.org/10.18185/erzifbed.461223

[4] E. Demirer, Y. Kayır, Analysis By Taguchi and ANOVA Methods For The Effect Of The Cutting Tool Height Adjustment On Cutting Forces In Turning AISI304 Stainless Steel Material, Gazi Journal of Engineering Sciences (GJES), 8(1) (2022).

[5] M. Dağlı, A. Demirer, E. Yumat, Hdpe Boruların Alın Kaynağında Kaynak Parametrelerinin Birleşme Mukavemetine Etkisinin Yüzey Cevap Metodu ile Optimizasyonu, Afyon Kocatepe Üniversitesi Uluslararası Mühendislik Teknolojileri ve Uygulamalı Bilimler Dergisi 6(2) (2023) 95-109. https://doi.org/10.53448/akuumubd.1289128

[6] T. Valarmathi, K. Palanikumar, S. Sekar, Modeling of thrust force in drilling of plain medium density fiberboard (MDF) composite panels using RSM, Procedia engineering 38 (2012) 1828-1835. https://doi.org/10.1016/j.proeng.2012.06.226

[7] B. Keshtegar, O. Kisi, M. Zounemat-Kermani, Polynomial chaos expansion and response surface method for nonlinear modelling of reference evapotranspiration, Hydrological Sciences Journal 64(6), (2019) 720-730. https://doi.org/10.1080/02626667.2019.1601727

[8] A. Akdulum, Y. Kayır, Prediction of thrust force in indexable drilling of aluminum alloys with machine learning algorithms, Measurement, 222 (2023) 113655,. https://doi.org/10.1016/j.measurement.2023.113655

[9] Y. Siyambaş, Ş. Bayraktar,Y. Turgut, Investigation of the effects of cutting parameters on diameter deviation in drilling of HSLA steel, Turkish Journal of Electromechanics & Energy, 2(1) (2017) 3-8.

[10] A. Akdulum, Y. Kayır, Investigation of the effect of u drills with different properties on thrust force, torque and spindle load, Politeknik Dergisi 26(1) (2023) 387-400,. https://doi.org/10.2339/politeknik.1113301

[11] U. Çaydaş, M. Çelik, AA 7075-T6 alaşımının delinmesinde kesme parametrelerinin yüzey pürüzlülüğü, takım sıcaklığı ve ilerleme kuvvetine etkilerinin araştırılması, Politeknik Dergisi 20(2) (2017) 419-425.

[12] M. Günay, T. Meral, M.E. Korkmaz, AISI 420 Martenzitik paslanmaz çeliğin delinebilirliğinin sonlu elemanlar yöntemiyle analizi, Gazi Mühendislik Bilimleri Dergisi 4(3) (2018) 223-229.

[13] İ. Korkut, M.A. Dönertaş, Kesme parametrelerinin frezelemede oluşan kesme kuvvetleri üzerindeki etkileri, Politeknik dergisi 6(1), (2003), 385-391.

[14] A. Yardımeden, A. Turan, AISI 1040 çeliğin tornalamasında kesme parametrelerinin kesme kuvvetine etkisi, Dicle Üniversitesi Mühendislik Fakültesi Mühendislik Dergisi 6(1) (2015) 51-69.

[15] Y. Kayır, S. Aslan,A. Aytürk, AISI 316Ti paslanmaz çeliğin tornalanmasında kesici uç etkisinin Taguchi yöntemi ile analizi, Gazi Üniversitesi Mühendislik Mimarlık Fakültesi Dergisi 28(2), (2013).

[16] M. Iliescu, A. Vlase, New mathematical models of axial cutting force and torque in drilling 20MoCr130 stainless steel, in: 10th WSEAS international conference on Mathematical and computational methods in science and engineering, Bucharest Romania, (2008) 210-215.

[17] M. Coşkun, İ. Çiftçi, H. Demir, AISI P20S kalıp çeliğinin işlenebilirliğinin incelenmesi, İmalat Teknolojileri ve Uygulamaları 2(2), (2021), 1-9. https://doi.org/10.52795/mateca.801431

[18] Ş. Bayraktar, Y. Siyambaş, Y. Turgut, Delik delme prosesi: bir araştırma, SAÜ Fen Bilimleri Enstitüsü Dergisi 21(2), (2017). https://doi.org/10.16984/saufenbilder.296833

[19] M.F. Aycan, Farklı martenzit hacim oranlarında kırılma tokluğu değerlerinin incelenmesi, Politeknik Dergisi 23(2), (2020), 277-282,. https://doi.org/10.2339/politeknik.520142

Manufacturing Technologies and Applications
MATECA

Effect of Short Carbon Fiber Content on the Mechanical and Tribological Behaviors of Polyurethane Foam-Based Composites

Harun Cug[1,*] , Wasim Amhemed Gliza Khalifa[1] , Yasin Akgül[2] , Andinet Kumella Eticha[3]

[1*]*Department of Mechanical Engineering, Engineering Faculty, Karabük University, Karabük, Türkiye*

[2] *Iron and Steel Institute, Karabuk University, Karabük, Türkiye*

[3] *School of Mechanical and Industrial Engineering, Addis Ababa Institute of Technology, Addis Ababa University, Addis Ababa, Ethiopia*

ABSTRACT

This study aims to investigate the effect of different weight fractions (0.5, 1.0, and 1.5%) of short carbon fibers (SCFs) on the mechanical and tribological properties of polyurethane (PU) foam composites. The samples were fabricated using the hand lay-up method. To examine the mechanical properties of neat PU foam and composites (PU-SCF), 3-point bending tests were conducted. Moreover, a 5 N load was applied to assess the wear resistance properties of samples. The result of this study revealed that the flexural strength of PU0.5SCF composite was higher than PU1.5SCF nearly by 9.46%. Whereas, the addition of 1.5% mass fractions of SCFs onto neat PU have improved the wear resistance property by 78.95%. Moreover, the study showed that incorporating higher contents of SCFs into neat PU resulted in a direct increment in the flexural modulus of the composite. Therefore, the study confirmed that as the addition of SCFs into PU increases, the flexural strength of PU-SCF composites decreases. This was explained by the poor dispersion of SCFs into the PU matrix. However, it was also revealed that the flexural modulus and tribological properties of the composites enhanced significantly along with the increment of SCFs content.

Keywords: Flexural modulus, Flexural strength, Polyurethane, Short carbon fibers, Wear.

Kısa Karbon Elyaf İçeriğinin Poliüretan Köpük Bazlı Kompozitlerin Mekanik ve Tribolojik Davranışları Üzerindeki Etkisi

ÖZET

Bu çalışma, kırpılmış karbon elyafların (SCFs) farklı ağırlık oranlarının (%0,5, %1 ve %1,5) poliüretan köpük (PU) kompozitlerin mekanik ve tribolojik özellikleri üzerindeki etkisini araştırmayı amaçlamaktadır. Numuneler kalıba döküm yöntemi kullanılarak üretilmiştir. Saf poliüretan (PU) köpük ve kompozitlerin (SCFs-PU) mekanik özelliklerini araştırmak için 3 nokta eğme testleri yapılmıştır. Ayrıca, numunelerin aşınma direnci özelliklerini değerlendirmek için 5N yük uygulanılmıştır. Bu çalışmanın sonucu, ağırlıkça %0,5 SCFs içeren PU köpük bazlı kompozitin eğilme mukavemetinin, ağırlıkça %1,5 SCF içeren numuneden yaklaşık %9,46 daha yüksek olduğunu ortaya koymaktadır. Bu nedenle, PU matrisine daha yüksek miktarda SCF eklenmesinin, SCFs-PU köpük kompozitlerinin eğilme özelliklerinde azalma ile sonuçlandığı söylenebilmektedir. Bununla birlikte, saf poliüretana ağırlıkça %1,5 SCF eklenmesi, aşınma direnci özelliğini yaklaşık %78,95 oranında iyileştirmiştir. Sonuç olarak, PU köpüğe eklenen SCFs içeriği arttıkça SCF-PU kompozitlerinin mekanik özelliklerinin azaldığı tespit edilmiştir. Bununla birlikte, kompozitlerin tribolojik özellikleri önemli ölçüde artmaktadır.

Anahtar Kelimeler: Eğilme modülü, Eğilme mukavemeti, Poliüretan, Kısa karbon elyaflar, Aşınma

---

1. INTRODUCTION

Composite materials, which have superior properties compared to traditional materials, consist of the combination of two or more components at a macroscopic level and without dissolving with each other [1]. Polyurethane (PU) based composites are thermosetting polymer composite types that have a wide range of application areas including biomedical, aeronautical, sports, industries, and automotive, due to higher properties of chemical stability, specific strength, low relative density, strong, good stiffness, and outrageous wear resistance [2–6]. Bulk (rigid) or foam-type PU matrixed composites are most popularly used as construction material, because of their elevated durability, great strength-to-weight ratios, and inflated corrosion resistance [5].

Numerous manufacturing techniques exist for producing homogeneous composite materials, including hand lay-up methods, electric hand blenders, dispersion techniques, foaming, dry processing, and the melt

---

extrusion of polymer powders [7]. The hand lay-up technique produces a homogeneous composite; however, it can occasionally lead to an uneven distribution of fibers within the matrix. In contrast, the electric hand blender mixing method is likely to yield a more uniform composite structure due to the continuous motion generated by the motor, which effectively disperses the fibers throughout the matrix. This advantage is not observed in the hand lay-up method, where the interrupted motion contributes to the occurrence of non-homogeneity.

According to the works of literature, since PU materials have high elasticity, toughness, and rapid cure time properties, nowadays polyurethane-based composites are increasing their application areas more than ever in industries and are also responsible for part of solutions in modern science. Hence, the number of studies on PU-based composite is drastically increased [5]. Despite PU's huge applications, their weak mechanical properties have been the barrier to their further applications in construction, automobile bodies, and aerospace structures. Thus, researchers have been trying to raise the mechanical properties of PU by adding organic and inorganic fillers into the PU matrixes [5]. Many types of fillers have been employed as reinforcement to improve PU's mechanical and physical properties [5,8–10]. Carbon fibers (CF) are the most commonly used inorganic fibers, because of their lightweight, excellent chemical stability, high-thermal resistance, and good mechanical properties. Lately, CF-based composites have become a better alternative for a wide range of applications [5,11]. Previous findings exhibited that too-short fibers show no significant reinforcing effects on the composite due to the smaller contacting area, while too-long fibers resulted in bad mobility when PU agents and fillers were agitated. Therefore, studies showed that the optimum average length of carbon fibers reinforced into a PU matrix is 3-12 mm [12]. Further, in most cases, short carbon fibers have a stronger effect on the composites compared to too short or long carbon fibers [9].

The literature survey indicated that fewer studies were conducted on short carbon fibers and their impacts on the mechanical properties of PU matrixed composites. For instance, the study of Yakushin et al. [9], exhibited that the compression strength of the PU foam was boosted by 20% with the addition of 4 wt.% SCFs. However, a significant decrement in the elongation at the break of the PU foams was observed as the content of CF increased to 8 wt.%. In another study [13], the effects of different types of fibers and fiber contents of 10 to 20% on the tensile strength and bending performance of the PU matrix composites were examined. According to the test outcomes, higher flexural bending strength and higher energy absorption were obtained for 20% CF reinforced composites compared to the same content of jute felt, jute tablets, and glass fiber reinforced composites. For PU foam-added carbon fiber reinforced plastics (CFRP) composite tubes the peak force and threshold force were increased nearly by 132% for PU foam-based CFRP composite tubes than pure CFRP polymer was investigated [14]. In addition, the effect of hardener on the mechanical properties of carbon fiber-reinforced phenolic resin composites was also evaluated in the work of Sulaiman et al., [3]. Results revealed that composites containing 15% hardener (hexamine) content exhibit enhancements in flexural strength, due to the hardener amount increasing the crosslinks between phenolic resin and carbon fibers.

Furthermore, the influence of SCF's content on the wear resistance characteristics of PU foam-based composites was explained in a few research works. The work of Li and Cai [15] reported that CF-reinforced polypropylene (PP) composite (CF/PP) had superior tribological characteristics compared to pure PP. In another study by Khun et al., the wear rate and friction coefficient of epoxy-based composites were remarkably reduced with the increment of chopped carbon fiber content [16]. Moreover, Zhao et al., [17], studied tensile strength, wear, and friction properties of rigid-type PU composite reinforced with CF. Test assessment exhibited that chemically surface-treated CFs improved the tribological properties of PU composites. Also, the tensile strength is enhanced with the inclusion of CFs. The effects of different weight fractions of chopped carbon fiber on the effectiveness of wear resistance enhancement of high-density polyethylene (HDPE) were studied by Yasin et al., [18]. In their study, they found that 10 wt.% SCFs composites displayed supreme wear efficiency in SBF fluid conditions. Further, under the influence of seawater lubrication, the tribological behaviors of CF/PEEK were studied [19]. The result indicated that when the volume fraction of CF was about 10% then it greatly improved the wear and friction behaviors of the CF/PEEK composite. Additionally, Alagarraja et al., [20], studied the wear properties of composites using reinforced matrix via synthetic and natural fibers of carbon, PU, jute, sugarcane, glass, and banana. According to test results, foam-type sandwich materials' wear resistance characteristics built up when the foam and natural fibers materials were merged.

Therefore, nowadays different polymer-based composites are available in a broad range due to their crucial applications in various areas. The majority of past literature studies presented in Table 1 were mainly focused on carbon fibers reinforced bulk (rigid) polyurethane-based composites. However, in this study, the influence of SCFs-reinforced PU-foam-based composites was investigated. Here, the effects of different

contents of SCFs (0.5, 1.0, and 1.5 wt.%) on the mechanical (flexural strength and flexural modulus) and wear resistance properties of PU-SCFs foam-based composites were examined. Moreover, the morphology of broken and worn surfaces of pure PU foam and PU-SCF composites was characterized by a scanning electron microscope (SEM).

Table 1. Summarized past studies

No	Sample Code	Results	Ref.
1	GF, SiC, and Al$_2$O$_3$-reinforced PU	Under an applied load of 5 and 10 N and sliding distance of 100 m, GF, SiC, and Al$_2$O$_3$-fillers enhanced the wear resistance properties of PU.	[21]
2	CFPC NP/PU	The application of the NP/PU nanocomposite coating resulted in notable enhancements in the flexural strength and impact resistance of the CFPC, with improvements of 9% and 14.7%, respectively.	[22]
3	SGF/PU	The wear performance of SGF/PU composites shows that wear volume increases with higher fiber content, while the specific wear rate decreases with increased load.	[23]
4	CFR-PU	The PU foam composite board reinforced with carbon fibers (CFR-PU) exhibits enhanced toughness and improved resistance to deformation.	[12]
5	DS-CFs/RPU	The tensile strength, impact strength, and interfacial shear strength (ILSS) of the dendritic short carbon fibers reinforced polyurethane (RPU) composites exhibited increases of 41.3%, 81.2%, and 28.9%, respectively, in comparison to pure RPU.	[24]

2. MATERIAL AND METHOD

2.1. Short Carbon Fibers

Short carbon fibers with an average length of 6-12 mm were purchased from Dost Kimya, Türkiye. Polyol and isocyanate used were supplied by Kimpur, Türkiye. The SEM images of short carbon fibers are depicted below in Figure 1.
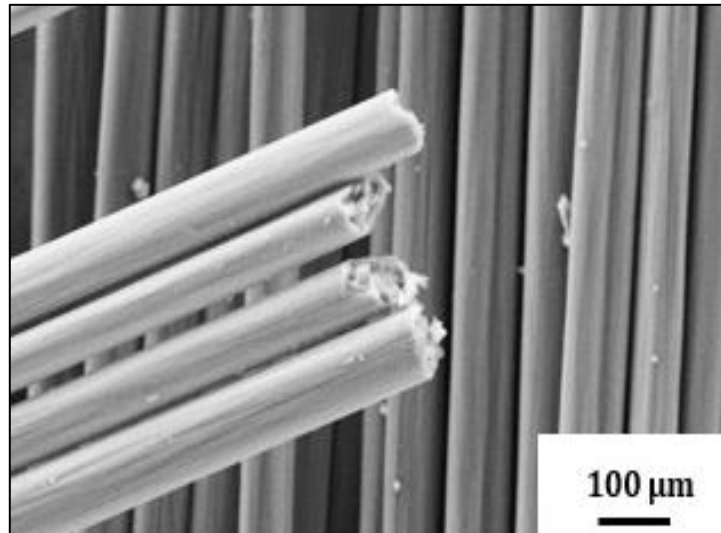

Figure 1. SEM images of short carbon fibers

2.2. Casting of Samples

Samples of PU-foam and PU-SCF composites were fabricated using a mold depicted below in Figure 2 depending on the compositions stated in Table 2. Different contents of SCFs (0.5, 1.0, and 1.5 wt.%) were homogeneously mixed with polymeric isocyanates in a beaker. Then, polyols that create curing are added to the homogenous mixture of SCFs and isocyanate. There was little time between homogenous mixing and casting of polyol. Thus, the composite mixture available in the liquid state was poured directly into the mold

after a quick mixing. Samples were cast evenly in the casting mold using the hand lay-up technique. Here, during the sample's preparation via the hand lay-up technique, there might be some limitations related to agglomeration due to the inability to ensure a homogeneous distribution of SCFs in the PU matrix. Thus, great care must be imposed in the composite production methods. The foaming reaction starts after curating and an increase in volume was observed. After the reaction was over, the samples were removed from the mold and ground by 240 grit sandpapers to prepare the samples according to ASTM D790 standard for the flexural bending test. These processes were carried out repeatedly for the production of each sample.

Table 2. Composition of composites

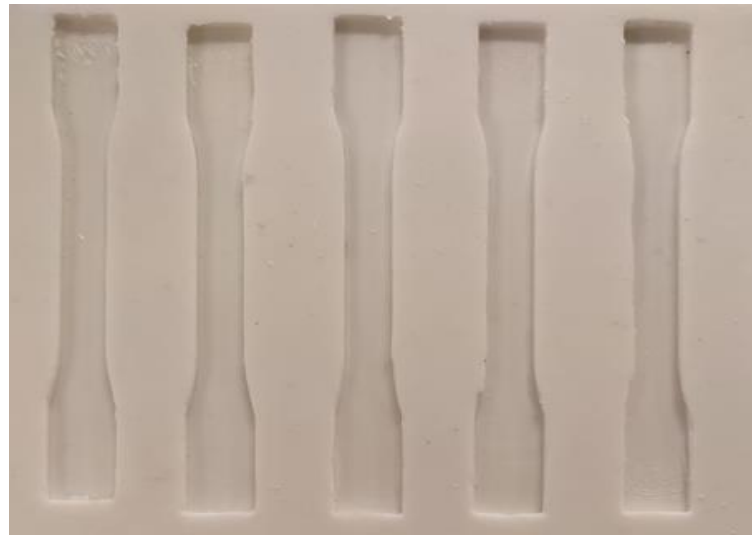| Sample Code	Short Carbon Fibers (SCFs)	Polyurethane (PU)
	Percentage (wt.%)	
PU	-	100
PU0.5SCF	0.5	99.5
PU1.0SCF	1.0	99
PU1.5SCF	1.5	98.5

Figure 2. Mold for Flexural test samples

Figure 3 shows the fabricated samples of composites and pure PU foam. Figures 3(a)-3(c) indicate PU foam-based composites reinforced with 1.5, 1.0, and 0.5 wt.% SCFs, respectively. A pure foam-based PU polymer sample was indicated in Figure 3(d).

Figure 3. PU-SCF foam-based composites and pure PU foam

3. CHARACTERIZATION

To facilitate the characterization of the mechanical properties, samples were fabricated with dimensions according to standards. The flexural bending and wear tests were conducted using machines illustrated in Figure 4. According to Figure 4(a), the flexural strength tests were carried out three times for each sample having a dimension of 158 mm × 13 mm × 4.5 mm at a constant speed of 2 mm/min using a Zwick Roell 600KN test device. During the test, the span length for each specimen is 127 mm. Mathematically the flexural strength "σ" and flexural modulus "E_F" of samples were analyzed via Eq. 1 and Eq. 2, respectively [25].

$$\sigma = \frac{3FL}{2wt^2} \tag{1}$$

$$E_F = \frac{mL^3}{4wt^3} \tag{2}$$

Where F is the applied load (N), L is the span length (mm), w designates sample width (mm), t designates the thickness of the specimens (mm), and m is the slope of the linear section in the load versus deformation curve.

On the other hand, wear tests were carried out by UTS Tribometer T10/20 apparatus as can be seen in Figure 4(b) under dry-sliding conditions. In the course of the wear test, an applied load of 5 N along with a stainless-steel ball diameter of 6 mm, a stroke of 10 mm, a sliding rate of 40 mm/s, and a sliding distance of 25 m were used. In addition, theoretically, the volumetric wear rate can also be calculated using Eq. 3. A scanning electron microscope (Zeiss Ultra Plus) was used to examine the morphology of damaged (i.e., broken and worn) surfaces of samples after damaged samples were coated with gold using a sputter coater (Quorum, Q150R ES Plus).

$$W_r = W_v = \frac{\frac{2ab}{3}c}{L} \tag{3}$$

where W_v designates volumetric wear loss (mm3/s), a is the stroke distance (mm), b represents wear width (mm), L designates sliding distance (mm), and c indicates wear depth (mm) [26,27].
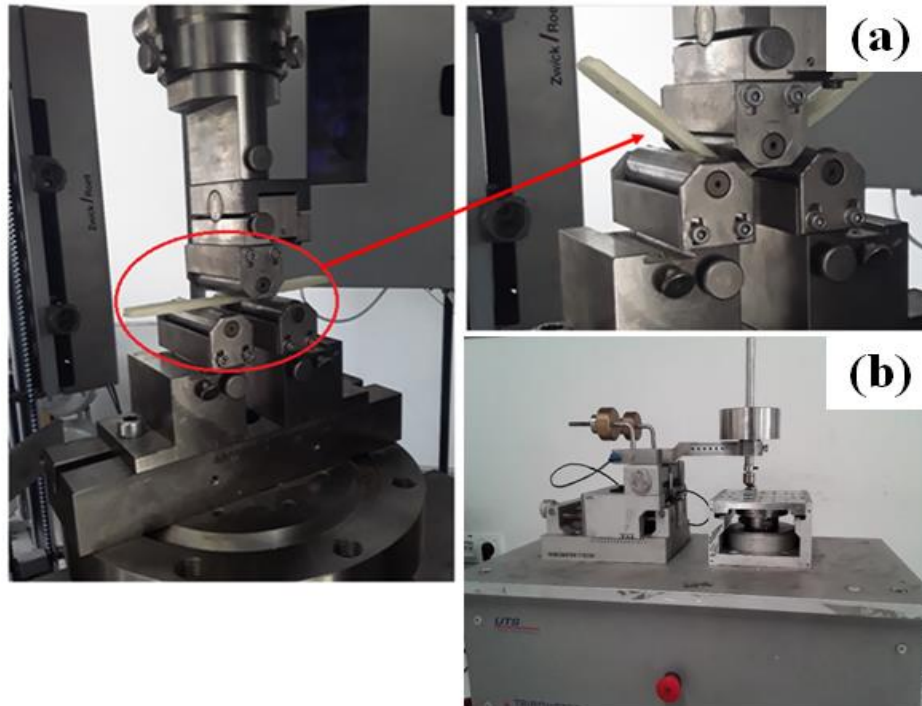

Figure 4. a) Zwick Roell flexural strength tester and b) UTS Tribometer T10/20 wear tester device

4. RESULTS AND DISCUSSION

4.1. Mechanical Properties

Figures 5(a) and 5(b) show the fracture surfaces of various contents of SCFs (1.0, and 0.5 wt.%) reinforced PU foam composites, respectively. In addition, the broken surface of neat PU foam is presented in Figure 5(c). The cause of the fracture is attributed to the existence of higher stress concentrations around a large number of pores resulting in PU matrix crack initiation. Also, it was said in the literature that the primary damage mechanism to appear is matrix crack initiation [14]. These micro PU matrix cracks originate from micro-pores formed during curing and tend to propagate and connect under applied load leading to SCF fracture and finally causing composite failure as can be noticed in Figure 5 [28].
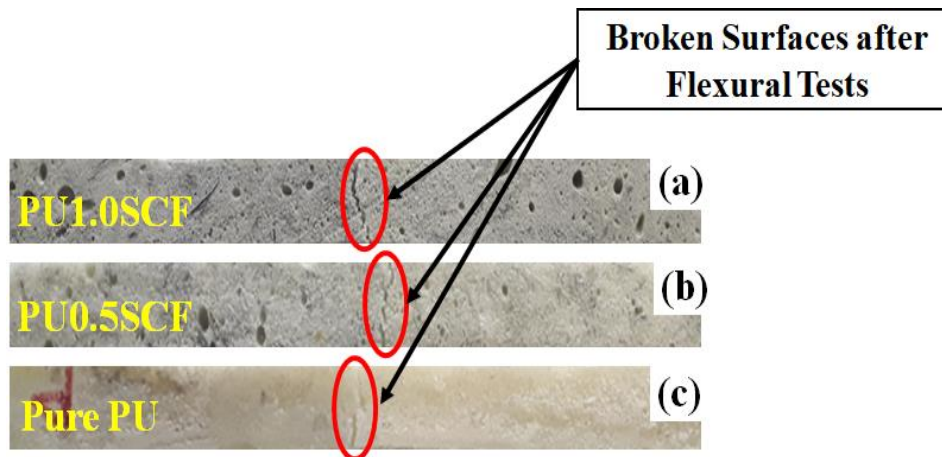

Figure 5. Flexural test results of pure PU foam and PU-SCF composites

Figure 6 expressed the force-deformation graphs of pure PU and PU composites reinforced with different contents of SCFs (0.5, 1.0, and 1.5 wt.%). As can be seen in the figures, a gradual increment in loading results in a notable increment in the load supporting of samples by gradual deformation. Thus, there were linear and nonlinear curves were noted in the load-deformation graph until the force reached its maximum peak value. After reaching the highest load point, the reinforced PU foam composites and PU-foam sample's force-deformation curve starts to decline considerably. This might be due to the presence of higher stress concentration and crack propagation factors around foam porosities [5]. Furthermore, as can be observed from the SEM image (i.e., Figure 7) the presence of weak interfacial bonding can be taken as a cause for the reduction of the load-carrying capacity of the PU-SCF composites compared with pure PU foam. And hence, these weak interfacial bonding between SCFs and PU matrix were responsible for the low load-carrying capacity of composites and also resulted in early deformation for SCFs incorporated composites than pure PU foam [14]. Thus, the maximum deformation of 5.95 mm was observed for pure PU foam at a peak load of nearly 142.33 N in contrast to all the samples illustrated in Figure 6. However, the addition of 0.5 wt.% SCFs into pure PU resulted in a deformation of 5.59 mm at a load of 61.62 N. Further adding of 1.5 wt.% SCFs in pure PU bring a reduction in the deformation by 37.21% compared to pure PU foam.

SEM observations were implemented on the fractured surfaces to verify the failure mechanism of samples. Figure 7(a) shows the presence of crushed PU matrix cells, porosities, and PU matrix cracks on the fractured surface of the PU foam sample. This is probably due to the absence of load-supporting fibers (SCFs). Figures 7(c) and 7(d) indicate the broken surfaces of PU1.0SCF and PU1.5SCF foam-based composites, respectively. Broken SCFs, PU matrix cracks, and broken composite pieces were noted for these samples after the flexural bending tests. On the other side, the PU0.5SCF composite (Figure 7(b)) has relatively better interfacial bonding between SCFs and PU matrixes as compared to both PU1.0SCF and PU1.5SCF. This might be due to as the contents of short carbon fibers increased; it was hard to mix them with the PU matrix because of the increase in viscosity. Hence, it resulted in poor dispersion of SCFs in the PU matrix. Also, voids are formed and shown in Figure 7(d) [5]. These defects are responsible for the reduction of the mechanical properties (flexural strength) of the composites.
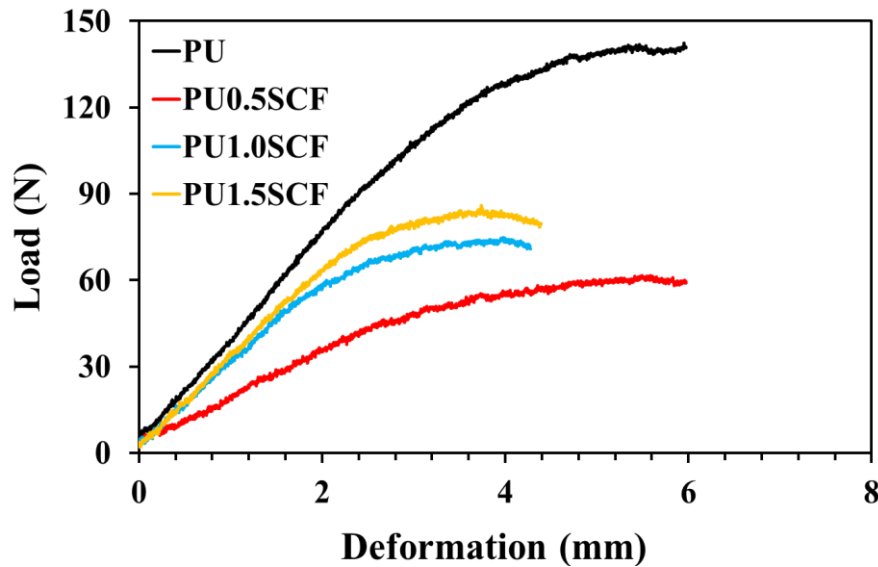
Figure 6. Load versus deformation curves for samples

On the contrary, when the fiber content is low, the possibility of diffusion of SCFs through the PU matrix is enhanced. Therefore, the probability of interfacial bond formation between fiber and matrix increased [28]. The SEM studies also indicate that in lower SCF-reinforced PU composites, damage to the matrix was more significant than fiber fracture. Conversely, in composites reinforced with higher SCFs, fiber damage was also notably evident.
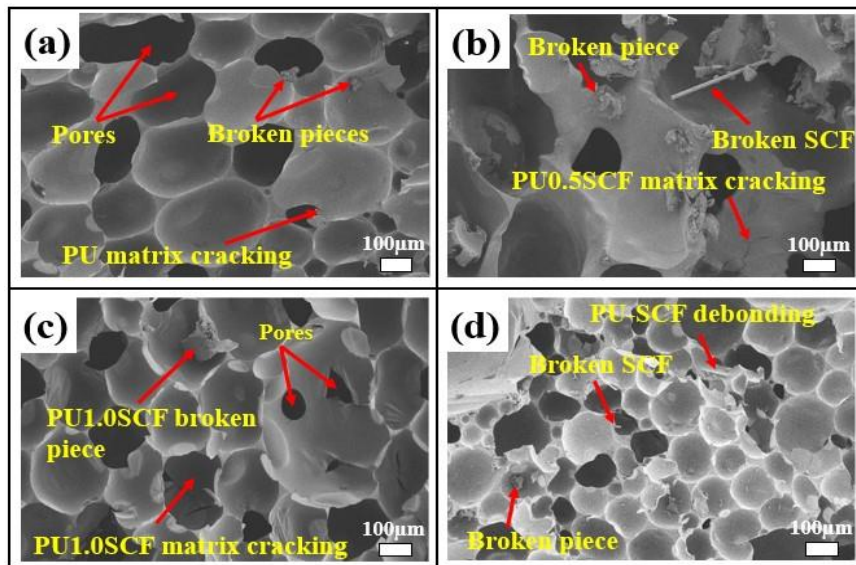

Figure 7. SEM images of broken surfaces of; (a) PU; (b) PU0.5SCF; (c) PU1.0SCF; (d) PU1.5SCF

Furthermore, the mechanical properties of the present samples were explained by conducting flexural bending tests. The flexural strength and modulus of pure PU polymer foam and PU-SCF composites are illustrated in Figure 8. As can be seen, it was determined that the maximum flexural strength was noticed for pure PU of 5.88 ± 1.57 MPa. In addition, the test result revealed the flexural strength of pure PU foam was better than PU0.5SCF and PU1.0SCF composite nearly by 15.52% and 173.5%, respectively. This might be due to, adding higher SCFs fillers as reinforcement into pure PU foam-based composites results in the agglomeration of fibers despite enormous care was given during the composite preparation, and hence, stress concentration increases around the irregular voids formed due to the agglomeration of fibers. Consequently, the mechanical strength of the material starts to deteriorate [5]. The other reason for the reduction in flexural strength with increment in SCF content is due to debonding, which occurs during the flexural bending test when the stress weakens the interactions between SCFs and the polyurethane matrix. This is shown in Figure 7(d), highlighting weak interfacial bonding. Consequently, the force transfer from the matrix to the fiber is

reduced, negatively impacting the flexural load-bearing capacity of the PU-SCF composite compared to the neat PU sample. Similar results were reported in the research work of Akgul et al. [29]. In their study, it was shown that the flexural strength of SCFs reinforced Polyester composite decreases with the increment of SCFs. In another study, it was also revealed that better flexural strength was observed in 5 wt.% carbon fiber reinforced polyester composite as compared to 10 wt.% [30]. On the other side, it was seen that the addition of SCFs into pure PU enhanced the flexural modulus of the reinforced PU composites. So, the composite having a higher content of SCFs (1.5 wt.%) (PU1.5SCF) became stiffer than composites with fewer contents of SCFs. For instance, incorporating 1.5 wt.% of SCFs into pure PU improved the flexural modulus of pure PU nearly by 91.36%. The study also found that 192.32 ± 153.98 MPa was the highest flexural modulus of the PU1.5SCF composite. Whereas, the lowest flexural modulus was reported for pure PU foam (100.5 ± 5.01 MPa).
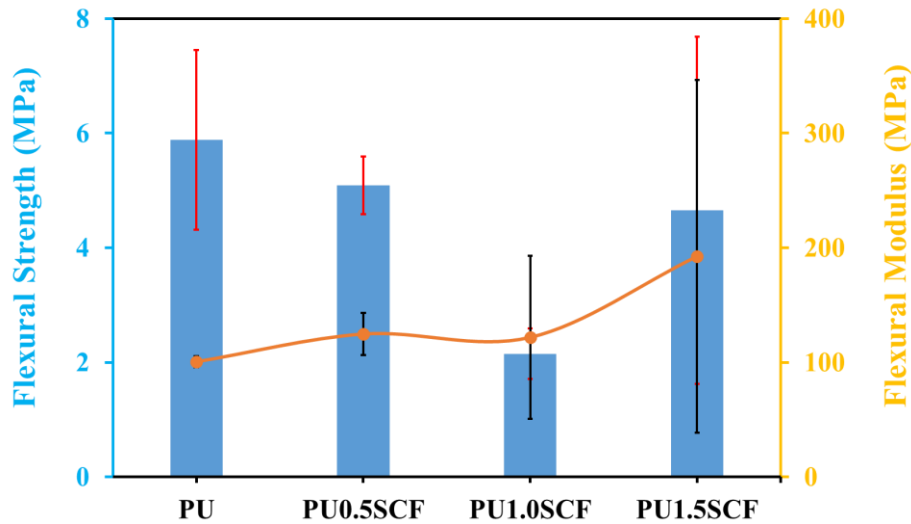

Figure 8. Flexural strength and flexural modulus of samples

4.2. Tribological Properties

The wear resistance results of pure PU foam and reinforced PU with different weight fractions of SCFs composites were indicated in Figure 9. According to test results, the highest wear resistance characteristics were noticed when 1.5 wt.% SCFs were added to the pure polyurethane matrix. This is attributed to the self-lubricating properties of short carbon fibers [16,18]. However, when the SCFs content decreased to 0.5 wt.% a remarkable reduction in the wear resistance was observed. This is due to the presence of lower contents of self-lubricating SCFs compared to samples with higher contents of SCFs (PU1.0SCF and PU1.5SCF). Additionally, as mentioned above the flexural modulus of the composite PU1.5SCF was improved by introducing higher contents of SCFs (1.5 wt.%) into pure PU compared to other samples. Thus, a higher modulus caused the sample to become stiffer and escalated wear resistance characteristics as well. So, as shown in Figure 9 the wear rate of PU1.5SCF was considerably lower in comparison to other samples.

SEM observations on worn surfaces of pure PU and PU-SCF foam-based composites were conducted and represented in Figure 10. The worn surface of the PU1.5SCF composite was relatively smooth and small size worn debris was examined as shown in Figure 10(d). This may prove higher SCFs content enhanced the wear resistance characteristics of composites. Therefore, when 1.5 wt.% SCFs were added to pure PU polymer foam; it led to an improvement in the wear resistance property approximately by 78.95%. Figure 10(c) shows, the worn surface of PU1.0SCF composite material. Here, delamination, wear debris, and broken short carbon fibers were observed. In addition, as depicted below Figure 10(a) indicates the worn surface of pure PU foam material. Here, higher contents of wear debris were noticed. Additionally, compared to all the samples the lowest wear resistance property was noticed for pure PU foam, (highest wear rate value of 0.228 mm3/m). This signifies SCF had a significant effect on the improvement of the wear resistance of composite materials. On the other hand, the worn surfaces of the PU0.5SCF composite are given in Figure 10(b). When 0.5 wt.% SCFs were added to the PU matrix, which resulted in a composite having a wear rate value of 0.164 mm3/m. The wear result of this study was in complete agreement with previous studies [16,18]. Further, the coefficient of friction (COF) created between contacting bodies had a notable effect on the wear properties of the contacted samples. Although applied load had a direct influence on the COF.

Nevertheless, in this study, the load value is constant for all experiments (5 N). However, the effect of COF can be defined as related to the content of SCF. Here, again considering Figure 9, it was shown because of an increment in SCF content led to a decrement in the COF. This might be related to the presence of a large number of stiff carbon fibers in the reinforced composite [25]. Thus, as demonstrated in Figure 9 the wear resistance characteristics of the composite samples are better than the pure PU foam. Therefore, the study investigates the least COF observed for PU1.5SCF with 1.52, while the highest COF of 2.22 noted for pure PU.
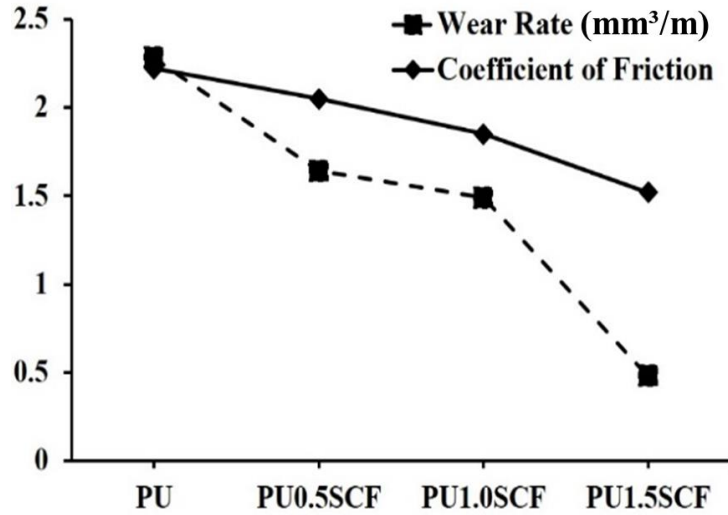

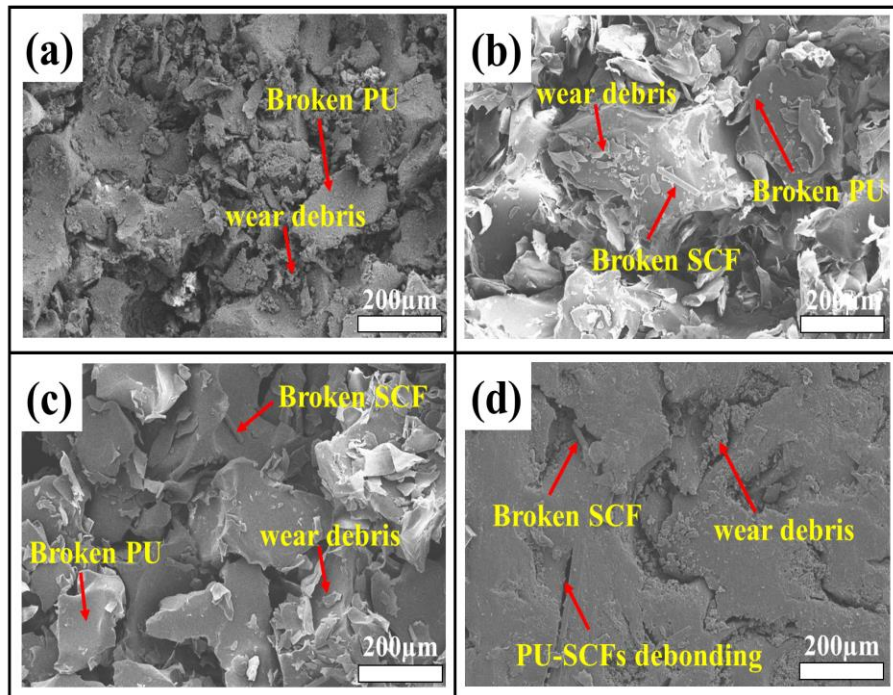Figure 9. Wear rate and coefficient of friction values for different samples

Figure 10. SEM images of worn surfaces of; (a) PU; (b) PU0.5SCF; (c) PU1.0SCF; (d) PU1.5SCF

5. CONCLUSIONS

The present study confirmed that the increment of short carbon fibers (SCFs) from (0.5-1.5 wt.%), resulted in a decrement in the flexural strength of SCFs reinforced polyurethane (PU) foam matrix composites. The addition of 0.5 wt.% SCFs into pure PU foam matrix cause higher flexural strength than 1.0 wt.% and 1.5 wt.% SCFs reinforced polyurethane foam composites. This was explained by the dispersion of SCFs in the PU matrix, stress concentration, and interfacial debonding factors. Whereas, incorporating various contents of SCFs into PU-based composite had a positive impact on enhancing the flexural modulus

of the composite. Moreover, this study found that the content of short carbon fibers had significant effects on the tribological characteristics of polyurethane foam-based composites. The wear resistance of the composites was increased nearly by 78.95% with the addition of 1.5 wt.% chopped carbon fibers into a pure PU foam matrix. Thus, a superior improvement in the wear resistance property was noticed for the PU1.5SCF composite. However, the lowest wear resistance was recorded for pure PU foam. This was attributed to the missing of self-lubricating reinforcement fibers like SCFs. Furthermore, a short carbon fiber content of 1.5 wt.% reinforced pure PU foam matrix had smoother worn surfaces compared to the worn surfaces of both pure PU foam (PU) and composite materials (PU0.5SCF and PU1.0SCF).

ACKNOWLEDGMENTS

REFERENCES

[1] M. Çakır, B. Berberoğlu, E-Cam Elyaf Takviyeli Epoksi Matrisli Kompozit Malzemelerin Elyaf Oranındaki Artış İle Mekanik Özelliklerindeki Değişimlerin İncelenmesi, El-Cezeri Journal of Science and Engineering, 5(3) 2018 734–740.

[2] S. A. Kumar, A. Lakshamankumar, K. Balasivaramareddy, B. Ramprasath, Fabrication and study on carbon fiber with epoxy and vinyl ester resins, in IOP Conference Series: Materials Science and Engineering, 402(1) 2018, 012160.

[3] S. Sulaiman, R. Yunus, N. A. Ibrahim, F. Rezaei, Effect of hardener on mechanical properties of carbon fibre reinforced phenolic resin composites, Journal of Engineering Science and Technology, 3(1) (2008) 79–86.

[4] N. Chowdhury, G. M. Faysal, T. Islam, H. Rahman, F. Yeasmin, A Study on Mechanical Properties of Carbon Fiber Reinforced Polymer Composite, 2020.

[5] A. Olszewski, P. Nowak, P. Kosmela, Lukasz Piszczyk, Characterization of Highly Filled Glass Fiber/Carbon Fiber Polyurethane Composites with the Addition of Bio-Polyol Obtained through Biomass Liquefaction, Materials, 14(6) (2021) 1391.

[6] K. Karthik, I. I. Ahmed, R. R. Renish, Experimental Investigation of Polymer Matrix for Heat Distortion Temperature Test, TechnoChem, 3(2), (2017) 243-251.

[7] M. K. Sain, P. Saraswat, A. Kumar, A. M. Vemula, Fabrication and characterization of homogenous and functionally graded glass fiber reinforced polymer composites, Materials Today: Proceedings, 66 (2022) 3602–3608.

[8] S. Jiang, Q. Li, Y. Zhao, J. Wang, M. Kang, Effect of surface silanization of carbon fiber on mechanical properties of carbon fiber reinforced polyurethane composites, Composites Science and Technology, 110 (2015) 87–94.

[9] V. Yakushin, U. Stirna, L. Bel'Kova, L. Deme, I. Sevastyanova, Properties of rigid polyurethane foams filled with milled carbon fibers, Mechanics of Composite Materials, 46(6) 2011, 679–688.

[10] S. K. Khanna, S. Gopalan, Reinforced polyurethane flexible foams, WIT Transactions on State-of-the-art in Science and Engineering, 20 (2005).

[11] A. R. Karaeva, N. V. Kazennov, V. Z. Mordkovich, S. A. Urvanov, E. A. Zhukova, Carbon Fiber-Reinforced Polyurethane Composites with Modified Carbon–Polymer Interface, in Proceedings of the Scientific-Practical Conference" Research and Development-2016" (Springer, Cham), 415–420, 2018.

[12] Y.-C. Chuang, T.-T. Li, C.-H. Huang, C.-L. Huang, C.-W. Lou, Y.-S. Chen, J.-H. Lin, Protective rigid fiber-reinforced polyurethane foam composite boards: Sound absorption, drop-weight impact and mechanical properties, Fibers and Polymers, 17(12) (2016) 2116–2123.

[13] L. Wang, W. X. Ding, Y. Sun, Effect of different fiber materials on mechanical properties of polyurethane composites, in 2015 2nd International Workshop on Materials Engineering and Computer Sciences, 406–411, (2015).

[14] T. A. Sebaey, D. K. Rajak, H. Mehboob, Internally stiffened foam-filled carbon fiber reinforced composite tubes under impact loading for energy absorption applications, Composite Structures, 255 (2021) 112910.

[15] J. Li, C. L. Cai, Friction and wear properties of carbon fiber reinforced polypropylene composites, in Advanced Materials Research (Trans Tech Publ), 284 (2011) 2380–2383.

[16] N. W. Khun, H. Zhang, L. H. Lim, C. Y. Yue, X. Hu, J. Yang, Tribological properties of short carbon fibers reinforced epoxy composites, Friction, 2(3), 2014, 226–239.

[17] G. Zhao, T. Wang, Q. Wang, Surface modification of carbon fiber and its effects on the mechanical and tribological properties of the polyurethane composites, Polymer composites, 32(11) (2011) 1726–1733.

[18] Y. Akgul, H. Ahlatci, M. E. Turan, M. A. Erden, Y. Sun, A. Kilic, Influence of carbon fiber content on bio-tribological performances of high-density polyethylene, Materials Research Express, 6(12), (2019) 125307.

[19] B. Chen, J. Wang, F. Yan, Comparative investigation on the tribological behaviors of CF/PEEK composites under sea water lubrication, Tribology International, 52 (2012) 170–177.

[20] K. Alagarraja, B. V. Ramnath, A. R. Prasad, E. Naveen, N. Ramanan, Wear behaviour of foam and fiber based sandwich composite–A review, Materials Today: Proceedings, 2021.

[21] S. Koçak, Y. Kaplan, Wear Characterization of Reinforced Polyurethane Composites Produced via Vacuum Casting, 45(6), (2021) 824–831.

[22] D. Zhang, K. Cai, J. Pan, L. J. Lee, J. M. Castro, A novel carbon nanotube nanopaper polyurethane coating for fiber reinforced composite substrates, Polymer Engineering & Sci, 61(4), 2021, 1041-1049.

[23] B. Suresha, G. Chandramohan, N. Dayananda Jawali, Siddaramaiah, Effect of short glass fiber content on three-body abrasive wear behaviour of polyurethane composites, Journal of Composite Materials, 41(22) (2007) 2701-2713,.

[24] R. Ma, W. Li, M. Huang, M. Feng, X. Liu, The reinforcing effects of dendritic short carbon fibers for rigid polyurethane composites, Composites Science and Technology, 170 (2019) 128–134.

[25] Y. Akgul, Y. A. Younes Alsbaaıe, A. K. Etıcha, H. Cug, Mechanical and tribological behaviors of chopped carbon/glass fiber reinforced hybrid epoxy composites, Mechanics Of Advanced Composite Structures, 9(2), 2022, 349–358.

[26] M. A. Erden, M. F. Tasliyan, Y. Akgul, Effect of TiC, TiN, and TiCN on microstructural, mechanical and tribological Properties of PM steels, Science of Sintering, 53(4), 2021.

[27] Y. Akgül, Effect of hydrothermal carbons content on wear propertıes of polyethylene matrıx composıtes, Eskişehir Technical University Journal of Science and Technology A-Applied Sciences and Engineering, 23(3) (2022) 207–215.

[28] Z. Haber, On the use of polyurethane matrix carbon fiber composites for strengthening concrete structures, 2010. Electronic Theses and Dissertations, 4368, https://stars.library.ucf.edu/etd/4368

[29] Y. Akgül, M. E. Yalçın, A. K. Eticha, Effect of Chopped Carbon Fibers Amount on the Mechanical and Tribological Properties of Polyester Matrix Composite, Düzce Üniversitesi Bilim ve Teknoloji Dergisi, 11(1) (2023) 189–198.

[30] R. B. Durairaj, G. Mageshwaran, V. Sriram, Investigation on mechanical properties of glass and carbon fiber reinforced with polyester resin composite, International Journal of ChemTech Research, 9(06) (2016) 424–431.

Manufacturing Technologies and Applications
MATECA

Investigation of the Bonding Performance of Parts Produced by FDM and SLA 3D Printing Methods

Salih Dağlı[1,*] iD

[1]Department of Mechanical Engineering, Engineering and Architecture Faculty, Sinop University, Sinop, Türkiye

ABSTRACT

In this study, the bonding properties of parts produced using additive manufacturing methods, which are frequently preferred today, were investigated. In this context, parts were produced by Stereolithography (SLA) and Fused Deposition Modelling (FDM) methods. The mechanical properties of the produced materials were determined by tensile test according to ASTM D638 standard. Afterwards, these parts were bonded in different combinations and the mechanical properties of the joints were determined according to ASTM D1002 standard. As a result, the tensile strength of Polylactic Acid (PLA) parts produced by FDM method was 65% higher than that of PhotoPolymer Resin (PPR) parts produced by SLA method, while the strain rates of PPR materials were 85% higher than PLA materials. When the failure load values obtained after the tensile test of the bonded joint specimens were examined, the best mechanical performance was obtained as 3086 N in the combination of PLA and composite material. The lowest damage load occurred in the combination of PPR and PLA material. When the displacement data resulting from the failure load were analysed, the highest values were obtained in the PPR-PPR material combination. In conclusion, bonding can be used for joining parts produced by additive manufacturing, but the choice of material should be based on the application.

Keywords: Additive manufacturing, Stereolithography (SLA), Fused deposition modelling (FDM), PLA, Adhesive joints, Failure load

FDM ve SLA 3D Baskı Yöntemleriyle Üretilen Parçaların Yapıştırma Performansının İncelenmesi

ÖZET

Bu çalışmada, günümüzde sıklıkla tercih edilen eklemeli imalat yöntemleri kullanılarak üretilen parçaların yapıştırma özellikleri incelenmiştir. Bu kapsamda Stereolitografi (SLA) ve Eriyik Yığma Modelleme (FDM) yöntemleri ile parçalar üretilmiştir. Üretilen malzemelerin mekanik özellikleri ASTM D638 standartına göre gerçekleştirilen çekme testi ile belirlenmiştir. Sonrasında bu parçalar farklı kombinasyonlarda yapıştırılarak bağlantıların mekanik özellikleri ASTM D1002 standartına göre belirlenmiştir. Sonuç olarak, FDM yöntemi ile üretilen Polylactic Acid (PLA) parçaların çekme dayanımları SLA yöntemi ile üretilen PhotoPolymer Resin (PPR) parçalara nazaran %65 oranında daha yüksek iken, PPR malzemelerinde şekil değiştirme oranlarının PLA malzemeye göre %85 oranında daha yüksek olduğu belirlenmiştir. Yapıştırma ile birleştirme işlemi yapılan bağlantı numunelerinin çekme işlemi sonrasında elde edilen hasar yükü değerleri incelendiğinde en iyi mekanik performans PLA ve kompozit malzeme birleşiminde 3086 N olarak elde edilmiştir. En düşük hasar yükü ise PPR ve PLA malzeme birleşiminde meydana gelmiştir. Hasar yükü sonucunda oluşan yer değiştirme verileri incelendiğinde ise PPR-PPR malzeme birleşiminde en yüksek değerler elde edilmiştir. Sonuç olarak, eklemeli imalatla üretilen parçaların birleştirilmesinde yapıştırma yöntemi kullanılabilir fakat malzeme seçiminin uygulamaya göre yapılması gerekmektedir.

Anahtar Kelimeler: Eklemeli imalat, Stereolitografi (SLA), Eriyik Yığma Modeleme (FDM), PLA, Yapıştırma bağlantıları, Hasar yükü

1. INTRODUCTION

In recent years, additive manufacturing (AM) technologies have led to revolutionary developments in many fields from industrial applications to medical applications such as dental and prosthesis. The additive manufacturing method, which can produce the desired products using 3D design (CAD) data, is frequently preferred in many industrial applications today due to its minimum material usage (low volume), acceleration of production processes, direct end use and affordable costs [1]. This method, also known as rapid prototyping, enables the production of parts with improved design and rapid production [2,3]. Also, the more advantages of the method are as follows: (a) the designed parts can be produced directly without any

process, (b) the internal structures of the parts to be produced can be created in full and hollow forms, (c) the product development stages can be reduced, (d) the parts can be manufactured anywhere without the need for large areas, and (e) instant production can be made according to customer demand [4,5] . In addition to new production, additive manufacturing methods are also used in applications such as part repair and the creation of additional structures to existing products [6].

Today, various additive manufacturing methods such as stereolithography (SLA), selective laser melting (SLE), direct metal laser sintering/melting (DMLS), fused deposition modeling (FDM) are used in industrial applications. These methods differ from each other in terms of the way materials are used, layer formation, part creation and the working process [7]. Some methods create parts by melting layers (such as SLM), while others form layers by solidifying a liquid material [8].

SLA has become one of the most widely used additive manufacturing technologies in recent years due to its superior features. In the SLA technique, photopolymer resin in liquid form is selectively cured layer by layer using a laser beam of a specific wavelength [9]. This process occurs as the laser initiates a photopolymerization reaction in the resin. The material solidifies in the regions where the laser is scanned vectorially, forming layers. These layers stack on top of each other, creating three-dimensional polymer structures with high dimensional accuracy [10,11]. This process enables the production of complex geometries, enabling applications that require high precision in areas such as biomedical, engineering and design. SLA technology offers much higher resolution compared to other 3D printing technologies used in industrial applications, enabling the production of parts with fine details, precise surface features and very low dimensional values [12]. Thanks to this method, parts with very complex geometries that cannot be produced with traditional methods can be easily produced with the desired technical specifications.

The FDM method is based on the principle of manufacturing parts in a layered manner by melting the polymeric material in the nozzle head at a certain temperature set in accordance with the process, and then moving the molten material in the profile defined in the machine to form layers [2]. Depending on the working principle of the FDM method, the production materials must have the ability to solidify by losing heat in a short time after they are melted in the nozzle head and transferred to the production table. Thermoplastic materials are used to meet this requirement in the FDM method. Thermoplastic materials are divided into Polyethylene Terephthalate Glycol (PETG), Acrylonitrile Butadiene Styrene (ABS) and Polylactic Acid (PLA) with different physical and chemical properties [13,14]. The variety of materials provides the opportunity to choose according to the properties of the part to be produced. Among thermoplastic materials, PLA is the most preferred material type in 3D manufacturing applications due to its low deformability in the production of large-sized parts, its complete biodegradability, its lightweight structure and high strength [15].

The assembly of parts produced using SLA and FDM technology is very important for the usability of this method. Considering the production of mechanical components consisting of many parts today, it is necessary to offer comprehensive solutions about joining processes. Problems are often encountered during the joining of polymer structured parts produced using additive manufacturing methods with traditional methods such as rivets and bolts. In riveting processes applied to these parts, the parts break and their structures deteriorate due to the instantaneous force applied suddenly. In bolting processes, while the holes reduce the load resistance of the part, cracks occur in the areas where the nut contacts [16]. Adhesive joints are preferred in applications due to their advantages such as providing solutions to the problems encountered in traditional joining methods, joining materials with different properties, and equal distribution of stresses to occur [17,18]. In order to efficiently utilize the advantages of the bonding method, the selection of the appropriate adhesive material and the geometry design in the bonding area play a critical role [19,20]. The manufacturing materials of the bonded parts and the overlap length of the bonding area are among the most critical factors determining the mechanical properties of adhesive joints [21]. Khosravani et al. [22] investigated the effects of device speed, nozzle temperature, and adhesive thickness on the mechanical properties of adhesive joints. Among the adhesive thickness values used in their study (0.2, 0.3, and 0.4 mm), they determined that a thickness of 0.2 mm provided the best performance. Gültekin et al. [21] examined the effects of manufacturing parameters and overlap length on the mechanical properties of PLA joints with different printing angles and infill ratios. Their study found that an increase in overlap length led to an increase in failure load. Additionally, they observed that increasing the infill ratio from 75% to 100% resulted in tensile strength improvements of 6.3% and 7.4%, respectively. Çoban et al. [23] investigated the mechanical effects of various parameters in adhesive bonding of PLA parts using adhesives with different strength properties. Their study examined factors such as infill ratio, adhesive thickness, and surface abrasion applied to the bonding area. They concluded that the type and thickness of the adhesive, as well as the surface abrasion process applied to the bonding area, significantly influence the mechanical properties of

adhesive joints. Atahan and Apalak [24] investigated the effect of bonding process on the strength of single lap joints in PLA specimens. In this context, they performed tensile, three and four point compression tests and observed that the strength increased slightly with the increase in loading rate. Dhilipkumar et al. [25] investigated the mechanical and vibration properties of doped parts with different stress ratios produced by FDM method using graphene doped adhesive in different geometric shapes. They determined that the 0 stress direction has higher tensile strength compared to other stress directions. They also observed that graphene reinforcement of the adhesive content increased the strength of single-lap bonded joints by 61.18%.

Using the bonding process to join dissimilar materials such as PPR and PLA combines the properties of two different materials to create a more functional and durable structure. When fragile parts such as PLA are considered, bonding processes result in less thermal and mechanical stresses than welding, bolted, etc. joining methods. In addition, PPR and PLA parts produced by additive manufacturing often have complex geometries, which can make mechanical joining difficult. Bonding offers an ideal solution to accommodate the different surface structures of both materials, resulting in more aesthetic and functional joints.

When the studies summarized above are examined, it is observed that there are numerous studies involving bonding applications with PLA materials. However, it has been noted that studies comparatively investigating the mechanical properties of parts produced from different materials are quite limited. Therefore, in this study, the mechanical properties of parts produced using SLA technology, which is underrepresented in the literature, were examined in detail by performing bonding processes with other materials. In this context, tensile specimens and joint specimens were produced from PPR and PLA materials using SLA and FDM methods, and bonding processes were applied. Subsequently, tensile tests were conducted to determine the mechanical properties of the bonded parts.

2. MATERIAL AND METHOD

2.1. Material

UV liquid resin is widely used in next-generation 3D printing technologies due to its high precision and surface tolerances. In the conducted study, UV-sensitive resin was preferred for its advantages, such as low surface roughness and high printing accuracy. The UV resin used in this study is the transparent UV Standard liquid resin produced by Anycubic. The technical specifications provided by the manufacturer for the product are presented in the table below.

Table 1. Properties of the used UV liquid resin material

Base material	Resin
Curing Wavelength	405 nm
Viscosity	150-200 mPa.s
Solid Density	1.05-1.25 g/cm^3
Tensile Strength	36-45 MPa
Elongation at break	8-12 %
Shrinkage	4.5-5.5 %
Hardness	82D

PLA material is a type of thermoplastic that is used as a building material in parts produced by FDM method and is produced from renewable resources and has the ability to dissolve in nature. In the study, PLA filament was used for the materials to be produced with 3D printer due to its easy availability, low cost and environmental friendliness. The technical values of the Anycubic brand PLA filament used are given in Table 2.

Table 2. Material properties of the used filament

Diameter	1.75 mm
Density	1.23 g/cm^3
Printing Temperature	190-230 °C
Tensile Strength	61 MPa
Elongation at break	3.8 %
Hardness	81D

In order to produce the joint specimens, carbon fiber fabric reinforced composite plates were used as a different material type in the bonding process and the mechanical properties of the composite materials used are given in Table 3 [26]. The composite materials have a carbon fiber content of 245 g.m^2 3k and were produced using vacuum infusion method.

Table 3. Mechanical properties of carbon fiber composite

E_1 (GPa)	$72^{\pm2.8}$
E_2 (GPa)	$72^{\pm2.8}$
G_{12} (GPa)	$5^{\pm0.3}$
ν_{12}	0.1
σ_{12} (MPa)	$650^{\pm28}$
τ_{12} (MPa)	$90^{\pm4.5}$

Araldite 2011 (Huntsman Advanced Materials Co., Ltd.) brand structural adhesive was utilized to bond the joint specimens with varying material properties. Its technical specifications are provided in Table 4 [27]. The two-component Araldite 2011 type adhesive is composed of epoxy and hardener (1:0.8 ratio), and it cures at 60°C [17].

Table 4. Technical properties of the used adhesive

Tensile Strength	33 MPa
Elasticity Modulus	1600 MPa
Poisson's Ratio	0.43
Curing Condition	60 ℃-75 min

2.2. Experimental Method

In this study, production was carried out using an Anycubic Photon Mono X brand SLA 3D printer and its associated equipment (Figure 1). Joint samples with dimensions of 25x125x5 mm were produced using Anycubic Standard UV precision resin. The production parameters for the SLA 3D printer were set to a layer thickness of 0.05 mm and a z-axis travel speed of 2 mm/s. After production, the resin residues on the parts were removed by washing them in a cleaning device with agitation using isopropyl alcohol for 6 minutes. Subsequently, the samples were cured under a UV LED lamp, with 3 minutes of clockwise rotation and 3 minutes of counterclockwise rotation.

Model Drawing → **SLA Printing Settings & Preview** → **SLA Printing Machine** → **Wash & Cure** → **PPR Final Product**
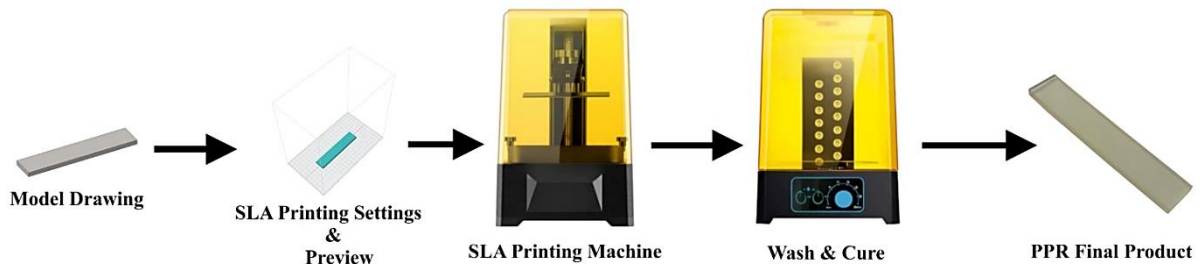
Figure 1. Part production process with SLA method

The PLA plates to be bonded were produced on Anycubic brand Kobra Combo 3 model FDM type printer (Figure 2). In the production of the parts; device nozzle temperature 220°C, layer thickness 0.12 mm, table temperature 70°C were used.
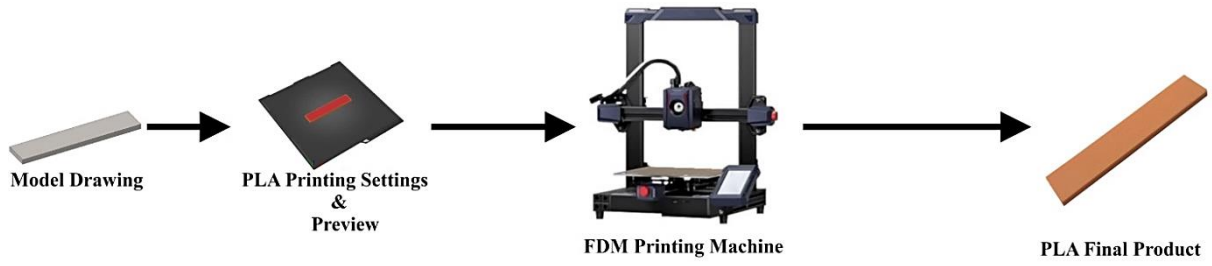
Figure 2. Part production process with FDM method

Care was taken to ensure that the produced PPR and PLA joint specimens were not exposed to external environmental factors (such as humidity and temperature) until the bonding and testing processes were completed.
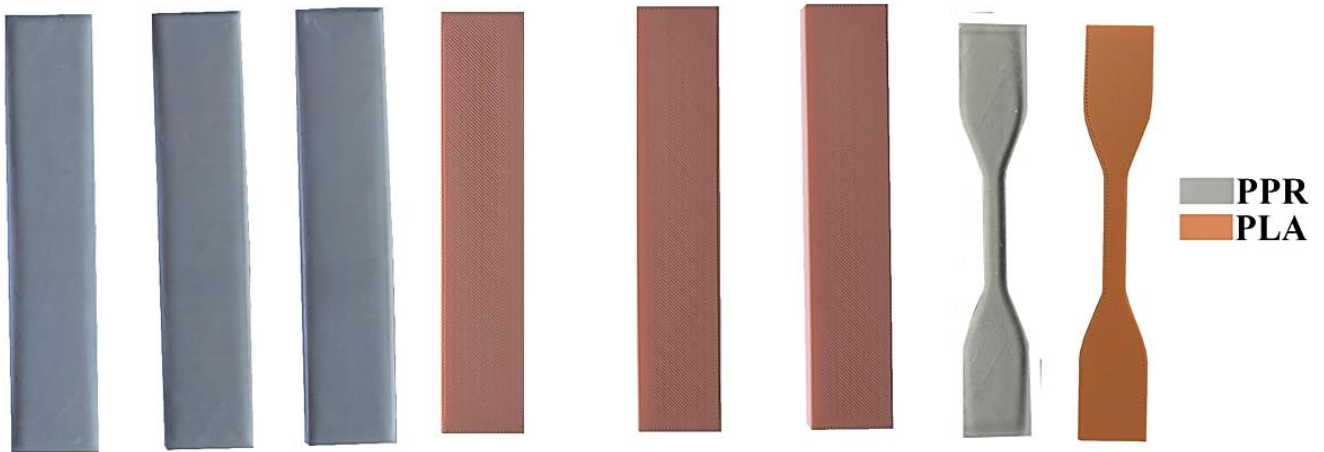

Figure 3. Production of PPR-PLA bonded plate and tensile bulk test specimens

After the production of PPR and PLA samples, the production phase of adhesively bonded joint was started. The model of the single-lap joint system to be produced is shown in Figure 4. The length, width and overlap length (L_o) of the single-lap adhesive joint specimens to be used in the application were produced as 125 mm, 25 mm and 25 mm, respectively.
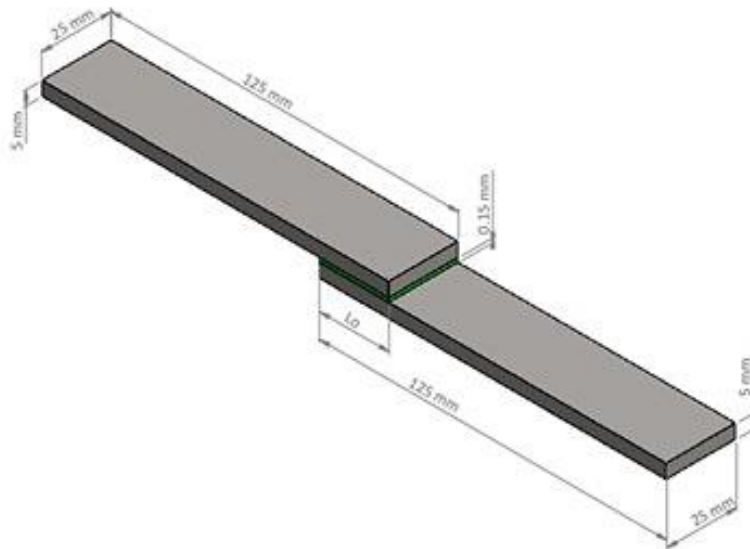
Figure 4. Joint geometry of the adhesion model

During the bonding application, mold and separator equipment were used to adjust the adhesive thickness and the distance of the bonding zone. Silicone lubrication was applied to the equipment to be used and the bonding process started. The bonding area of PPR and PLA plates was cleaned with isopropyl alcohol before the process. The parts were waited for a while to dry after cleaning. Then, the adhesive was applied to the bonding area of the parts with the help of a gun. The adhesive thickness and overlap length of the samples were adjusted using auxiliary equipment. Finally, the bonded parts were placed in an oven at 60°C for 75 minutes for the curing process. After the curing process, the specimens were cooled at room temperature and the overflowing adhesives were cleaned from the joint of the parts (Figure 5).
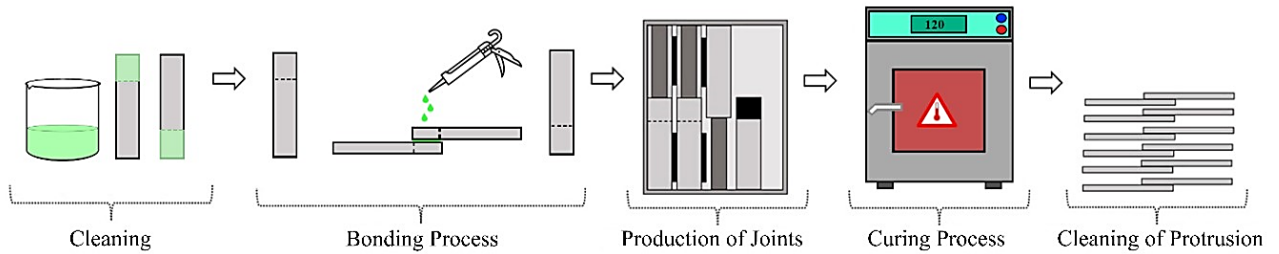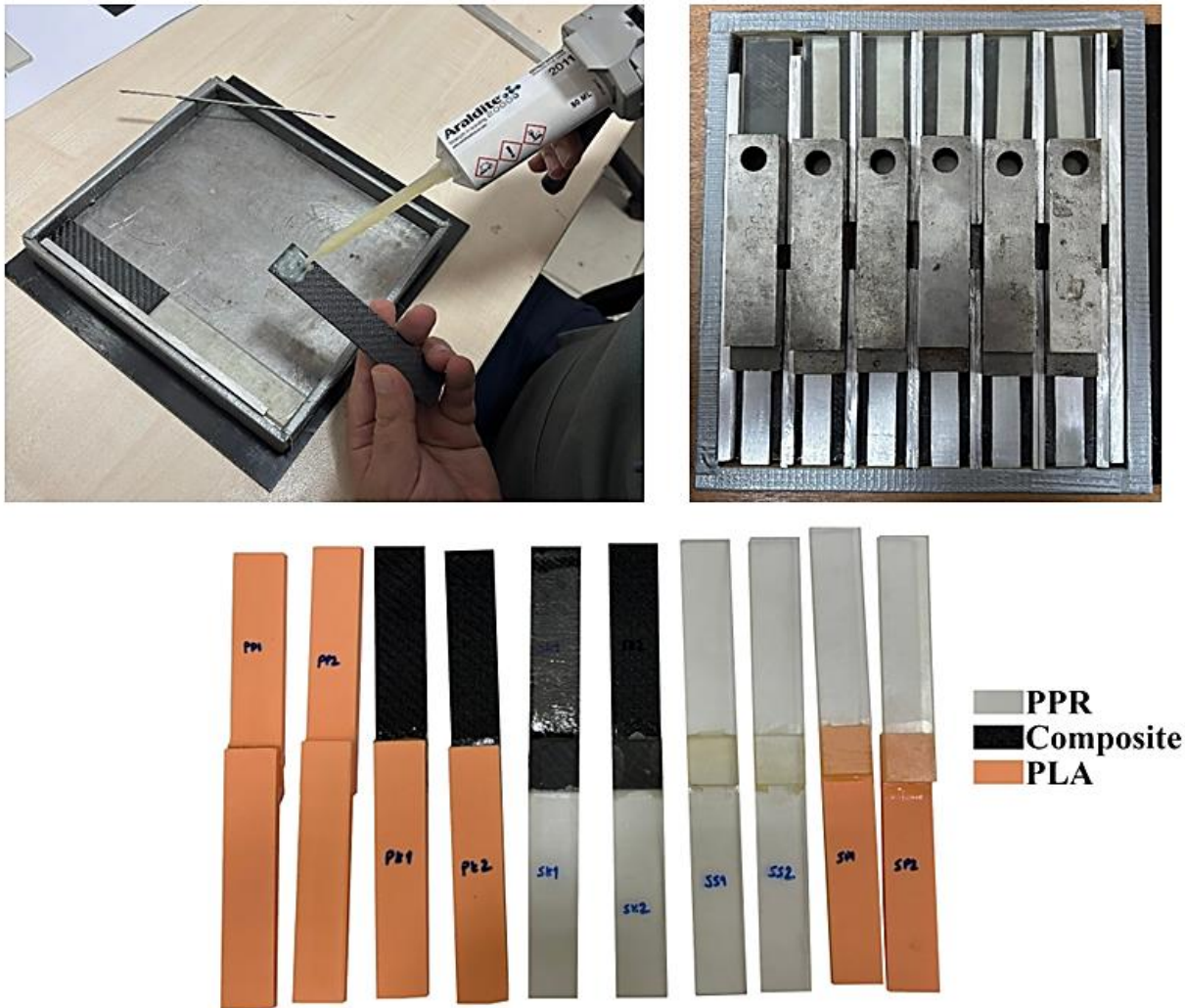

Figure 5. Bonding process

Figure 6. Production of adhesive specimens

The experimental parameters of the fabricated adhesive joint specimens are given in Table 5.

Table 5. Experimental parameters

Material	Sample Code
PPR-PPR	SS
PPR-PLA	SP
PPR-Composite	SK
PLA-PLA	PP
PLA-Composite	PK

The PPR and PLA tensile specimens were tested in Shimadzu tensile testing machine at a tensile speed of 5 mm/min. The bonded joint specimens were tested at a tensile speed of 1 mm/min on the same machine. For each parameter, 3 specimens were tested to obtain more accurate results. The application stage of the tensile testing process is given in Figure 7.

Figure 7. The tensile testing process for tensile and adhesive specimens

3. RESULTS AND DISCUSSION

3.1. Tensile Test Results of PPR and PLA Specimens

The stress-strain results obtained from the tensile tests applied to PPR and PLA bulk tensile specimens are shown in Figure 8.
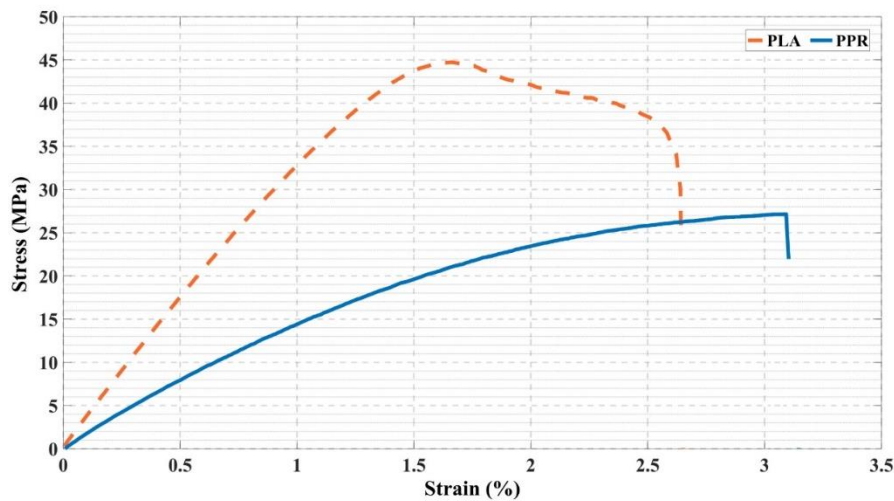

Figure 8. The stress-strain results of the PPR and PLA bulk specimens

The tensile strength, modulus of elasticity, and strain values of the PPR and PLA bulk parts were determined from the true stress-strain graphs obtained after the tensile test. The averages of the data determined as a result of the tensile test are provided in Table 6.

Table 6. The mechanical properties of PPR and PLA bulk specimens

Sample	Tensile Strength (MPa)	Elongation (%)	Elasticity Modulus (MPa)
PPR	27.13	3.09	784
PLA	44.77	1.66	1450

When comparing the mechanical properties of PPR and PLA tensile specimens provided in Figure 8 and Table 6, it is observed that PLA material demonstrates higher mechanical performance compared to PPR material. Upon examining the modulus of elasticity values obtained from the tensile test, it was determined that PLA specimens are 85% higher than PPR specimens. At this point, it is evident that PLA specimens have a more rigid structure due to their high modulus of elasticity. Additionally, the tensile strength of PLA specimens was found to be 65% higher than that of PPR specimens. The higher strength and rigidity of PLA specimens can be attributed to the interwoven bonding of layers with filaments, which enhances the material's overall strength and stiffness. In contrast, PPR specimens lack any binding agent between their internal layers, resulting in lower mechanical properties compared to PLA specimens [22]. Although PLA specimens exhibit higher strength values, they show lower elongation before fracture. Furthermore, a noticeable decrease in strength was observed in PLA specimens after reaching a distinct yield point. Considering this behavior, it can be concluded that parts produced from PLA material undergo brittle fracture. On the other hand, PPR specimens demonstrate 86% higher elongation compared to PLA specimens. Therefore, PPR materials exhibit a more ductile behavior compared to PLA materials. Additionally, the graph indicates that PPR specimens undergo softer deformation. In conclusion, while PLA materials possess higher tensile strength and rigidity, PPR materials are more ductile and have greater deformation capability.

3.2. Tensile Test Results of Single Lap Joint (SLJ) Specimens

The average failure loads and displacement (elongation) values determined after the tensile testing of single-lap joint (SLJ) adhesive joint specimens, produced by bonding PPR and PLA materials with each other and in alternating configurations, are shown in Figure 9. Upon evaluating the findings, it was determined that the failure loads in the joints varied depending on the types of materials bonded.
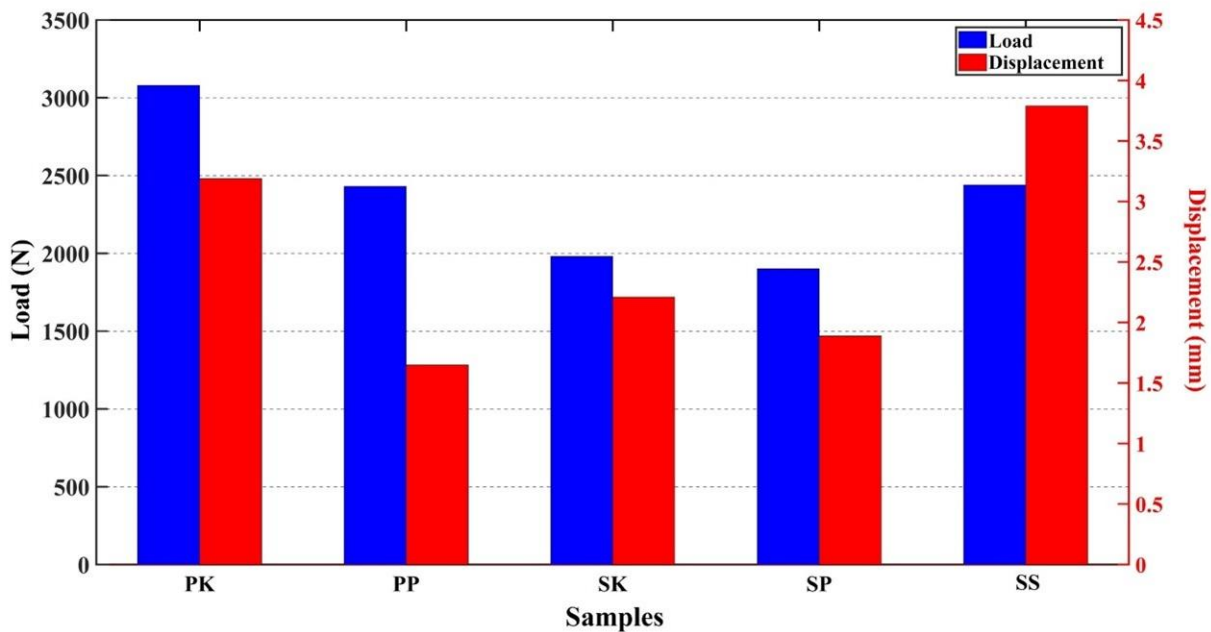

Figure 9. Tensile results of the SLJ adhesive specimens

When examining the results of the single-lap bonded joint specimens provided in Figure 9, it was determined that the PK (PLA-Composite) specimens exhibited the highest strength performance. This high strength performance was achieved due to the high elasticity values of the PLA and composite materials used in these specimens. Additionally, the surface roughness of the PLA and composite materials improved adhesion properties, further enhancing the strength performance. On the other hand, SP (PPR-PLA) specimens showed the lowest strength performance. The failure load values of SK (PPR-Composite) and SP specimens were found to be quite close to each other. It was observed that due to the precise surface properties of SLA-manufactured parts, rapid separation occurred at the bonded joint areas. In general, when comparing strength performance, PK was found to have a 62.2% higher load-bearing capacity than SP. Furthermore, it can be said that the mechanical properties of the materials, such as tensile strength and modulus of elasticity, also significantly influenced the failure loads of the bonded specimens made from different material types [20].

When examining the displacement values of the bonded joint specimens, it was observed that SS specimens had the highest values. Due to the flexible nature of PPR materials, they exhibited better elongation performance under load. In addition to their high load-bearing performance, PK specimens also showed high displacement values. The lowest displacement value was found in PP specimens, which is attributed to the more rigid structure of PLA materials. When analyzing the displacement (elongation) data in the graph provided in Figure 9, it was determined that SS had a 129.7% higher value compared to PP. This is because PPR materials have a higher ability to deform under load and can undergo more significant deformation.

In conclusion, it was determined that the mechanical properties of the bonded materials significantly influence the mechanical strength of the bonded joints. A higher modulus of elasticity contributes to better strength performance.
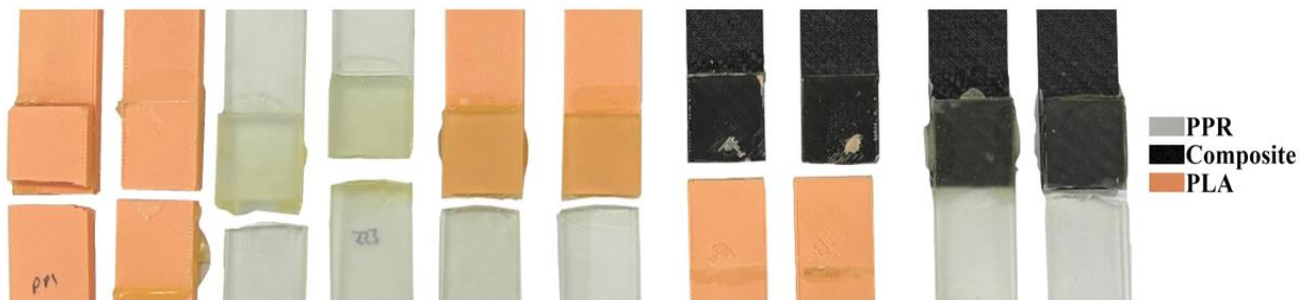

Figure 10. Failure surfaces of the SLJ adhesive specimens

The separation zones and bonding surfaces resulting from the tensile tests of the bonded joint specimens are shown in Figure 10. In some specimens, the parts completely separated at the bonding interface, while in others, failure occurred within the bonding region. It was observed that complete separations occurred in specimens made from more rigid materials, such as PLA and composites. However, the instantaneous stresses generated at the joint regions of the bonded joints reduce the strength of the bonded joints. The proper distribution of stresses in the bonding area is crucial for improving the performance of the bonded joints. In this context, when the failure loads and the mechanical properties of the bonded materials are evaluated together, it can be concluded that the variation in failure loads is due to the stiffness characteristics of the materials [21] .

When examining the surfaces of the bonding area, considering the types of damage in the bonded parts, it was observed that adhesion failure (failure at the interface between the adhesive layer and the bonded material) occurred in the majority of the joint specimens. Additionally, in some areas of the bonding surfaces, cohesive failure (failure within the adhesive layer) was observed due to the non-uniform distribution of the adhesive or its presence on only one surface of the part. In some specimens where PPR parts were bonded, fractures occurred in the bonding region, and the failure was attributed to defects in the base material.These findings highlight the importance of stress distribution, material properties, and surface preparation in determining the failure behavior and performance of bonded joints.

4. CONCLUSIONS

In this study, single-lap adhesive joints with a lap length of 25 mm were produced using different materials produced using SLA and FDM technology, and the mechanical properties of the parts produced by

different additive manufacturing methods at the end of the adhesive bonding process were examined. The following results were obtained in the study:

- It was determined that the tensile specimens produced from PLA material have better mechanical properties in terms of tensile strength and modulus of elasticity compared to the specimens produced from PPR material. However, the strain rates of PPR specimens were found to be very high compared to PLA specimens. The modulus of elasticity values of PLA specimens were 85% higher than PPR specimens.
- It was observed that the tensile strength of the samples produced from PLA material was 65% higher than the samples produced from PPR material. PLA tensile specimens offer higher tensile strength and stiffness, while PPR specimens are more flexible and have higher strain capability.
- The damage loads of the bonded joint specimens were found to differ according to the type of material bonded. The highest damage load value was obtained in PK specimens where PLA and composite materials were bonded. For this reason, it was determined that the selection of the materials to be bonded is very important in the applications to be realized.
- PPR materials produced by SLA method performed better than other material types in terms of unit elongation values under load due to their high strain capability.
- When the failure load capacities of the bonded joints were analyzed, it was determined that PK had 62.2% higher value than SP. When the displacement data were analyzed, it was determined that SS had 129.7% higher value than PP.
- In order to improve the performance of adhesive joints, it was determined that homogeneous stress distribution in the adhesion zone contributes positively to the mechanical performance of the parts.
- PLA materials can be preferred in applications requiring high mechanical strength and PPR materials can be preferred in applications requiring flexibility.

The following suggestions are presented for future studies.

Studies can be conducted for different lap lengths and bonding thicknesses in bonding joints. Also, studies can be carried out to increase the bonding surface area by creating recesses in the bonding area. For PPR and SLA materials, different filling ratios can be produced and the effect on bonding performance can be examined.

REFERENCES

[1] O. Abdulhameed, A. Al-Ahmari, W. Ameen, S.H. Mian, Additive manufacturing: Challenges, trends, and applications, Adv. Mech. Eng. 11, (2019), 1687814018822880.

[2] H.K. Sürmen, Eklemeli İMALAT (3B baski):Teknolojiler ve uygulamalar, Uludağ Univ. J. Fac. Eng. 24 (2019) 373–392. https://doi.org/10.17482/uumfd.519147.

[3] T. Ma, Y. Zhang, K. Ruan, H. Guo, M. He, X. Shi, Y. Guo, J. Kong, J. Gu, Advances in 3D printing for polymer composites: A review, InfoMat, (2024), e12568.

[4] Ü.G. Başcı, R. Yamanoğlu, Yeni nesil üretim teknolojisi: FDM ile eklemeli imalat, Int. J. 3D Print. Technol. Digit. Ind. 5, (2021), 339–352. https://doi.org/10.46519/ij3dptdi.838281.

[5] K. V Wong, A. Hernandez, A review of additive manufacturing, Int. Sch. Res. Not., (2012) 208760.

[6] S. Hartomacıoğlu, E. Kaya, B. Eker, S. Dağlı, M. Sarıkaya, Characterization, generative design, and fabrication of a carbon fiber-reinforced industrial robot gripper via additive manufacturing, J. Mater. Res. Technol., 33 (2024) 3714–3727.

[7] O. Özsolak, Eklemeli imalat yöntemleri ve kullanılan malzemeler, Int. J. Innov. Eng. Appl., 3 (2019) 9–14.

[8] D.S. Aydın, Ç.V. Yıldırım, Ş. Şirin, Üretim parametrelerinin seçici lazer ergitme yöntemi ile Ti6Al4V alaşımının çekme dayanımı, elastisite modülü ve uzama özelliklerine etkisi, Düzce Üniversitesi Bilim ve Teknol. Derg., 12 (2024) 1-17. https://doi.org/10.29130/dubited.1134020.

[9] J. Jin, J. Yang, H. Mao, Y. Chen, A vibration-assisted method to reduce separation force for stereolithography, J. Manuf. Process, 34 (2018) 793-801. https://doi.org/https://doi.org/10.1016/j.jmapro.2018.03.052.

[10] J.Z. Manapat, Q. Chen, P. Ye, R.C. Advincula, 3D printing of polymer nanocomposites via stereolithography, macromol, Mater. Eng., 302 (2017) 1-13. https://doi.org/10.1002/mame.201600553.

[11] G. Taormina, C. Sciancalepore, F. Bondioli, M. Messori, Special resins for stereolithography: In situ generation of silver nanoparticles, Polymers (Basel). 10, (2018). https://doi.org/10.3390/polym10020212.

[12] A. Husna, S. Ashrafi, A.A. Tomal, N.T. Tuli, A. Bin Rashid, Recent advancements in stereolithography (SLA) and their optimization of process parameters for sustainable manufacturing, Hybrid Adv., 7 (2024) 100307. https://doi.org/10.1016/j.hybadv.2024.100307.

[13] I. Khan, I. Barsoum, M. Abas, A. Al Rashid, M. Koç, M. Tariq, A review of extrusion-based additive manufacturing of multi-materials-based polymeric laminated structures, Compos. Struct. (2024), 118490.

[14] A. Rasheed, et al., Experimental investigation and Taguchi optimization of FDM process parameters for the

enhancement of tensile properties of Bi-layered printed PLA-ABS, Mater. Res. Express, 10 (2023) 95307.

[15]   E. Brancewicz-Steinmetz, J. Sawicki, Bonding and strengthening the PLA biopolymer in multi-material additive manufacturing, Materials (Basel). 15, (2022). https://doi.org/10.3390/ma15165563.

[16]   I. Khan, M. Tariq, M. Abas, M. Shakeel, F. Hira, A. Al Rashid, M. Koç, Parametric investigation and optimisation of mechanical properties of thick tri-material based composite of PLA-PETG-ABS 3D-printed using fused filament fabrication, Compos. Part C Open Access, 12 (2023) 100392.

[17]   Y. Korkmaz, K. Gültekin, Improving the mechanical performance of adhesively bonded CFRP composite joints exposed to harsh mediums with the reinforcement of boron nanostructures, J. Adhes. Sci. Technol., 37 (2023) 1959-1982.

[18]   A.Y. Kanani, X. Hou, J. Ye, A novel dissimilar single-lap joint with interfacial stiffness improvement, Compos. Struct. 252, (2020), 112741.

[19]   İ. Saraç, H. Adin, Ş. Temiz, Experimental determination of the static and fatigue strength of the adhesive joints bonded by epoxy adhesive including different particles, Compos. Part B Eng., 155 (2018) 92-103.

[20]   I. Manoj, A. Jain, Strength improvement and failure analysis of dissimilar FDM printed single-lap joints with tailored interface geometry, Int. J. Adhes. Adhes. 136, (2025), 103876.

[21]   K. Gültekin, B. Özakın, F. Yüksel, E. Danışmaz, Farklı Baskı Açıları ve Dolgu Oranlarında Üretilen Polilaktik Asit Plakalarla Birleştirilmiş Yapıştırma Bağlantılarının Deneysel Analizi TT-Experimental Analysis of Adhesive Joints Bonded with Polylactic Acid Plates Produced with Different Printing Ang, Karadeniz Fen Bilim. Derg., 14 (2024) 789-801. https://doi.org/10.31466/kfbd.1436278.

[22]   M.R. Khosravani, P. Soltani, K. Weinberg, T. Reinicke, Structural integrity of adhesively bonded 3D-printed joints, Polym. Test., 100 (2021) 107262.

[23]   N. Polat Çoban, N. Anaç, F. Mert, Eklemeli imalat ile üretilen pla parçaların yapıştırılmasında yapıştırma parametrelerinin mekanik dayanımına etkisinin incelenmesi, J. Polytech, 26, (2023).

[24]   M.G. Atahan, M.K. Apalak, Loading-rate effect on tensile and bending strength of 3D-printed polylactic acid adhesively bonded joints, J. Adhes. Sci. Technol., 36 (2022) 317-344.

[25]   T. Dhilipkumar, R. Venkatesan, V.S. Hiremath, S. Kesavan, K. P, K. V Shankar, O. Alduhaish, Enhancing structural performance of 3D-printed adhesively bonded flat-joggle-flat polymer joints with graphene-reinforced adhesive, Polym. Compos. 45 (2024) 16335–16346. https://doi.org/https://doi.org/10.1002/pc.29037.

[26]   I.A. Akpinar, K. Gültekin, S. Akpinar, H. Akbulut, A. Ozel, Research on strength of nanocomposite adhesively bonded composite joints, Compos. Part B Eng., 126 (2017) 143-152.

[27]   R. Niu, Y. Yang, Z. Liu, Z. Ding, H. Peng, Y. Fan, Durability of two epoxy adhesive BFRP joints dipped in seawater under high temperature environment, Polymers (Basel), 15 (2023) 3232.

Manufacturing Technologies and Applications
MATECA

Investigation on Weldability and Post-Weld Heat Treatment of A 333 Gr.6 and A350LF-2 Steels

Esin Tuğba Şimşek Çelik[1,*] (ID), Başar Ersegün Çelik[2] (ID), Şükrü Talaş[1] (ID)

[1]*Sivas Cumhuriyet University, Hafik Kamer Ornek Vocational School of Higher Education, Department of Transportation Services, Rail Systems Management Program, Sivas, Türkiye*
[2]*Afyon Kocatepe University, Institute of Natural Sciences, Afyonkarahisar, Türkiye*
[1]*Department of Metallurgical and Materials Engineering, Faculty of Technology, Afyon Kocatepe University, Afyonkarahisar, Türkiye*

ABSTRACT

In this study, as the first welding process, GTAW (Gas Tungsten Arc Welding) welding process was carried out on 9.53 mm thick A 333 Gr.6 pipe and A350LF-2 flange steels using 2.4 mm ER70S-6 electrode and SMAW (Manual Arc Welding) welding process was carried out using 2.5 mm E 7018-1 electrode for filler and cover passes. As the second welding process, GTAW welding process was carried out on 5.49 mm thick A 333 Gr.6 pipe and A350LF-2 flange steels using 2.4 mm ER70S-6 electrode and SMAW welding process was carried out using 2.5 mm E 7018-1 electrode for filler and cover passes. Post-weld heat treatment was applied during the first welding process. No post-weld heat treatment was applied during the second welding process. The effect of heat treatment on some mechanical properties of the materials and the changes that occur after stress relief were investigated for the welds made with the same materials, the same electrodes, the same welding methods but with different thicknesses. Tensile test, bending test, hardness test, notch impact test was performed as mechanical tests of the welded parts, macro images were taken and comparisons were made. As a result, the effects on the weld quality were investigated and results indicate that welding processes were successfully carried out with given filler electrodes and steel pipes.

Keywords: A 333 Gr.6, A350LF-2, GTAW, SMAW

A 333 Gr.6 ile A350LF-2 Çeliklerinin Kaynaklanabilirliğinin ve Kaynak Sonrası Isıl İşlemlerinin İncelenmesi

ÖZET

Bu çalışamada ilk kaynak işlemi olarak, 9.53 mm kalınlığında A 333 Gr.6 boru ile A350LF-2 flanş çeliklerinin GTAW (Gaz Tungsten Ark Kaynağı) kaynak işlemi 2,4 mm ER70S-6 elektrodu kullanılarak, SMAW (Manuel Ark Kaynağı) kaynak işlemi ise dolgu ve kapak pasoları için 2,5 mm E 7018-1 elektrodu kullanılarak gerçekleştirilmiştir. İkinci kaynak işlemi olarak, 5.49 mm kalınlığında A 333 Gr.6 boru ile A350LF-2 flanş çeliklerinin GTAW kaynak işlemi 2,4 mm ER70S-6 elektrodu kullanılarak, SMAW kaynak işlemi ise dolgu ve kapak pasoları için 2,5 mm E 7018-1 elektrodu kullanılarak gerçekleştirilmiştir. İlk kaynak işlemi gerçekleştirilirken kaynak sonrası ısıl işlem uygulanmıştır. İkinci kaynak işlemi gerçekleştirilirken kaynak sonrası ısıl işlem uygulanmamıştır. Aynı malzemelerle, aynı elektrotlarla, aynı kaynak yöntemleriyle ama farklı kalınlıklarda gerçekleştirilen kaynaklara ısıl işlem uygulamanın malzemelerin bazı mekanik özelliklerine olan etkisi ve gerilme giderme sonrası meydana gelen değişiklikler incelenmiştir. Elde edilen kaynaklı parçaların mekanik testleri olarak çekme testi, eğme testi, sertlik testi, çentik darbe testi gerçekleştirilmiş, makro görüntüleri çekilmiş, karşılaştırılmaları yapılmıştır. Sonuç olarak kaynak kalitesi üzerindeki etkiler araştırılmış ve sonuçlar verilen dolgu elektrotları ve çelik borularla kaynak işlemlerinin başarıyla gerçekleştirildiğini göstermektedir.

Anahtar Kelimeler: A 333 Gr.6, A350LF-2, GTAW, SMAW

1. INTRODUCTION

Pipes are widely produced and utilized in large quantities globally, particularly in heavy industries such as offshore transportation and oil extraction [3]. Pipelines in offshore platforms are constructed from a range of materials, selected based on factors such as cost, functional requirements, operating conditions (pressure and temperature), and corrosion rate, among others [1, 2]. This widespread use is attributed to low carbon steels due to their high strength, excellent weldability, resistance to high temperatures, and effective surface protection against environmental factors. Additionally, it is more cost-effective compared to other alloy

steels like low alloy steel and especially stainless steel [4, 5]. In the pipeline industry, medium and high carbon steels are generally avoided due to their increased brittleness and reduced weldability, particularly for offshore applications [6]. As a result, low carbon steel is preferred for offshore pipelines among designers, fabricators, and regulators. It is commonly used in the construction of pipelines for high-temperature vessels, heat exchangers, compressors, and transmission lines [6, 7]. A333 Grade 6 pipe, in particular, is referred to as a low-temperature pipe because it can withstand impacts to produce ductile failure at temperatures as low as -45°C [8]. ASTM A333 Gr.6 and ASTM A350 LF-2 are commonly used in environments with temperatures as low as -50°C. The primary challenge in welding these materials is ensuring that they maintain toughness at such low temperatures. Although low-temperature carbon steel typically exhibits good toughness and plasticity, the reheating process during welding can cause grain growth, which leads to a reduction in both toughness and plasticity. Therefore, using the appropriate welding process, consumables, parameters, and carefully controlling heat input are crucial to meet the required toughness in low-temperature conditions [9]. ASTM A350 LF-2 is low-strength and relatively cost-effective, known for their excellent weldability. This is largely due to the absence of elements, such as chromium (Cr), nickel (Ni), and molybdenum (Mo), which makes them easier to weld [10].

In the study by Wang & Chang [9], automatic and high-efficiency TIG (Tungsten Inert Gas) welding was applied for root and hot welding of ASTM A333 Gr.6 (low-temperature carbon steel, designed for -50°C) and ASTM A312/A358 TP304/304L (austenitic stainless steel, designed for -196°C) pipes. The study explored the design of the welding process, welding parameters, and tests and analyses of the mechanical properties of the welds, focusing on the advantages of automatic TIG welding. The results showed that automatic TIG welding improved efficiency by twofold compared to traditional manual TIG welding, leading to enhanced quality in process piping. In the study by Nissan & Baker [10], six ASTM A350 LF2 flanges exhibited a wide variation in low-temperature (-50°F) Charpy impact toughness, with values ranging from as low as 4 J to over 298 J. These flanges, characterized by relatively low strength with minimum yield strength of 248 MPa and tensile strength between 483 and 655 MPa, had similar yield and ultimate tensile strengths (UTS), despite the significant differences in toughness values. A detailed chemical and microstructural analysis was conducted to investigate the cause of this variability. Most of the flanges contained aluminium and had a fine grain structure, with the toughness variation largely attributed to the cooling rate after normalizing. Flanges cooled in still air showed the lowest toughness, while those forced air cooled exhibited the highest toughness. For flanges at this strength level, a quench and temper process is not required to achieve good low-temperature toughness; however, a minimum cooling rate, such as forced air cooling after normalizing, is necessary to ensure both good toughness and overall strength. In the study by Ghosh et al. [11], weld joints of SA 333 Gr. 6 steel pipes were prepared using a GTAW root pass and a V-groove SMAW filler. The objective was to characterize the base metal, weld deposit, and heat-affected zone (HAZ) of the pipe weld in terms of their chemical composition, metallurgical structure, mechanical properties, and fracture mechanics. The fracture toughness of the welds and HAZ was evaluated using J-integral parameters. Additionally, the fracture mechanics properties of the base metal, weld, and HAZ were compared and correlated, with a further correlation drawn between the fracture mechanics properties of the weld and HAZ and their respective microstructures. In the study by Efzan et al. [12], the microstructure of A333 Grade 6 steel pipe was analysed using light microscopy to characterize the material's structure. A hardness test was also performed to assess the material's resistance to applied force. The study concluded that A333 Grade 6 low-carbon steel has a microstructure with smaller grain size and lower pearlite content, which supports its high strength and ductility. The average hardness value measured for the steel was 166.836 HV, well within the acceptable range for oil and gas pipelines, where the maximum hardness allowed is 250 HV. Given its hardness level, A333 Grade 6 steel is well-suited for use in offshore platform pipelines.

In this study, as the first welding process, GTAW welding process was carried out on 9.53 mm thick A 333 Gr.6 pipe and A350LF-2 flange steels using 2.4 mm ER70S-6 electrode and SMAW welding process was carried out using 2.5 mm E 7018-1 electrode. As the second welding process, GTAW welding process was carried out on 5.49 mm thick A 333 Gr.6 pipe and A350LF-2 flange steels using 2.4 mm ER70S-6 electrode and SMAW welding process was carried out using 2.5 mm E 7018-1 electrode. Post-weld heat treatment was applied during the first welding process. No post-weld heat treatment was applied during the second welding process. The effect of heat treatment on some mechanical properties of the materials and the changes that occur after stress relief were investigated for welds made with the same materials, the same electrodes, the same welding methods but with different thicknesses. Tensile, bending, hardness, notch impact tests were performed as mechanical tests on the welded parts, macro images were taken and comparisons were made to observe the effects on the weld quality.

2. MATERIAL AND METHOD

2.1. Experimental Studies

In this study, GTAW (Gas Tungsten Arc Welding) welding process was carried out on 9.53 mm thick A 333 Gr.6 pipe and A350LF-2 flange steels using 2.4 mm ER70S-6 electrode as the first welding process and SMAW (Manual Arc Welding) welding process was carried out using 2.5 mm E 7018-1 electrode for filler and cover passes. The first welding process was given the code W-A; the properties of base metals, welding electrodes, welding methods and position of welding passes used in the W-A coded welding process are shown in Figure 1. The chemical composition of the A 333 Gr.6 steel is given in Table 1, the chemical composition of the A350LF-2 flange steel is given in Table 2, the chemical composition of the ER70S-6 electrode is given in Table 3, and the chemical composition of the E 7018-1 electrode is given in Table 4.
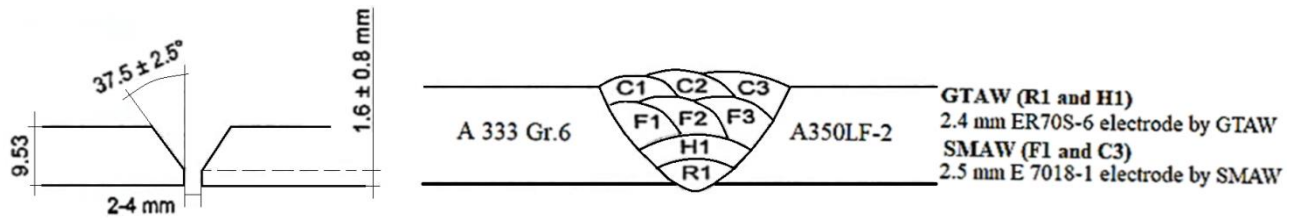

Figure 1. Weld groove, base metals, welding electrodes, welding methods and welding passes used in the W-A coded welding process

Table 1. Chemical composition of A 333 Gr.6 steel (wt. %)

C	Si	Mn	Cr	Mo	P	S	Ni	V	Al	Sn	Cu	Nb	Ti
0.11	0.24	1.05	0.03	0.06	0.012	0.001	0.038	0.037	0.028	0.009	0.069	0.002	0.012

Table 2. Chemical composition of A350LF-2 steel (wt. %)

C	Si	Mn	P	S	Cr	Ni	Mo	Nb	V	Cu	Al
0.200	0.280	0.840	0.008	0.001	0.090	0.090	0.040	0.005	0.003	0.280	0.030

Table 3. Chemical composition of ER70S-6 electrode (wt. %)

C	Si	Mn	P	S	Cr	Ni	Mo	Cu	V	Al	Ti+Zr
0.08	0.86	1.60	0.013	0.008	0.03	0.01	<0.01	0.05	<0.01	<0.01	0.01

Table 4. Chemical composition of E 7018-1 electrode (wt. %)

C	Si	Mn	P	S	Cr	Ni	Mo	Nb	Cu	V
0.06	0.59	1.59	0.022	0.007	0.05	0.02	0.01	0.01	0.03	0.02

In the W-A coded welding process, a total of 8 passes were applied, including 1 root pass, 1 hot pass, 3 filler passes, and 3 cover passes. The root pass and hot pass were made with the GTAW method, and the filler passes and cover passes were made with the SMAW method. In the W-A coded welding process, the welding passes, welding current and voltage, welding travel speed, and total heat input values are given in Table 5.

In the W-A coded welding process, the preheating temperature was 100 °C. The temperature between passes is 250 °C. The post-weld heat treatment (PWHT) temperature was 620 °C and applied for 60 minutes. The heating rate and cooling rate were kept constant at 180 °C/h. The thermal cycle and PWHT of the W-A coded welding process are given in Figure 2.

In this study, as the second welding process, GTAW welding process was performed using 2.4 mm ER70S-6 electrode and SMAW welding process was performed using 2.5 mm E 7018-1 electrode on 5.49 mm thick A 333 Gr.6 and A350LF-2 pipe flange. The second welding process was given the code of W-B. The base metals, electrode types, welding methods and welding passes used in the W-B coded welding process are shown in Figure 3.
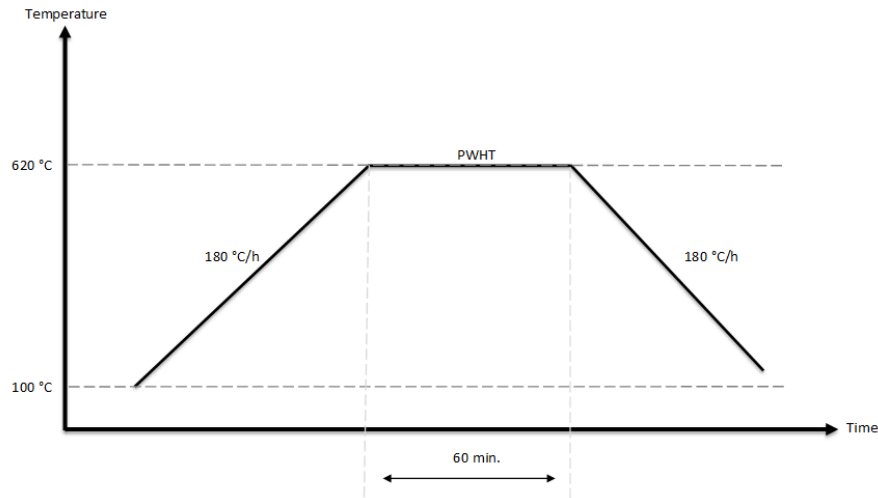
Figure 2. The thermal cycle and PWHT of the W-A coded welding process.

Table 5. Welding passes, welding current, welding voltage, welding travel speed and total heat input values in the W-A coded welding process.

Weld layers	Process	Class	Dia (mm)	Polarity	Amper range	Voltage range	Travel Speed (mm/min)	Heat input (KJ/mm)	Interpass Temp. (°C)
Root	GTAW	ER 70S-6	2.4	DCEN	102	10	41.18	1.49	100
Hot	GTAW	ER 70S-6	2.4	DCEN	162	10	56.63	1.72	185
Fill	SMAW	E 7018-1	2.5	DCEP	83	26	69.51	1.86	190
Fill	SMAW	E 7018-1	2.5	DCEP	90	26	74.32	1.89	190
Fill	SMAW	E 7018-1	2.5	DCEP	95	28	85.19	1.87	185
Cover	SMAW	E 7018-1	2.5	DCEP	91	28	82.30	1.86	200
Cover	SMAW	E 7018-1	2.5	DCEP	93	25	98.39	1.42	180
Cover	SMAW	E 7018-1	2.5	DCEP	92	25	102.15	1.35	200
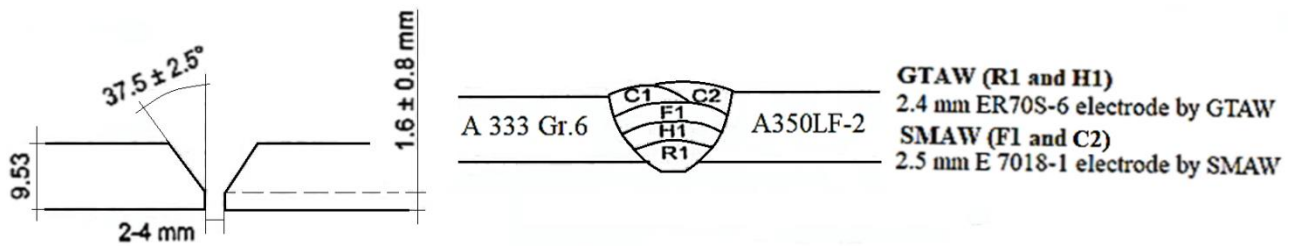
Figure 3. Weld groove, base metals, electrode types, welding methods and welding passes used in the W-B coded welding process.

In the W-B coded welding process, 5 welding passes were applied, including 1 root pass, 1 hot pass, 1 fill pass, and 2 cover passes. The root pass and hot pass were made with the GTAW method, and the fill and cover passes were made with the SMAW method. In the W-B coded welding process, the welding passes, welding current, welding voltage, interpass temperature, welding travel speed, and total heat input values are given in Table 6. In the W-B coded welding process, the preheating temperature is 100 °C. The temperature between weld passes is 185 °C. Heat treatment was not performed after welding. In this study, pure Argon gas was used as a shielding gas during GTAW welding with a gas flow rate of 12-15 lt/min.

Table 6. Welding passes, welding current, welding voltage, welding travel speed and total heat input values in the W-B coded welding process.

Weld layers	Process	Class	Dia (mm)	Polarity	Amper range	Voltage range	Travel Speed (mm/min)	Heat input (KJ/mm)	Interpass Temp. (°C)
Root	GTAW	ER 70S-6	2.4	DCEN	100	11	66.97	0.99	100
Hot	GTAW	ER 70S-6	2.4	DCEN	135	11	118.00	0.76	175
Fill	SMAW	E 7018-1	2.5	DCEP	90	26	105.30	1.33	185
Cover	SMAW	E 7018-1	2.5	DCEP	82	26	130.04	0.98	180
Cover	SMAW	E 7018-1	2.5	DCEP	82	26	122.00	1.05	185

2.2. Mechanical Tests Applied to Welded Parts

Tensile, bending, Charpy V notch impact and hardness tests were performed on welded parts. The hardness tests were carried out using Qness brand hardness tester device with a setting of HV10 and 15s dwelling time. Instron-5989 was used as the tensile test device with a cross-head speed of 3 mm/min. In the bending tests, 4 bending samples (BT) from each of the welds coded W-A and W-B were used. Charpy V notch impact test was performed using Instron (450 J) device. The parameters and conditions employed in the bending tests are given in Table 7.

Table 7. Parameters and conditions used in the bending test of W-A and W-B coded welded samples.

Specimen No	Type of Bend	Position (Deg)	Dimension (mm)	Bend Angle (°)	Former Dia. (mm)
W-A-BT-1	Face Bend	45	38	180	38
W-A-BT-2	Face Bend	225	38	180	38
W-A-BT-3	Root Bend	135	38	180	38
W-A-BT-4	Root Bend	315	38	180	38
W-B-BT-1	Face Bend	45	38	180	4t
W-B-BT-2	Face Bend	225	38	180	4t
W-B-BT-3	Root Bend	135	38	180	4t
W-B-BT-4	Root Bend	315	38	180	4t

3. RESULTS and DISCUSSION

3.1. Tensile Test and Bending Test Results

A 3-point 180° bending test was applied to the test piece samples. The samples showed successful performance in the 180° bending test without tearing, and visible discontinuity or defect was not detected on the test specimens. The successful results of the samples that were bent to 180° three-point bending test show that the welding process was carried out correctly and the selected filler metals were suitable for material combination selected for this process. It is important to note that weld metals are prone to lower fatigue performances due to any flaw at the root welds and this may lead to the structural damage in welds such as friction stir welding [14, 15]. Nevertheless, it has been demonstrated that root welds exhibit lower levels of stress in relation to fatigue failure when compared with cover welds. This is attributable to the divergent stress directions exhibited by these welds, whereby root welds are subject to compression stress, whilst cover welds experience tensile stress [14]. Tensile test results on samples (TT) obtained from the welding processes coded W-A and W-B are given in Table 8. The tensile test results graph is given in Figure 4.

Table 8. Tensile test results on samples obtained from the welding process coded W-A and W-B (UTS: Ultimate Tensile Stress, UTL: Ultimate Total Load, YS: Yield Strength)

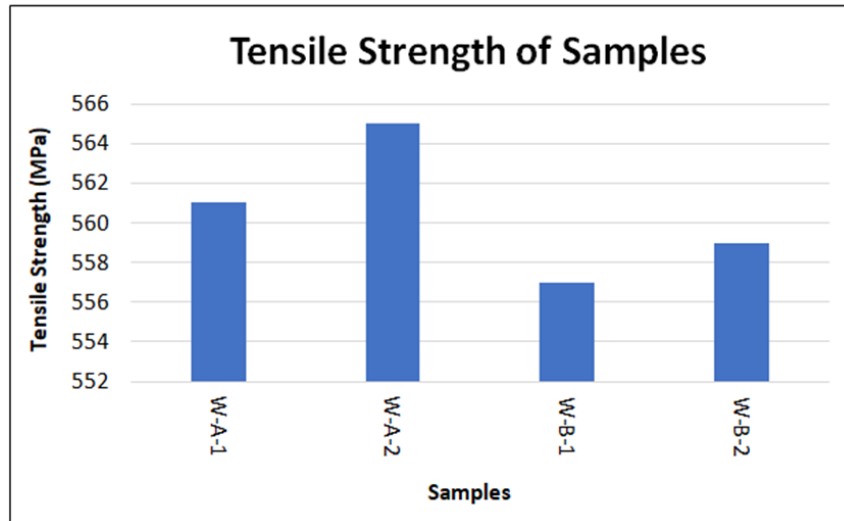| Specimen No	Dimension (mm)	Area (mm^2)	UTL (KN)	YS (MPa)	UTS (N/mm^2)
W-A-TT-1	8.40x19.00	159.60	89.60	382.84	561
W-A-TT-2	8.20x19.00	155.80	88.10	393.57	565
W-B-TT-1	5.00x13.10	65.50	36.50	419.30	557
W-B-TT-2	4.70x13.10	61.57	34.40	428.26	559

Figure 4. Tensile strength of W-A-1, W-A-2, W-B-1, W-B-2

An analysis of the graph in Figure 4 indicates that the tensile strength of the W-A coded weld samples exceeds that of the W-B coded weld samples. The maximum tensile strength recorded was 565 MPa, observed in the W-A-2 coded weld sample, while the minimum was 557 MPa, recorded in the W-B-1 coded weld sample. Both tensile test results in each series produced very close results and the difference in results is insignificant (< 0.1%), making the third test unnecessary. When all mechanical properties are evaluated collectively, irrespective of material thickness, it has been deduced that the application of welding might have created residual stress on the joint and its surroundings, which has a detrimental effect on its strength properties and results in a brittle failure. It has been established that residual stresses occur during the welding process, due to a reduction in percent elongation, an increase in fracture toughness in the welded area and the heat affected zone (HAZ). In samples that have undergone heat treatment, it has been determined that the application of welding increases the yield strength and tensile strength, as well as the percentage elongation [16, 17]. Furthermore, the effects of residual stress have been found to decrease with an increase in impact toughness. The findings of this study demonstrate that, while the stress relief process following welding does not fully restore the properties of the material prior to welding application, it does restore a substantial portion of these properties and enhances its strength, thereby confirming its necessity.

3.2. Hardness Test Results

Hardness values were taken in the W-A coded welding process, the W-B coded welding process at 15 points along the line for the cover pass and at 15 points along the line for the root pass. Hardness measurements were made according to ASTM E92-23 standard. Hardness distribution is a measure of line hardness and example of line hardness measurement is shown in Figure 5. Minimum recommended range for Vickers hardness measurement is shown in Figure 6. Hardness distribution values of welding processes coded W-A, W-B are shown in Figure 7a-b.
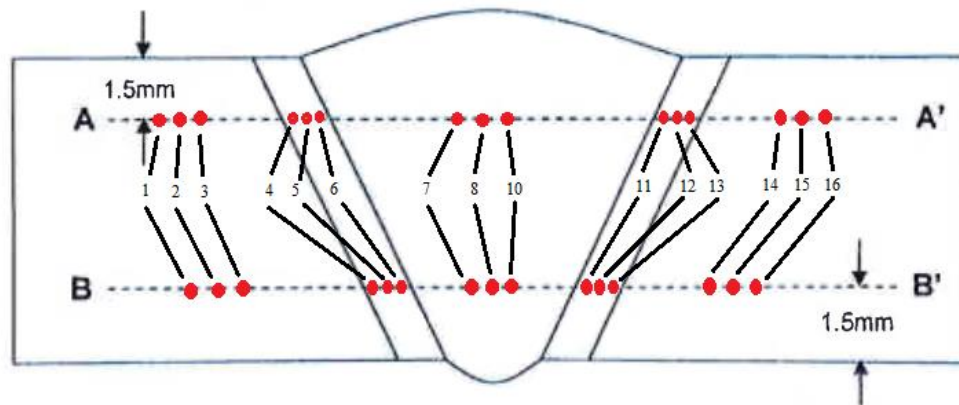

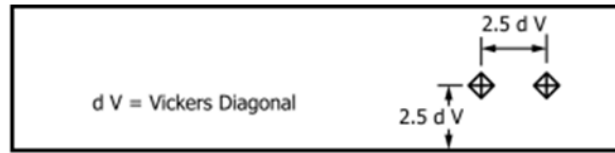Figure 5. Example of line hardness measurement.

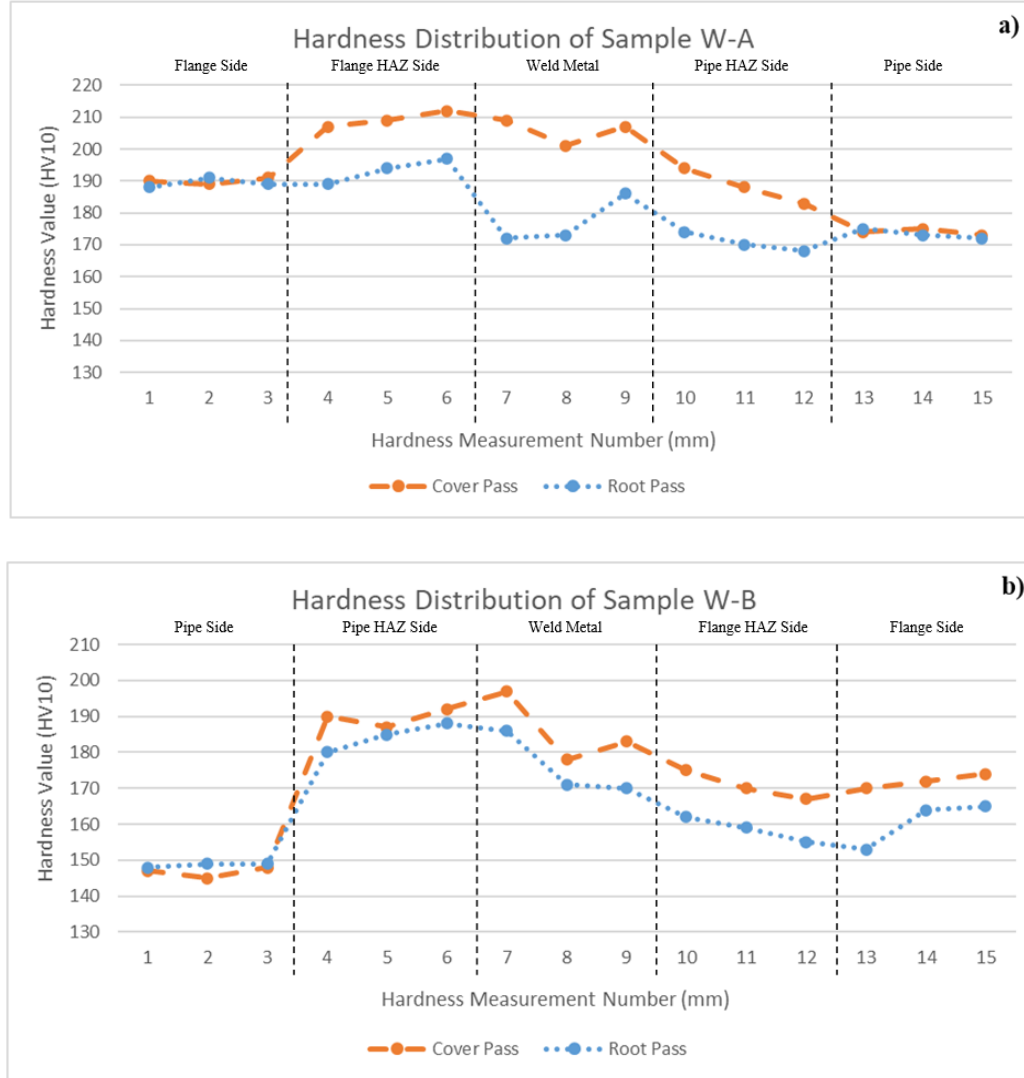Figure 6. Minimum recommended range for Vickers hardness measurement.

Figure 7. Line Hardness distribution for a) the W-A coded welding process b) the W-B coded welding process.

Figure 7a presents a graphical representation of the hardness values of the cap pass and root pass for the W-A welding process. It can be observed that the hardness value of the cap pass in the weld filler metal is higher than that of the root pass. The highest recorded hardness value is 212HV, which is observed in the HAZ (Heat Affected Zone) of cap pass. In the root pass, the lowest recorded hardness value is 168HV, which was observed in the A333 Gr6 base metal region. Figure 7b presents the hardness values of the cap pass and root pass for the W-B welding process. It can be observed that the hardness value of the root pass in HAZ is nearly identical to that of the cap pass. The highest recorded hardness value is 197HV, which is observed in the cap pass weld metal region. The lowest hardness value observed in the A333 Gr6 base metal region is 145 HV. Upon examination of the hardness graphs, it becomes evident that the transitions of local hardness values are softer in the heat-treated sample, with the hardness values of the root and cap pass being relatively similar. In contrast, in the unheat-treated sample, local hardness transitions are observed to be harder, with a notable difference in hardness values between the root and cap passes, which can be traced back to residual stresses at root and cover passes, the latter is tensile, and the former is compressive, respectively [14]. These stresses are relieved when heat treatment is applied and the difference between the hardness values is smaller whereas non heat-treated specimens contain such differences in stress and hence difference in hardness

values are larger [18, 19]. The results of the hardness analysis indicated that the observed variations in strain and softening within the welds can be attributed to the processes of recovery and recrystallization. These two phenomena were identified as the predominant factors influencing the alterations in hardness within both the heat-affected zones (HAZ) and the base metal regions during the process of multilayer welding [20].

3.3. Charpy V Notch Impact Test Results

The notch impact test results of the W-A and W-B coded welded samples are shown in Table 9. 3 impact test values were obtained from each sample and the average impact toughness values are presented. The distribution of the average impact toughness values of the W-A and W-B coded welded samples is shown in Figure 6.

Table 9. Charpy V Notch Tests results on samples obtained from the welding process coded W-A and W-B.

| Specimen No	Notch Location	Dimension (mm)	Test Temp. (°C)	Impact Toughness Value (J)			Average (J)
W-A-NT-1	F+5mm (Pipe Side)	10x10x2V	-46	220	230	182	211
W-A-NT-2	F+2mm (Pipe Side)	10x10x2V	-46	62	138	28	76
W-A-NT-3	Weld Centre Line	10x10x2V	-46	92	90	104	95
W-A-NT-4	F+2mm (Flange Side)	10x10x2V	-46	170	150	184	168
W-A-NT-5	F+5mm (Flange Side)	10x10x2V	-46	170	198	158	175
W-B-NT-1	F+5mm (Pipe Side)	10x4x2V	-53	84	90	80	85
W-B-NT-2	F+2mm (Pipe Side)	10x4x2V	-53	84	66	14	55
W-B-NT-3	Weld Centre Line	10x4x2V	-53	42	40	36	39
W-B-NT-4	F+2mm (Flange Side)	10x4x2V	-53	32	58	32	41
W-B-NT-5	F+5mm (Flange Side)	10x4x2V	-53	32	38	24	31
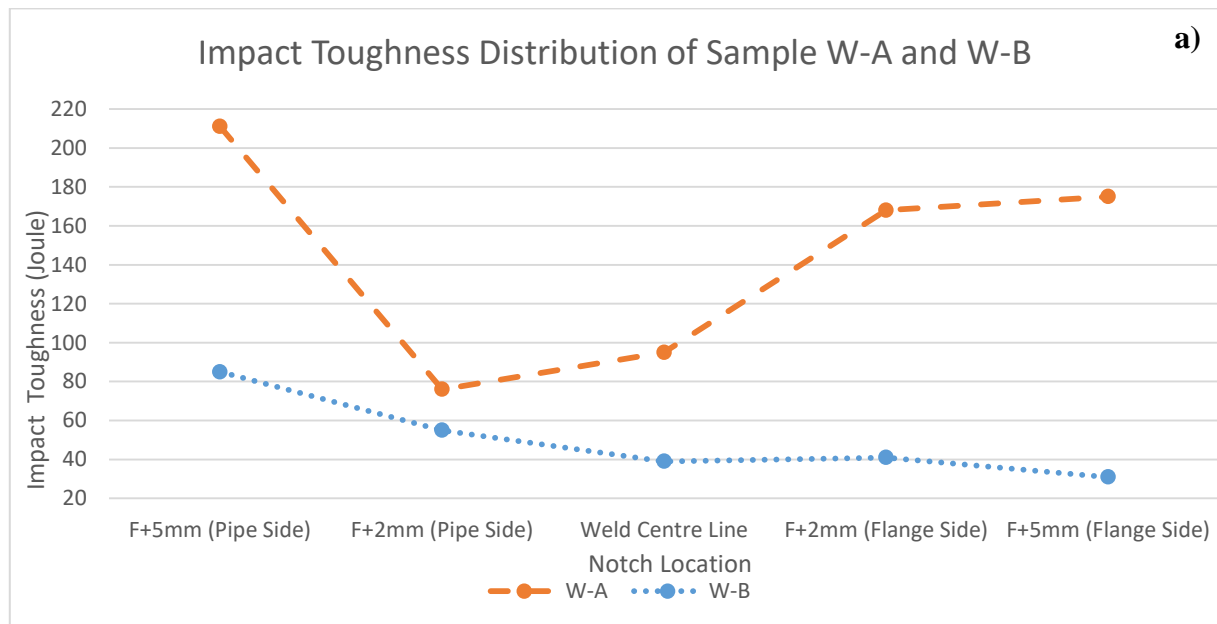
Figure 8. Impact toughness distribution for the W-A and W-B coded welding processes.

When Figure 8 is examined, it can be seen that the impact toughness of the W-A coded weld samples is higher than the impact toughness of the W-B coded weld samples. The lowest average impact toughness

value belongs to the W-B coded weld sample, which is 31 J. The highest average impact toughness value belongs to the W-A coded weld sample, which is 211 J. This situation is due to the increase in toughness due to heat treatment. Metallic materials become brittle below a certain temperature (transition temperature) and the impact toughness of the material decreases significantly. Above this temperature the material becomes ductile and thus, the crack formation and propagation become more difficult and the impact toughness increases as with finer grain increasing the impact toughness.

In steels, carbon and other alloying elements affect the impact toughness at a certain temperature as well as the transition temperature. As the carbon content in steels increases, ductility decreases and the transition temperature increases. Other alloying elements also affect the impact resistance and transition temperature. For example, the addition of Mn to a steel containing Fe-%0.05 C reduces the transition temperature. While the transition temperature of an alloy containing Fe-%0.05 C is 70 °C, it decreases to 10 °C with the addition of 0.5% Mn, to -20 °C with the addition of 1% Mn, and to a value lower than -60 °C with the addition of 2% Mn. The transition temperature decreases with the increase in the Mn/C ratio. In practice, Mn content above 1.4% and 2% C provides the desired tensile properties. A nickel content of up to 2% effectively reduces the transition temperature. The silicon content above 0.25% increases the transition temperature. Molybdenum, like carbon, rapidly increases the transition temperature. For high purity iron, oxygen content above 0.003% causes intergranular fracture and low energy absorption. When oxygen content increases from 0.001% to 0.057%, the transition temperature increases from -15 °C to 340 °C. This also reveals the importance of deoxidation. In low carbon steels, if the normalization process is carried out at a very high temperature after hot rolling, the transition temperature decreases. The cooling rate and deoxidation after normalization should be taken into consideration. Cooling in air and deoxidation with aluminum further reduce the transition temperature. Coarse grained steels have low impact resistance and high ductile-brittle transition temperatures [13, 21, 22].

3.4. Macro Image Results

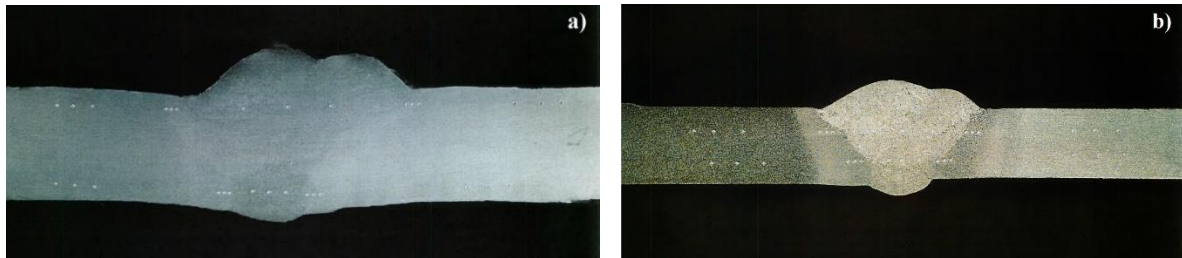Macro images of welding processes coded W-A, W-B are shown in Figure 9a-b.

Figure 9. The macro image of a) the W-A coded welding process b) the W-B coded welding process.

When the macro images of the samples are examined, it is clearly seen that the heat treatment reduces the HAZ in the welded sample with code W-A in Figure 9a. In the welded sample with code W-B in Figure 9b, the HAZ region is larger because no heat treatment was applied after welding and also because of the lower base metal thickness.

A thorough examination of the macrostructure images reveals the absence of weld pits, cracks, voids, inadequate fusion, low penetration, slag residues and burning grooves in the weld area. This observation indicates that the welding parameters have been appropriately selected. Additionally, it is observed that weld sag and errors resulting from excessive welding amperage do not occur. The macrostructure photographs demonstrate the distinction between the two passes and the clear delineation of the weld area, HAZ, and base material regions. The orientation of grains in the weld area is observed to be aligned with the heat flow, and the HAZ region is found to be wide, a consequence of the high heat input in both passes and the slow welding speed.

3.5. Microstructural Image Results

Microstructural images of weld metals and their subzones obtained from different welding processes are shown in Figure 10a-j.
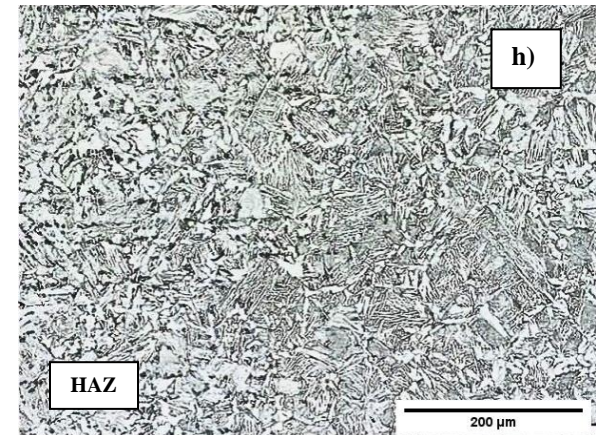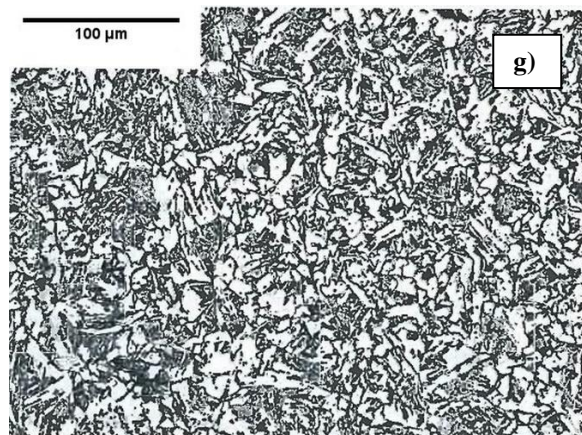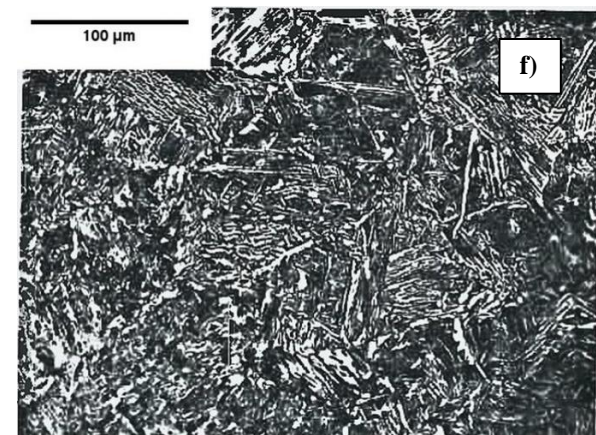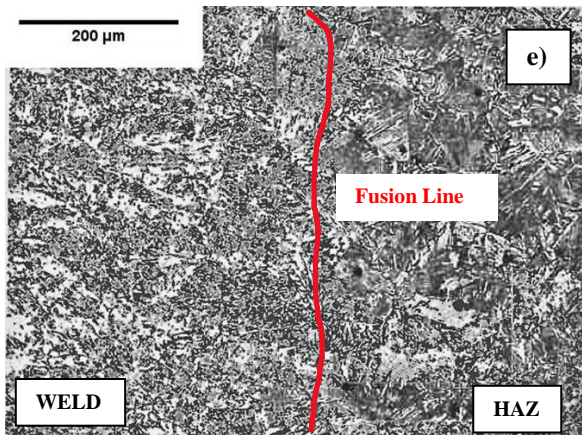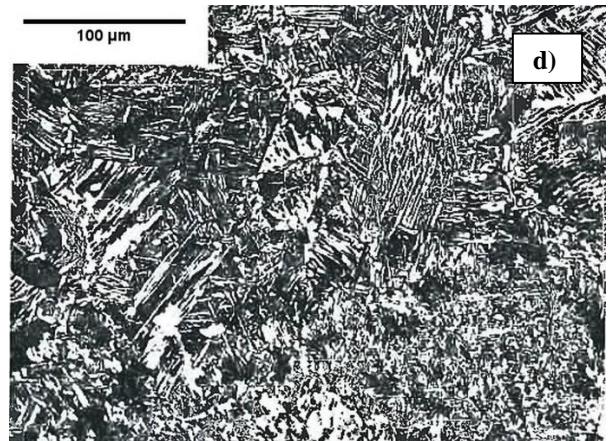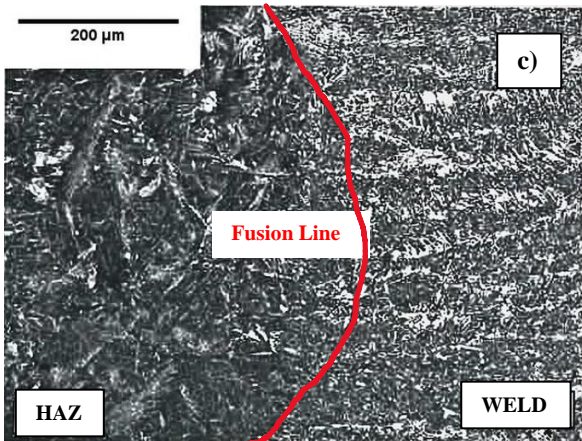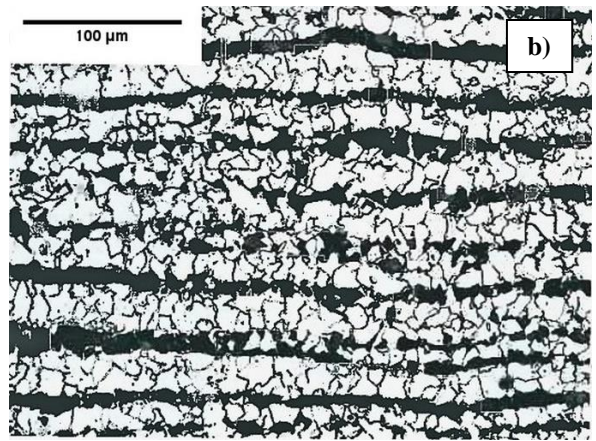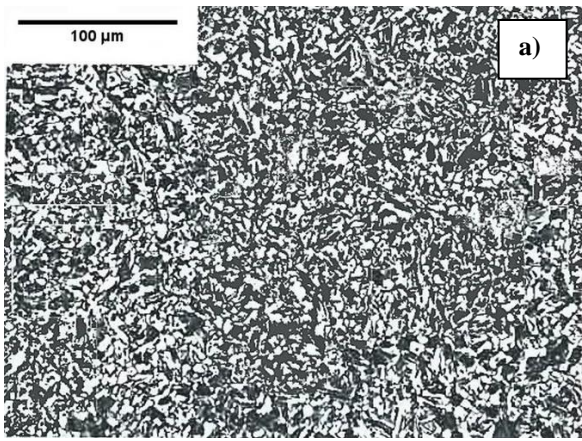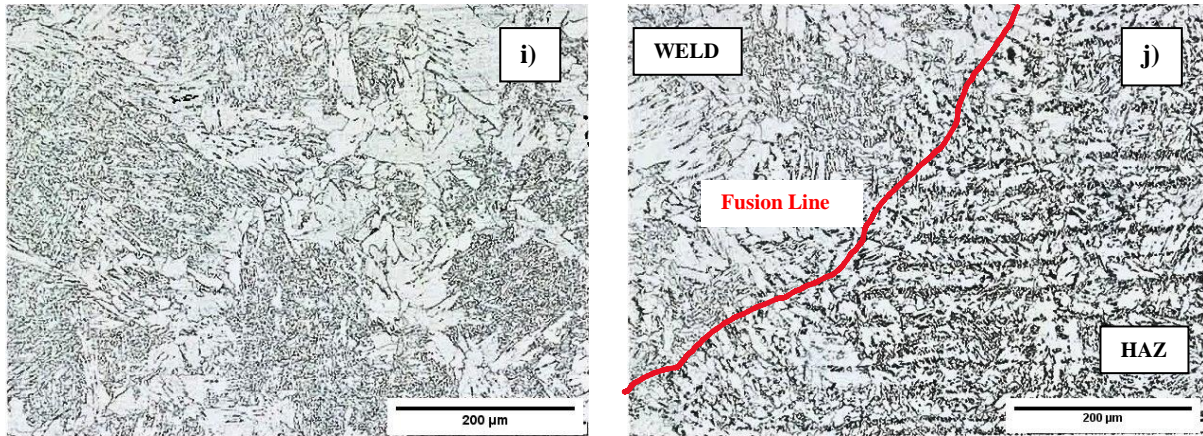
Figure 10. Microstructural images of a) A350LF-2 Base Metal b) A 333 Gr.6 Base Metal c) A350LF-2 Fusion Line d) A350LF-2 Fusion Line (200x magnification) e) A 333 Gr.6 Fusion Line f) A 333 Gr.6 Fusion Line (200x magnification) g) Weld Metal h) PWHT HAZ i) PWHT Weld Metal j) PWHT Fusion Line

The microstructure in Figure 10a shows that the A350LF-2 base metal has a fine-grained structure. Very fine ferrite grain along with small amounts of ferrite-cementite aggregates between subgrains can be observed. A heat treatment followed by high deformation ratio may result in such microstructures in low carbon steels. As seen in the microstructure in Figure 10b, the A 333 Gr.6 base metal consists of comparatively larger ferrite grains along with banding structures which are reminants of rolling during the hot deformation process, indicating that the rolling process took place at temperatures where microsegregation of carbon or cementite structure occur. A hypoeutectoid ferrite forms due to carbon redistribution prior to phase transformation i.e. A3 to A1 and it is followed by carbon concentration imbalance during hot rolling, which is also helped by recrystallization of new nuclei [23, 24]. Figure 10c shows that the right side of the A350LF-2 fusion line is the weld metal and the left side is the HAZ (Heat Affected Zone). The weld metal contains very high amount of fine-grains and acicular ferrite structures which are visible in the weld metal region, whilst structures similar to the Widmanstatten ferrite structure are visible in the heat-affected zone (HAZ). The grain boundaries are decorated with grain boundary ferrite with very small amounts of ferrite plates emanating from proeutectoid ferrite subgrains. However, Figure 10d shows very different microstructure and it presents dominantly ferrite side plates with fine cementite films in between them, i.e. similar to Bainite structures but it is not fully conclusive with the 200x magnification of the A350LF-2 fusion line image. In Figure 10e, the right side of the A333 Gr.6 fusion line is identified as the HAZ, while the left side corresponds to the weld metal. The weld metal consists of fine acicular ferrite structure with slightly increased number of recovered proeutectoid ferrite or grain boundary ferrite. The HAZ region exhibits grain coarsening with increased level of widmanstaten ferrite protruding into the grain interior and there are more over recovered coarsened ferrite subgrains inside thegrains and along the grain boundary. In Figure 10f, the 200x magnification of the A333 Gr.6 fusion line reveals the presence of mixture of coarse high temperature, that is, upper bainitic structures and ferrite cementite side plates with acicular structures between the ferrite-cementiteregions as it is difficult to see fine pearlite at this carbon level. In Figure 10g, an increase in fine ferrite grain structures are observed in the weld metal region, indicating the presence of small amount of acicular sturctures which are smaller in size and length. Such small grains are possible to produce when weld metal has higher amounts of Mn and or Si as they are responsible to produce effect similar to carbonto lesser effect, that is, lower the critical cooling rate and hence refine the grain structure and its interior with possibly increasing the amount of fine oxides [25]. Figure 10h reveals the presence of carbide formations between ferrite grain boundaries on the weld filler metal side of the heat-treated HAZ (left side). On the right side, the growth and coarsening of the Bainite structures is evident with acicular ferrite. Plated structures bear a resemblance to ferrite side plates and irregular form of subgrains which are possibly product of coarsening as evidenced by the microstructure analysis depicted in Figure 10i. It is observed that the ferrite side plate structures have undergone a coarsening process in the heat-treated weld metal. In comparison, the Ferrite structures appear to have experienced a reduction in thickness. Upon examining the microstructure in Figure 10j, it is evident that the Bainite and acicular structures have undergone a coarsening process on the weld filler metal side of the heat-treated Fusion Line (left side). Highly recovered coarse ferrite appears to form on the HAZ region side (right side).

4. CONCLUSION

The present study investigates the effect of heat treatment on the mechanical properties of materials, and the changes that occur after stress relief, in welds made with the same materials, the same electrodes, and the same welding methods, but with different thicknesses. The following findings were obtained:

- When tensile samples are examined, the maximum tensile strengths of the samples subjected to heat treatment with code W-A are higher than those of the samples without heat treatment with code W-B. The main reasons for this can be said to be the elimination of residual stresses after heat treatment and the reduction of grain structures of the normalized material.
- The samples demonstrated successful performance in the 180° bending test, with no observable breakage, tearing, or visible discontinuity or defect. The positive outcomes observed in the 180° three-point bending test on the samples indicate that the welding process was executed correctly and that the selected filler metals were appropriate for the material combination utilised in this process.
- The hardness value of the coke pass weld filler metal of the sample subjected to heat treatment with code W-A is similar to the hardness value of the A333 Gr6 base metal. This confirms that the heat treatment is smooth and homogeneous.
- When the effect of heat treatment on the material is examined, it is seen that the average fracture toughness of the W-A sample is much higher than the W-B sample. The reason for this can be said to be the reduction of grain sizes due to the elimination of residual stresses caused by heat treatment.
- A thorough examination of the macrostructure photographs reveals that no weld pits have been formed. Furthermore, no cracks, voids, lack of fusion, low penetration, slag residues or burning grooves have been observed in the weld area. Consequently, it can be concluded that the welding parameters have been selected at appropriate values.
- In the W-A welding process, which is performed with a material approximately twice as thick, the material thickness increases the cooling rate and encourages the hardening tendency, so this situation is prevented by applying heat treatment after welding, thus eliminating the stresses.
- The data demonstrate that, although the stress relief process after welding does not completely restore the properties of the material before welding application, it restores a significant portion of these properties and increases the strength of the material, thus proving its necessity.
- A study of the microstructures of non-heat-treated welding processes reveals the presence of ferrite, pearlite, acicular ferrite, Widmanstatten ferrite, and fine bainite structures. Conversely, the microstructures of heat-treated welding processes exhibit ferrite, pearlite, laminar pearlite, coarse bainite, and acicular ferrite structures.

REFERENCES

[1] J.M. Tanzosh, Chapter A3: Piping Materials, in Piping Handbook, New York, McGraw-Hill, 2000.
[2] Norsok Standard, M-001 Material Selection, Norwegian Petroleum Industry, Norway, 2004.
[3] M. Stipanicev, F. Turcu, L. Esnault, O. Rosas, R. Basseguy, M. Sztyler, I.B. Beech, Corrosion of carbon steel by bacteria from North Sea offshore seawater injection systems: Laboratory investigation, Bioelectrochemistry 97, (2013), 76-88. https://doi.org/10.1016/j.bioelechem.2013.09.006
[4] S. Papavinasam, Chapter 3 – Materials, Corrosion Control in the Oil and Gas Industry, 2014.
[5] M.F. Ashby, Materials Selection in Mechanical Design, Burlington: Elsevier Publisher, 2005.
[6] A.J. Bryhan, W. Troyer, Weldability of a low carbon Mo-Nb X-70 pipeline steel, Welding Research, 1980.
[7] P. Smith, Piping Materials Selection and Applications, Burlington: Gulf Professional Publishing, 2005.
[8] American Society for Testing and Materials (ASTM), ASTM A333: Standard specification for seamless and welded steel pipe for low-temperature service, American Society for Testing and Materials (ASTM), Washington, 2013.
[9] Z. Wang, Y. Li, C. Chang, Application of automatic TIG welding for Yamal LNG process piping fabrication International Journal of Oil, Gas and Coal Engineering 6, (2018), 44-49. https://doi.org/10.11648/j.ogce.20180604.11
[10] A.B. Nissan, K.C. Baker, Determination of the cause of low temperature charpy toughness values in ASTM A350 LF2 Flanges, Proceedings of the 28th ASM Heat Treating Society Conference, USA, 2015: pp. 342-349.
[11] P.K. Ghosh, P.K. Singh, K.K. Vaze, H.S. Kushwaha, Characterisation of pipe welds and HAZ in primary heat transport system piping of pressurised heavy water reactors, Science and Technology of Welding and Joining, 9 (2004) 200-208.
[12] M.E. Efzan, S. Kesahvanveraragu, J. Emerson, Microstructural characterization and hardness properties of A333 grade 6 low carbon steel in offshore platform pipelines, Journal of Advanced Research in Materials Science 2 (2014) 1-9.

[13] E.S. Kayalı, C. Ensari, F. Dikeç, Metalik malzemelerin mekanik deneyleri, İTÜ Kimya-Metalurji Fakültesi, Ofset Atölyesi, İstanbul, 1996.

[14] S. Fowler, A. Toumpis, A. Galloway, Fatigue and bending behaviour of friction stir welded DH36 steel, Int J Adv Manuf Technol 84, (2016), 2659-2669.

[15] T.L. Dickerson, J. Przydatek, Fatigue of friction stir welds in aluminium alloys that contain root flaws, Int J Fatigue 25, (2003), 1399–1409.

[16] I.V. Vlasov, A.I. Gordienko, V. M. Semenchuk, Heat treatment effect on structure and mechanical properties of gas metal arc-welded pearlitic steel, Russ Phys J, 67, (2024), 1590-1598. https://doi.org/10.1007/s11182-024-03286-y

[17] X. Wang, D. Wang, L. Dai, C. Deng, C. Li, Y. Wang, K. Shen, Effect of post-weld heat treatment on microstructure and fracture toughness of X80 pipeline steel welded joint, Materials, 15(19), (2022), 6646.

[18] K.A.M.B. Gonçalves, G.L. de Faria, R.H.M. de Siqueira, T.R. de Oliveira, M.S.F. de Lima, Heat treatment effects on the hardness and wear behavior of laser-welded AISI40 martensitic steel plates, Int J Adv Manuf Technol 114, (2021), 1155-1163.

[19] C. Köse, R. Kaçar, The effect of preheat & post weld heat treatment on the laser weldability of AISI 420 martensitic stainless steel, Mater Design 64, (2014), 221-226.

[20] L. Yu, K. Nishimoto, H. Hirata, K. Saida, Hardness prediction of the heat-affected zone in multilayer welded SUS316 stainless steel based on dislocation density change behavior, Metall Mater Trans A, 55, (2024) 1788-1803.

[21] L.E. Svenson, B. Gretoft, Microstrcuture and impact toughness of C Mn weld metals, Welding Journal, (1990) 454-461.

[22] A. Ilić, I. Miletić, R.R. Nikolić, V. Marjanović, R. Ulewicz, B. Stojanović, L. Ivanović, Analysis of influence of the welding procedure on Impact Toughness of welded joints of the High-Strength Low-Alloyed Steels, Applied Sciences 10(7), (2020), 2205.

[23] C.F. Jatczak, D.J. Girardi, E.S. Rowland, On banding in steel, Transactions of the ASM 48, (1956), 279-305.

[24] P.G. Bastien, The mechanism of formation of banded structures. Journal of the Iron and Steel Institute, 187, (1957), 281-291.

[25] G. Evans, Effect of Si on the microstructure and properties of C-Mn all weld metal deposits, Metal Construction (1986).

Manufacturing Technologies and Applications
MATECA

On Biomedical Applications of Additive Manufacturing Bibliometric Analysis

Halime İlayda Doğan[1,*] (ID), Ahmet Mavi[2] (ID)

[1] *Department of Manufacturing Engineering, Institute of Science, Gazi University, Ankara, Türkiye*
[2]*Manufacturing Engineering, Faculty of Technology, Gazi University, Ankara, Türkiye*

ABSTRACT

This study aims to provide a comprehensive bibliometric analysis of the literature on the applications of additive manufacturing in the biomedical field. The analysis examines data from a total of 1130 studies published in the Web of Science (WoS) database up to August 19, 2024. VOSviewer software was used for data visualization and analysis. The findings indicate that the first study on biomedical applications of additive manufacturing was published in 2012, and a total of 1130 studies were conducted between 2012 and 2024. Among these studies, the year 2023 was identified as the most prolific publication period, with 193 studies. The majority of the analyzed works were found to be research articles. Furthermore, it was determined that these studies were conducted with contributions from 5249 different authors across 78 countries. The unique contribution of this study lies in its comprehensive examination of trends in additive manufacturing within the biomedical field, offering insights and recommendations for future research. In addition to presenting numerical data, the study provides a detailed analysis and comparison with the existing literature. In conclusion, this study is expected to serve as a valuable resource for researchers and academics planning to conduct studies on the biomedical applications of additive manufacturing.

Keywords: 3D printing, Additive manufacturing, Tissue engineering, Biomaterials, Bioprinting

Eklemeli İmalatın Biyomedikal Uygulamaları Üzerine Bibliyometrik Analiz

ÖZET

Bu çalışma, eklemeli imalatın biyomedikal alanındaki uygulamalarına ilişkin literatürün kapsamlı bir bibliyometrik analizini sunmayı amaçlamaktadır. Analiz kapsamında, Web of Science (WoS) veri tabanında 19 Ağustos 2024 tarihine kadar yayınlanan toplam 1130 çalışmaya ait veriler incelenmiştir. Verilerin görselleştirilmesi ve analizi için VOSviewer yazılımı kullanılmıştır. Elde edilen bulgular, eklemeli imalatın biyomedikal uygulamaları üzerine ilk çalışmanın 2012 yılında yayınlandığını ve 2012-2024 yılları arasında toplam 1130 çalışma gerçekleştirildiğini göstermektedir. Bu çalışmalar arasında, 2023 yılının 193 çalışma ile en yoğun yayın dönemi olduğu belirlenmiştir. İncelenen çalışmaların büyük çoğunluğunun makale türünde olduğu tespit edilmiştir. Ayrıca, bu çalışmaların 5249 farklı yazar tarafından, 78 ülkeden katkı sağlanarak gerçekleştirildiği belirlenmiştir. Bu çalışmanın özgün katkısı, eklemeli imalatın biyomedikal alanındaki yaklaşımlarını kapsamlı bir şekilde ortaya koyarak gelecek araştırmalara yönelik öneriler sunmasıdır. Araştırmada, sadece sayısal veriler sunulmamış, bunlar detaylı bir şekilde analiz edilerek literatürdeki mevcut durumla karşılaştırılmıştır. Sonuç olarak, bu çalışmanın eklemeli imalatın biyomedikal uygulamaları üzerine araştırma yapmayı planlayan bilim insanları ve akademisyenler için değerli bir kaynak oluşturacaktır.

Anahtar Kelimeler*: 3B baskı, Eklemeli imalat, Doku mühendisliği, Biyomalzemeler, Biyobaskı*

1. GİRİŞ

Bibliyometrik analizi sistematik literatür taramasından ayıran özellik, bir konunun mevcut durumuna ilişkin nesnel ve sayısal verilere ulaşmak için kullanılan ve görselleştirme yazılımlarıyla akademik yaklaşımları takip etmeyi kolaylaştıran bir analiz yöntemi olmasıdır. Bibliyometrik analiz sayesinde anahtar kelimeler, ülkeler, yazarlar, kurumlar ve dergilerin üretkenliği, gelişmiş veya gelişmesi gereken araştırma konuları, literatürdeki eksiklikler, iş birliği bağlantıları ve bir konudaki çalışmaların geniş kapsamı etkileri üzerine sayısal verilere ulaşılabilir. Günümüzde sistematik literatür taramasının hazırlık adımı olarak da kullanılabilecek bibliyometrik analiz, birçok sınırlamaya sahip olmasına rağmen herhangi bir araştırmanın ilk adımı olarak önem arz etmektedir [1].

Üç boyutlu (3B) baskı olarak da bilinen eklemeli imalat (Eİ), 1980'li yılların sonlarından bu yana ilerletilen yenilikçi imalat teknikleri grubunu ifade etmektedir [2]. Amerikan Test ve Malzeme Topluluğu (ASTM) F2792-10 standardına göre Eİ, "geleneksel imalat yöntemlerinin aksine, malzemelerin 3 boyutlu model verilerinden nesneler oluşturmak için genellikle katman katman malzemeleri birleştirme süreci" olarak tanımlanmaktadır [3]. Eİ teknolojisi 40 yılı aşkın süredir geliştirilmeye devam etmekte olup otomotiv, havacılık, tüketici ürünleri ve biyomedikal gibi çeşitli endüstrilerde ticari uygulamalara dönüştürülebilecek bir olgunluk seviyesine ulaşmıştır [4,5]. Yüksek performanslı metaller [6], seramikler [7], polimerler [8] ve hidrojeller [9] gibi malzemelerin hızlı gelişimi, eklemeli imalatın uygulama alanlarının genişlemesine katkı sağlamaktadır. Ayrıca, birden fazla renk ve malzemede baskı yapabilme gibi makine teknolojilerindeki ilerlemeler bu sürekli evrilen imalat sürecinin potansiyelini artırmaktadır [10].

Eklemeli imalatın biyomedikal uygulamaları, üç boyutlu model verileri ve sürekli eklemeli baskı teknolojilerine dayanarak geliştirilmiştir [11]. Geleneksel imalat proseslerinin aksine Eİ; yüksek üretim hassasiyeti, sadeleştirilmiş süreçler, malzeme tasarrufu, daha kısa üretim süreleri ve artan üretim verimliliği ile karmaşık üç boyutlu yapıları doğrudan tek parça halinde oluşturabilir ve kişiselleştirilmiş gereksinimleri karşılamak amacıyla farklı medikal alanlarda kullanılabilmektedir [11-13]. Canlı doku ve organların yapısı, gereken esneklik ve dayanıklılığı sağlayacak malzemeler seçilerek uygun eklemeli imalat yöntemiyle üretilebilmektedir [14]. 3B baskı ile üretilen doku ve organ modelleri, cerrahi planlama ve tıbbi eğitim gibi farklı amaçlar için de kullanılmaktadır [15]. İmplantların üretiminde kemik özelliklerine uygun bir yapı elde edebilmek amacıyla parça gözenekliliği de ayarlanarak kemik implant uyumu iyileştirilmektedir [16]. Hastaya özel tasarlanan implantlar ve tıbbi cihazlar tedavi sürecinin başarı oranlarını artırmaktadır [14-16]. Bu nedenle Eİ teknolojisinin çeşitli biyomedikal alanlarında kullanımı önem kazanmaktadır.

Bu konu ile ilgili olarak yapılan araştırmalara nerelerden ulaşabileceği ve bu alana dair yapılan çalışmaların genel olarak güncel araştırmaları inceleyen bir çalışmaya ihtiyaç olduğu düşünülmüştür. Bundan dolayı çalışmanın sonuçlarının eklemeli imalatın biyomedikal alanındaki çalışmalara ve uygulamalarına katkı sağlayacağı öngörülmektedir. Bu çalışmanın amacı, eklemeli imalatın biyomedikal alanı ile ilgili akademik eserleri tarayarak sonuçları bibliyometrik analiz yöntemiyle sunmaktır.

Eklemeli imalatın biyomedikal alanındaki uygulamalarını inceleyen bir literatür çalışması, bu alandaki mevcut yaklaşımları ortaya koymanın yanı sıra, eksik kalan veya daha az çalışılmış konuların belirlenmesi açısından önem arz etmektedir. Anahtar sözcük analizi, bu doğrultuda, araştırmacılar için detaylı bir yol haritası sunmakta ve literatürdeki boşlukların belirlenmesine olanak sağlamaktadır. Yapılan analizlerde, özellikle kişiselleştirilmiş implant tasarımı, biyoyazıcı teknolojilerinin optimizasyonu ve biyomalzemelerin uzun vadeli biyouyumluluğu gibi konuların nispeten az çalışıldığı tespit edilmiştir. Bu alanlarda yapılan çalışmaların hem biyomedikal araştırmalara hem de klinik uygulamalara katkı sağlayacağı düşünülmektedir.

2. YÖNTEM

Bu çalışmada, sayısal veriler ve sayısal ölçüm göstergeleri kullanılarak gerçekleştirilen bibliyometrik analizlerle, eklemeli imalatın biyomedikal uygulamaları kavramına dair araştırmaların kapsamlı bir perspektifle araştırmacılara sunulması hedeflenmektedir.

19.08.2024 tarihinde, "additive manufacturing", "biomedical" ve "3D printing" anahtar kelimeleriyle "all fields" arama yapıldığında, sonuç olarak 1136 adet veri elde edilmiştir. Yıllara göre inceleme yapıldığında 2012 yılından 2024 yılına kadar, bu konuda birçok çeşitli kategoriden 30 tanesi erken erişim aşamasında olan; 1026 makale, 110 bildiri, 20 kitap bölümü, ve 4 editöryal yazıya ulaşılmıştır. Veri tabanı olarak Web of Science (WoS)' da yer alan veriler esas alınmıştır. Elde edilen verilerin, yıl ve kategori analizi için WoS; anahtar sözcük, yazar, atıf, ülke, kurum, kaynak ve bibliyografik eşleşmeleri bakımından analizi için ise VOSviewer uygulamasından yararlanılmıştır.

3. BULGULAR

### 3.1. Yayınların Yıllara Göre Analizi

Eklemeli imalatın biyomedikal alanındaki eserlerin yayınlanma süreçleri ilk olarak 2012 yılında başlamıştır. 2012 yılından 2024 yılına kadar her yıl yayınlanan eserlerin sayısı Şekil 1' de grafik ile gösterilmiştir. 2016 yılından itibaren ciddi bir artış gösteren yıllık yayın sayısının 2023 yılında 194 adet yayın ile en fazla yayın yapılan yıl olduğu gözlenmektedir.
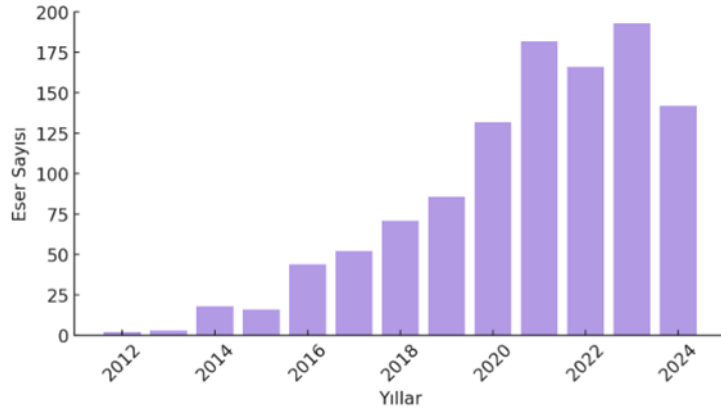
Şekil 1. Yıllara göre yayınlanan eserlerin analizi.

3.2. Yayınların Farklı Kategorilere Göre Analizi

Eklemeli imalatın biyomedikal uygulamalarının yayınları Şekil 2' de bulunan grafikte görüldüğü üzere birçok farklı kategori içerisinde yer almaktadır.
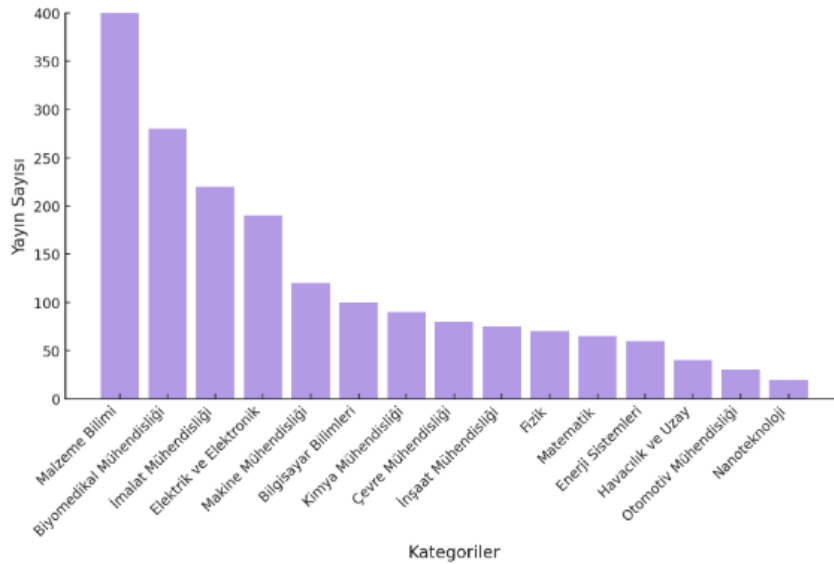
Şekil 2. Yayınların farklı kategorilere göre analizi.

419 (%36,4) adet yayın ile materials science multidisciplinary (çok disiplinli malzeme bilimi), 245 (%21,2) adet yayın ile engineering biomedical (biyomedikal mühendisliği), 202 (%17,5) adet yayın ile engineering manufacturing (imalat mühendisliği), 188 (%16,3) adet yayın ile materials science biomaterials (malzeme bilimi biyomalzemeler) konularının bu alanda önde gelen kategoriler olduğu görülmüştür.

3.3. Anahtar Sözcük Analizi

Anahtar sözcük analizi, literatürde hangi konuların daha fazla çalışıldığını ve hangi alanların nispeten daha az araştırıldığını belirlemek için önemli bir araçtır. Elde edilen analizler doğrultusunda en sık kullanılan terimler ve bunların literatürdeki bağlamı şu şekilde özetlenebilir:

- **3D Printing:** Tıbbi modelleme, cerrahi planlama ve kişiye özel implant üretimi gibi geniş bir uygulama alanına sahiptir. 3B baskı, özellikle cerrahi operasyonlar öncesinde hasta bazlı simülasyonlar için yoğun şekilde kullanılmaktadır.
- **Tissue Engineering:** Doku mühendisliği, biyomalzemeler ve hücresel yapılar üzerine yapılan çalışmalar, eklemeli imalat ile desteklenen en önemli alanlardan biridir. Bu alandaki araştırmaların büyük bir kısmı biyoyazıcılar ve hücre bazlı üretim tekniklerine odaklanmaktadır.

- **Biomaterials:** Biyouyumlu polimerler, seramikler ve metaller gibi malzemeler, eklemeli imalat ile biyomedikal uygulamalara entegre edilmektedir. Özellikle kemik doku mühendisliği ve protez üretimi açısından biyomalzemeler kritik öneme sahiptir.
- **Bioprinting:** Canlı hücrelerin katman katman basılması ile doku ve organ üretimi hedeflenmektedir. Biyoyazıcı teknolojileri, doku mühendisliği ve rejeneratif tıp açısından büyük bir potansiyele sahiptir.

Eklemeli imalatın biyomedikal alanındaki uygulamaları ile ilgili yayınlarda en sık kullanılan anahtar sözcüklerin incelenmesi için uygun kriterler ile filitreleme yapılmıştır. En az 10 kez tekrar eden anahtar sözcükler filtrelendiğinde 2707 kelimeden aralarında yoğun olarak ilişki bulunan 54 adet anahtar sözcük tespit edilmiştir. Bu 54 gözlem birimine odaklanılarak gerçekleştirilen analiz sonucunda 6 grup, 437 ağ ve 1860 ağ gücü belirlenmiştir.
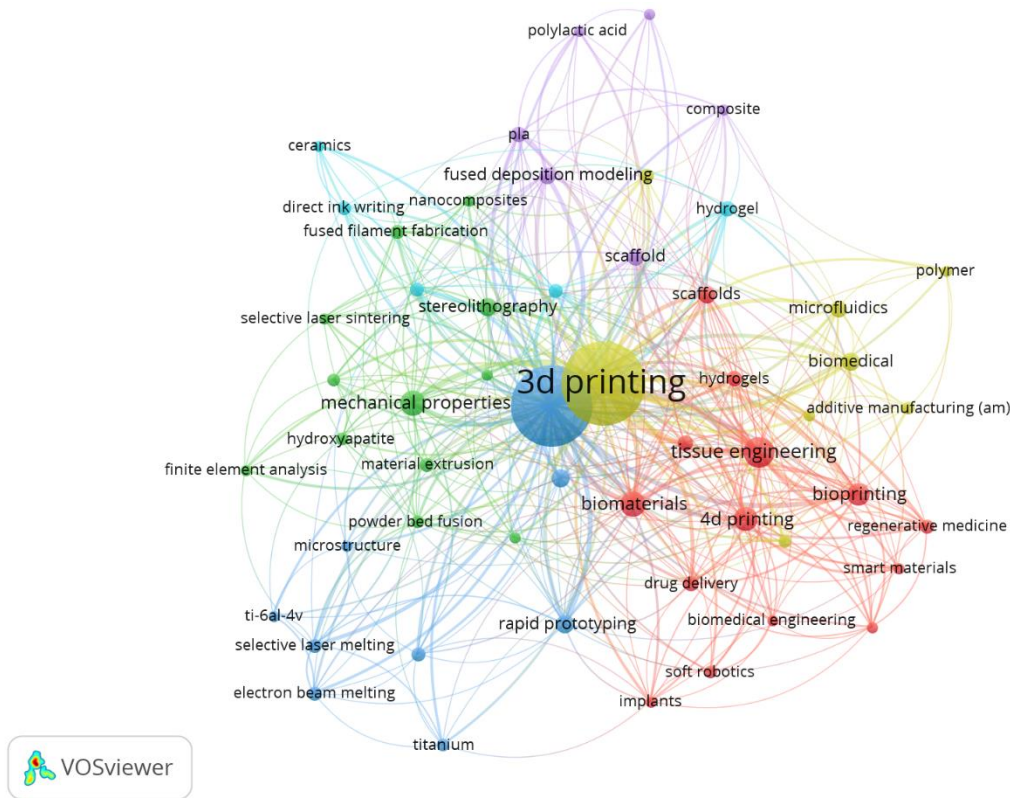

Şekil 3. En fazla kullanılan anahtar sözcüklerin haritası.

Veri sonuçlarına bakıldığında 539 adet ile 3d printing (3B yazıcı), 511 adet ile additive manufacturing (eklemeli imalat), 78 adet ile tissue engineering (doku mühendisliği), 50 adet ile biomaterials (biyomalzemeler) ve 43 adet ile bioprinting (biyoyazıcı) ifadeleri öne çıkan sözcüklerdir. Ağ gücü açısından en güçlü ifadeler 3d printing, additive manufacturing ve tissue engineering olmuştur.

Yapılan analizler göstermektedir ki, eklemeli imalatın biyomedikal alanındaki kullanımına ilişkin çalışmaların büyük bir bölümü, tıbbi cihaz üretimi, biyoyazıcı teknolojileri ve kişiselleştirilmiş tedavi yöntemlerine odaklanmaktadır. Bununla birlikte, biyomalzemelerin uzun vadeli biyouyumluluk testleri ve biyoyazıcı ile üretilen dokuların klinik kullanım olanakları gibi bazı konuların henüz yeterince araştırılmadığı tespit edilmiştir. Gelecekteki çalışmaların bu alanlara yönelmesi önerilmektedir.

3.4. Ortak Yazar Analizi

Ortak yazar analizine göre, en çok iş birliği kuran yazarları belirlemek üzere, 5249 yazardan minimum 2 eser ve minimum 2 atıf kriterleri seçilerek bağlantı haritasının görseli meydana getirilmiştir. Belirlenen kriterleri sağlayan 539 yazar arasından en fazla iş birliği yapan 29 yazarın ağ haritası oluşturulmuştur (Şekil 4). Bu 29 yazarın oluşturduğu birimler ile yapılan analiz sonucunda 7 grup, 53 ağ ve 81 ağ gücü belirlenmiştir.
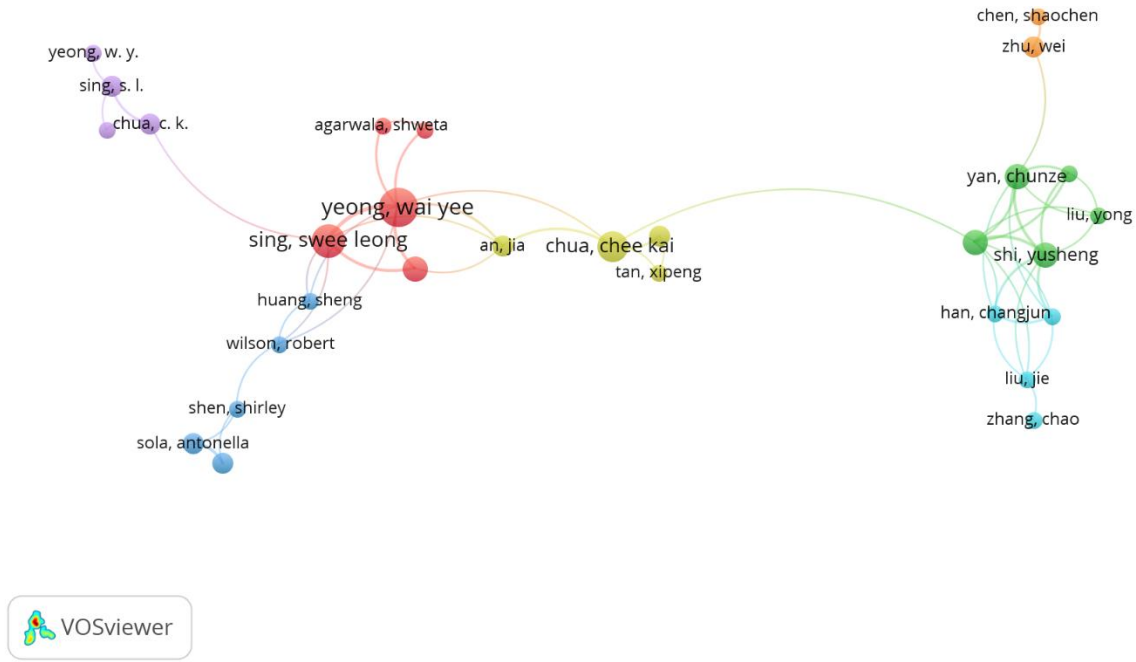
Şekil 4. Ortak yazar iş birliği analizi.

En fazla atıf sayısına sahip olan yazarlar, 2340 atıf ile Susmita Bose, 2256 atıf ile Amit Badyopadhyay ve 1673 atıf ile Wai Yee Yeong olmuştur. En çok yayın üreten yazarlar arasında da 13 yayın ile Susmita Bose, 13 yayın ile Amit Badyopadhyay ve 10 yayın ile Wai Yee Yeong ilk üçte yer almaktadır. Maksimum atıf sayısına sahip olan ve maksimum sayıda eseri olan ilk üç yazardan yalnızca Wai Yee Yeong en bağlantılı yazarlar arasında olduğu gözlemlenmiştir.

3.5. Yazar Atıf Analizi

Atıf bağlantılarını belirleyebilmek için minimum 5 eser ve minimum 5 atıf kriterleri ile bir bağlantı haritası oluşturulmuştur. Aralarında sık bağlantı olduğu tespit edilen 22 unsur ile oluşturulan analiz sonucunda 5 grup, 54 ağ ve 236 ağ gücü olduğu belirlenmiştir. Maksimum atıf sayısına sahip olan yazarlar 2340 atıf ile Susmita Bose, 2256 atıf ile Amit Badyopadhyay olarak tespit edilmiştir. Bu iki yazarın, ağ gücü bakımından da sıaralamalarına bakıldığında ilk iki sırada yerlerini koruduğu tespit edilmiştir.
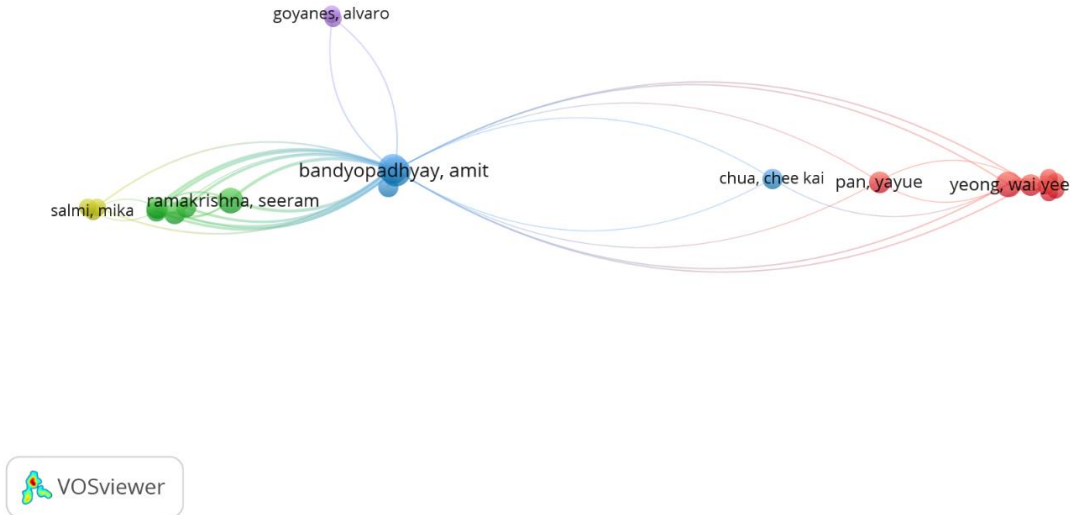

Şekil 5. Yazarların atıf analizi.

3.6. Ülke Atıf Analizi

Toplam 78 ülkeden yayınlanan eserlerin ülkeleri, aldıkları atıf sayıları bakımından ağ analizi haritası meydana getirmek üzere, herhangi bir ülkenin minimum 5 eser ve minimum 5 atıf kriterlerini sağlamasına

göre birbiriyle iş birliği kurulan 50 adet ülkenin gözlem birimini oluşturduğu, Şekil 5'te bulunan haritaya göre değerlendirme gerçekleştirilmiştir. 7 grup, 508 ağ ve 2830 ağ gücü olduğu belirlenmiştir.
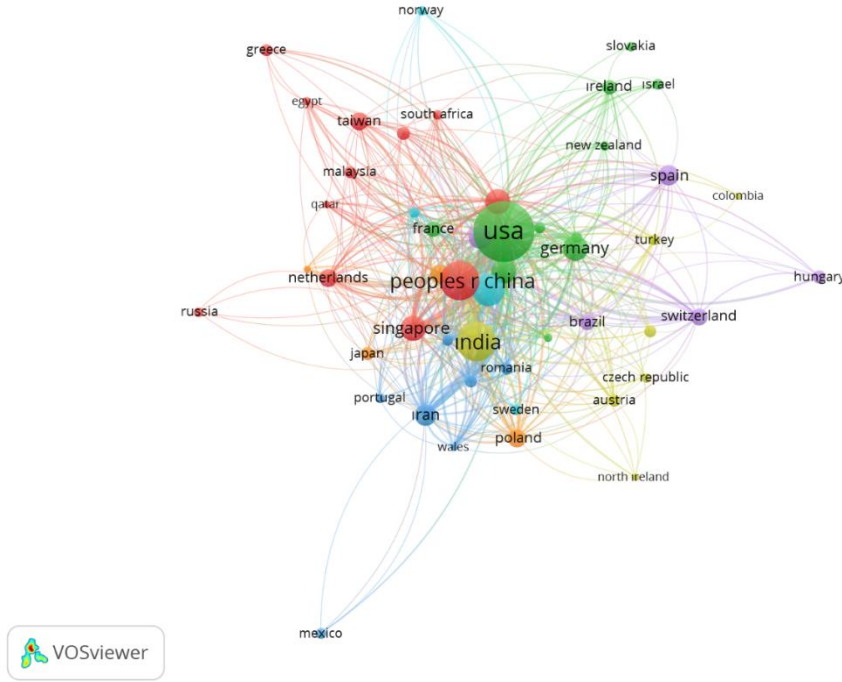

Şekil 6. Ülkelerin atıf ağ analizi.

En fazla yayın yapan ülkelerden 330 yayın ile ABD, 135 yayın ile Çin ve yine 135 yayın ile Hindistan önde gelen ülkeler olduğu görülmüştür. Ağ gücü açısından da bu ülkelerin ilk üç sırada yer aldığı gözlemlenmiştir. En çok atıf sayısına sahip ülkeler arasında ise, 22727 atıf ile ABD, 7067 atıf ile Avustralya ve 5039 atıf ile Çin olmuştur.

3.7. Kurum Atıf Analizi

Eserlerin yayınlandığı kurumların aldığı atıflara ait bir haritasını oluşturabilmek için toplam 1537 kurum arasından en az 5 yayında yer alan ve en az 5 atıf almış olan kurumlar için filtreleme uygulandığında 94 adet kurumun seçildiği bu kriterleri sağladığı saptanmıştır. Şekil 7, yoğun olarak iş birliği içerisinde olan ve en az 5 yayında yer alan 87 adet kurumun haritası gösterilmektedir. 9 grup, 451 ağ ve 798 ağ gücü belirlenmiştir.
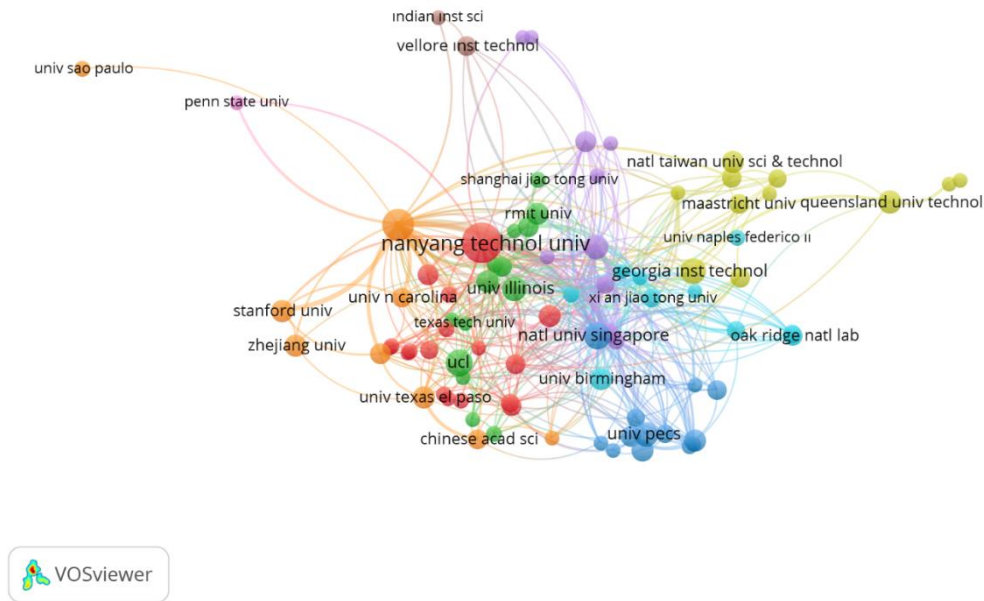

Şekil 7. Kurumların atıf ağ analizi.

En fazla yayın yapan kurumlar arasında, 35 eser ile Nanyang Technological University, 21 eser ile Washington State University ve 16 eser ile National University of Singapur önde gelen kurumlardır. En çok atıf alan kurumlardan ise, 4606 atıf ile Nanyang Technological University, 4516 atıf ile Melbourne University ve 2583 atıf ile Washington State University kurumları ilk sıralarda yer almıştır.

3.8. Eserlerin Kaynak Analizi

Eserlerin yayınlandığı kaynakların aldığı atıflara ait bir haritasını oluşturabilmek için toplam 447 kaynak arasından minimum 5 eser içeren ve minimum 5 atıf almış olan kaynaklar için filtreleme uygulandığında 47 adet derginin seçildiği bu kriterleri sağladığı saptanmıştır. Şekil 8, yoğun olarak iş birliği içerisinde olan ve en az 5 yayın yapılmış olan 46 adet kurumun haritası gösterilmektedir. 9 grup, 229 ağ ve 331 ağ gücü olduğu gözlemlenmiştir.
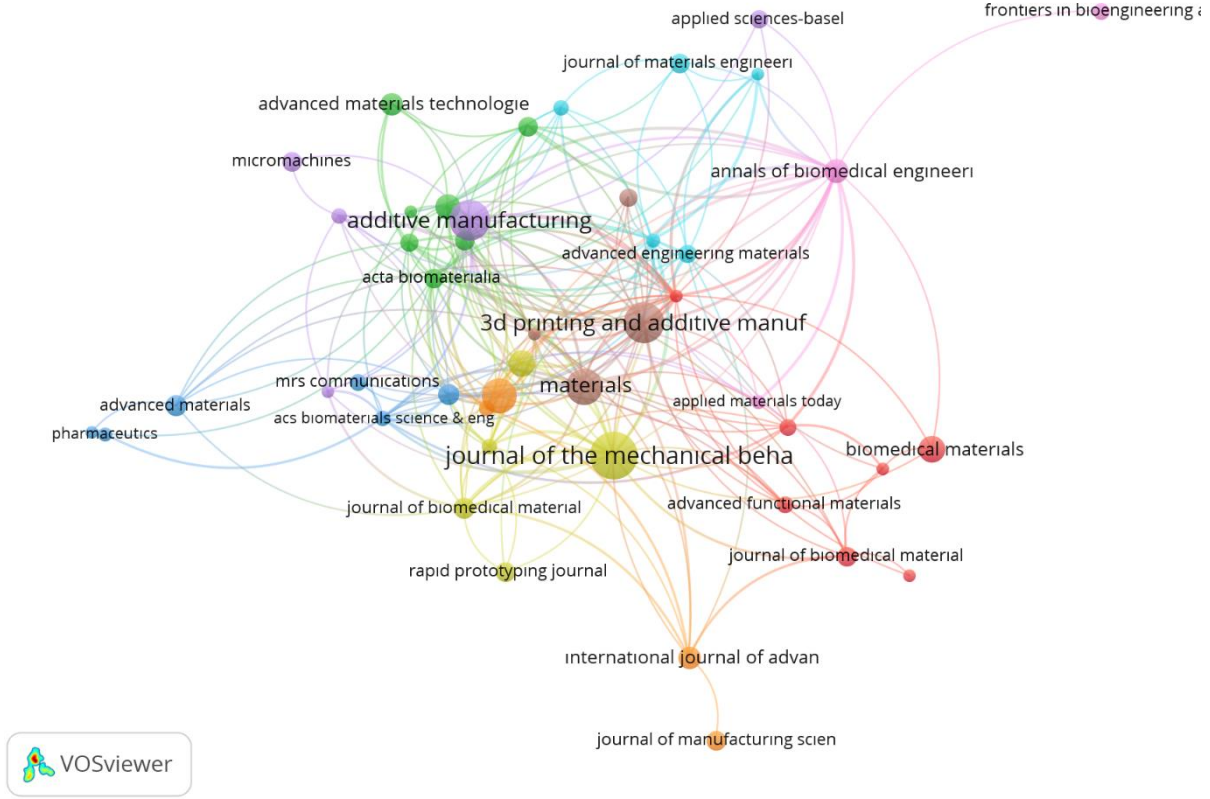

Şekil 8. Eserlerin yayınlandığı kaynakların analizi.

En fazla yayın yapan kaynakların, 61 adet yayın ile "journal of the mechanical behavior of biomedical materials", 45 adet yayın ile "additive manufacturing" ve 44 adet yayın ile "3d printing and additive manufacturing" adlı kaynaklar olduğu tespit edilmiştir.

3.9. Eserlerin Bibliyografik Eşleşme Analizi

Bibliyografik eşleşme, bağımsız iki kaynağın ortak bir çalışmayı referans göstermesi durumunu tanımlar. Minimum 5 atıf alma kriteri ile filtrelenen ve birbiriyle ağı olan 760 eser ile oluşturulan analizin sonucunda 17 grup, 25328 ağ ve 37144 ağ gücü olduğu gözlemlenmiştir. Maksimum sayıda bibliyografik eşleşmeye sahip olan eserler 4442 atıf ile Tuan D. Ngo (2018), 1855 atıf ile Martin (2017) ve 1324 atıf ile Bose (2013) olduğu belirlenmiştir. Maksimum ağ gücüne sahip eserler ise Li (2020a), Jia (2023) ve Puppi (2020) olmuştur.
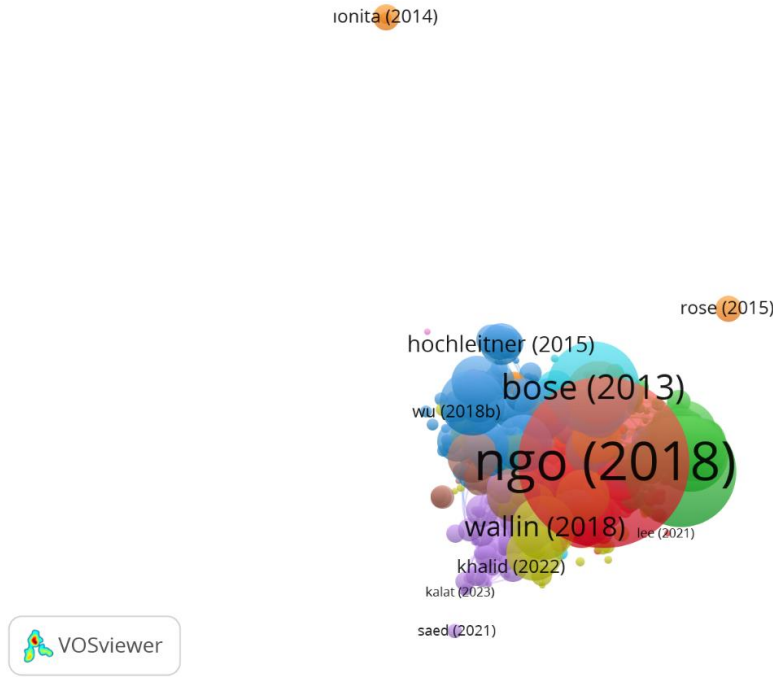
Şekil 9. Eserlerin bibliyografik eşleşme analizi.

3.10. Yazarların Bibliyografik Eşleşme Analizi

Minimum 5 yayın yapmış olma ve minimum 5 atıf alma kriterleri ile belirlenen ve birbirleriyle bağlantısı olan 41 yazar ile gerçekleştirilen analiz sonucunda göre 6 grup, 676 ağ ve 58371 ağ gücü gözlemlenmiştir.
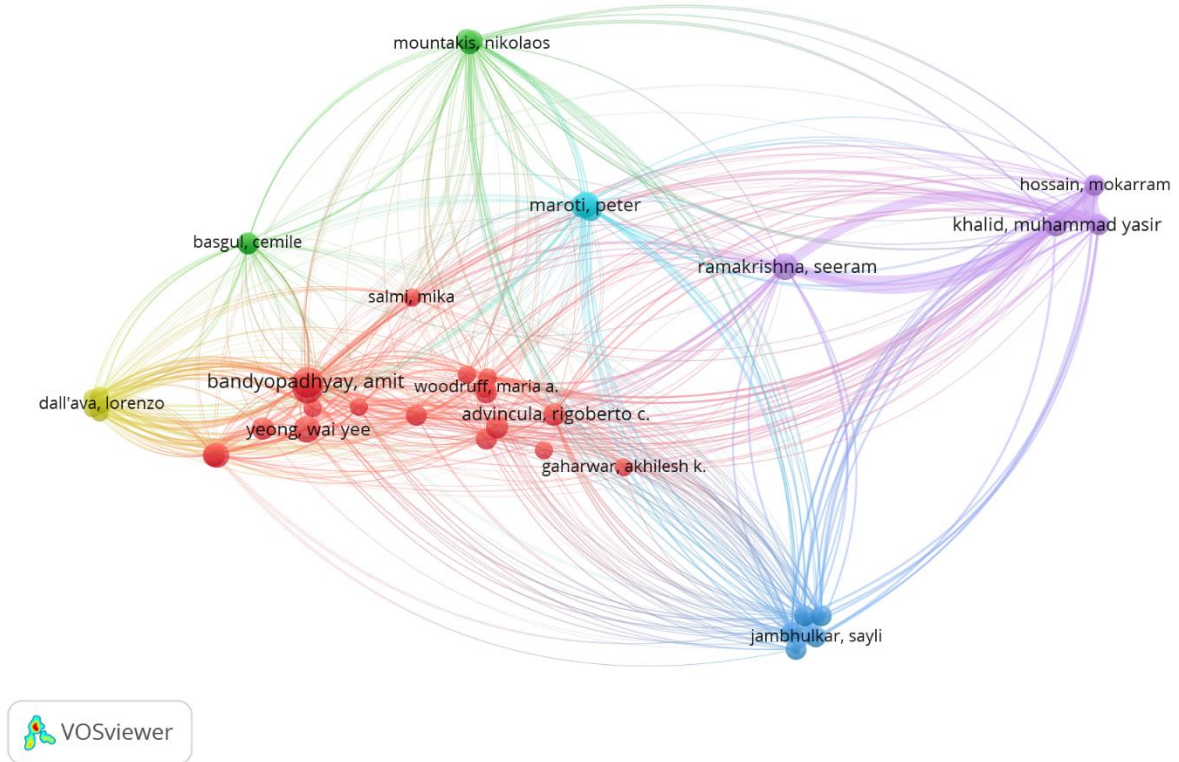
Şekil 10. Yazarların bibliyografik eşleşme analizi.

En fazla sayıda bibliyografik eşleşme olan yazarların 2340 atıf ile Susmita Bose, 2256 atıf ile Amit Badyopadhyay ve 1673 atıf ile Wai Yee Yeong olduğu görülmüştür.

3.11. Yazarların Eş atıf Analizi
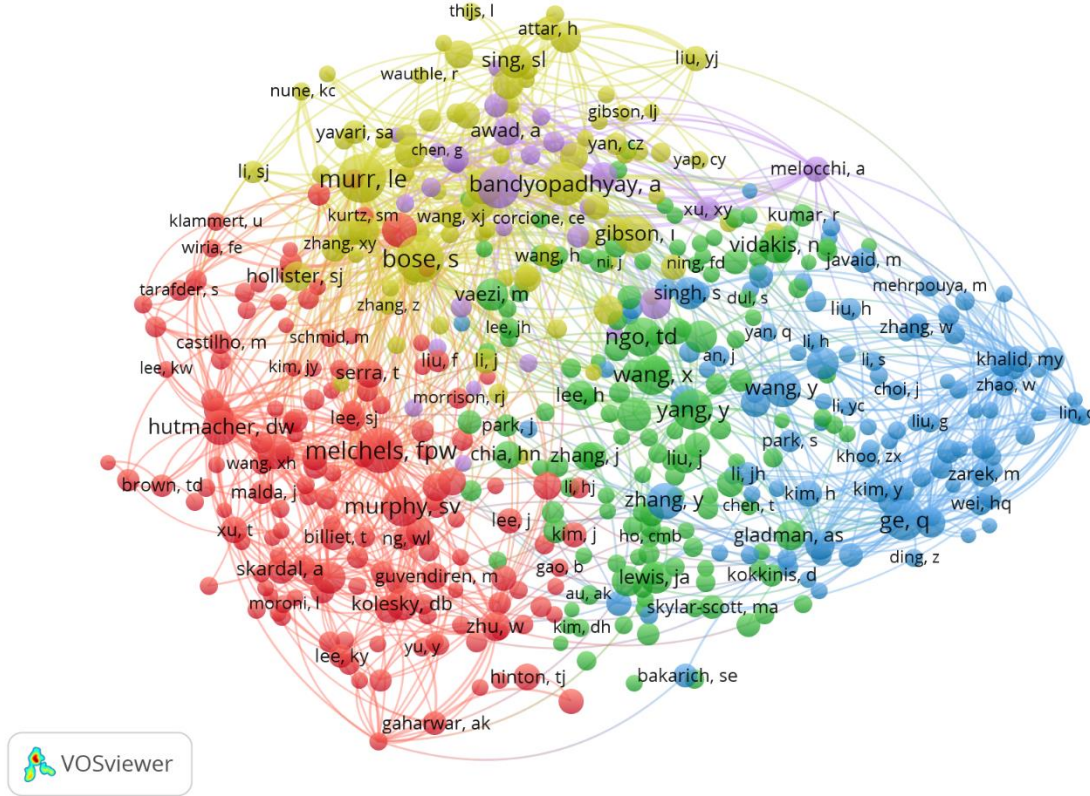
Şekil 11. Yazarların eş atıf analizi.

4. SONUÇLAR

Bu çalışmada elde edilen sayısal veriler, eklemeli imalatın biyomedikal uygulamalarındaki gelişiminin nicel boyutunu ortaya koymaktadır. Ancak, bu verilerin derinlemesine yorumlanması, çalışmanın amacına uygun olarak teknolojik gelişmeler ve uygulamalardaki trendlerle ilişkilendirildiğinde daha anlamlı hale gelmektedir. Örneğin, 2012–2024 yılları arasında artan yayın sayısının, özellikle 2023 yılında 194 yayına ulaşması, eklemeli imalata yönelik araştırmalarda artan ilgi ve teknolojik gelişmelerin bir göstergesidir. Bu yaklaşım, Bose ve arkadaşları ile Ngo ve arkadaşları tarafından bildirilen, teknolojinin evrimi ve uygulama alanlarının genişlemesiyle paralellik göstermektedir [13, 17].

Yayınların farklı kategorilere dağılımı, disiplinlerarası bir yaklaşımın benimsendiğini açıkça ortaya koymaktadır. Multidisipliner malzeme bilimi, biyomedikal mühendislik ve imalat mühendisliği gibi kategorilerde yoğunluk, eklemeli imalatın sadece üretim teknikleri olarak değil aynı zamanda klinik uygulamalar ve malzeme geliştirme süreçlerinde de kritik bir rol oynadığını işaret etmektedir. Bu durum, Tan ve arkadaşları ile Chimene ve arkadaşlarının çalışmalarıyla uyumlu olup, eklemeli imalatın farklı disiplinlerdeki entegrasyonunu desteklemektedir [8, 18].

Anahtar sözcük analizi sonuçlarına göre; "3B baskı", "doku mühendisliği", "biyomalzemeler" ve "biyoyazıcı" gibi ifadelerin öne çıkması, bu alanlarda yoğunlaşan araştırmaların, kişiselleştirilmiş tıp ve rejeneratif uygulamalara yönelik literatürdeki artan ilgiyi yansıttığını göstermektedir. Bu bulgu, Javaid ve Haleem ile Tasneem ve arkadaşlarının çalışmalarıyla paralellik arz etmektedir; her iki çalışma da biyomedikal uygulamalarda bu terimlerin ve teknolojilerin önemine vurgu yapmaktadır [14, 15].

Sonuç olarak, sayısal veriler yalnızca yayın sayısı, kategori dağılımı ve anahtar sözcük frekansları gibi nicel ölçütleri sunmaktan öte, eklemeli imalatın biyomedikal alandaki dinamik yapısını ve geleceğe yönelik araştırma potansiyelini de gözler önüne sermektedir. Bu kapsamlı yorum, literatürdeki benzer yaklaşımlarla karşılaştırıldığında, mevcut teknolojik ilerlemelerin ve disiplinlerarası etkileşimlerin altını çizmekte, çalışmanın bilimsel katkısını güçlendirmektedir.

Çalışma kapsamında WoS veri tabanında biyomedikal alanında eklemeli imalat üzerine yayınlanan akademik yayınların günümüze kadar olan gelişim süreci incelenmiştir. Belirlenen kriterler aralığında ilgili kavramları içeren yayınlar zamana göre incelendiğinde, eklemeli imalatın biyomedikal uygulama alanlarında yapılan ilk yayınının 2012 yılında yapıldığı görülmüştür. Araştırma kapsamında eklemeli imalatın

biyomedikal uygulamaları ile ilgili en fazla yayının 2023 yılında yapıldığı tespit edilmiştir. 2012 yılından bu yana yayın sayısında değişkenlik görülmekle birlikte genel yönelimin son yıllarda artış olduğu gözlemlenmektedir. Ek olarak, yayınlanan eserler konuları bakımından sınıflandırıldığında, üçte birinden fazlasının multidisipliner malzeme bilimi kategorisinde yer aldığı görülmüştür. Bu da, konuyla ilgili eserlerin hem anatomi, fizyoloji, biyokimya gibi tıbbi alanlarda, hem de mekanik, dayanıklılık ve performans gibi mühendislik alanlarının gelişmesinin sonucudur.

Eklemeli imalatın biyomedikal uygulamalarını içeren eserler incelendiğinde 3B yazıcı ve eklemeli imalat terimlerinin yoğun olarak kullanıldığı tespit edilmiştir. Bu terimlere ek olarak; doku mühendisliği, biyomalzeme, biyoyazıcı ve mekanik özellikler gibi terimler de bu alanda yayınlanan makalelerde önde gelen terimler arasında yer almaktadır.

Eklemeli imalat alanındaki biyomedikal uygulamalar üzerinde; ABD, Çin, Hindistan, İngiltere, Almanya, Avustralya, Singapur ve İtalya başta olmak üzere dünyada birçok ülkede çalışılmaktadır. Susmita Bose, Amit Badyopadhyay ve Wai Yee Yeong gibi bu alanda en çok yayın yapan bilim insanlarının da bu ülkelerden olduğu görülmüştür. Nanyang Technological University, Washington State University ve National University of Singapur bu konuyla ilgili en çok akademik yayının da yine bu ülkelerin üniversitelerinde yapıldığını göstermektedir.

Bu araştırmadan elde edilen diğer bir sonuç ise, 4442 adet atıf ile en fazla atıf sayına sahip "Additive manufacturing (3D printing): A review of materials, methods, applications and challenges" (Eklemeli İmalat (3B baskı): Malzemeler, yöntemler, uygulamalar ve zorlukların gözden geçirilmesi) adlı akademik makalenin Melbourne Universitesi Mühendislik Fakültesi öğretim üyesi Tuan D. Ngo tarafından yazılmıştır. Makalenin içeriğinde; eklemeli imalatın başlıca yöntemleri, kullanılan malzemeler ve biyomedikal, havacılık, inşaat gibi temel sektörlerdeki trend uygulamaları ve karşılaşılan zorlukların detaylı olarak anlatıldığı görülmüştür [17].

Biyomalzemeler ve kişiselleştirilmiş tıp cihazları alanındaki ilerlemeler, klinik uygulamalara yönelik önemli etkiler yaratmaktadır. Gelecek vadeden çalışma konuları olarak biyoyazıcı teknolojisinin optimizasyonu, doku modelleme yöntemlerinin geliştirilmesi ve biyomalzemelerin uzun dönemli biyouyumluluğu üzerine odaklanılması önerilmektedir.

Bu çalışma, eklemeli imalatın biyomedikal alandaki uygulamalarına dair genel bir çerçeve sunmanın yanı sıra, bu alanda gelecekte araştırma yapmayı planlayan bilim insanları için yeni öneriler ortaya koymaktadır. Özellikle biyomalzeme tasarımında kişiselleştirilmiş yaklaşımlar, biyoyazıcı teknolojisinin optimizasyonu ve 3B baskının klinik uygulamalara entegrasyonu konuları gelecekte daha fazla araştırma gerektiren alanlar olarak dikkat çekmektedir.

5. SINIRLAMALAR VE GELECEK ÖNERİLER

Bu çalışmanın en önemli sınırlamalarından biri, yalnızca WoS veri tabanına dayalı olmasıdır. Diğer akademik veri tabanlarının dâhil edilmemesi, potansiyel olarak farklı bakış açılarının göz ardı edilmesine neden olabilir. Ayrıca, biyomalzemeler ve biyomedikal uygulamalara dair niteliksel çalışmalar bu analiz kapsamının dışında kalmıştır. Bu sınırlılıklar, gelecekte daha kapsamlı veri kaynaklarının ve metodolojilerin dâhil edilmesi gerekliliğini ortaya koymaktadır.

Gelecek araştırmalar, biyoyazıcı teknolojilerinin klinik uygulamalardaki etkinliğini, biyomalzemelerin uzun dönem performansını ve disiplinlerarası çalışmalarla daha büyük veri havuzlarını kapsayan analizlerin gerekliliğini vurgulamalıdır. Ayrıca, 3B baskı teknolojisinin doku ve organ baskısındaki pratik uygulamalarının etkinliğini incelemek, gelecek çalışmalar için önemli bir başlık olarak görülmektedir.

TEŞEKKÜR

KAYNAKLAR

[1] D. Dirik, İ. Eryılmaz, T. Erhan, Post-truth kavramı üzerine yapılan çalışmaların VOSviewer ile bibliyometrik Analizi, Sosyal Mucit Academic Review, 4(2), 2023, 164-188.

[2] J. Tuomi, K-S. Paloheimo, J. Vehviläinen, A novel classification and online platform for planning and documentation of medical applications of additive manufacturing, Surgical Innovation, 21(6), 2014, 553-559.

[3] C. Aumund-Kopp, A. Riou., 3rd ed., EPMA Introduction to Additive Manufacturing. European Powder Metallurgy Association, Shrewsbury, 2019.

[4] H. Yang, P. Rao, T. Simpson, Y. Lu, P. Witherell, A. R. Nassar, E. Reutzel, S. Kumara, Six-sigma quality management of additive manufacturing, Proceedings of the IEEE, Institute of Electrical and Electronics Engineers. 109(4), 2021, 347–376.

[5]   D. Gu, X. Shi, R. Poprawe, D. L. Bourell, R. Setchi, J. Zhu, Material-structure-performance integrated laser-metal additive manufacturing, Science, 372, 2021, (6545).

[6]   A. Vafadar, F. Guzzomi, A. Rassau, K. Hayward, Advances in metal additive manufacturing: a review of common processes, ındustrial applications, and current challenges, Appl. Sci., 11(3), 2021, 1213.

[7]   Y.Lakhdara, C.Tucka, J.Binnerc, A.Terryb, R.Goodridge, Additive manufacturing of advanced ceramic materials, Progress in Materials Science 116, 2021, 10073.

[8]   L. J. Tan, W. Zhu, K. Zhou, Recent progress on polymer materials for additive manufacturing, Adv. Funct. Mater. 30, 2020, 2003062.

[9]   D. Chimene, R. Kaunas, A. K. Gaharwar, Hydrogel bioink reinforcement for additive manufacturing: a focused review of emerging strategies, Advanced Materials, 1902026, 2020.

[10] M.I. Mohammed, J. Tatineni, B. Cadd, G. Peart, I. Gibson, Applications of 3D topography scanning and multi-material additive manufacturing for facial prosthesis development and production, in: Proceedings of the 2016 International Solid Freeform Fabrication Symposium, University of Texas at Austin, 2016.

[11] M.E. Prendergast, J.A. Burdick, Recent advances in enabling technologies in 3D printing for precision medicine, Advanced Materials, 32 (13), 2020.

[12] E. Guzzi and M. Tibbitt, Additive manufacturing of precision biomaterials, Advanced materials, 32 (13), 2020.

[13] S. Bose, D. Ke, H. Sahasrabudhe, A. Bandyopadhyay, Additive manufacturing of biomaterials, Progress in materials science, 93, 2018, 45–111.

[14] M. Javaid, A. Haleem, 3D printed tissue and organ using additive manufacturing: an overview, Clinical Epidemiology and Global Health, 8(2), 2020, 586-594.

[15] I. Tasneem, A. Ariz, D. Bharti, A. Haleem, M. Javaid, S. Bahl, 3D printing technology and its significant applications in the context of healthcare education, Journal of Industrial Integration and Management, 8(01), 2023, 113-130.

[16] S. He, J. Zhu, Y. Jing, S. Long, L. Tang, L. Cheng, Z. Shi, Effect of 3D-printed porous titanium alloy pore structure on bone regeneration: A review, Coatings, 14(3), 2024, 253.

[17] T.D. Ngo, A. Kashani, G. Imbalzano, K.T. Nguyen, D. Hui, Additive manufacturing (3D printing): A review of materials, methods, applications and challenges, Composites Part B: Engineering, 143, 2018, 172-196.

[18] D. Chimene, R. Kaunas, A.K. Gaharwar. Hydrogel bioink reinforcement for additive manufacturing: a focused review of emerging strategies, Advanced materials, 1902026, 2020.

Manufacturing Technologies and Applications
MATECA

Effect of Heat Treatment at Different Temperatures on The Structural and Tribological Properties of Electroless Ni-B Coated 32CrMoV12-10 Alloy

Erdoğan Koray Özyurt[1] Muharrem Pul[2,*]

[1]*Department of Defense Technologies, Institute of Science and Technology, Kırıkkale University, Kırıkkale, Türkiye*
[2]*Kırıkkale Vocational School, Kırıkkale University, Kırıkkale, Türkiye*

ABSTRACT

In this article, Ni-B (nickel-boron) plating process was performed on 32CrMoV12-10 barrel material, which is widely used in the defense industry and produced by forging method, by electroless plating method in aqueous solution prepared in a bath. The coated samples were then heating process at 250, 300, 350 and 400°C temperatures. The effects of these heat treatments on tribological and microstructural properties were investigated. Cauliflower-like surface structure was formed on all coated samples. In XRD analysis, it was observed that an amorphous structure was formed in the sample heating processsat 250°C in argon environment. The highest hardness was measured on the surface of the sample heating processsat 350°C in argon environment, while the lowest hardness was measured on the surface of the sample with amorphous structure and heating process at 250°C in argon environment. It was observed that there was a notable increase in the wear endurance of the samples heating process at 300°C, 350°C and 400°C in argon environment. It was concluded that heat treatment in an open atmosphere causes oxidation at the steel interface, which prevents the diffusion of nickel into the steel in the plating process. The surface roughness of the sample heating process at 250°C in an amorphous argon atmosphere was higher than all other samples. The best surface roughness value was obtained at the argon atmosphere 350°C treatment conditions. When all the data supporting each other are brought together, it is determined that the most suitable heat treatment temperature is at 350°C in argon atmosphere instead of high temperature heat treatment after Ni-B plating process on an industrial scale.

Keywords: 32CrMoV12-10 alloy, Electroless plating, Nickel-Boron coating, Heat treatment, Mechanical properties, Tribology

Farklı Sıcaklıklardaki Isıl İşlemin Akımsız Ni-B Kaplamalı 32CrMoV12-10 Alaşımının Yapısal Ve Tribolojik Özelliklerine Etkisi

ÖZET

Bu çalışmada, savunma sanayinde yaygın olarak kullanılan ve dövme yöntemi ile üretilen 32CrMoV12-10 namlu malzemesine, banyo içerisinde hazırlanan sulu çözeltide akımsız kaplama yöntemi ile nikel-bor (Ni-B) kaplama işlemi gerçekleştirilmiştir. Kaplanan numuneler daha sonra farklı sıcaklıklarda ısıl işleme tabi tutulmuştur. Bu ısıl işlemlerin tribolojik ve mikro yapısal özellikler üzerine etkileri incelenmiştir. Tüm kaplanan numunelerde karnabahar benzeri yüzey yapısı oluşmuştur. XRD analizi, argon atmosferinde 250°C'de ısıl işlem uygulanan numunenin yapısının amorf olduğunu göstermiştir. En yüksek sertlik değeri argon atmosferinde 350°C'de ısıl işlem uygulanan numunede, en düşük sertlik ise amorf yapıya sahip argon atmosferinde 250°C'de ısıl işlem uygulanan numunede ölçülmüştür. Argon atmosferinde 300, 350 ve 400°C'de ısıl işlem uygulanan numunelerin aşınma dirençlerinin önemli ölçüde iyileştiği görülmüştür. Açık atmosferde ısıl işlemin çelik ara yüzeyinde oksidasyona neden olduğu ve bu durumun kaplama işleminde nikelin çeliğe difüzyonunu engellediği sonucuna varılmıştır. Amorf argon atmosferinde 250°C'de ısıl işleme tabi tutulan numunenin yüzey pürüzlülüğü diğer tüm numunelerden daha yüksek bulunmuştur. En iyi yüzey pürüzlülük değeri argon atmosferinde 350°C işlem koşullarında elde edilmiştir. Birbirini destekleyen tüm veriler bir araya getirildiğinde endüstriyel ölçekte nikel-bor (Ni-B) kaplama işleminden sonra yüksek sıcaklık ısıl işlemi yerine argon atmosferinde 350°C'de en uygun ısıl işlem sıcaklığının olduğu belirlenmiştir.

Anahtar Kelimeler: 32CrMoV12-10 alaşımı, Akımsız kaplama, Nikel-Bor kaplama, Isıl işlem, Mekanik özellikler, Triboloji

1. INTRODUCTION

The historical evolution of weapons has taken place in parallel with technological advancements, resulting in the continuous improvement of the desired properties of weapons such as high durability, low weight, high wear resistance and corrosion resistance. Research has shown that weapon parts are subjected to high stresses and therefore manufacturing materials must have high durability. Therefore, it is important that the materials have high durability and impact resistance to achieve long life and high dimensional stability in weapon parts [1-3]. In recent years, due to the need to increase the firing life of weapons beyond the world standards, development studies on weapon parts such as barrels have gained importance. In order to extend the service life, it is emphasized that the factors affecting the service life of the parts, such as material selection, heat treatment applications and coating, should be selected at the optimum level [4].

Coating is the process of layering or deposition of another material, which is considered as a sub-material and on which functionality is desired to be imparted, so as to enhance the physical, chemical and mechanical properties of a material. The types of surface coatings known and applied to obtain surfaces with different types of characteristics include hard chrome plating, electroless plating, thermal spray, weld overlay, CVD, PVD, ion implantation and laser surface treatment [5]. Electroless coatings refer to a surface coating method based on the controlled reduction reaction of metal ions such as copper, nickel, silver, gold and similar metal ions, without the need for electric current, accompanied by the catalytic properties of the surface. Nickel-phosphorus and nickel-boron are the most important electroless deposition coatings for improving chemical and physical wear properties [6]. Electroless nickel plating is the deposition of nickel without the use of electric current. The plating takes place by autocatalytic chemical reduction of nickel ions by hypophosphite, amino borane or borohydride compounds. The process is carried out by immersing the material to be plated in a solution. The plating bath consists of aqueous solutions of chemical substances consisting of metal salt, reducing agent, pH level adjusting buffer solution and reaction rate adjusting catalysts. The reducing agent ensures the reduction of metal ions. Electroless nickel plating is based on electrochemical deposition in which the reducing agent acts as a catalyst and adheres to the material during the plating process [5, 6]. Electroless nickel plating is preferred in a wide range of industrial applications such as petroleum, chemical and plastic industries, optics, printing, mining, aviation, nuclear, automotive, electronics, computers, paper, textile and food machinery due to its superior technical properties such as excellent chemical and physical wear resistance, uniform coating thickness in all areas, solderability and weldability, excellent coating hardness and lubricity [5, 6].

When the literature is reviewed, it is seen that similar studies have been carried out on the investigation of electroless coating and properties of different steel alloys. In the studies of Taha-Tijerina et al., the tribological properties of electroless Ni-B film were evaluated under extreme pressure conditions when D2 tool steel samples were coated with 3 μm, 6 μm and 12 μm coating thicknesses and heat treatment (200 °C for 90 minutes) were applied. The results showed that the chemical-free technology improved the coefficient of friction (COF) of tool steel with 3 μm and 12 μm coating by 15% to 30%, respectively. When this improvement was increased by applying heat treatment to the coated components, it was stated that improvements of 24-38% were shown between 3 mm and 12 mm, respectively [7]. In another study by Cies´lak et al.; a process scheme was developed for the production of Ni-B layers and composite coatings with nickel-boron matrix and a dispersant phase in the form of boron nanoparticles. In order to improve the performance of the produced coatings, a heating process was carried out at 400 ∘C and the performance of Ni-B and composite Ni-B/B coatings was investigated after the heat treatment process. When the results were evaluated, it was stated that the heat treatment of the coatings caused the crystallization of the amorphous matrix and significantly increased the hardness. On the other hand, the high hardness of the crystalline nickel boride phases was reported to contribute to the high brittleness and cracking of the coatings [8]. In a similar study by Arias et al., the tribological properties were evaluated before and after one hour of heat treatment at 450 °C in Ni-B autocatalytic coatings deposited on AISI/SAE 1018 carbon steel. According to the tribological evaluation, heat treatments applied to Ni-B coatings were found to improve their tribological performance. As a result of the research, it was stated that it was confirmed that the hardness and wear resistance of Ni-B coatings could be significantly improved by applying an adequate heat treatment [9]. In a study conducted by Çelik et al., the surface of commercially pure titanium (Grade 2) was coated with electroless Ni–B and then heat treated at 400 C for one hour. The analysis results showed that the electroless Ni–B coating had a significantly amorphous structure when deposited. In addition, it was determined that the coating structure crystallized after heat treatment and the wear resistance of pure titanium increased after chemical-free Ni–B coating. In particular, it was stated that the wear resistance and surface hardness of pure titanium increased significantly after heat treatment [10]. In the study of Bülbül et al., electroless Ni–B coating was deposited on AISI 316L stainless steel and its structural, tribological and corrosion properties

were characterized. Microstructural analysis showed that the non-chemical Ni–B coating deposited on AISI 316L steel substrate exhibited a typical cauliflower-like structure and exhibited amorphous growth. From this study, it was concluded that this treatment could not only improve the hardness and wear resistance of 316L stainless steel, but also provide cathodic protection without losing the original properties of 316L stainless steel [11].

In this experimental study; 32CrMoV12-10 (1.7765) barrel material produced by forging method was used. Due to its good mechanical properties, 32CrMoV12-10 steel is mostly preferred in high temperature applications. However, some tools or work dies made of 32CrMoV12-10 steel may be subject to frequent wear. Therefore, distinct surface treatments are applied to improve the tribological features of 32CrMoV12-10 and similar tool steels and to increase their wear resistance [12]. Industrial reclaimed steels are steels used in machine manufacturing that are highly amenable to hardening due to their carbon content (0.25% C to 0.6% C). The reclamation process is defined as the hardening and subsequent tempering of steel materials to give them high toughness properties. These steels are used in the production of medium caliber weapons due to their superior mechanical properties after the treatment process. They are also widely used in the manufacture of machine parts, crankshafts, axle shafts and splined shafts [13]. 32CrMoV12-10 is a hot work tool steel with high thermal shock endurance, high thermal conductivity and high toughness over long periods of time. This steel is used in various applications such as pressure casting of heavy metals, hot forging and forming dies, extrusion dies of materials such as aluminum, copper, brass and gun barrel production [14]. Based on the literature researches and past studies, the stages of the processes to be carried out were determined; in order to determine the best conditions of the plating baths, chemicals that will use nickel ions as a source, complexing agents, stabilizing agents, plating bath solution mixing speed and bath pH value were determined. The samples were then coated according to this plan in an electroless Ni-B coating bath. The Ni-B coated materials were then heating process at 250, 300, 350 and 400°C in argon atmosphere and 400°C in open atmosphere respectively. Since oxidation is expected to increase with the increase in heat treatment temperature, the open atmosphere experiment was carried out at 400 °C, which is the highest temperature within the operating limit conditions. In the study in the literature, it is stated that the crystallization temperature of Ni-B coating is 300°C - 350°C [15]. In the study subject to this article, the values in the literature were taken into consideration and it was deemed appropriate to examine the lower and upper values of these values. In the first step during the characterization studies, the surface and cross-sectional images of the Ni-B coated samples subjected to heat treatment at different temperatures were observed using FE-SEM device and the thickness of the coating was measured and the structures occured on the surface were examined in detail. After determining that the coatings were successfully applied, XRD analysis, hardness, wear and surface roughness tests were performed on the samples and the tribological strength properties were examined parametrically depending on the heat treatment temperature differences in the coating.

The main purpose of this study is to develop a coating that can increase the service life of the weapon by increasing the mechanical properties of the barrel. Therefore, in this study, 32CrMoV12-10 barrel material, which is widely used in the defense industry and produced by the forging method, was prepared in the form of plate samples. Ni-B coating was applied to the prepared samples by the electroless coating method in the bath prepared in an aqueous solution. Subsequently, heat treatments were applied at different temperatures and the effects of heat treatment parameters on the tribological and microstructural properties of the final product were investigated comprehensively. The obtained data were evaluated and an attempt was made to determine the optimum parameter within the selected heat treatment parameters.

2. MATERIAL AND METHOD

2.1. Preparation of samples and electroless Ni-B coating

In this study, plate-shaped specimens with dimensions of 29×29×3 mm were prepared by wire erosion cutting method from 32CrMoV12-10, which is a material frequently preferred in gun barrel production as a base metal. Table 1 shows the chemical composition and some mechanical properties of 32CrMoV12-10 steel.

Table 1. Chemical combination and mechanical properties of 32CrMoV12-10 steel [16].

C	Mn	Si	Cr	Mo	V	P	S	Fe
0,3 – 0,35	≤ 0,6	≤ 0,35	2,8 – 3,2	0,8 – 1,2	0,25 – 0,35	≤ 0,025	≤ 0,01	Remain

Yield Strength Rp 0.2 (MPa)	Tensile Stress Rm (MPa)	Elongation A (%)	Heat Treatment Condition	Brinell Hardness (HB)
≥ 740	≤ 1080	≥ 10	Tempering	Tempered 265–320

NiCl2.6H2O (Tekkim ≥97 %), C2H8N2 (Merck ≥99 %), NaBH4 (Tekkim ≥97 %), Pb(NO3)2 (Tekkim ≥98 %) and NaOH (Tekkim ≥97 %) were used as plating bath components. The surfaces of the selected base metal samples were cleaned with acetone to remove unwanted impurities. The surfaces to be coated were first sanded with Silicon carbide paper abrasives with 120, 240, 400, 600, 800 and 1200 mesh abrasives and then polished using 3 μm and 1 μm diamond suspension. The base metal to be coated was then cleaned with acetone and washed with ethanol. The samples were then placed in 15% HCl solution by volume and 2% inhibitor for 90 seconds. Samples were then soaked in 5% H2SO4 solution by volume for 30 seconds and dried, which made the base metal ready for coating. Rinses were performed at regular intervals using distilled water. In order to evaluate the cross-sectional morphology and thickness of the coated samples, the samples were cut and then bakelined. After these treatments, they were subjected to sanding processes (120, 240, 400, 600, 800, 800, 1200 mesh abrasive) and polishing using diamond suspension (9 μm, 3 μm, 1 μm) [17].

In the second stage, the preparation of electroless Ni-B plating baths was initiated. Nickel chloride hexahydrate (NiCl2-6H2O) was selected as the nickel ion source and its solution was used at a concentration of 20 g/L. Ethylenediamine (C2H8N2) was added at a concentration of 110 g/L as a complexing agent with the dissolution of nickel, i.e. to prevent a sudden decrease in the pH of the reaction medium and precipitation of the nickel ions to be reacted, and stirring was continued. Considering that the baths using NaBH4 can easily decompose in acidic and neutral conditions, the plating baths must be in an alkaline environment. Therefore, sodium hydroxide (NaOH) solution was gradually added to the reaction solution at a concentration of 75 g/L to prevent decomposition due to low pH. After adding NaOH to the plating bath, the bath was heated. When the bath temperature approached the desired reaction temperature for plating, Lead (II) nitrate Pb(NO3)2 solution was added at a concentration of 0.026 g/L as stabilizer to maintain the stability of the plating bath and prevent decomposition. Sodium borohydride (NaBH4) was dissolved in a different beaker with a concentration of 0.925 g/L and added to the plating bath as a reductant to realize the reduction of nickel in aqueous solution during the plating process. After the bath components were added, when the process temperature was reached (90±1°C), pH control was performed (pH >13) and the samples were dipped in the bath and coated for one (1) hour [17].

In this study, heat treatment was applied to the NiB coated surfaces at different temperatures and times in the final stage of the preparation of the test specimens. For this purpose, heat treatment was carried out in Protherm brand split furnace in argon atmosphere at temperatures of 250, 300, 350, 400°C and in Protherm brand chamber furnace in open atmosphere at 400°C for 1 hour. Since oxidation is expected to increase due to the increase in tempered temperature, the open atmosphere experiment was carried out at 400°C, which is the highest temperature within the operating limit conditions [17].

2.2. Characterization of Coatings

In order to determine the effects of heat treatment parameters on the tribological and microstructural properties of electroless Ni-B coated 32CrMoV12-10 (1.7765) barrel material, firstly, the cross-section and surface morphology of the coated samples were examined with "HITACHI SU 5000" SEM, (scanning electron microscope). XRD analyses were then performed to investigate the phase structure in the coated samples. The analyses were performed on a Malvern Panalytical Empyrean device using Cu Kα X-ray radiation with a wavelength of 1.54 Å in the range of 2θ=10°-90° and a scanning speed of 2°/min. Hardness measurements of the coatings were performed with Anton Paar Nanoindentation (NHT3) hardness tester by applying a maximum load of 30 mN for 10 s. At least five measurements from various locations were weighted and averaged to get the hardness values. In the second part of the mechanical tests, wear tests were carried out. For this purpose, abrasion tests were performed on UTS Tribometers brand abrasion tester with 6 mm diameter alumina ball, 2 N normal load, 20 (mm/s) sliding speed, 1 (Hz) frequency, 10 mm abrasion track spacing, 150 meters abrasion distance and 2500 seconds duration. In addition, the width measurements of the wear pits occured on the sample surfaces after the wear tests were performed on the Olympus GX51 brand metal microscope. Wear volumes were calculated according to the measured wear widths. The calculations were performed with the help of SolidWorks 3D design program. In the last stage of the experiments, roughness values, which are an indicator of the surface quality of the NiB coatings obtained, were measured. Surface roughness measurements were made on MahrSurfPS1 surface roughness device by taking measurements from 16 different regions on the coated surfaces and calculating the average surface roughness values [17].

3. RESULTS AND DISCUSSIONS

3.1. Microstructural Analysis

FESEM images of the surfaces of 32CrMoV12-10 specimens with electroless Ni-B coatings heating process at 250°C, 300°C, 350°C, 400°C in argon atmosphere and 400°C in open atmosphere are given in Figure 1.
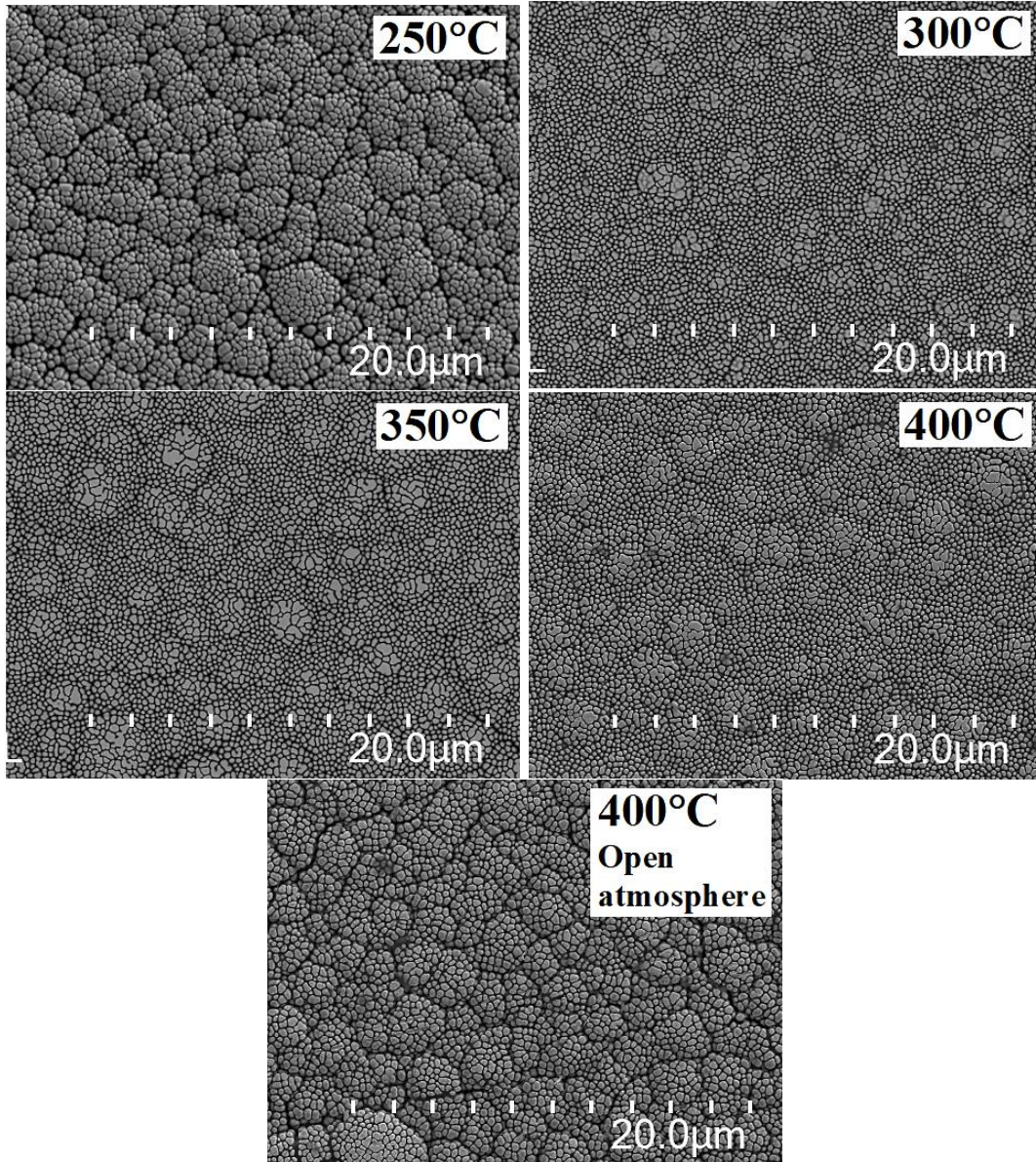

Figure 1. Surface micrographs of Ni-B coated samples heat treated at 250°C, 300°C, 350°C, 400°C in argon atmosphere and 400°C in open atmosphere [17, 18].

Looking at the BSE images in Figure 1, it is seen that changes in heat treatment temperatures lead to differences in the surface morphology of Ni-B coatings. In electroless Ni-B coatings, a columnar structure is expected due to the growth mechanism and nodular growth starts as a secondary layer. The cauliflower-like structure in the coatings is also due to the growth mechanism (Figure 1) [19]. When the surface morphologies of the obtained coatings were examined; a regular cauliflower-like microstructure occurred in all of the Ni-B coating samples heating process at different temperatures. This is a desired morphological feature. Doğan et. al. reported that the formation of a similar surface structure [20].

In the sample heating process at 250°C in argon atmosphere, the nodules are more open and the rough structure on the surface is noticeable. At this temperature, the opening between the nodules is clearly visible.

With the increase in heat treatment temperature, the increased regularity in nodule formation created a tighter structure, resulting in a smoother and more distinct appearance. In parallel with the literature, it is expected that the surface roughness will gradually decrease with increasing heat treatment temperature. However, the surface roughness is in a similar value range at close heat treatment temperatures [7]. When the images were carefully examined, it was observed that a tighter nodule structure and a smoother surface were obtained in the heat treatment performed above 250°C in an argon atmosphere. It is evaluated that the surface morphology becomes blacker with increasing heat treatment temperature. However, it is observed that the nodules expanded, i.e. the tight structure of the nodules started to separate from each other under open atmosphere 400°C heat treatment conditions (Figure 1). In experiments under open atmosphere conditions, oxygen in the environment enters between the nodules and forms oxide layers there. The oxide formed on the surface causes the volume of the nodules to expand, which causes the nodules to appear more discrete. As a result, the stable structure is disrupted. FESEM images taken to examine the thickness and coating morphology of the realized coatings are given in Figure 2.
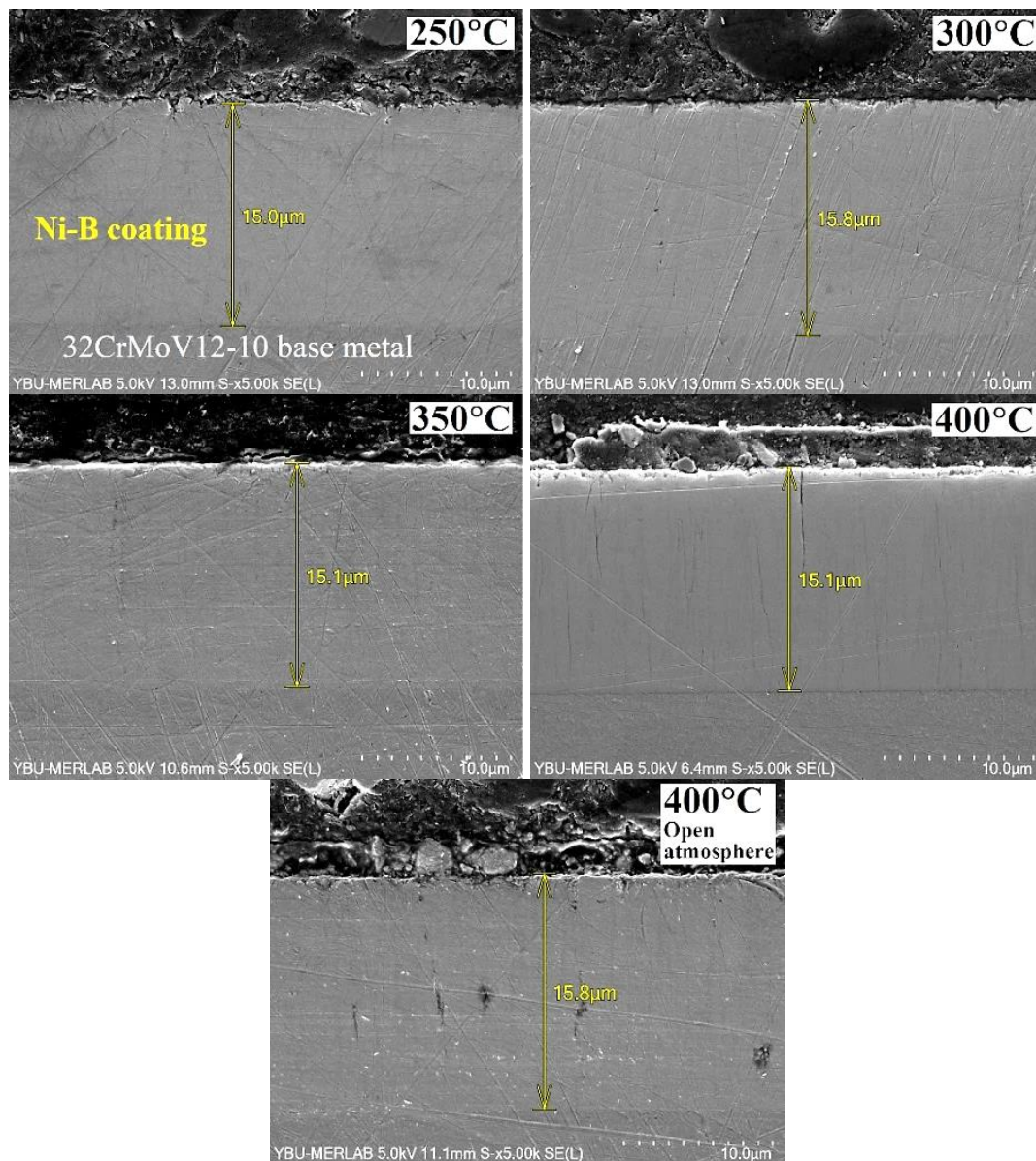

Figure 2. Cross- Sectional images of Ni-B coated samples heat treated at 250°C, 300°C, 350°C, 400°C in argon atmosphere and 400°C in open atmosphere [17].

Looking at the cross-sectional images in Figure 2, it is seen that a uniform coating is obtained in all of the samples at the coating thicknesses. The difference between the lowest and highest thickness measured is 0.8 μm. With this situation, it was observed that the coating thicknesses were maintained in heat treatments performed at different ambient and heat treatment temperatures. A coating thickness of 15 to 15.8 μm was

obtained on all samples. Taha-Tijerina et al. reported that 12 um coating thickness was obtained in 60 minutes [7]. Therefore, the 15 um coating thicknesses obtained were considered to be successful and compatible with the literature. It is understood that different temperatures applied in heat treatments do not cause any significant difference on the coating thickness of the samples.

3.2. XRD Phase Analysis

The graph created according to the values obtained from the XRD analysis of the electroless Ni-B coated 32CrMoV12-10 test specimens heating process at 250°C, 300°C, 350°C, 400°C in argon atmosphere and 400°C in open atmosphere is given in Figure 3.
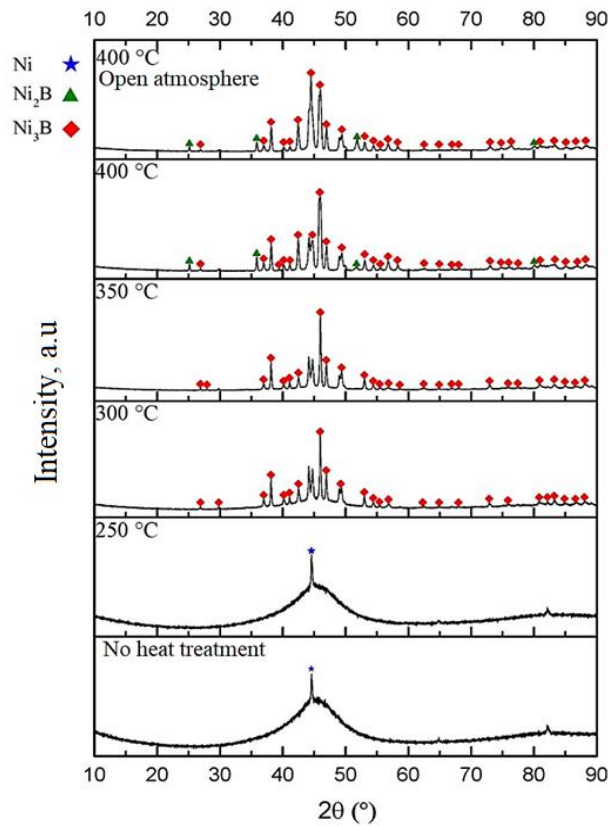

Figure 3. XRD diagram of Ni-B coated samples heat treated at 250°C, 300°C, 350°C, 400°C in argon atmosphere and 400°C in open atmosphere [17].

When Figure 3 is examined; it is understood that in Ni-B coatings, the structure of the sample without heat treatment and the sample heating process at 250°C in argon atmosphere is amorphous and there is no crystalline order. At 300°C and above, the samples subjected to heat treatment show crystal structure formation. Ni3B phases developed throughout the sample heating procedure at 300°C and 350°C. Unlike the others, Ni2B peaks were observed at 25.1 2θ (°), 35.8 2θ (°), 51.8 2θ (°) and 80.0 2θ (°) in addition to Ni3B phases in samples heating process at 400°C in argon atmosphere and 400 °C in open atmosphere. In 2007, Anik et al. [21] reported in their XRD analysis of Ni-B coated 304 stainless steel materials that Ni2B phases did not form below 400°C and Ni2B and Ni3B phases formed above 400°C, and similar results were obtained in our current study. According to XRD phase analysis, it was observed that the structure of the coatings was generally affected by different heat treatment conditions.

3.3. Hardness Investigations

In hardness measurements, a weighted average of the values obtained after taking measurements from at least 5 different points for each sample was taken. Figure 4 shows an optical microscope image taken from a sample for which hardness measurements were made, and Figure 5 shows a graph based on the average values obtained from the hardness measurements.
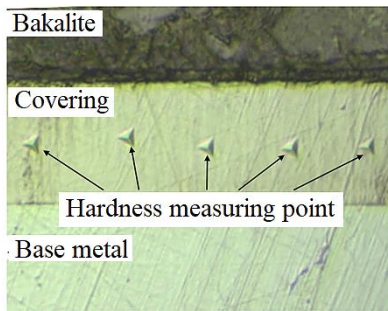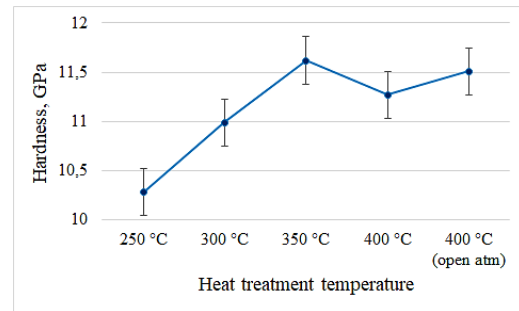
Figure 4. Hardness measurement points [17].

Figure 5. Hardness values of Ni-B coated samples heat treated at 250°C, 300°C, 350°C, 400°C in argon atmosphere and 400°C in open atmosphere.

Examining Figure 5, it can be demonstrated that the sample heating method at 250°C in an argon environment yields the lowest hardness value. Because of the amorphous nature of this sample, the XRD examination shows that the lowest value in the hardness test findings was reached at 250°C in an argon environment. The creation of the Ni3B phase in the structure as a result of heat treatment at 300°C in an argon environment was found to improve the hardness value in comparison to other hardness values. According to Çelik et al., heat treatment causes the coating's amorphous structure to crystallize, and the resulting Ni2B and Ni3B phases raise the hardness values [22]. The sample heated to 350°C in an argon environment produced the greatest hardness value. Subsequently, a significant decrease was observed in the hardness values measured as a result of heat treatment at argon atmosphere 400°C and open atmosphere 400°C compared to the heat treatment conditions at argon atmosphere 350°C. This hardness reduction was more pronounced in the 400°C open atmosphere than in the heating process specimen. Pal et al. reported that in the hardness test on Ni-B coated samples on mild steel, the lowest hardness value was obtained in the amorphous sample, while the highest hardness value was obtained at 350°C. After 350°C, a downward graph was observed in the hardness value [23]. With this result, it was observed that similar results were found with the literature. In addition, the high hardness value at 400□C in the open atmosphere can be attributed to the presence of Fe_2O_3 (iron oxide) formed on the coating. Because Fe2O3 (iron oxide) formed on the coating surface in the open atmosphere has a hardness of approximately 70 HRC. However, the hardness value of the 35CrMoV12-10 alloy used in this study is an average of 300 HB. This value corresponds to 32 HRC. Therefore, it can be stated that one of the reasons for the difference between the hardness values is oxidation.

3.4. Wear Behavior

3.4.1. Determination of friction coefficient

Ball-on-disk wear tests of Ni-B coated specimens were performed using alumina balls. As a result, the time-dependent variation of the coefficient of friction was determined and the results are shown in Figure 6.
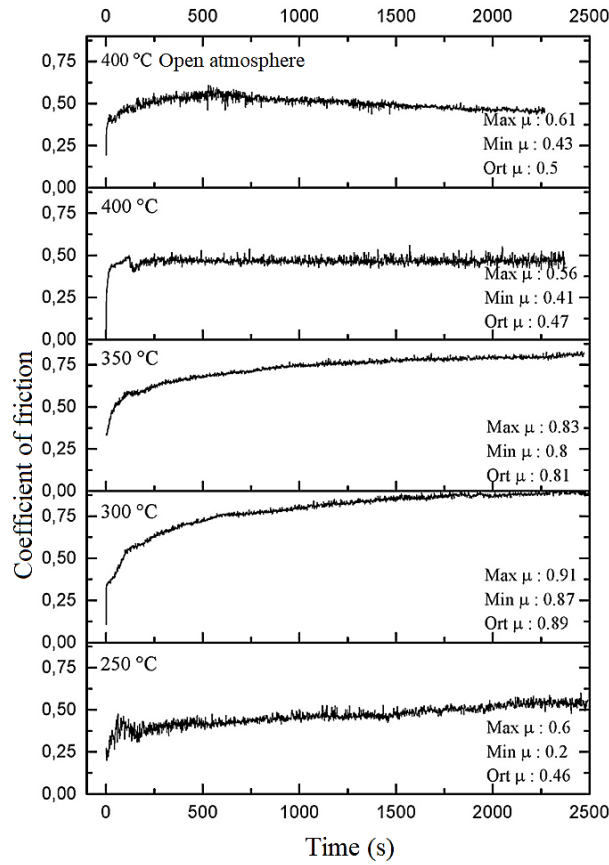
Figure 6. Change of friction coefficients of Ni-B coated samples heat treated at 250°C, 300°C, 350°C, 400°C in argon atmosphere and 400°C in open atmosphere [17].

3.4.2. Analysis of wear surfaces and calculation of wear volume

Optical microscope images of the widths of the scars formed after wear are given in Figure 7. When the graph in Figure 6 is examined, it is seen that the lowest coefficient of friction value is 0.43 in the sample heating process in 400°C in argon atmosphere and the highest coefficient of friction value is 0.89 in the sample heating process in 300°C in argon atmosphere. Arias et al. reported that similar coefficient of friction values were obtained in NiB coated and heating process steel material at 400°C [24]. Looking at the widths of the wear track in Figure 7, it is understood that the lowest width is formed in the sample heating process at 350°C in argon atmosphere and the maximum width of the wear track is formed in the sample heating process at 400°C in open atmosphere. In this case, it is seen that the heat treatment temperature has an effect on the coating structure and changes the friction coefficient values and wear volume amounts in the wear tests. Zhao et al. emphasized that the best mechanical performance was obtained from the heating process sample at 350°C [25].
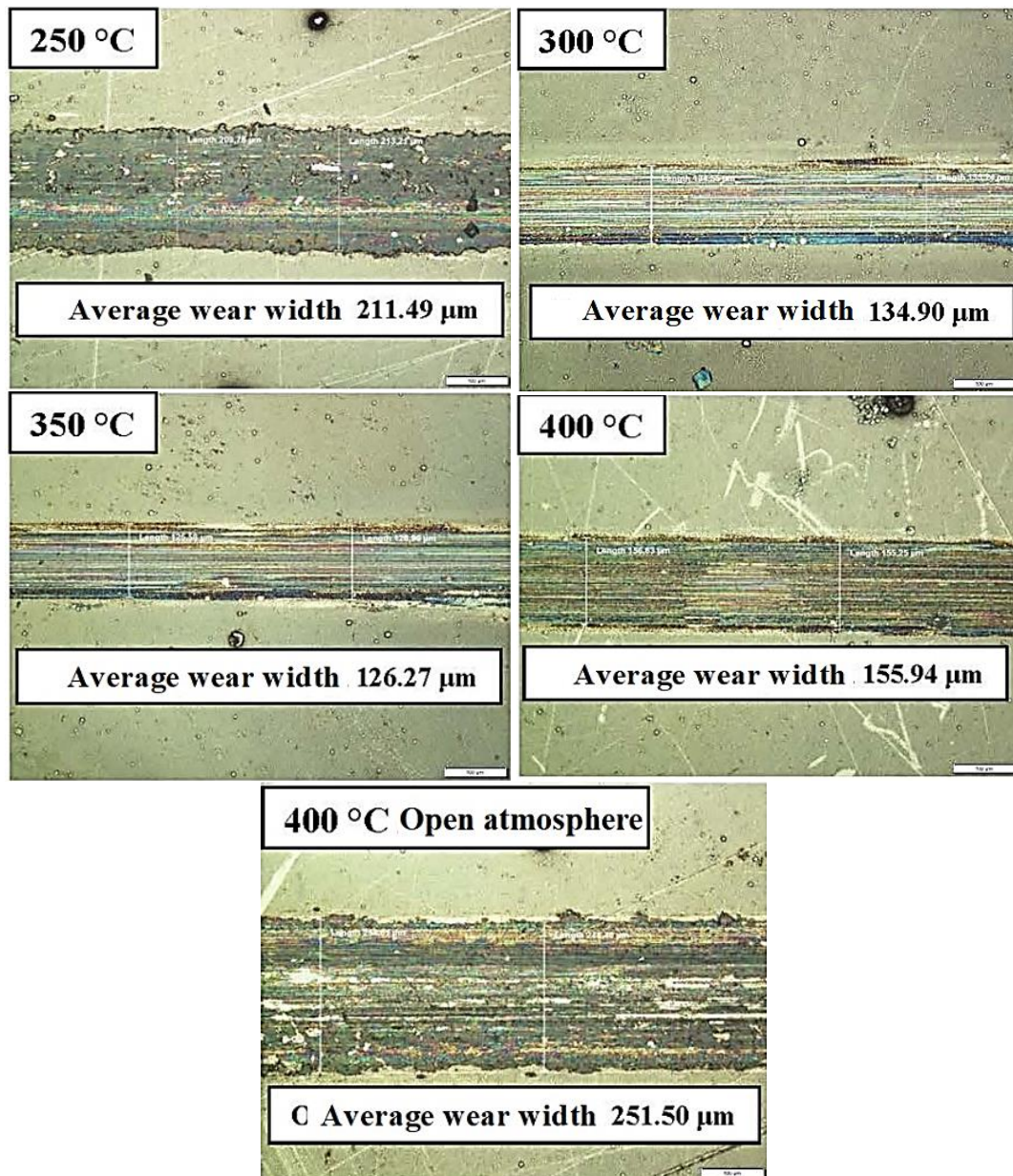
Figure 7. Wear widths of Ni-B coated samples heat treated at 250°C, 300°C, 350°C, 400°C in argon atmosphere and 400°C in open atmosphere [17].

According to the measured wear widths, wear volumes were calculated using SolidWorks 3D design program. The values of the calculated wear volumes are shown in Table 2 and the graphs created according to these values are shown in Figure 8.

Table 2. Wear volume results of coatings [17].

Samples Wear	Volumes [mm^3]
250°C Argon Atmosphere	26.3×10^{-4}
300°C Argon Atmosphere	6.9×10^{-4}
350°C Argon Atmosphere	5.6×10^{-4}
400°C Argon Atmosphere	10.6×10^{-4}
400°C Open Atmosphere	44.3×10^{-4}

When the time-dependent change graphs of the friction coefficients given in Figure 6 and the images of the wear surface widths shown in Figure 7 are evaluated in more detail;

Although the coefficient of friction is low; when the wear widths are examined under the heat treatment condition at 250°C in argon atmosphere, it is seen that the coating is lifted from the surface and the coating is broken (Figure 7). It was evaluated that diffusion at the interface was not sufficient due to the amorphous

structure and therefore adhesion was not good. As a result, it is seen that the wear volume is high with a high wear width.

When the wear widths are examined under the heat treatment conditions at 300°C and 350°C in argon atmosphere, it is seen that the adhesion improves without fractures with the increase in heat treatment temperature. It is clearly seen that the wear resistance has improved according to the test performed under the heat treatment condition at 250°C in argon atmosphere. This is due to the hard Ni3B phase formed on the surface. It was observed that the wear volume decreased between 36% and 40% with the formation of the Ni3B phase. When we look at the friction coefficient results, it is clearly seen that the friction curve is not smooth and shows significant fluctuations in the heat treatment condition at 300°C and 350°C in argon atmosphere. During the abrasion test, hard coating particles are accumulated due to the load. As a result of the compression of these particles between the surface of the abraded ball and the surface of the sample part, an increase in friction occurs. The reason for this fluctuation can be attributed to this phenomenon.

When the wear widths of the sample heating process at 400°C in argon atmosphere were examined, an increase of nearly 30 μm was observed in the wear width compared to the sample heating process at 350°C in argon atmosphere. However, there was an 89% increase in the wear volume values. The reason for this is interpreted as the material wears more due to the decrease in the hardness value of the material as a result of the formation of Ni2B particles in the argon atmosphere at 400°C temperature heat treatment condition. Looking at the friction coefficient result, it showed a very rapid increase at the beginning of the wear test and then remained stable throughout the test.

Considering the results of open atmosphere heat treatment at 400°C; Compared to the sample heating process at 400°C in argon atmosphere, there was a significant increase in wear width and wear volume and fractures occurred in the wear scar. It is thought that when heat treatment is carried out in an open atmosphere, the steel interface is oxidized as a result of oxygen coming to the surface, and the diffusion of nickel into the steel is prevented. Therefore, diffusion may be prevented, reducing adhesion. To understand the reason for this situation, the interface needs to be examined in more detail. A similar comment can be made for the friction coefficient results. An uneven friction curve and significant fluctuation are clearly visible.

Looking at the results of the open atmosphere 400°C heat treatment condition; compared to the sample heating process at 400°C in argon atmosphere, there was a significant increase in wear width and wear volume and fractures occurred in the wear track. When heat treatment is performed in an open atmosphere, it is thought that the steel interface is oxidized as a result of the oxygen coming to the surface, which prevents the diffusion of nickel into the steel. Therefore, diffusion may be prevented in between, reducing adhesion. For the cause of this situation, the interface needs to be examined in more detail. A similar interpretation can be made for the friction coefficient results. A non-uniform friction curve and significant fluctuation is clearly visible. Mukhopadhyay et al. evaluated the tribological behavior of heat-treated coatings at room temperature, 100°C, 300°C and 500°C. It was observed that wear resistance and COF were better in 300°C than in 100°C and 500°C. This was attributed to the synergistic effects of various phenomena occurring in 300°C, such as the formation of the tribo-oxidative layer, the mechanically mixed layer composed of compacted debris patches, phase transformation occurring during the wear process, wear mechanism and microstructure [25].

3.4.3. Surface roughness investigations

The graph created according to the values obtained from surface roughness measurements made at 16 different points on Ni-B coated surfaces is shown in Figure 9. When the graph in Figure 9 is examined, the differences in the roughness measurements made from the surface of the same sample are striking. According to these values, it can be said that the surface is not of the same thickness throughout the coating. Looking at the differences between the measurement values, it is understood that there are indentations or protrusions on the Ni-B coating surface.

In order to examine the surface morphology in more detail, a cross-sectional BSE microstructure image is shown in Figure 10. When looking at Figure 10, the rough structure on the coating surface can be seen very clearly. The average roughness values (Ra) determined by calculating the arithmetic mean of 16 surface roughness measurements made for each sample are given in the graph in Figure 11.
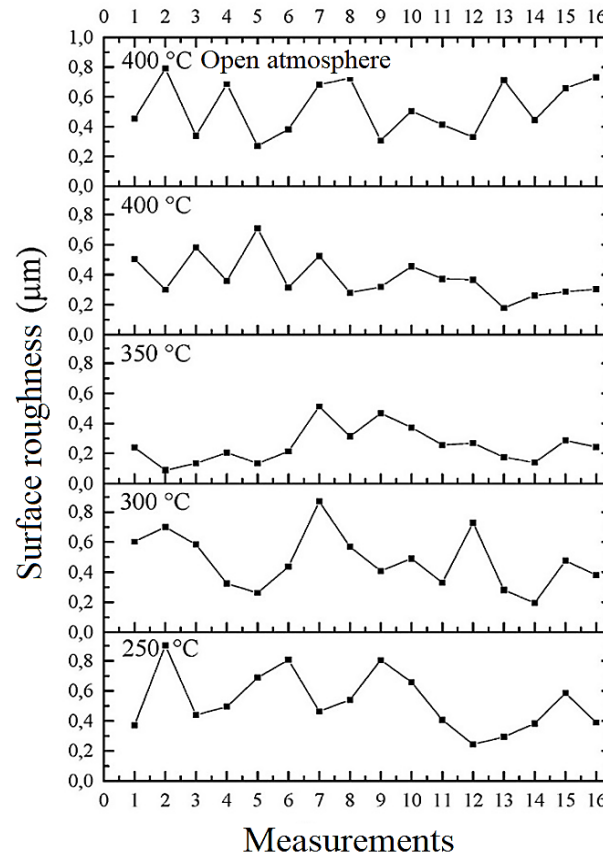
Figure 9. Roughness measurement values from 16 different regions of Ni-B coated samples heat treated at 250°C, 300°C, 350°C, 400°C in argon atmosphere and 400°C in open atmosphere [17].
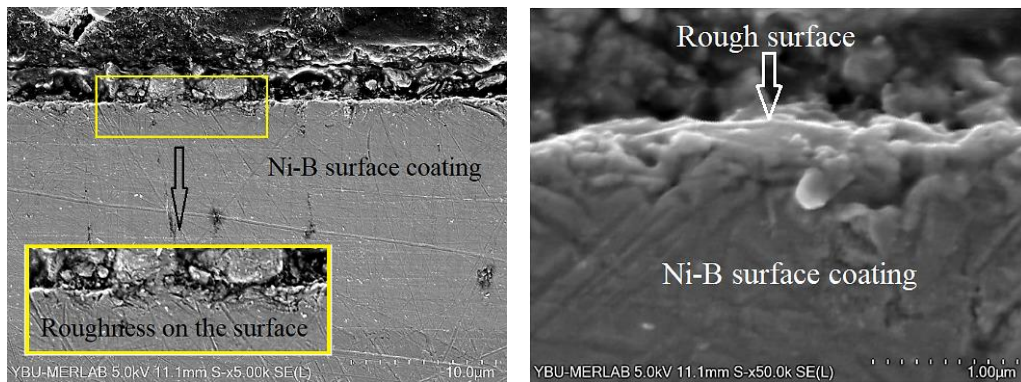

Figure 10. Ni-B coating cross sections at different magnifications [17, 18].
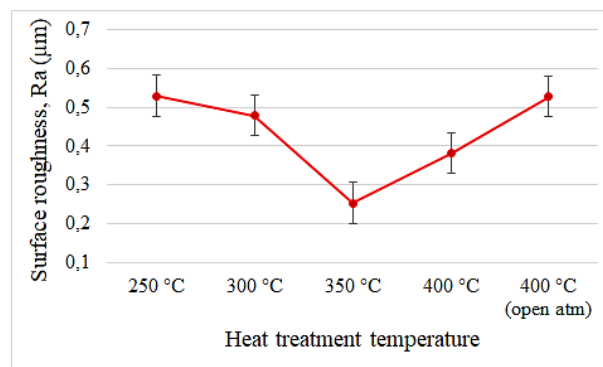

Figure 11. Average (Ra) roughness measurement values of Ni-B coated samples heat treated at 250°C, 300°C, 350°C, 400°C in argon atmosphere and 400°C in open atmosphere [17, 18].

When Figure 11 is examined, it is clearly seen that the heat treatment after coating has an effect on surface roughness. When the heat treatment was increased to the temperature conditions of 300°C in argon atmosphere, an improvement in surface roughness was observed. As in all the data obtained from previous examinations and supporting each other, the lowest roughness value of 0.253 microns was obtained from the sample heating process at 350°C in argon atmosphere. The highest roughness values occurred in the irregular and amorphous 250°C and 400°C samples treated in an open atmosphere. In order to support these evaluations with XRD analysis, the graph in Figure 12 is given.
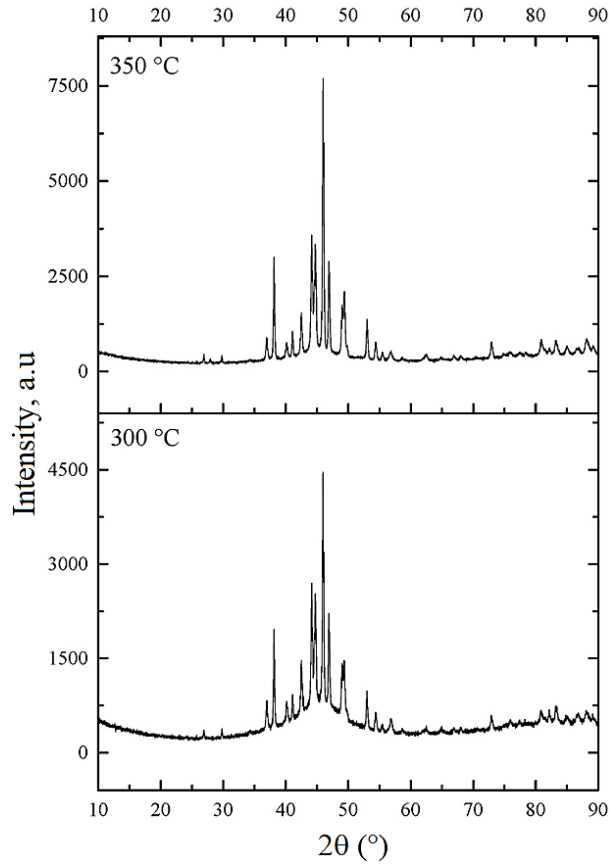

Figure 12. XRD analyzes of argon atmosphere 300°C and 350°C [17].

When the XRD patterns in Figure 12 are examined, it is seen that the peak intensities of the sample treated at 350°C in argon atmosphere are higher than the sample treated at 300°C in argon atmosphere. This indicates that the crystallinity in the Ni3B phase increases with increasing temperature. The increase in crystallinity caused a decrease in surface roughness. When the temperature is further increased, Ni2B phase also starts to form in the structure. It is thought that the Ni2B phase in the structure increases the surface roughness of the samples treated in argon atmosphere 400°C and open atmosphere 400 °C.

4. CONCLUSIONS

The results obtained from this experimental study, in which NiB was coated on 32CrMoV12-10 alloy, which is also used as barrel material, by electroless method and heat treatment was performed at different environments and temperatures, are summarized below:

- Cauliflower-like surface structure was formed on all coated samples. The cauliflower-shaped nodules formed on the surface of the samples heat-treated at 300°C, 350°C and 400°C in argon atmosphere were seen to be tighter. Samples heat-treated at 250°C argon atmosphere and 400°C open atmosphere showed a rough surface structure with more discrete and larger nodules.
- XRD analysis showed that the structure was amorphous due to the inadequacy of the heat treatment at 250°C argon atmosphere. Ni3B phases were formed in the samples heating process at 300°C and 350°C in argon atmosphere. In addition to Ni3B phases, Ni2B phases were also observed in the samples heating process at 400°C in argon atmosphere and 400°C in open atmosphere.

- As a result of hardness measurements, the highest hardness value occurred in the sample heating process at 350°C in argon atmosphere and the lowest hardness value occurred in the sample treated at 250°C with amorphous structure.

- In the abrasion tests, it was observed that the coating lifted from the surface and the coating was broken due to insufficient diffusion in the argon atmosphere under 250°C temperature conditions. Accordingly, the wear width and volume also increased. It was clearly seen that the wear resistance of the samples heating process at 300°C, 350°C and 400°C in argon atmosphere increased. It was concluded that this was due to the hard Ni3B particles formed on their surfaces. The wear resistance increased between 36% and 40% with the formation of the Ni3B phase. There was an increase in the wear width of the sample treated at 400°C in an argon atmosphere compared to the sample treated at 350°C. There was also a significant increase in the wear width and wear volume of the sample heat-treated at 400°C in an open atmosphere compared to the sample heat-treated at 400°C in an argon atmosphere. This was attributed to the oxidation of the steel interface due to the presence of oxygen on the surface, which prevented the diffusion of nickel into the steel. In surface roughness measurements, the surface roughness of the amorphous sample heating process at 250°C in argon atmosphere was higher than all other samples. The best surface roughness value was observed at 350°C in argon atmosphere.

- When all the data supporting each other are brought together, the best results of the findings obtained as a result of the analysis and test were obtained in the heat treatment experiment performed at 350°C in argon atmosphere. Instead of high temperature heat treatment after nickel-boron (Ni-B) plating on an industrial scale, the most suitable heat treatment temperature was determined to be 350°C in an argon atmosphere. It is thought that performing the process under these conditions will save energy costs.

REFERENCES

[1] M. Karslı, Polymer Composite material selection for light weapons, Master's Thesis, Karadeniz Technical University, Institute of Science and Technology, Turkey, 2016.

[2] S. Yavuz, Anodic oxidation of gun body material AA7075-T6 alloy, Master's Thesis, Karadeniz Technical University, Institute of Science and Technology, Turkey. 2018.

[3] E. Göksu, Weapons in Turkish culture, second ed., Otüken Publishing, Tokat, 2015.

[4] A.T. Rutci, Development of barrel material used in light weapons and examination of processing parameters, Master's Thesis, Sakarya University, Institute of Science and Technology, Turkey, 2019.

[5] J.R. Davis, Surface hardening of steel, first ed., Materials Park, ASM International ,2002.

[6] J.R. Davis, Surface engineering for corrosion and wear resistance, first ed., ASM International, 2001.

[7] J. Taha-Tijerina, K. Aviña-Camarena, R. Torres-Sánchez, C. Dominguez-Ríos, D. Maldonado-Cortes, Tribological evaluation of electroless Ni–B coating on metal-working tool steel, The International Journal of Advanced Manufacturing Technology, Int J Adv Manuf Technol, 103 (2019) 1959–1964.

[8] G. Ciesᶥlak, M. Gostomska, A. Dabrowski, T. Ciciszwili-Wyspianska, K. Skroban, A. Mazurek, E. Wojda, M. Głowacki, T. Rygier, A. Gajewska-Midziałek, Properties of Ni-B/B Composite Coatings Produced by the Electroless Method under Semi-Technical Line Conditions, Processes, 12 (2024) 1280. https://doi.org/10.3390/pr12061280

[9] S. Arias, M. Gómez, E. Correa, F. Echeverría-Echeverría, J. Guillermo Castaño, Effect of heat treatment on the tribological properties of Nickel-Boron electroless coating, Revista Facultad de Ingeniería, 27:47 (2018) 103-110. http://doi.org/10.19053/01211129

[10] İ. Çelik, M. Karakan, F. Bülbül, Investigation of structural and tribological properties of electroless Ni–B coated pure titanium, Proc IMechE Part J: J Engineering Tribology, 230:1 (2016) 57–63. http://doi.org/10.1177/1350650115588568

[11] F. Bülbül, H. Altun, V. Ezirmik, Ö. Küçük, Investigation of structural, tribological and corrosion properties of electroless Ni–B coating deposited on 316L stainless steel, Proc IMechE Part J: J Engineering Tribology, 227:6 (2012) 629-639. http://doi.org/10.1177/1350650112464928

[12] H. Çep, H. Kovacı, H. Çimenoğlu, A. Çelik, Effects of Chrome Plating, Boriding, Nitrocarburizing, Nitriding and Post-oxidation Treatments on The Tribological Properties of DIN 32CrMoV12-10 Steel, Erzincan University Journal of Science and Technology, 14(3) (2021) 936-949. https://doi.org/10.18185/erzifbed.959667

[13] https://www.aubertduval.com (Download Date, 25 September.2023)

[14] H. Çep, Improvement of barrel life and ballistic performance made of DIN 32CrMoV12-10 steel with different surface treatments. PhD Thesis, Istanbul Technical University, Graduate Education Institute, Turkey, 2022.

[15] Y. Jia, J. Lai, J. Yu, H. Qi, Y. Zhang, H. He, Tribological behaviors of electroless nickel-boron coating on titanium alloy surface, Chinese Journal of Mechanical Engineering, 37 (2024) 13. https://doi.org/10.1186/s10033-024-00990-1

[16] https://portal.totalmateria.com/tr Reference: WL 1.7765: 2008 / Steel tube for machine guns - 32CrMoV12-10-Quenched and tempered steel (Download Date: 25.08.2023)

[17] E.K. Özyurt, A study of the nickel-boron coating of the barrel material 32CrMoV12-10 alloy and after coating heat treatment parameters effects on tribological strenght of the alloy, Master's Thesis, Kırıkkale University, Institute of Science and Technology, Turkey, 2024.

[18] E.K. Özyurt, M. Pul, Effect of heat treatment parameters on surface roughness in electroless nickel-boron coating of barrel material 32CrMoV12-10 alloy, 4th International Conference on Engineering and Applied Natural Sciences, Konya, 2023: pp. 452-456.

[19] F. Doğan, E. Duru, M. Uysal, et al., Investigation of mechanical and tribological characteristics of Ni-B coatings deposited on steel, Boron 6:1 (2021) 209 – 215.   https://doi.org/10.30728/boron.762584

[20] V. Vitry, L. Bonin, Increase of boron content in electroless nickel-boron coating by modification of plating conditions, Surface & Coatings Technology, 311 (2017) 164-171. http://dx.doi.org/10.1016/j.surfcoat.2017.01.009

[21] M. Anik, E. Körpe, E. Şen, Effect of coating bath composition on the properties of electroless nickel-boron films, Surface and Coatings Technology, 202 (2008) 1718-1727. https://doi.org/10.1016/j.surfcoat.2007.07.031

[22] S. Pal, N. Verma, V. Jarayam, S. K. Biswas, Y. Riddle, Characterization of phase transformation behavior and microstructural development of electroless Ni–B coating, Materials Science and Engineering A, 528:28 (2011) 8269-8276. doi:10.1016/j.msea.2011.07.060

[23] S. Arias, J. G. Castaño, E. Correa, F. Echeverría, M. Gómez, Effect of heat treatment on tribological properties of ni-b coatings on low carbon steel: wear maps and wear mechanisms, Journal of Tribology, 141:9 (2019) 091601. https://doi.org/10.1115/1.4043906

[24] F. Zhao, H. Hu, J. Yu, J. Lai, H. He, Y. Zhang, H. Qi, D. Wang, Mechanical and tribological properties of Ni-B and Ni-B-W coatings prepared by electroless plating, Lubricants, 11:42 (2023) 1-13. https://doi.org/10.3390/lubricants1102004

[25] A. Mukhopadhyay, T. K. Barman, P. Sahoo, Effects of heat treatment on tribological behavior of electroless Ni–B coating at elevated temperatures, Surface Review and Letters, 25:2 (2018) 1850014. https://doi.org/10.1142/S0218625X18500142

Manufacturing Technologies and Applications
MATECA

Influence Degree and Scheme of Hot Reduction on Properties of the Carbon Steel

Igor Alex Vakulenko[1,*] , Serhii Plitchenko[2] , Ahmet Fatih Yılmaz[3]

[1,]Department of Condensed State Physics, Dniprovsky State Technical University, Kamianske, Ukraine*
[2]Department of Applied Mechanics and Materials Science, Ukrainian State University of Science and Technology, Dnipro, Ukraine
[3]Department of Mechanical Engineering, Engineering Faculty, Karabük University, Karabük, Türkiye

---

ABSTRACT

This study examines the impact of hot plastic deformation at 1250°C on austenite grain refinement and mechanical properties in carbon steel for railway wheels. The deformation strategies—single-step versus two-step compression with equivalent total strain—were compared to assess their effects on austenitic microstructure and material performance. Austenite grain size was quantified via light microscopy and quantitative structural analysis, while mechanical properties were evaluated using a universal tensile testing machine, following the ASTM E8 standard, at room temperature. (strain rate: 10^{-3} s^{-1}) Results reveal that austenite grain refinement occurs proportionally with increasing deformation, irrespective of the compression scheme. However, the deformation strategy significantly influences strength and ductility at lower strain levels. Specifically, two-stage compression at smaller strains (e.g., below 60% total deformation) enhances ultimate tensile strength by up to 10% and ductility by 30–40% compared to single-step compression. This improvement is attributed to partial retention of austenite substructure during interrupted deformation, which alters dynamic recrystallization kinetics and promotes dislocation redistribution. The differential effect diminishes progressively with higher strain levels, and beyond 60% deformation, both schemes yield equivalent grain sizes and mechanical properties due to complete recrystallization and microstructural homogenization. These findings underscore the critical role of deformation sequencing in optimizing mechanical performance during thermomechanical processing, particularly for applications requiring tailored strength-ductility balances in high-temperature-formed carbon steels.

Keywords: Austenite, Grain size, Hot plastic deformation, Carbon steel, Strength

Sıcak Haddelemenin Karbon Çeliğinin Özellikleri Üzerine Etki Derecesi ve Mekanizması

ÖZET

Bu çalışma, demiryolu tekerleklerinde kullanılan karbon çeliğinde 1250 °C'de uygulanan sıcak plastik deformasyonun, östenit tane incelmesi ve mekanik özellikler üzerindeki etkisini incelemektedir. Aynı toplam deformasyon oranına sahip tek aşamalı ve iki aşamalı sıkıştırma stratejileri, östenitik mikro yapı ve malzeme performansı üzerindeki etkilerini değerlendirmek amacıyla karşılaştırılmıştır. Östenit tane boyutu, ışık mikroskobu ve kantitatif yapısal analiz yöntemleri kullanılarak nicelendirildi; mekanik özellikler ise oda sıcaklığında (deformasyon hızı: 10^{-3} s^{-1}) gerçekleştirilen çekme testleriyle değerlendirildi. Elde edilen sonuçlar, sıkıştırma şemasından bağımsız olarak deformasyon arttıkça östenit tane incelmesinin orantılı olarak gerçekleştiğini göstermektedir. Bununla birlikte, deformasyon stratejisi daha düşük deformasyon seviyelerinde mukavemet ve süneklik üzerinde belirgin bir etki göstermektedir. Özellikle, toplam deformasyonun %60'ın altında kalan durumlarda uygulanan iki aşamalı sıkıştırma, tek aşamalı sıkıştırmaya kıyasla çekme mukavemetini %10'a kadar, sünekliği ise %30–40 oranında artırmaktadır. Bu iyileşme, kesintili deformasyon sırasında östenit alt yapısının kısmi korunmasına bağlı olup, bu durum dinamik yeniden kristalleşme kinetiğini değiştirerek dislokasyon yeniden dağılımını teşvik etmektedir. Deformasyon seviyesi arttıkça aradaki fark kademeli olarak azalmış ve %60'ın üzerindeki deformasyonlarda tam yeniden kristalleşme ve mikro yapısal homojenleşme neticesinde her iki sıkıştırma yöntemi de eşdeğer tane boyutları ve mekanik özellikler sergilemiştir. Bu bulgular, termomekanik işlem sırasında mekanik performansın optimize edilmesinde deformasyon sıralamasının kritik rolünü, özellikle yüksek sıcaklıkta şekillendirilen karbon çeliklerinde istenen mukavemet-süneklik dengesinin sağlanmasında vurgulamaktadır.

Anahtar Kelimeler: Östenit, Tane boyutu, Sıcak plastik deformasyon, Karbon çeliği, Mukavemet

---

1. INTRODUCTION

At a constant rate of hot reduction carbon steel, the ratio of temperature and degree of plastic deformation determines balance at development of hardening and softening processes. The simultaneous influence of several process parameters during hot reduction of carbon steel significantly complicates development of measures to stabilize structure of austenite. By analogy with the heating of cold-formed metal, structural changes after hot plastic deformation develop in a similar sequence. The effect of austenite softening, based on the reduction accumulated defects of the crystal structure, depends on their redistribution to a certain extent. The movement of grain boundaries with large angles of disorientation during collective recrystallization allows not only to reduce density of dislocations[1], but also to lead to a complete replacement crystal geometric characteristic of the deformed metal [2,3].

Another process softening of the deformed metal is based on a change at substructure from the development of dislocation recombination [4]. In general, the effect of micro- and substructure elements on a set of properties can be divided into components from the state of solid solution, accumulated density of dislocations, structure and shape of boundaries or subboundaries, etc.[5–7]. The relationship between by increased of defects in the crystalline structure, their annihilation, and distribution in austenite allows one to control at structure formation of the hot-rolled products.

The purpose of the study is evaluation by influence hot deformation scheme of the carbon steel on its structure and properties.

2. MATERIAL AND METHOD

The material for the research was carbon steel from fragments of the all-rolled railway wheel, with a carbon concentration of 0.61 % and other chemical elements in accordance with the requirements of regulatory documentation for wheels. Samples for the analysis of structural changes during hot compression had a shape of cylinders with a diameter of 20 mm and a height of 40 mm [8]. Heating the hot deformation temperature (ε) (1240 °C) was carried out in electric furnaces, preventing oxidation and decarburization of the metal surface. The blanks were deformed by 10-60 %, at a deformation rate of about 10^{-2} s^{-1}. After completion of hot deformation, the blanks were cooled in air. The structure of the metal was examined under a light microscope. To identify austenite grain, steel after hot deformation etched in a sodium picrate solution [9], and structure of the pearlite colony, it was etched in 4 % HNO3 in ethanol. Austenite grain size (dA) was determined using quantitative metallography in accordance with the ASTM E112 standard. [10]. Mechanical properties (yield strength (σy) and tensile strength (σs), relative elongation (δ) and reduction in area (ψ)) were determined from analysis of tensile curves at room temperature and a strain rate of 10^{-3} s^{-1}.

3. EXPERIMENT AND OPTIMIZATION RESULTS

In general, the structure austenite at process of hot plastic deformation carbon steel is determined by the heating temperature, speed and magnitude of compression [11]. Considering that a certain sequence operations of compression work piece, for obtaining individual elements of a railway wheel, is ensured by maintaining a practically identical deformation rate, its contribution to the change grain size of austenite can be considered constant in value.

The temperature ranges for the development of recrystallization, for most metallic materials, is determined by the ratio:

$$T_A \sim K \cdot T_B \tag{1}$$

where T_A is a temperature of the process under study, K is a coefficient, T_B is a solidus temperature, on the phase diagram [3].

At $K = 0.4$-0.6, the grains after recrystallization have a predominantly elongated shape, and at $K > 0.6$ they are close to equiaxed. Considering the wheel blank deformation temperature about at 1240-1250 °C and $K > 0.8$, the austenite grains correspond to a convex polygon.

Depending conditions of hot plastic deformation, formation substructure can have a qualitatively different effect on the austenite structure. At case of small reductions, when the dislocation density is relatively small, the rearrangement of dislocations during formation of subboundaries can be carried out without significant annihilation [1,2].

The movement of dislocations from the internal volumes of grains to the periphery, against the background of a gradual increase at angle disorientation of subboundaries, will be partially compensated for the inevitable effect of a decrease at dislocation density. Thus, at temperatures significantly below hot

reduction temperature of the wheel blank, at relatively low degrees of deformation, it is possible to observe development of austenite recrystallization by different mechanisms (Fig. 1, *a, b*).

On other hand, the preservation texture of hot-deformed metal can contribute to growth share of pearlite colonies with a violation of the regular structure (Fig. 1, *c-f*). If we take the average size of the structure section, which is separated by a layer of structurally free ferrite (Fig. 1, *c-f*) as d_A, the obtained value will not take into account preserved a part of subboundaries of hot-deformed austenite.
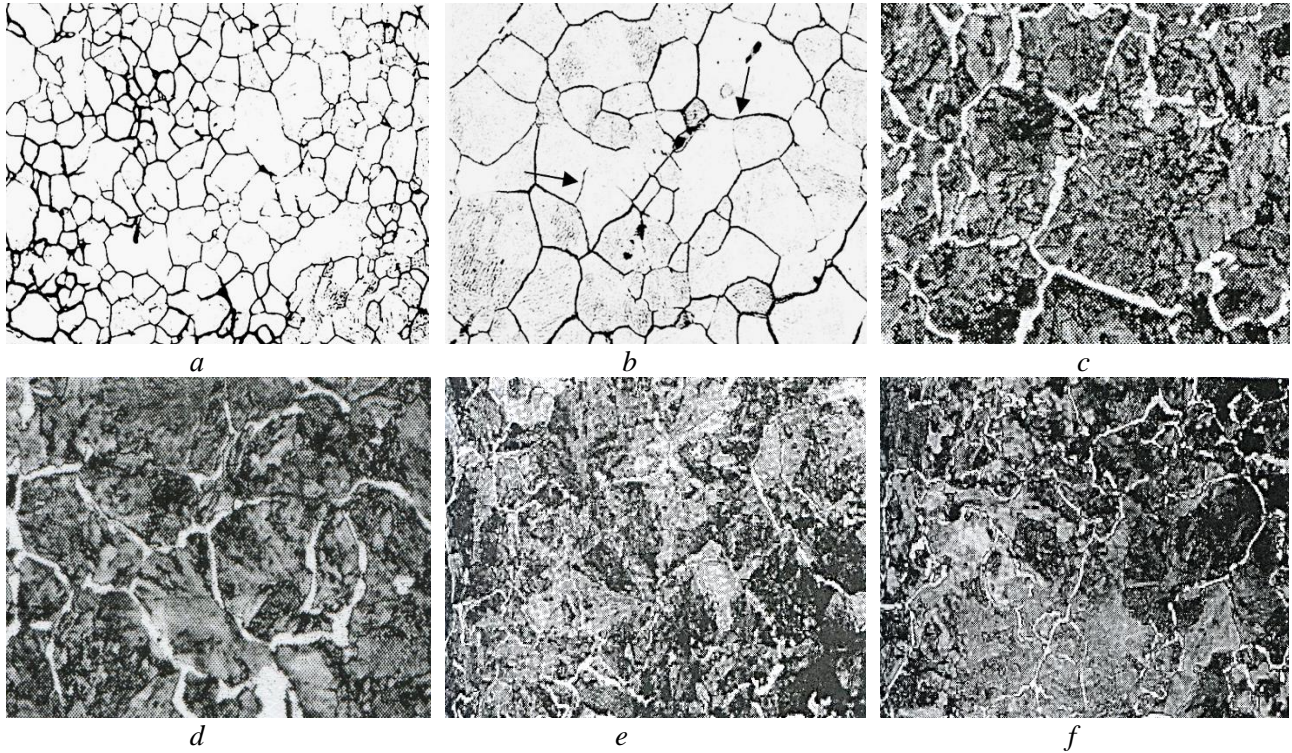

Figure 1. Influence degree of hot reduction (*a, b, c* – 10; *d* – 18; *e* – 40, *f* – 60 %) at temperature of 950 °C (*a*), 1100 °C (*b*), 1240 °C (*c-f*) [7] on the structure of steel with 0.6 % C. Magnification: *a, b, e, f* – 100; *c, d* – 150

As a result, the nature influence austenite grain size on the complex properties of the hot-rolled metal will be distorted. This is confirmed by the ambiguous correlation between sizes of the austenite grain and pearlite colony [8,12–14]. Thus, the possible error in estimating d_A, after various degrees of hot deformation, can be taken as constant, not having a qualitative effect on size of the austenite grain. Compared with normal grain boundaries, the boundaries between fragments, in addition to the intermediate position in disorientation between normal boundaries and subboundaries [15], can differ in shape and structure. Considering with an increase in d_A the probability of the decay uniform distribution of dislocations into periodic structures increases [16], fragmentation in a large grain should begin earlier than in a small one and with a smaller number of accumulated dislocations.

Based on this, for a constant deformation rate, the ratio of temperature and degree of compression can change mechanism of austenite recrystallization. Thus, when forming disk of the wheel, the work piece on a press with a force of 100 MN is subjected to deformation about 10%. Considering proximity to critical deformation (8-10 %, [1,2]), at the development of recrystallization, minor deviations in a uniformity distribution of compression along the height of the work piece [8] can lead to a structure heterogeneity of austenite.

A deformation 10 % at a temperature of 950 °C is accompanied by the formation of grains with a shape close to a polyhedron (Fig. 1, *a*). Similar compression at 1100 °C is accompanied by a completely understandable increase in d_A (Fig. 1, *b*). The absence parts of the boundaries and their specific curvature (Fig. 1, *b*, indicated by an arrow) can be considered as evidence formation of "special boundaries" [15].

On other hand, combination of the above-mentioned features indicates development of secondary recrystallization by the coalescnce mechanism. Compared to disk, formation other elements of the wheel occur after more significant deformations (40-50 %). Taking into account the high rate of development austenite recrystallization processes during hot reduction [3,4], possible influence of the austenite state on a formation of the pearlite colonies may manifest itself on the dependence properties of the steel (Fig. 2). Secondary recrystallization observed during hot deformation is believed to be influenced by special

boundary formation and dislocation cell coalescence. These microstructural evolutions contribute to mechanical property changes and were supported by micrograph observations (Fig. 1b).
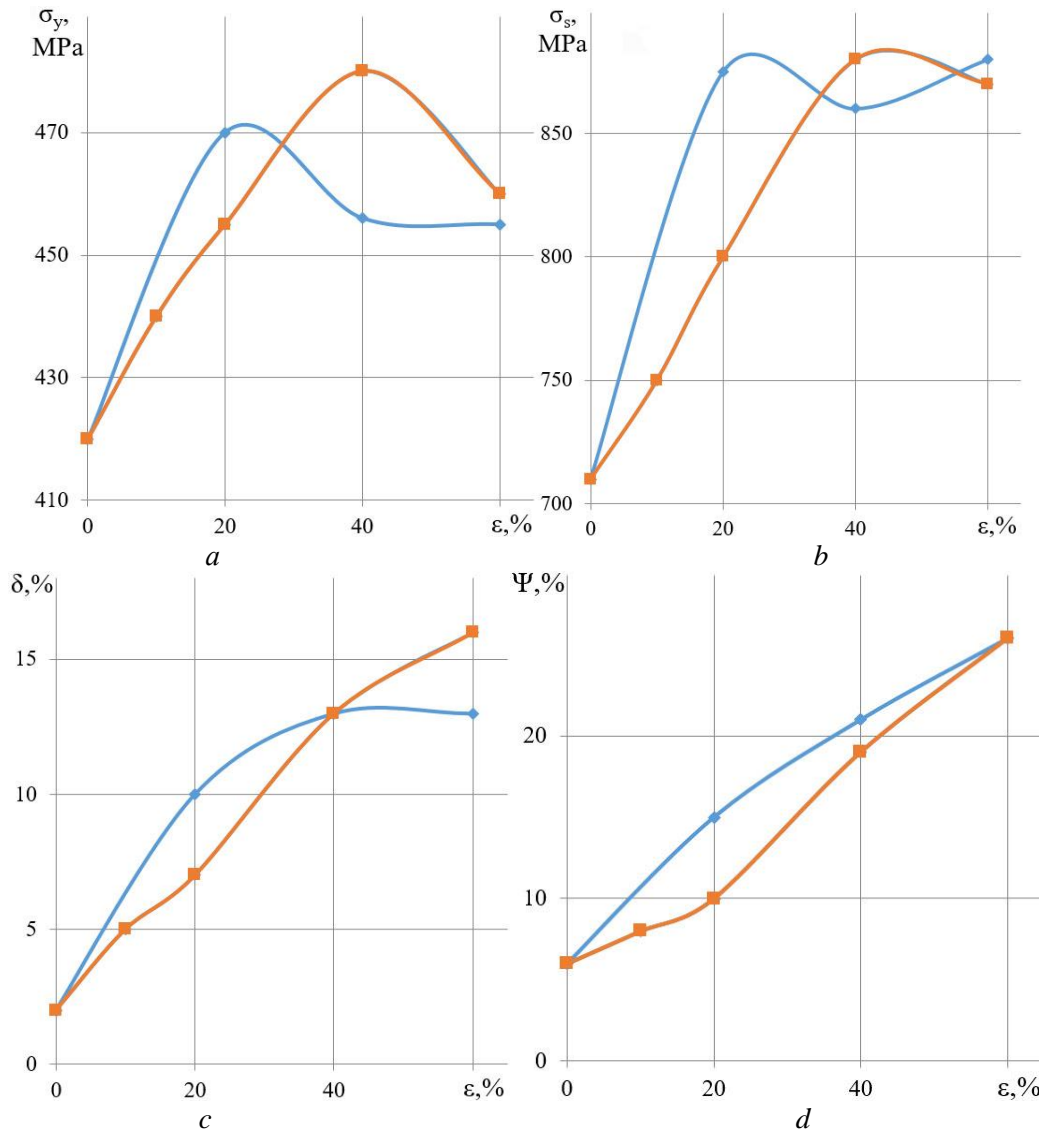

Figure 2. The influence of the degree single (■ – *1*) and double (♦ – *2*) deformation at a temperature of 1240 °C of steel with 0.6 % *C* on σ_y (*a*), σ_s (*b*), δ (*c*) and ψ (*d*)

In addition to a certain dependence on the degree of hot deformation, influence of the deformation scheme is revealed, from the replacement of a single reduction by a double reduction with the same shares (Fig. 2, curves *1* and *2*, respectively). The growth of ε single reduction is accompanied by a monotonic increase in σ_y, σ_s, δ and ψ.

Against the background of qualitative coincidence of the nature change in properties after a single compression, the effect of double deformation has certain features. Replacing a single 20 % deformation with a double one led to an increase in σ_y to 3 %, and σ_s to 10 %. Such an effect can be associated with the influence of a part preserved austenite substructure on the pearlite transformation.

Moreover, if the effect of replacing a single 20 % deformation with a double one (10 + 10 %) can somehow be explained by the proximity to critical deformation during development of recrystallization (10 %) and the formation of a certain number of special boundaries (Fig. 1, *b*), the nature of change in properties after compression of 40 and 60 % requires additional explanation.

Fig. 3 shows the structure of steel after double compression. It is difficult to detect the structural features of pearlite colonies from the structural elements, although there seems to be a greater presence of small fragments after replacing a single deformation (Fig. 1, *e*) with a double one (Fig. 3, a). The nature of the dependence d_A on the magnitude and scheme of deformation is shown in Fig. 4, *a*.

With an increase in the degree of single hot compression, d_A decreases monotonically. Replacing single compression with double compression did not change the nature of dependence but had an insignificant

effect on the absolute values of d_A. If for single compression of 40 and 60 %, d_A are respectively equal to 120 and 107 μm, then after double $\varepsilon = 20 + 20$ %, $d_A = 140$ μm, and after $\varepsilon = 30 + 30$ %, a match with single compression (106 μm) was obtained. It can be expected that in proportion to the decrease total compression, the differences at structural state of austenite after single and double deformation should increase, which in turn must affect d_A.

This tendency is evidenced by the value of d_A (75 μm) after compression according to the scheme $10 + 10 + 10$ % [16] (Fig. 4, *a*, point 3). For a detailed analysis possibility preserving of the part effect substructure after hot deformed of austenite on d_A, used the relationship [17]:

$$F = A\varepsilon^{-b} \tag{2}$$

where F is the grain area, $d_A = k\sqrt{F}$; k is the grain shape coefficient; ε is degree of deformation in %; A and b are constants.

For the shape of austenite grains close to a polyhedron, $k = 1.86$ [9]. After taking the logarithm of (2), we obtain:

$$lgF = lgA - blg\varepsilon \tag{3}$$

at $lg\varepsilon \to 0$, $lgF = lgA$, and $b = -\Delta lgF / \Delta lg\varepsilon$.

As a result of extrapolation of the ratio $lgF \sim f(lg\varepsilon)$ (Fig. 4, *b*) at $lg\varepsilon = 0$, the values of lgA were determined. For the studied steel, with a single deformation, the value of $lgA = 5.3$, and $b = 1.13$.

Similar values were obtained for double compression: $lgA = 5.3$, and $b = 1.36$. Formally, value of A does not depend on the deformation scheme, which is confirmed by Fig. 4, *b* and corresponds to value $d_A = 830$ μm. Considering that, according to various estimates, d_A during heating of a railway wheel blank can vary at range of 800 to 1000-1500 μm [8], the obtained extrapolation result (Fig. 4, *b*) illustrates good agreement.

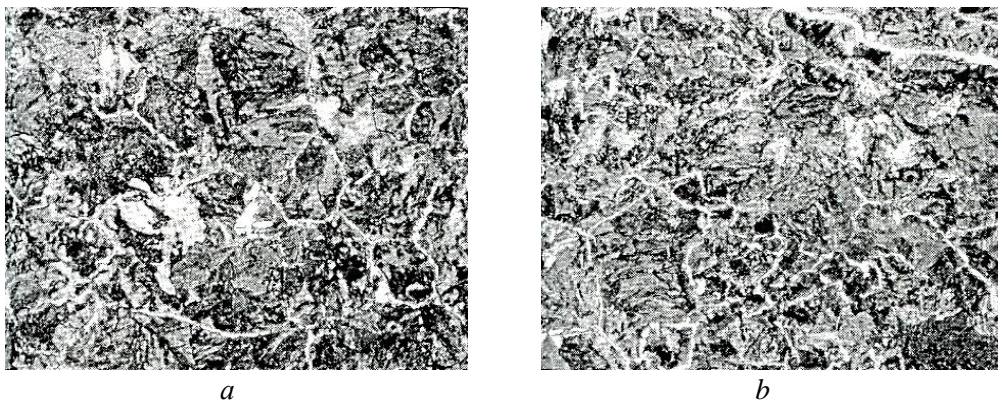<center>*a*   *b*</center>

Figure 3. Influence of two-step hot compression (a: 20%+20%, b: 30%+30%) at 1240 °C on the austenite grain morphology of 0.6% C steel. The micrographs indicate finer fragmentation in the two-step deformation scheme, especially at lower compression stages.

As follows from [18], the exponent b is a structurally sensitive characteristic and obeys the relation:

$$b = b_1 - (m + g + s) \tag{4}$$

where b_1 is a certain value; m is the contribution from hot work hardening of austenite; g is the presence of a substructure and s is the duration of pause after deformation.

From (4) it follows that in proportion to the decrease at effect of m, g and s, b will increase up to a maximum value (b_1), but not more than 2 [17].

According to the wheel blank compression technology, the contribution s is practically constant for different deformation schemes. By representing (4) as (5) and substituting $b_1 = 2$, we can estimate the influence of the hot compression scheme on the total contribution of hot work hardening and presence substructure of the austenite, on the grain size:

$$(m + g) = 2 - b \tag{5}$$

After calculations, we found that for the identical degree of hot deformation, after a single compression, the substructure effect is preserved to a greater extent $(m + g) = 0.87$ than after a double compression $(m + g) = 0.64$.

The current model describing the relationship between deformation degree and austenite grain size is based on a power-law correlation, as shown in Equations (2) and (3). This aligns with classical models such as those presented by Verner [17] and Holt [16].
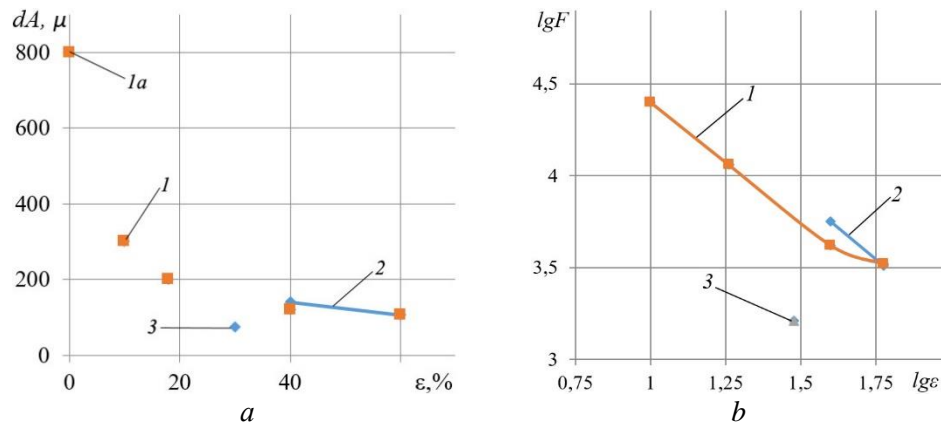

Figure 4. (a) Evolution of austenite grain size (dA) with respect to total strain and deformation scheme. (1a – heating only, 1 – single-stage, 2 – double-stage, 3 – triple-stage). (b) Log-log plot of grain area (F) vs strain (ε) for determination of model parameters (A, b).

With continuous deformation, the effect of the austenite substructure on the development collective recrystallization is proportional to the degree of deformation, which is determined by the condition of its continuity of propagation. With constant holding after deformation, dA will be inversely proportional degree of compression. With fractional compression, conditions of deformation propagation change, which can affect the development of recrystallization processes.

Compared with a single compression, dividing the deformation into certain parts should lead to a decrease at intensity of strain hardening of austenite and number of defects at crystalline structure as a whole.

Indeed, after first compression, in addition to the twice lower degree of deformation, the high-rate development of dislocation recombination will lead to certain substructure changes, such as polygonization or fragmentation. At process of repeated deformation, substructure changes will already be dependent on the previous deformation of the metal. The more developed substructure observed in single-stage deformation is attributed to continuous dislocation accumulation, which enhances polygonization and inhibits early recrystallization. This differs from the double-stage where partial relaxation occurs between stages.

Based on this, the austenite substructure after a single compression will inevitably differ from the deformation in two stages, which is confirmed by the complex of metal properties. The obtained qualitative result requires additional experimental confirmations, in order to explain the mechanism of the observed phenomenon in more detail. Despite this, the obtained result of the influence of the hot deformation scheme of carbon steel can be useful in developing the technology of thermal strengthening of rolled products using heating for hot reduction of metal.

4. CONCLUSIONS

The evolution of austenite grain size (dA) and the mechanical response of carbon steel under varying hot deformation schemes demonstrates a consistent trend with increasing strain. Specifically, dA decreases from 140 µm at 20% deformation to approximately 106 µm at 60% strain during single-stage processing. Regardless of the deformation mode employed, increasing the degree of compression exerts a qualitatively similar influence on grain refinement and the overall mechanical performance of the steel. However, at moderate strains ($\varepsilon \approx 20\%$), the application of a two-stage deformation approach significantly enhances the strength–ductility balance, yielding up to a 10% increase in tensile strength and an improvement in ductility by as much as 40% when compared to single-stage processing. This can be attributed to alterations in the recrystallization dynamics and substructure development of austenite, where two-stage deformation facilitates more controlled grain evolution. As strain approaches or exceeds 60%, the differences in grain size and yield strength between single- and double-stage deformation become negligible due to the completion of

dynamic recrystallization. Consequently, for thermomechanical processing routes where the total strain remains below the critical threshold of 60%, a double-stage deformation strategy is recommended to optimize the synergy between strength and ductility without compromising microstructural stability.

REFERENCES

[1]   F. Haessner, Recrystallization of metallic materials, Dr.Riederer Verlag GmbH, Stuttgart, 1978.

[2]   H. Gleiter, B. Chalmers, High-angle grain boundaries, Pergamon Press Oxford, 1972.

[3]   A. Chamanfar, S.M. Chentouf, M. Jahazi, L.-P. Lapierre-Boire, Austenite grain growth and hot deformation behavior in a medium carbon low alloy steel, Journal of Materials Research and Technology, 9, (2020), 12102–12114.

[4]   I. Vakulenko, S. Plitchenko, D. Bolotova, K. Asgarov, Influence hot plastic deformation on the structure and properties of carbon steel of the railway wheel, Zeszyty Naukowe. Transport/Politechnika Śląska, (2023).

[5]   I.A. Vakulenko, L. Vakulenko, D. Bolotova, B. Kurt, H. Asgarov, Ö. Çölova, Influence structure on the plasticity of carbon steel of the railway wheel rim in operation, Zeszyty Naukowe. Transport/Politechnika Śląska, (2022) 183–192.

[6]   A.F. Yilmaz, Assessment of Combinability of S235JR-S460MC Structural Steels on Fatigue Performance, Transactions of the Indian Institute of Metals 77, (2024), 323–331. https://doi.org/10.1007/s12666-023-03113-x.

[7]   J.-W. Seo, H.-M. Hur, S.-J. Kwon, Effect of mechanical properties of rail and wheel on wear and rolling contact fatigue, Metals (Basel) 12, (2022), 630.

[8]   A.I. Babachenko, Reliability and durability of railway wheels and tires, Dn-vsk: GVUZ" PGASA, (2015).

[9]   R. Thackray, E.J. Palmiere, O. Khalid, Novel etching technique for delineation of prior-austenite grain boundaries in low, medium and high carbon steels, Materials 13, (2020), 3296.

[10] I.O. Vakulenko, Structural analysis in materials science, Makovetsky, Dnepropetrovsk, 2010.

[11] S. Gnapowski, M. Opiela, E. Kalinowska-Ozgowicz, J. Szulżyk-Cieplak, The Effects of Hot Deformation Parameters on the Size of Dynamically Recrystallized Austenite Grains of HSLA Steel, Advances in Science and Technology. Research Journal 14, (2020).

[12] Yu. Liang, S. Xiang, Y. Liang, M. Yang, Z. Wei, H. Xiong, J. Li, Effect of original oustenite grain size on the microstructure and toughness of pearlite steel , Materials Reports, 31, (2017), 77–81.

[13] F. Zhang, Y. Zhao, Y. Tan, X. Ji, S. Xiang, Study on the nucleation and growth of pearlite colony and impact toughness of eutectoid steel, Metals (Basel), 9, (2019), 1133.

[14] F.B. Pickering, B. Garbarz, The effect of transformation temperature and prior austenite grain size on the pearlite colony size in vanadium treated pearlitic steels, Scr. Metall.;(United States) 21 (1987).

[15] G.D. Sukhomlin, Specific Boundaries in Ferrite of Low-Carbon Steels, Metallofızıka I Noveıshıe Tekhnologıı 35 (2013) 1237–1249.

[16] D.L. Holt, Dislocation cell formation in metals, J Appl Phys 41 (1970) 3197–3201.

[17] R. Verner, Izmeljchenie zerna pri goryacheyj deformacii, in: Chernihe Metallih, 1969: pp. 34–43.

[18] I.G. Uzlov, O.N. Perkov, I.A. Vakulenko, Vliyanie skhemy goryachey deformatsii zagotovki na svoystva metalla oboda tselnokatanykh zheleznodorozhnykh koles, Fundamentalnye i Prikladnye Problemy Chernoy Metallurgii 5 (2002) 196–199.